INFORMATION TO USERS

The most advanced technology has been used to photograph and reproduce this manuscript from the microfilm master. UMI films the text directly from the original or copy submitted. Thus, some thesis and dissertation copies are in typewriter face, while others may be from any type of computer printer.

The quality of this reproduction is dependent upon the quality of the copy submitted. Broken or indistinct print, colored or poor quality illustrations and photographs, print bleedthrough, substandard margins, and improper alignment can adversely affect reproduction.

In the unlikely event that the author did not send UMI a complete manuscript and there are missing pages, these will be noted. Also, if unauthorized copyright material had to be removed, a note will indicate the deletion.

Oversize materials (e.g., maps, drawings, charts) are reproduced by sectioning the original, beginning at the upper left-hand corner and continuing from left to right in equal sections with small overlaps. Each original is also photographed in one exposure and is included in reduced form at the back of the book.

Photographs included in the original manuscript have been reproduced xerographically in this copy. Higher quality 6" x 9" black and white photographic prints are available for any photographs or illustrations appearing in this copy for an additional charge. Contact UMI directly to order.

Dynamical theory for high-energy electron reflection

Ma, Yiqun, Ph.D.

Northwestern University, 1990

NORTHWESTERN UNIVERSITY

DYNAMICAL THEORY FOR HIGH ENERGY ELECTRON REFLECTION

A DISSERTATION

SUBMITTED TO THE GRADUATED SCHOOL
IN PARTIAL FULFILLMENT OF THE REQUIREMENTS

for the degree

DOCTOR OF PHILOSOPHY

Field of Materials Science and Engineering

by

Yiqun Ma

EVANSTON, ILLINOIS

June 1990

DYNAMICAL THEORY FOR HIGH ENERGY ELECTRON REFLECTION

Yiqun Ma

ABSTRACT

High energy electron reflection (HEER) is an important technique in surface science, which uses the information carried by high energy electrons reflected from surfaces to study surface structures and surface electronic states. With the development of the application of reflection high energy electron diffraction (RHEED), reflection high energy electron microscopy (RHEEM) and reflection high energy electron energy loss spectroscopy (RHEEL) in surface science, the usefulness of HEER has been widely recognized and demonstrated. However, the development in HEER has been stagnated by slow development of dynamical theory for this technique. For a long time, the theory of HEER did not progress much further than kinematic principle, although the dynamical approach has been attempted by many authors. A stationary dynamical solution for an arbitrary surface for HEER has not been ever obtained. The importance of dynamical analyses and stationary solutions for HEER is due to the facts that high energy electron scattering from a crystal surface is basically a dynamical phenomenon and the RHEED patterns and RHEEM images in experiments are the

results of stationary diffraction processes between incident electrons and crystal surface.

There are three major achievements in HEER introduced in this thesis:

i) The introduction of the concept of current flow has solved the Bloch wave solution in reflection and removed the confusion around the wave points in the "band gap" in the Bragg case.

ii) Taking the multislice calculation in the reflection case as the Picard iteration leads to the emerging of the BMCR method (Bloch wave + Multislice Combined for Reflection).

iii) The edge patching method (the EPMO method) has solved the problem of edge effects in multislice calculation for reflection and finally makes the infinitely convergent (convergence not limited by iteration thickness) stationary dynamical solution for HEER obtainable for arbitrary surfaces.

These developments hopefully will have important impacts on HEER.

Professor L. D. Marks
Department of Materials
Science and Engineering
Northwestern University
Evanston, IL 60208
U. S. A.

"The true value of a human being is determined primarily by the measure and the sense in which he has attained liberation from the self."

_____ Albert Einstein

ACKNOWLEDGEMENTS

I am deeply indebted, and wish to extend my sincere gratitude to my thesis advisor, Professor L. D. Marks, whose wealth of knowledge, patience and understanding guided me through all the difficulties encountered during the course of this work.

Additionally, during the course of my tenure at Northwestern University, I had the deep pleasure to be associated with many of my groupmates and people inside and outside the department and their help and sharing offered me a enjoyable and friendly working environment, for which I would like to express my sincere thanks to them.

My special thanks go to my groupmate John Bonevich. Many schematic diagrams in this thesis are due to his work on Macintosh computers.

I would also like to thank Z. Y. Zhao and Dr. H. P. Cheng for several helpful discussions on the boundary value problem in quantum mechanics.

Special and deep thanks are extended to my dear wife, S. Liu, whose emotional support and diligent typing help me finally finish the last chapter of this work.

Lastly, I would like to thank the sponsor of this

project, National Science Foundation. Without its financial support, current achievements can never be made.

TABLE OF CONTENTS

LIST OF TABLES

LIST OF FIGURES

multislice method.

surface for the same conditions as for Fig.4.4 but with a vicinal surface 2.5° off [010)]zone axis: (a) diffraction pattern and (b) y-modulated representation of the same. In (a) some of the stronger satellite spots are indexed.

value is fully real.

and step-down (ii). The thicknesses of the
first and last slices are 0 and 607.5Å
respectively. The thickness difference between
two nearest slices is 50Å, the size of unit
cell in the calculation 16ax1a, the size of
unit cell displayed 8ax2a and the absorption
10%. The beam incidence is 25mRad. The step is
introduced in at t=101.2Å.

numbers of both (i) and (ii) are: 1, 100, 300, 600, 900, 1000, 1100, 1200, 1300, 1500, 1700, 2050.

Fig.5.21. (a) Experimental RHEED pattern taken from GaAs   218
(001) surface by Cho (1971). The incident
glancing angle is about 1° and the azimuth is
along the [1̲1̲0] orientation. Electron energy
is 40keV. (b) Schematic diagram of GaAs(001)
surface view at normal incidence.

Fig.5.22. (a) Diagram of the primitive unit cell of GaAs   218
along the [1̲1̲0] zone axis. Slice constructions
for multislice calculations for a perfect GaAs
(001) surface (b) and a GaAs(001) surface with
one missing row reconstruction along the
incident beam direction (c).

Fig.5.23. Calculated RHEED patterns for three different   219
surfaces: (a) perfect GaAs(001) surface, (b)
GaAs(001) surface with the 2x2 reconstruction
and (c) GaAs(001) surface with the 2x8
reconstruction. Electron energy is 40keV. The
incident glancing angle is 1° and the azimuth
is along [1̲1̲0] orientation.

Chapter I. Introduction

1.1. General review of studies on high energy electron reflection

The history of surface investigations using reflected high energy electrons can be traced back to the early development of electron diffraction in a solid. Since the time when the first reflection high energy electron image (RHEEM) was obtained by Ruska [1] and the first reflection high energy electron diffraction pattern (RHEED) by Nishikawa and Kikuchi [2-3], it has developed both theoretically and experimentally in different directions: imaging (RHEEM), diffraction (RHEED) and energy loss spectroscopy (RHEEL). The combination of these approaches has proved to be a powerful tool to study the structure and electronic state of crystal surfaces and the correlation between the two, because of the rapid development of this field in the first half of this century. The image and diffraction pattern of reflected electrons offer information of the structure of crystal surfaces, while the energy spectrum of reflected electrons can show the electronic state of the surface.

The advantages of using reflected high energy electrons can be listed as:

i) Short wave-length and high resolution in images.

ii) Relatively small inelastic scattering with respect to the incident wave.

iii) Relatively small absorption with respect to the incident wave.

iv) High surface sensitivity for small glancing incident angles.

v) Modern techniques can combine these different approaches together in one microscope, which will lead to a combination of surface science and traditional electron microscopy.

With the development of ultra-high vacuum (UHV) techniques and electron optical systems, there has been a revival of interest in high energy electron reflection, as opposed to low energy electron reflection which is utilized for both diffraction (LEED) [4-5] and imaging (RLEEM) [6]. Experimentally, the new revival has resulted in developments in the studies of molecular beam epitaxy (MBE) using RHEED patterns [7-9] and the studies of various surface features by high resolution RHEEM [10-11].

Significant progress was made in RHEED applications to crystal growth recently. Intensity oscillations in the specularly reflected and various diffracted beams in the RHEED patterns were found to correspond to layer-by-layer growth

[12-13]. The technique of RHEED has already been widely used in surface investigations such as surface recrystallization, reconstruction, relaxation [14] and surface resonance [15].

The images obtained in high resolution RHEEM can provide real space information concerning structural variation on crystal surfaces as a comparison to the reciprocal space information in RHEED, which is similar to dark field imaging in transmission high energy electron microscopy (THEEM). The full power of RHEEM was demonstrated by the studies of Shimizu et al.[16], in which the surface dynamic processes were recorded in-situ by RHEEM.

Energy loss analysis in the reflection mode was initiated by Cowley [17]. It has been recently applied for surface investigation in both real space (RHEEM) and reciprocal space (RHEED) [18]. Information about the composition, atomic coordination of surface layers of crystals together with information of surface structures can be revealed by this technique.

The developments in these fields have showed some promise, although RHEEM is limited by a severe foreshortening of the images due to the small glancing incidence angle and RHEED is limited by the smearing of the pattern resulting from surface inelastic scattering, surface relaxations and

imperfections.

1.2. Experimental development of reflection high energy electron microscopy (RHEEM)

Since 1933, when Ruska [1] first imaged the surface of solids with electrons reflected from the surface, the technique of reflection high energy electron microscopy (RHEEM) has experienced an unsteady development. This is due to: 1) the competition of other surface imaging techniques, such as replica and shadowing technique, scanning electron microscopy (SEM); 2) the underdeveloped EM instrument in the early days. The arrangement of the imaging system used by Ruska is shown in Fig.1.1. Since it used high angle scattered electrons, the resolution was poor. In 1940, Borries [19] used small angle scattered electrons to image gold surfaces. The resolving power was improved to 500Å (Fig.1.2). Unfortunately, the advent of the replica method in THEEM which yielded valuable information in many fields of surface study, resulted in low interest in RHEEM. However, apart from defects and uncertainty in the replica process itself, there is a basic limitation imposed on the replica method because: 1) it is not the surface itself which is examined in the microscope; 2) it is impossible to study the surface at high resolution; 3) it

is impossible to carry out in-situ studies on the surface.
Therefore, RHEEM was revived with the works of Cossleft [20],
Fert and Saporte [21], Menter (Fig.1.3) [22], Haine et al.[23]
and Page [24] in 1950's.

RHEEM, however, was abandoned again with the development
of SEM which achieved the same or better resolution under far
more favorable circumstances.

The interest in RHEEM was revived in 1975 by Cowley and
Nielsen [10-11] with the emphasis put on diffraction contrast
for the purpose of studying the crystalline structure of solid
surfaces. Since then, experiments have been done with ordinary
as well as specially modified UHV electron microscopes. The
types of specimens studied include metals, semiconductors and
insulators.

In 1980's, Osakabe et al. [25] first used a UHV electron
microscope with a modified specimen holder for RHEEM. The
specimen holder is capable of both heating (1200C) and cooling
(20K), which makes in-situ observation possible. The process
of cleaning by heating Si(111) surfaces with 1x1 and 7x7
structures was clearly shown in both the RHEEM image and RHEED
patterns. The phase transition from the 1x1 structure of the
cool dirty surface to a 7x7 structure of the heated clean surface
was observed. It was found that gold deposition produced the

transformation of the 7x7 structure to 5x1, 3x3 and 6x6 structures. Further studies of the same group [26] suggested that the phase transition was first order and a model of the 7x7 structure was proposed based upon ordered vacancies or adatoms instead of the static displacements of the surface atoms. Simultaneously, the image contrast of dislocations and atomic steps on Si(111) surface were also recorded [27].

Later on, Hsu [28-30] applied RHEEM to the surface of single crystal metals (Au, Pt) and semiconductors in a conventional electron microscope. Regularly spaced steps on the vicinal surface were recorded and atomic steps on the terraces resolved in the RHEEM images, and the images of surface dislocations were confirmed. The highest resolution was 9Å (Fig.1.4).

RHEEM was first introduced to study the mechanism of MBE on GaAs low miller indices surfaces by Cooman et al. [31] in 1984. Compared to THEEM in this area, RHEEM is more informative and the specimen preparation is reduced to a minimum.

Studies using RHEEM were also carried out on single crystal oxide surface by Uchida et al.[32]. Surface steps of atomic height on MgO smoke particles were detected in RHEEM. The same group also investigated the effects of different treatments for cleaning a surface, such as Ar-ion bombardment, annealing, chemical etching and electron-polishing on the single crystal

metal surface [33]. The images clearly showed the high quality of flat Au(111) surface after being annealed for one hour at 500C in UHV.

An important step in RHEEM was started by Shimizu et al.[34], in which the in-situ observation method was first introduced into the RHEEM studies. A gas inlet device was constructed for an UHV electron microscope. The dynamical processes of oxidation on Si(111)-7x7 surface at various temperatures were studied in-situ by RHEEM. The oxidation temperature of the Si(111)-7x7 surface was found at about 730-750C. The observation of 7x7 lattice fringes during the oxidation was also reported. Their recent studies revealed more information about the formation and diffusion of surface vacancies, distribution of hollows on the terraces of the Si(111)-7x7 surfaces and the growth kinetics [16]. The quantitative data included an activation energy of 1.4eV for the surface diffusion of the vacancies on Si(111)-7x7 surface and a reaction rate of 0.23 at 630C for forming two vacancies by an impinging oxygen molecule on the surface.

More detailed investigations on various crystal surfaces by RHEEM are continuously reported. Double contours of monatomic steps on single crystal surfaces were observed [35-36]; the effects of azimuth on RHEEM images were studied [37]; and the

observation of crystal surfaces on Si cylindrical single crystal specimen was recently reported [38].

There are several major advantages to RHEEM:

i) RHEEM can be used directly for bulk specimens. Thus the specimen preparation for RHEEM is much easier than that for THEEM, HREM and FIM, and the information loss during the preparation is not a problem.

ii) Because RHEEM is a direct observation technique and there is an opportunity for the in-situ observation of surface reactions by RHEEM, it is possible to investigate the surface at relatively high resolution while carrying out physical or chemical experiments on the surface (such as interaction with gas, crystal growth, mechanical deformation and ion sputtering etc.).

iii) Conventional THEEM facilities can be used to perform RHEEM. This will greatly extend the usage of THEEM facilities.

iv) Combination of RHEEM with RHEED and REEL for surface investigation can provide otherwise unobtainable information about the surface.

v) The theoretical limit of resolution for RHEEM is around 10Å [11,39]. The best resolution obtained to date in RHEEM is 9Å. Its resolving power is considerably stronger than other surface imaging technique except scanning tunneling microscopy (STM).

STM is a big challenge to the RHEEM technique. It also

has atomic resolving power and can work in a much broader environment. However, due to the small gap between scanning tip and the investigated surface and the speed limitation of the mechanical motion of the tip, the observation of in-situ dynamical surface reaction is difficult for STM. In addition, it is still not a direct imaging technique. The recorded physical quantity is the height instead of the intensity reflected from the objects.

Low energy electron reflection microscopy (RLEEM) is another alternative technique to RHEEM. As RHEEM is related to RHEED, RLEEM is associated with LEED. The difficulty of making a suitable electron optical system suggests that the resolution of the technique is limited.

Clear surface atomic images have been routinely obtained using high resolution electron microscopy (HREM) technique [40-41]. In HREM, however, only a projection of the surface is imaged and the two dimensional information is reduced to one dimensional.

Scanning reflection electron microscopy (SREM), which makes use of the scanning capability of STEM facilities, has a similar imaging geometry to that of RHEEM, except that the electron beam is scanned across the surface, instead of being static as in RHEEM. Nevertheless, like SEM, its resolution is limited by the beam size and energy dissipation of the electron in the

bulk, although in principle it should equal that in RHEEM.

Like all other techniques, RHEEM has its limitations:

i) Foreshortening is the major disadvantage of RHEEM, which is decided by the geometry of RHEEM.

ii) The resolution of RHEEM is mainly limited by chromatic aberration (10Å), which means that atomic imaging by RHEEM will be very difficult, if not impossible.

iii) Because of the geometry of RHEEM, the surface in the direction of the incident beam can not be completely focused. This makes the interpretation of RHEEM images complicated.

As a summary, the surface features and phenomena that have been investigated and observed using RHEEM up to now are:

i)   Surface steps   [25,27,28,30,34,36,37,38]

ii)   Surface dislocations   [28,30,39,41,42,43]

iii)   Surface reconstructions   [25,26,34,35]

iv)   Superlattices   [31]

v)   Surface Oxidation   [34,35]

vi)   Surface vacancy formation   [35]

vii)   Surface stacking faults   [98]

     The materials studied by RHEEM are:

i)   Graphite   [98]

ii)   Diamond   [42,45]

iii)   MgO   [32]

iv)	PbS	[45]
v)	Fe_2O_3	[46]
vi)	$TiS_{1.5}$	[46]
vii)	Au	[28,29,33,36,37,]
viii)	Pt	[28,29,33,36,37,45]
ix)	GaAs	[30,46,47]
x)	GaP	[48]
xi)	$Ga_xAl_{1-x}As$/GaAs	[31,49]
xii)	Au/MgO	[50]
xiii)	Si	[25,26,27,34,35, 36,38,49,51,52]

1.3. Experimental development of reflection high energy electron diffraction (RHEED)

Unlike RHEEM, since Nishikawa and Kikuchi [2,3] first obtained the RHEED pattern, the technique has experienced a steady development. This is mainly because the information in RHEED is obtainable without complicated electron optics. RHEED is widely used in surface science as an alternative technique to LEED for studying surface reconstruction, nucleation, crystallization and the mechanism of crystal growth. In many cases, it is applied in a special RHEED apparatus [53] instead of being associated with an electron microscope, i.e. an electron

optical system.

The usefulness of RHEED was recognized for its early applications in surface studies, such as oxide films on crystal surfaces [54], metal films formed by liquid phase epitaxy (LPE) [55] and surfaces covered by organic molecules [56]. However, the development of RHEED was overshadowed by vigorous progress in transmission high energy electron diffraction (THEED) combined with THEEM. For a long time, the RHEED method for studying surface structure was considered to be unimportant because of the rapid development of THEED and LEED, although significant progress in RHEED has still been made by a relatively limited number of researchers, such as Trepte et al., Sewell et al. [58], Cho [59] and Menadue [60].

Trepte et al. clearly demonstrated that the diffraction pattern and Kikuchi map in reflection are available for identifying the zone axis and reconstructions on a single crystal Cu surface. Oxygen adsorption on Cu surface was observed as additional spots in a RHEED pattern. Different high miller index Cu surface planes, based on low miller indices surfaces such as (001), (111), and (011) were identified in the diffraction pattern. In a short report in 1969, Henderson et al. [61] showed RHEED patterns from iodine covering Si(111) surface in different zones using 40keV electrons. The patterns proved that in agreement

with the LEED results, iodine formed a hexagonal net of atoms with silicon spacings. As the author pointed out, the available polish and etch techniques produce satisfactory surfaces, although RHEED experiments demand a very smooth flat surface which is critical to the experiment. No charging of the surface was found in RHEED mode as might be expected from highly resistive silicon. The author also noticed an important advantage of RHEED when the sample is illuminated by a small and well confined primary beam.

The observation of β-SiC formation on Si (111) surfaces was first reported using the RHEED technique [62]. Strong evidence of SiC was found by measuring the lattice constant. The temperature related formation and desorption processes of SiC on Si (111) were observed using in-situ RHEED. The authors pointed out from geometrical considerations that RHEED might be a more sensitive technique for polycrystalline particle-like surface impurities.

In the studies of Menadue [60], Si (111) surfaces were examined by RHEED in UHV. The intensities of the {hhh} systematic set of the Bragg reflections from the 2nd and 7th orders were quantitatively measured as a function of azimuth angle, rocking angle and temperature. It is interesting that the mean inner potential V_o is determined by the refractive shift of the {hhh}

reflections towards the shadow edge. The quantitative result of V_o is 12.0±0.4eV for Si, which is very close to the calculated data for Si: 11.47eV [63]. The intensity of the low-order Bragg reflections from the net planes parallel to the Si(111) surface was plotted as the function of the incidence azimuth. Intensity peaks were clearly shown at azimuths near low-index zone axes. This was later called the surface resonance phenomena in RHEED. In their conclusions, the authors made several important points:

i) The contribution of the surface structure to high order reflections becomes rapidly less important as the penetration increases at higher angles of incidence. Thus the higher order peak intensities and their variation with temperature are suitable for comparison with a n-beam dynamical theory for the Bragg case.

ii) The measured peak intensities are well reproduced for a given specimen for each surface structure when it is reformed. Thus the relative intensities for different surface structures could be compared.

iii) Surface non-flatness must be a prime consideration.

More impressive development in RHEED was made by the group of Ino in 1977 [13,64-65]. A new RHEED apparatus (Fig.1.5) was set up in UHV especially for RHEED studies. Various surface phenomena on the Si(111) surface such as the effect of heating,

SiC structure, 7x7 surface reconstruction, 19x19 Ni structure and 5x1 Au structure were observed in RHEED patterns (Fig.1.6). The patterns by Ino et al. are much clearer and more informative than any other obtained before, and reveal the full power of RHEED for solid surface investigation. The intensity distribution of electron waves in reciprocal space was studied by different methods, for instance, oscillating the crystal to investigate the intensity distribution along the rods as it is done in X-ray analysis. RHEED has been routinely used to identify the surface reconstructions and surface steps [66-69].

A recent important development in RHEED was the discovery of the correlation between intensity oscillations in RHEED pattern and crystal growth on the surface during the MBE process [7-9]. The oscillation was found during the doping of Sn in the growth of GaAs by MBE. After the Sn doping flux was cut off and the Ga flux was reopened, a periodic and decaying RHEED intensity oscillation with time was observed. The period of the oscillation was equal to the time required to deposit one monolayer of GaAs. The intensity of the oscillation gradually decayed into a stable RHEED pattern.

A model for the oscillation was first given by Harris et al [7]. It was considered that the oscillation arises from an increase in the stress around each surface Sn atom as the GaAs

coverage increases, so that at near-complete coverage, the Sn atom is forced out of its lattice site onto the surface again.

However, the phenomenon was latter observed in all kinds of film growth by MBE. A detailed observation was made of the oscillations of the specularly reflected and various diffracted beams in the RHEED pattern during the MBE growth of GaAs, $Ga_xAl_{1-x}As$ and Ge by Harris et al.[9] and Van Hove et al.[13,70-71]. The oscillation was also reconfirmed in the RHEED pattern during the MBE growth of Si(001) and Ge(001) by Aarts et al.[72]. The results show a correlation between the amplitude of the oscillations and various parameters, such as substrate temperature, incidence angle and azimuth of electron beam. Because the periodicity of oscillation in all observations corresponds exactly to the growth of a single monolayer, it provides an absolute measurement of the growth rate.

Since the intensity oscillation is a common phenomenon in MBE growth, it should be considered as an intrinsic property of each system, although it may be enhanced by the presence of certain impurities. Therefore, Van Hove et al. [13] proposed a new model for the phenomenon and interpreted the oscillations as a consequence of the competition between nucleation and step growth. In their argument, which is based upon kinematic theory, the diffracted beams from flat terraces on a surface with random

steps are remodulated by surface steps as:

$$A = \sum_i A_i . \exp[i.\underline{S}.\underline{R}] \qquad (1.1)$$

where A_i is the amplitude of total wave including dynamic effects diffracted from the ith terrace. The momentum transfer is $\underline{S}=2\pi(\underline{k}_f-\underline{k}_i)$ where $k_i=k_f=1/\lambda$ are the initial and final wave vectors. ki is a vector from the origin to the edge of the ith step. If $\underline{k}_i$ is expressed as $\underline{k}_i=\underline{d}_i+\underline{L}_i$, where $\underline{d}_i$ is perpendicular to the surface and $\underline{L}_i$ is parallel to the surface, then the diffracted amplitude is

$$\sum_i A_i . \exp[i.\underline{S}_\perp.\underline{d}_i] . \exp[i.\underline{S}_\parallel.\underline{L}_i] \qquad (1.2)$$

where $S_\perp$ and $S_\parallel$ are the components of $\underline{S}$, perpendicular and parallel to the surface respectively. For Bragg diffraction, $\underline{S}_\perp.\underline{d}_i$ is always an integral multiple of π, while $\underline{S}_\parallel.\underline{L}_i$ continuously varies from 0 to 2π when the crystal grows layer by layer. The later term causes the intensity oscillation and the waviness of cross section width of reciprocal lattice rod.

Another interesting new development in RHEED is spot splitting which was observed first in RHEED half a century ago (Kikuchi) and reconfirmed by sensitive intensity measurement by Pukite et al. [69,73]. There had been no further studies and explanations until Pukite et al.. The results showed that the splitting is related to both the vicinal angle of surfaces and

incidence azimuth.

All these developments in RHEED indicate that kinematic theory is not enough for RHEED patterns. Unfortunately, the development of a dynamical theory for electron reflection has been rather slow, compared to that of electron transmission. This is largely due to the complexity of the boundary value problem and the nature of the Bloch waves in the Bragg case. Unlike reflection of X-rays, for which two-beam analysis is enough, high energy electron reflection is basically a n-beam dynamical phenomenon.

1.4. Development of a dynamical theory for high energy electron reflection

1.4.1. Bethe theory

Like the development of dynamical theory for the electron transmission case, early development for electron reflection case was based upon the Bethe theory [74]. The Bethe theory uses a plane wave expansion to solve the Schrodinger equation in momentum space [75] which is parallel to energy band analysis in energy space. The only difference between them is which variable, E or $\underline{k}$, is taken as an independent variable in the E-$\underline{k}$ relation. E is the total energy of the given system and $\underline{k}$ the crystal momentum.

In 1954, Miyake et al. [76] first applied the Bethe theory to the study of an anomalous enhancement of the specular beam in RHEED patterns when the reflection happened to fall on a Kikuchi line. The authors indicated that enhancement of the specular reflection occurred when a Bragg reflection in a side direction took place inside the crystal and proposed that the phenomenon can be interpreted as the result of "the Bragg reflection on a side plane". The total reflection of internal waves at the surface played an important role in producing the enhancement. However, a basic problem was determining the wave points which are excited in and between bands. Therefore, the major part of the discussion was qualitative. Later on, Kohra et al. [77] used the Bethe theory to explain the phenomenon for a four-beam case. An enhanced specular beam was shown in the calculated rocking curve. In the paper, the role of energy flow for determining wave points was first mentioned. Unfortunately, a quantitative and analytical formalism of energy flow for the reflection case was not discussed.

Ten years later, Kawamura et al. [78] studied the intensity anomaly and its temperature dependence using the Bethe theory for the eight-beam case. The most impressive statement in the paper is: "The dispersion surface is generally a complex hyper surface, on which those tie points (i.e. wave points) that are

physically allowable must be selected; thus eigenvalues $k_\perp$ corresponding to the negative energy flow into the crystal should be omitted." Unfortunately the train of thought just stopped there and the next statement led elsewhere. For a long time, how to handle a complex dispersion surface and energy flow both analytically and numerically has not been found. This has been a major obstacle to the development of dynamical theory of electron reflection.

In 1970's, Colella and Menadue [79,80] introduced an alternative way of applying the Bethe theory to the reflection case. To avoid the dilemma of determining wave points on the dispersion surface, an additional bottom boundary was introduced. Because of the back reflection from the bottom, all possible Bloch waves are excited in the crystal. Therefore, there are 2n Bloch waves and 2n equations due to the boundary conditions and the problem has a unique solution, which means that the determination of excited wave points on the complex dispersion surface is not necessary. When absorption is introduced and the distance between the top boundary and bottom boundary is set large enough, the model becomes close to the real reflection from the surface of a bulk crystal. The forward transmission waves are attenuated to zero at the bottom and the back reflection has only a virtual existence. The same method was brought up

by Moon [81] simultaneously, who used the Hill's determinant method for the eigenvalue search. The method has two basic disadvantages: i) The computation speed is slowed down by introducing a 2nx2n matrix and one additional bottom boundary; ii) The physical mechanism of reflection is concealed in the numerical processes and the analysis of energy flow becomes impossible, although it plays an important role in understanding the physics of electron reflection. Another fault of the approach is the surface truncation; the crystal potential is truncated at the top atomic layer, and the space right above the top layer is considered as free space, while a real surface potential exponentially extends into vacuum. Some experiments have indicated that the effects of transition layers of surfaces on the results are nontrivial. This was latter on discussed by Britze et al. [82] using the WKB method, in which the potential varies continuously in the transition region between crystal and vacuum and a variation of the topmost interlayer spacing is allowed for. In the transition region, the Schrodinger equation was solved approximately using the WKB method. The authors claimed that the assumption of a continuous potential transition instead of a potential step is important, while the exact form of the transition potential is essentially unimportant. Nevertheless, the validity of the method has not been rigorously examined

both theoretically and experimentally. The role of the surface potential in high energy electron reflection has not been well understood.

1.4.2. "Parallel multislice" method

The Bloch wave method in principle is only suitable for a perfect and periodic crystal, while a lot of surface phenomena result from surface imperfections, such as surface steps, clusters, dislocations, reconstructions, relaxations and a surface potential. This means that it is necessary to find alternative ways which are adapted to the simulation of surface imperfections. Borrowing the concept of slice used by Darwin [83] for X-ray diffraction in crystals, Maksym et al. [84] developed a new method for electron reflection in which a crystal is considered perfect and periodic in the plane parallel to surface, and the non-periodic modulation of the potential only occurs in the direction normal to the surface. Then the crystal is sliced along the plane parallel to the surface. The whole concept of the method is quite similar to that of scattering matrix method [85] used for transmission case. However, unlike the scattering matrix which starts off with plane wave equation, it starts off with the Schrodinger equation. Both the crystal potential and crystal wave are expanded in two dimensions parallel to the surface:

$$V(\underline{r})=\sum_q V_q(z) \cdot \exp[i.\underline{q}_1.\underline{\rho}] \qquad (1.3)$$

$$\psi(\underline{r})=\exp[i.\underline{k}_1.\underline{\rho}]\sum_{q_1}\phi_{q_1}(z)\exp[i.\underline{q}_1.\underline{\rho}] \qquad (1.4)$$

where $\underline{k}_1$ is the parallel component of the incident wave vector.

Substituting (1.3) and (1.4) into the Schrodinger equation,

the coefficients ϕ_{q_1} obey the following system of equations which

are equivalent to the Schrodinger equation in 3-D momentum space:

$$d^2\phi_{q_1}/dz^2+k^2_{q_1}\phi_{q_1}=(2m/h^2)\sum_{q_{11}}.V_{q_1-q_{11}}.\phi_{q_{11}} \qquad (1.5)$$

where

$$k_{q_1}^2=(2mE/h^2)-|\underline{k}_1+\underline{q}_1|^2 \qquad (1.6)$$

Equation (1.5) was solved by an integration algorithm using

the boundary condition:

$$\phi_{q_1} \to \delta_{q_{11_0}}\exp[-ik_{q_1}z]+R_{q_1}\cdot\exp[ik_{q_1}z] \quad \text{for } z\to\infty \qquad (1.7)$$

$$\to T_{q_1}\cdot\exp[-ik_{q_1}z] \quad \text{for } z\to-\infty \qquad (1.8)$$

Equation (1.5) latter on was solved by Ichimiya [86] using a

matrix approach, which mathematically is similar to the scattering

matrix method for transmission. There are two major differences

between the two: i) the reflection waves are included in the

former, while they are omitted in the latter, ii) the transform

matrix in exponential form is diagonalized by eigenmatrices

in the former, while it is calculated directly by expanding

the exponential matrix into a power series in the latter.

The "parallel multislice" approach was latter on widely

used in RHEED and RHEEM analyses in various materials [87-89]. Good agreement between experimental and theoretical data was claimed. However, the limitation of the approach is that it is inherently unsuitable to calculate the reflection waves from the crystal defects involving structural variation along beam direction. The validity of the method requires verification from a more fundamental method--the Bloch wave method and the claim of agreement with experimental data in certain circumstance is not a proof of its theoretical integrity. Finally, conservation of energy, momentum and energy flow along the boundary can not be analyzed by the method, which is important for the understanding of reflection physics.

1.4.3. "Vertical Multislice" method

Another alternative approach for reflection dynamical calculation was introduced by Peng and Cowley [90-91], which was based upon the multislice formulation developed by Cowley and Moodie [92-94]. Unlike Maksym's method and the scattering matrix method, the slices of crystal are taken normal to surface as they are for profile image simulations for transmission. The periodicity of the crystal potential breaks down at the surface and an artificial periodicity is imposed by assuming the whole slice of crystal and vacuum repeats in the direction

normal to the surface. The initial state, i.e. the incident electron wave is constructed as a plane wave in the vacuum which has a wave vector tilted to the surface with a small angle of interest and is smoothed by a Gaussian to reduce the artificial effects of wave edge. The wave function inside and outside the crystal are then calculated by multislice. Because there is no restriction on the way of constructing the phase grating of successive slices, it is possible to include any desired modification of the structure, such as surface relaxations, clusters, steps, even dislocations. This is the most significant feature of the method. The surface potential is also automatically included in the phase grating, which means no surface truncation. The fast computation speed for the many-beam cases is another character of the multislice algorithm developed by Cowley and Moodie.

However, the edge effects caused by imposed artificial periodicity on the unit cell and the limitation of beam size inherently stand in the way of getting a stationary solution. It usually needs more than 1500Å to reach the stationary solution. This means that the incident beam size should be at least larger than 75Å in width for a incidence angle smaller than 25mRad, if the edge effects are to be minimized. This requires the size of sampling array larger than 2024x64, which makes the calculation

difficult to handle. If simulations of surface defects are performed, the size of the array needs to be even larger. In addition, like other numerical methods, the physics is concealed by numbers and this method is also not adapted for analyses of energy flow, variation of the Bloch states, excitation of surface resonance states and external and internal reflection.

1.4.4. Other Approaches

In 1977, Shuman tried to use the column approximation to simulate surface dislocation in the Bragg case. The columns were set up normal to surface and the incident beam in the Bragg case. This violates the conditions for the column approximation: $\partial\phi_o/\partial\chi_g=0$, $\partial\phi_g/\partial\chi_g=0$ [96]. In addition, Shuman modelled the surface of the crystal as a truncated surface so that the displacement and stress field around a dislocation on the surface is identical to that around one in an infinite crystal. This apparently can not explain the large asymmetric features commonly observed around a surface dislocation core. All of these suggest that the column approximation which is successfully used in the Laue case is generally inadequate in the Bragg case.

The real-space method developed by Van Dyck [97] physically is not very much different from the multislice method developed by Cowley and Moodie. It uses a different mathematical approach

to evaluate convolution in real space. The scattering matrix method in principle is similar to the "parallel multislice" method as mentioned before. Therefore, one should not expect these methods to produce more information than the three discussed.
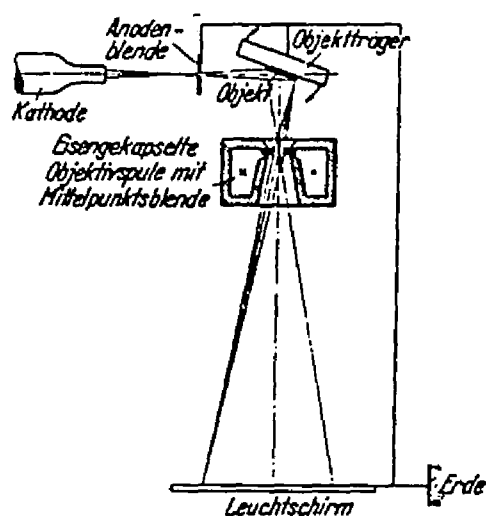
Fig.1.1. Schematic diagram of the earliest reflection election microscope (Ruska, 1933).
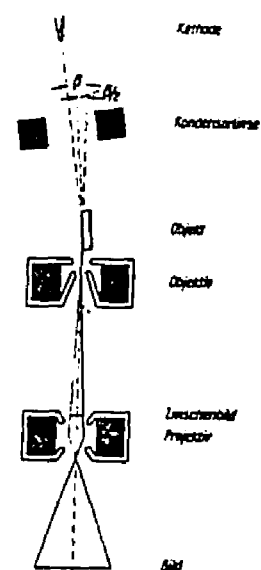
Fig.1.2. Schematic diagram of reflection microscope with a glancing incidence angle. (Borries, 1940)
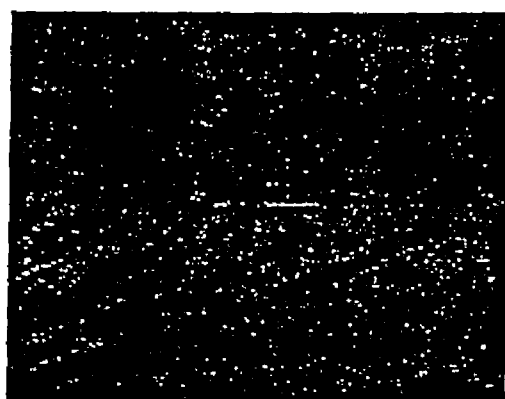
Fig.1.3. Reflection electron micrographs of cleavage steps on mica. (Menter, 1953)

Fig.1.4. High resolution image of Au surface. Steps are resolved in light band. (Hsu, 1983)
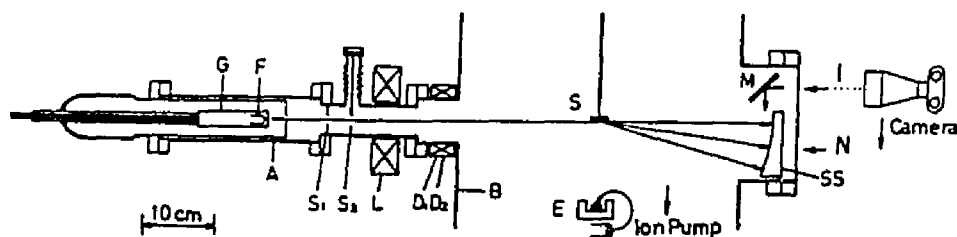
Fig.1.5. RHEED apparatus. G:electron gun. F: filament. A: anode. S_1: first slit. S_2:second slit. L: magnetic lens. D_1 and D_2: beam deflectors. B: bell jar. S: sample. E: E-gun evaporator. SS: spherical screen. M: mirror.
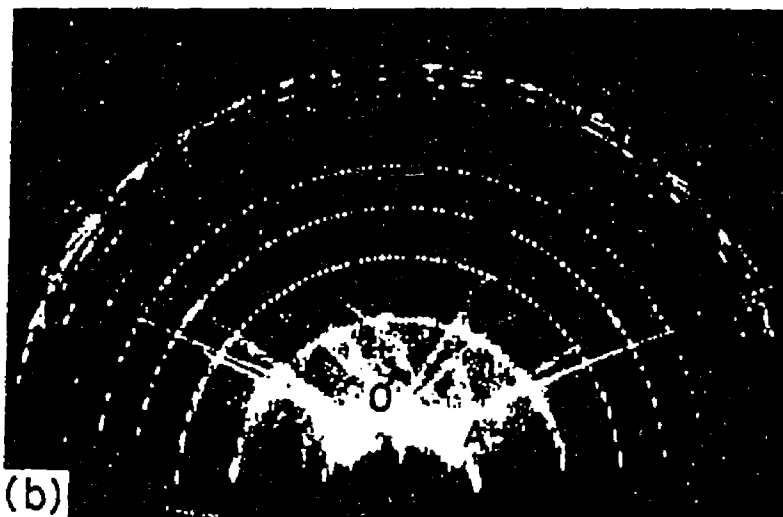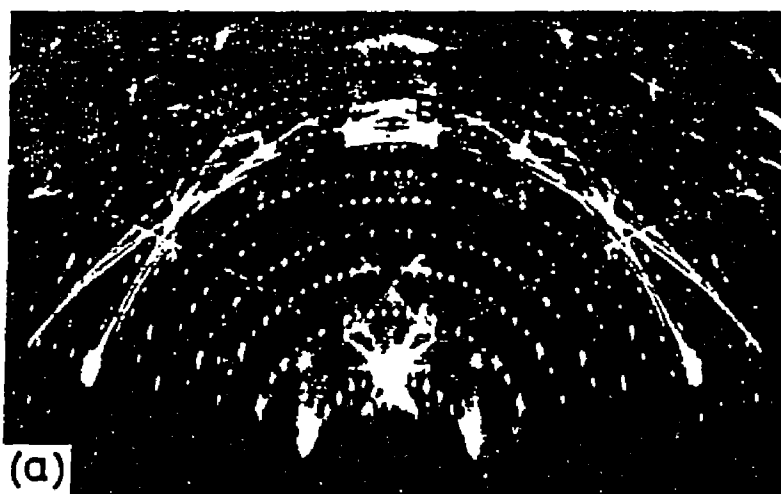
Fig.1.6. Typical RHEED patterns (20kV) taken from S_i(111) surface with the 7x7 structure. (a) and (b): [112] and [110] incidence, respectively. (Ino, 1977)

Chapter II. <u>Bloch wave solution for high</u>
<u>energy electron reflection</u>

2.1. <u>Introduction</u>

In principle, the Bloch wave method is very powerful method of understanding electron diffraction and is widely used for transmission. One of the main advantages of the Bloch wave method is that it allows access to substantial physical insights which are not often readily available in strictly numerical methods. In addition, for a thicker crystal in the Bragg diffraction case, it can be faster and more effective than numerical methods, such as multislice methods ("parallel" or "vertical"). However, the development of the Bloch wave method for RHEED or RHEEM was blocked for many decades by the difficulties of dealing with a complex dispersion surface and the wave points in the band gap between the real dispersion surfaces. This is related to the problem of evanescent waves for reflection.

This chapter will give a detailed description of both analytical and numerical solutions of the Bloch wave approach for the reflection case, in part recapping some of the earlier development of others, such as Metherell [1], and in part presenting new work particularly on the boundary value problem

solved by introducing current flow. In the process of this analysis, the importance of reflectivity via the current flow will be shown in terms of understanding the physics of reflection.

2.2. Bloch wave formulation in the general case

The general theory of dynamical electron diffraction in a crystal was first proposed by Bethe [2]. A systematic development of the theory can be found in the paper by Metherell [1]. According to the Bloch theorem, the electron wave function in a periodic potential has the form of the Bloch function:

$$\psi(\underline{r})=\exp[i2\pi\underline{k}.\underline{r}]u_{\underline{k}}(\underline{r}) \qquad (2.1)$$

where $h\underline{k}$ is the crystal momentum which characterizes the Bloch states in a specific periodic potential and $u_{\underline{k}}(\underline{r})$ has the periodicity of the Bravais lattice. Therefore $\psi(\underline{r})$ can be expanded as the Fourier series:

$$\psi^{(j)}(\underline{r})=\sum_{\underline{q}}C_{\underline{q}}^{(j)}\exp[i2\pi(\underline{k}^{(j)}+\underline{q}).\underline{r}] \qquad (2.2)$$

where $C_{\underline{q}}^{(j)}$ (j=1,2.....) are the Fourier coefficients, $\underline{k}^{(j)}+\underline{q}$ the wave vectors of the plane components of the Bloch wave function and j denotes the specific excited Bloch state.

Substituting the Bloch wave function $\psi(\underline{r})$ and the Fourier expansion of the crystal potential $V(\underline{r})$ into the time

independent Schrodinger equation, the equation is converted

into the form in $\underline{k}$ space:

$$\sum_{m=1,N}\{(1-\delta_{mn})U_{\underline{q}m-\underline{q}n}+\delta_{mn}[K^2-(\underline{k}^{(j)}+\underline{q})^2]\}C_{\underline{q}m}^{(j)}=0 \qquad (2.3)$$

where

$$\delta_{mn}=\begin{cases} 1 & m=n \\ & \\ 0 & m\neq n \end{cases} \qquad m,n=1,2\ldots\ldots N$$

$K^2=2meE/h^2+U_o$ and $U_{\underline{q}}=2meV_{\underline{q}}/h^2$, $V_{\underline{q}}$ is the Fourier coefficient of

the crystal potential, N the number of the Bloch states

excited. Equation (2.3) can also be written in matrix form:

$$\begin{vmatrix} K^2-(\underline{k}_{(j)}+\underline{q}_1)^2 & U_{\underline{q}1-\underline{q}2} & U_{\underline{q}1-\underline{q}3} & \cdots\cdots\cdots U_{\underline{q}1-\underline{q}N} \\ & & & \\ U_{\underline{q}2-\underline{q}1} & K^2-(\underline{k}^{(j)}+\underline{q}2)^2 & U_{\underline{q}2-\underline{q}3} & \cdots\cdots\cdots U_{\underline{q}2-\underline{q}N} \\ & & & \\ & & & =0 \\ \cdots\cdots\cdots\cdots\cdots\cdots\cdots\cdots\cdots\cdots\cdots\cdots & & & \\ U_{\underline{q}N-\underline{q}1} & U_{\underline{q}N-\underline{q}2} & U_{\underline{q}N-\underline{q}3} & \cdots K^2-(\underline{k}^{(j)}+\underline{q}_N)^2 \end{vmatrix}\begin{vmatrix} C_{\underline{q}1}^{(j)} \\ \\ C_{\underline{q}2}^{(j)} \\ \\ \cdots \\ \\ C_{\underline{q}N}^{(j)} \end{vmatrix}$$

or $\qquad\qquad |U|C_{\underline{q}}^{(j)}=0 \qquad\qquad (2.4)$

The condition for nontrivial solutions of Equation (2.4) is

given by:

$$\text{Det}|U|=0 \qquad (2.5)$$

Equation (2.5) is the dispersion equation determining the E-

$\underline{k}$ relation in a periodic crystal potential, which is analogous

to the dispersion equation in free space:

$$E-h^2\underline{k}^2/2m=0 \qquad (2.6)$$

Equation (2.5) can also be expressed as a polynomial equation:

$$f^{(2N)}(E,\underline{k})=0 \qquad (2.7)$$

where the superscript 2N indicates that f is the 2Nth order of $\underline{k}$ and E is the total energy of the electron in the crystal. The E-$\underline{k}$ relation plays a central role in energy band theory and is similarly important in the dynamical theory of electron diffraction. The difference is which one is chosen as the independent variable, E for diffraction theory or $\underline{k}$ for energy band theory. However, both energy band analysis and the constant energy surface for diffraction theory are on the same seven-dimensional complex dispersion hypersurface in E-$\underline{k}$ space, which is defined by Equation (2.7) and determines the totality of the allowed electronic states, both energy states and momentum states in the crystal [3]. Equation (2.7) can be further expressed as:

$$f^{(2N)}(E,\underline{k}^r,\underline{k}^i)=0 \qquad (2.8)$$

where superscript r denotes the real part of $\underline{k}$ and i the imaginary part of $\underline{k}$. We have:

$$\underline{k}=(k_x^r\underline{i}+k_y^r\underline{j}+k_z^r\underline{k})+i(k_x^i\underline{i}+k_y^i\underline{j}+k_z^i\underline{k}) \qquad (2.9)$$

Because the wave with non-zero imaginary part of $\underline{k}$ is not a propagating wave for the case without absorption, it cannot be an intrinsic state of the system. Therefore, the states with imaginary crystal momentum $\underline{k}$ are not discussed in the

energy band theory, i.e.

$$k_x^i = k_y^i = k_z^i = 0 \tag{2.10}$$

But electron diffraction is basically an externally excited process and a wave with imaginary crystal momentum $\underline{k}$ (evanescent wave or non-propagating wave) can be excited. If the coordinates are set up such that the xy plane is parallel to the surface and the z axis is inward normal to the surface (Fig. 2.1), for the continuity of the wavefunction and its derivative on the boundary, there is no imaginary component of $\underline{k}$ along the surface: $k_x^i = k_y^i = 0$. Therefore, dynamical theory of electron diffraction basically deals with a 5-D dispersion hypersurface:

$$f^{(2H)}(E, k_x^r, k_y^r, k_z^r, k_z^i) = 0 \tag{2.11}$$

In the Laue case, $k_z^i = 0$ (neglecting absorption), which can be proved algebraically. Then the problem is further reduced down to 4-D. A dispersion surface for the Laue case is the result of presenting an equal-energy section of the 4-D dispersion hypersurface in the 3-D Euclidean space.

For a specific external excitation, E is determined, as far as elastic scattering is concerned and k_x and k_y are determined by the boundary conditions. Equation (2.7) then has the following form:

$$f'^{(2H)}(k_z^r, k_z^i) = 0 \tag{2.12}$$

2N values of $k_r^r + ik_r^i$ can be obtained from Equation (2.12) and the excited wave points on the dispersion surface can be uniquely located. The difficulties of understanding the nature of the evanescent wave, i.e. a wave with imaginary $\underline{k}$, is basically due to the fact that the wave point of an evanescent wave cannot be presented in Euclidean geometrical space and the theory loses a powerful visual tool. This has impeded the development of dynamical theory in the Bragg case for decades. Later on, it will be shown that the difficulties can be removed when the nature of wave propagation is further analyzed.

Some fast eigenvalue searching methods, such as Krylov-Faddecv's method [4] and Hill's determinant method [5] can be introduced to solve Equation (2.12). Both eigenvalues and their corresponding eigenvectors can be obtained simultaneously.

The total electron wave inside the crystal can then be written as the following:

$$\psi(\underline{r}) = \sum_{j=1,M} \varepsilon^{(j)} \psi^{(j)}(\underline{r}) = \sum_j \varepsilon^{(j)} \sum_g C_g^{(j)} \exp[i2\pi(\underline{k}^{(j)} + \underline{g}) \cdot \underline{r}] \qquad (2.13)$$

where $\{\varepsilon^{(j)}\}$ are the coefficients of the excited Bloch waves. These coefficients together with the plane waves outside the crystal are determined by boundary match.

2.3 <u>Boundary conditions</u>

2.3.1. <u>Two kinds of boundary value problems</u>

For wave propagation, there are two basic kinds of boundary value problems: propagation in a semi-infinite medium and that in a finite medium. Wave propagation in an infinite free space or medium is not relevant to dynamical diffraction theory. For electron diffraction in a crystal, there are two crystal models: semi-infinite crystal and a slab type crystal. Because of reflection from the bottom boundary, among excited Bloch states, there should be the difference between "forward states" and "backward states", which seems clear in the Laue case. Physically, this can be explicitly explained by taking a one dimensional mechanical wave equation as an analogy:

$$\partial^2 U(x,t)/\partial x^2 - (a^2)\partial^2 U(x,t)/\partial t^2 = 0 \qquad (2.14)$$

where U is the displacement of medium. It has the solution:

$$U(x,t) = A\exp[i2\pi(kx - \omega t)] \qquad (2.15)$$

Substituting (2.15) into (2.14), we obtain the following dispersion relations:

$$k^2 - a^2\omega^2 = 0; \quad k = \pm\sqrt{a^2\omega^2} \qquad (2.16)$$

Then the general solution of (2.14) is given by:

$$U(x,t) = A_1\exp[i2\pi(kx + \omega t)] + A_2\exp[i2\pi(-kx - \omega t)] \qquad (2.17)$$

If the boundary condition is given for a semi-infinite model:

$$U(0,t)=A_o\exp[i2\pi\omega_o t] \tag{2.18}$$

and then $A_2=0$ for no back reflection, the true solution of the problem is given by:

$$U(x,t)=A_o\exp[i2\pi(kx+\omega_o t)]; \quad k=\sqrt{a^2\omega_o^2}=|a\omega_o| \tag{2.19}$$

The reason for $A_2=0$ is equivalent to omitting the reflected Bloch states in a crystal. Mathematically, a semi-infinite crystal only has one boundary with vacuum, which gives 2N equations for the continuity of wave function and the derivative of the wave function. Therefore, only N Bloch waves can be included, otherwise the problem has no unique solution.

2.3.2. Energy flow and current flow

Two critical questions are how to define "forward state" and "backward state" for the Bloch wave and whether the number of the "forward" or "backward" states is N or not. Several authors [6-7] have discussed the role of energy flow in this problem, but no detailed approach was given. For a plane wave, $\psi(\underline{r})=A\exp[i2\pi\underline{k}.\underline{r}]$, its orientation is easily defined as the orientation of its wave vector $\underline{k}$ or the momentum $\underline{p}=h\underline{k}$, because the plane wave is the eigenstate of the momentum operator. Nevertheless, it no longer holds for a Bloch wave $\psi(\underline{r})=u(\underline{r})\exp[i2\pi\underline{k}.\underline{r}]$, because the Bloch waves are the eigenstates of the Hamiltonian of a periodic system and $h\underline{k}$

("crystal momentum") does not represent the momentum of the wave field. The Bloch wave as an eigenstate of the Hamiltonian has a series of possible momentum values. In other words, it is an expansion of the eigenfunctions of momentum operator.

In general, the orientation of a wave is determined by its energy flow instead of its momenta. The energy flow of an electromagnetic wave is represented by the Poynting vector, which is determined by the disturbance of medium; $1/2(\underline{E}x\underline{H})$ [8]. A matter wave is interpreted as the "probability" wave, for which there is no medium, so the energy is carried by particles instead of being stored in medium. Therefore, it is logical to consider the probability current flow for a matter wave as corresponding to the Poynting vector for an electromagnetic wave. Physically, the significance of current flow is equivalent to that of energy flow for matter wave. We have:

$$\rho_z = \int_0^\infty E\underline{S}(\underline{r}, E, t) \, dE \qquad (2.20)$$

In the case of a stationary state and elastic scattering, it simply becomes:

$$\rho_z = E\underline{S} \qquad (2.21)$$

where $\underline{S}$ is current flow and ρ_z energy flow. Both $\underline{S}$ and ρ obey

the conservation law. If $\underline{S}$ is conserved along a boundary, so is ρ, and vice versa (Appendix 2.1, Fig.2.2). As the Poynting vector of an electromagnetic wave is perpendicular to the dispersion surface [8-9], the current flow for a matter wave is also perpendicular to the real section of dispersion surface [10]. The current flow is given by:

$$\underline{S}=\psi^*\psi\underline{v} \qquad (2.22)$$

where $\underline{v}$ is the group velocity of the matter wave:

$$\underline{v}=\nabla_k E(\underline{k})/h \qquad (2.23)$$

Then,

$$\underline{S}=(\psi\psi^*/h)\,\nabla_k E(\underline{k}) \qquad (2.24)$$

$\nabla_k E(\underline{k})$ is perpendicular to the dispersion surface. There is an important but also difficult question which needs to be answered. In Section 2.2, it has been pointed out that the dispersion surface primarily is a seven dimensional complex hypersurface and $\underline{k}$ could be complex with non-zero imaginary part. On the other hand, the current flow and the group velocity lose their physical meaning in the complex space and moreover $E(\underline{k})$ is not differentiable in the complex space according to the Cauchy-Riemann Theorem [9], because E must be real and then $E(\underline{k})$ is non-analytic. Therefore, the differentiation of E with respect to $\underline{k}$ is both unfeasible and

physically meaningless. However, it is not correct to think that current flow, group velocity and energy as a function of $\underline{k}$ can lose their physical significance once $\underline{k}$ is extended into complex space. One can endow certain physical significance (decaying of the wave) to an imaginary momentum ($\underline{p}=h\underline{k}$), while restricting its dependent variable, energy or group velocity within real space.

The problem now is obtaining the mathematical representation of current flow or group velocity, when the $\underline{k}$ vector is extended to complex space. Energy is a basic physical quantity and should not be affected by such an extension. A logical extension of the mathematical presentation of the group velocity for the above is as the follows (Appendix 2.2):

$$\underline{v}_p = (1/h)\, dE(k_x^r + ik_x^i)/dk_x^r \qquad (2.25)$$

in one dimension and

$$\underline{v}_p = (1/h)\, \nabla_{\underline{k}} E(\underline{k}) \qquad (2.26)$$

in three dimensions, where $\underline{v}_p$ is the group velocity and the superscript r refers to the real part of $\underline{k}$.

The general form of a wave packet in one dimension is given by:

$$\psi(x,t) = \exp[i2\pi(k_o^r x - E(k_o)t/h^2)]\exp[-2\pi k_o^i x]\, F[x-(dE(k_o)/dk^r).t]$$

$$(2.27)$$

Equation (2.27) mathematically expresses three kinds of wave packets existing in the real world:

i) $k_o^i=0$; $dE(k_o)/dk^r\neq0$: non-evanescent wave packet propagating in a medium without absorption.

ii) $k_o^i\neq0$; $dE(k_o)/dk^r=0$: evanescent wave packet standing in a medium without absorption.

iii) $k_o^i\neq0$; $dE(k_o)/dk^r\neq0$: evanescent or non-evanescent wave packet propagating in a medium with absorption.

A non-decaying stationary wave packet for which $k_o^i=0$ and $dE(k_o)/dk^r=0$ does not physically exist. In the case of an evanescent wave or a wave in the medium with absorption, for which the $\underline{k}$ vector is extended into complex space while group velocity, current flow and energy are within real space, we similarly have:

$$\underline{S}=(\psi\psi^*/h)\,\nabla_{\underline{k}r}E(\underline{k}) \tag{2.28}$$

which corresponds to (2.24). Nevertheless, the orientation of $\nabla_{\underline{k}r}E(\underline{k})$ no longer has a decisive geometrical relation with respect to the real dispersion surface in the Euclidean space since the value of $\nabla_{\underline{k}r}E(\underline{k}^r+i0)$ is not necessarily equal to the value of $\nabla_{\underline{k}r}E(\underline{k}^r+i\underline{k}_o^i)$ and $\underline{k}=\underline{k}^r+i\underline{k}_o^i$ is no longer on the real dispersion surface. In other words, the question that whether or not current flow of an evanescent wave or the wave in the

medium with absorption is perpendicular to dispersion surface loses its original meaning.

As a summary, we have several points listed as the following:

i) If a Bloch wave as a wave packet is evanescent in a certain direction in the medium without absorption, its current flow or group velocity is zero in that direction and its crystal momentum is purely imaginary.

ii) If a Bloch wave as a wave packet is not evanescent in a certain direction in the medium without absorption, its current flow or group velocity is not zero in that direction and its crystal momentum is purely real.

iii) If a Bloch wave as a wave packet propagates in a certain direction in the medium with absorption, its current flow or group velocity is not zero in that direction because of the absorption of the medium, while its wave packet core decays in that direction and its crystal momentum is complex with both real and imaginary parts.

iv) The current flow and energy flow are equivalent to each other for a charged matter wave; the former is more specific for a matter wave, while the latter is a more general term. "Current flow" will be the only term used later.

v) The orientation of an evanescent or absorbed wave, i.e. the

orientation of its current flow or group velocity is not necessarily perpendicular to the real section of dispersion hypesurface $E(\underline{k}^r+i\underline{k}^i)$. This is simply because $\underline{k}$ is not on it when $\underline{k}^i{\neq}0$.

2.3.3. Numerical analysis of current flow

After a full discussion of the physical significance of current flow or group velocity in electron diffraction, it is necessary to have a numerical analysis to examine its validity in a real system. The current flow of matter wave is given by:

$$\underline{S}(\underline{r},t)=(h/2im)\ [\psi^*(\nabla\psi)-(\nabla\psi^*)\psi] \tag{2.29}$$

which can be found in the texts on quantum mechanics.

Substituting the Bloch wave function (2.2) into (2.29), we have (Appendix 2.3):

$$\underline{S}=(2\pi h/m)\ [\textstyle\sum_q|C_q^{(j)}|^2(\underline{k}^{r(j)}+\underline{q})]\exp[-4\pi\underline{k}^{i(j)}.\underline{r}] \tag{2.30}$$

where $\underline{k}^{r(j)}$ is the real part of the wave vector, $\underline{k}^{i(j)}$ the imaginary part of the wave vector, $\{C_q^{(j)}\}$ the coefficients of plane wave $\underline{q}$ and the superscript j denotes a specific excited Bloch state. Equation (2.30) shows that the current flow of a Bloch wave is proportional to the expectation value of all of its possible wave vectors ($\underline{p}=h\underline{k}$) if the wave is normalized: $\sum_q|C_q^{(j)}|^2=1$. The current flow of a plane wave is [12]:

$$\underline{S}=(2\pi h\underline{k}/m)\ |C|^2 \tag{2.31}$$

The resulting differences between (2.30) and (2.31) arise from the fact that the Bloch wave states are eigenstates of the Hamiltonian, while plane waves are eigenstates of the momentum operator. The exponential part in (2.30) is dependent upon $\underline{r}$, but it does not affect the sign of $\underline{S}$, because it is always positive. If the coordination is set up as that shown in Fig.2.1, we have:

$$\underline{S}_z = (2\pi h/m)\exp[-4\pi k_z^{i(j)}z]\sum_g|C_g^{(j)}|^2(\underline{k}_z^{r(j)}+\underline{g}_z) \qquad (2.32)$$

where subscript z denotes the z component of vector. The Bloch wave which physically exists in the semi-infinite crystal must satisfy $S_z^{(j)}\geq0$ and $k_z^{i(j)}\geq0$ for the cases both with and without absorption (Fig.2.3). This can be proved analytically [11] (Appendix 2.4). From Equation (A2.4.8), we have:

$$\underline{S}^{(j)}\cdot\underline{k}^{i(j)}\begin{cases}>0 & V_I>0 \\ =0 & V_I=0\end{cases} \qquad (2.33)$$

For $k_x^{i(j)}=k_y^{i(j)}=0$, then:

$$\underline{S}_z^{(j)}\cdot k_z^{i(j)}\begin{cases}>0 & V_I>0 \\ =0 & V_I=0\end{cases} \qquad (2.34)$$

Equation (2.34) analytically confirms that any Bloch wave in the medium without energy source ($V_I(\underline{r})\geq0$) can either exponentially decay ($k_z^{i(j)}>0$, $S_z^{(j)}>0$ or $k_z^{i(j)}<0$, $S_z^{(j)<0}$) or keep

constant ($k_r^{\perp(j)}=0$) in the direction of wave propagation, which is consistent with the analysis on the Equation (2.19). Equation (2.34) also characterizes four kinds of formerly discussed wave fields:

i) $V_I=0$ (no absorption) $S_x^{(j)}=0$, $k_r^{\perp(j)}=0$; a non-evanescent standing wave in an ideal medium.

ii) $V_I=0$ (no absorption) $S_x^{(j)}=0$, $k_x^{\perp(j)}\neq0$; an evanescent standing wave in an ideal medium.

iii) $V_I=0$ (no absorption) $S_x^{(j)}\neq0$, $k_x^{\perp(j)}=0$; a propagating wave without decaying.

iv) $V_I>0$ (with absorption) $S_x^{(j)}>0$, $k_x^{\perp(j)}>0$ or $S_x^{(j)}<0$, $k_{xi}^{(j)}<0$; an evanescent or propagating wave in the medium with absorption. When absorption is introduced, the mechanism of evanescence and absorption are mixed and both of them are characterized as $S_x^{(j)}>0$ and $k_x^{\perp(j)}>0$ or $S_x^{(j)}<0$ and $k_r^{\perp(j)}<0$. However, the numerical results show the differences between the two. The magnitude of $k_r^{(j)}$ for an evanescent wave is much larger than that for a non-evanescent Bloch wave since the decay of an evanescent wave is due to both the evanescent mechanism and the absorption in the evanescent region rather than the only absorption mechanism for a non-evanescent Bloch wave.

As far as numerical analysis is concerned, we first consider the condition without absorption. The crucial point

here is whether or not the numerical results show that the number of Bloch waves satisfying the conditions $S_z^{(j)}=0$ and $k_z^{(j)}>0$ (evanescent wave) or $S_z^{(j)}>0$ and $k_z^{(j)}>0$ (non-evanescent wave) is exact N (N=M/2). If not, there must be either faults in the above physical analysis or numerical mistakes, because the boundary match exclusively requires the number of the excited Bloch states in the semi-infinite crystal to be exactly N, otherwise the boundary value problem becomes mathematically over-conditioned or under-conditioned.

In the Laue case, the crystal is also modeled as a semi-infinite one. However, the physical reason for the modeling is different from that in the Bragg case. For the Laue case, it is due to weak back reflections from the boundaries with respect to the transmitted waves, while for the Bragg case, it is due to no back reflections because there is no bottom boundary. The reason why the dynamical theory for the Laue case has not encountered the above-mentioned dilemma is that in the Laue case $|k_z^{r(j)}|>>|q|$ and $k^{i(j)}=0$, which result in $S_z^{(j)} \cdot k_z^{r(j)}>0$, i.e. the orientation of current flow in the z axis, is always the same as that of $\underline{k}$ vector. Therefore, the analysis of the current flow becomes unnecessary and the quadrate of $k_z^{r(j)}$ in dispersion Equation (2.4) algebraically indicates that half of the $k_z^{i(j)}$ are positive and another half

are negative. The high energy approximation in the Laue case $((K+k_z^{i(j)})=2K)$ is based upon this physical background. But for the Bragg case, all the above relations: $|k_z^{r(j)}|>>|g|$, $k^{i(j)}=0$ and then $S_z^{(j)}.k_z^{r(j)}>0$ break down. In addition the phenomenon of N positive + N negative for 2N $k_z^{r(j)}$ is not necessarily always true. Then the analysis of current flow becomes necessary unless we introduce an artificial bottom boundary following Colella [12]. In addition, analyzing current flow in the Bragg case is not only significant for solving the boundary value problem, but also useful in understanding the physical insights of electron reflection.

Table 2.1 is the numerical result for a GaAs(001) surface for the case both with and without absorption. The coordinates are shown in Fig.2.1. The beam direction is along the (010) Laue zone axis and 9 beams are included. For the absorption treatment, the imaginary parts of the Fourier potential coefficients are taken as 10% of their real parts.

For a more comprehensive explanation, Table 2.2 lists the populations of the positive and negative values of three arrays; $k_z^{r(j)}$, $S_z^{(j)}$ and $k_z^{i(j)}$, $j=1....2N$ and shows the relationship between them in both the Laue case and the general case in which the Bragg case is included. Superscript "+" denotes the positive value, "-" the negative value and "0"

the zero value. $n(N_a^+, N_i^+)$ means the number of Bloch states with positive current flow or positive imaginary part of $\underline{k}$ vector. The notation "$\Rightarrow$" means not only equal but also one-to-one correspondence. For example, $N_a^+ + N_a^- \Rightarrow N_i^\cdot$ means that when $S_x^{(j)} \neq 0$, there must be $k_r^{i(j)} = 0$ vice versa. The subscripts "r" and "i" refer to the real and imaginary parts of wave vectors respectively. "NA" indicates the condition without absorption and "WA" indicates the condition with absorption.

Although in general, the populations of positive and negative values in each array are no longer regularly distributed as they are in the Laue case, which is indicated by "?", the arithmetic relation of these population numbers is unchanged. The facts that $N_a^+ + N_i^+ = N$ or $N_a^- + N_a^- = N$ for the case without absorption and $N_a^+ = N_i^+ = N$ or $N_a^- = N_i^- = N$ for the case with absorption clearly confirm that no more or no less than N Bloch waves are excited in the semi-infinite crystal. Note that the Bloch waves with the negative $k_r^{i(j)}$ have no physical significance in a semi-infinite crystal, because an infinite value of $S_x^{(j)}$ deep in the crystal is physically impossible.

Another important relation is $N_i^+ + N_i^- \Rightarrow N_a^\cdot$ for the case without absorption, which means that when $k_r^{i(j)} \neq 0$, $S_r^{(j)} = 0$. The physical significance of this relation is that evanescent

waves only propagate along the surface and the current flow of evanescent waves can not penetrate into the crystal. In other words, in the z direction the wave packet of the evanescent wave is stationary and the amplitude of the wave packet core is attenuated. When absorption is included, the above relation is replaced by $N_i^+ = N_s^+ = N$ and $N_s^- + N_i^- = 0$, and all waves are decaying in the crystal because of the absorption. The current flow of an evanescent wave which originally is exactly parallel to the surface now becomes into the crystal. It represents the energy absorption in the region that the attenuated wave packet extends instead of the motion of the whole wave packet. Comparing the data in the case with absorption in Table 2.1 to that without absorption, one finds that the $k_z^{i(j)}$ of evanescent waves are noticeably larger than those of non-evanescent waves. This shows that with absorption, the attenuation mechanism for evanescent waves is different from that for non-evanescent waves, although both their current flow and wave amplitude decay similarly in the region with absorption. The mechanisms of both evanescence and absorption are involved in evanescent waves, while only absorption is involved in non-evanescent waves.

2.4. Boundary match in the Bragg case

Having refined the problem to N Bloch waves, we now introduce the boundary conditions as described by Metherell [1]. The electron wave in vacuum can be written as:

$$\Phi(\underline{r}) = \exp[i2\pi\underline{\chi} \cdot \underline{r}] + R_{o'}\exp[i2\pi\underline{k}_{o'} \cdot \underline{r}] + \sum_{q'} R_{q'}\exp[i2\pi\underline{k}_{q'} \cdot \underline{r}]$$

$$(2.35)$$

where the first part is the incident wave, the second part is the specular reflection wave and the third part the back-diffracted wave, $\underline{k}_{o'}$ and $\underline{k}_{q'}$ the corresponding wave vectors, and $R_{o'}$ and $R_{q'}$ the reflection coefficients of the outgoing plane wave branches. $\underline{k}_{o'}$ and $k_{q'}$ are related to the incident wave vector χ by the following equations, which are valid in the Laue case [1]:

$$\underline{k}_{o'} = \underline{\chi} - 2\underline{\chi}_n \qquad (2.36)$$

$$\underline{k}_{q'} = \underline{\chi} - 2\underline{\chi}_n + \underline{q} + \underline{s}_q$$

$$= \underline{k}_{o'} + \underline{q} + \underline{s}_q \qquad (2.37)$$

where $\underline{\chi}_n$ is the projection of the incident wave vector on the surface normal $\underline{n}$, $\underline{q}$ the reciprocal lattice vector and $\underline{s}_q$ the excitation error. Referring to Fig.2.1, MN is the surface of crystal and the z axis is parallel to the surface normal $\underline{n}$ and points inward into the crystal. S_1 and S_2 are the dispersion surface in vacuum and S_3 is the Ewald sphere. The excitation error s_q and the surface normal $\underline{n}$ are always parallel to each

other and towards the same direction. $\underline{s}_q$ starts from the reciprocal lattice point $\underline{q}$ and ends on the Ewald sphere at point P. Applying analytical geometry, we can prove that the vector QP is equal to $\underline{k}_{q'}$, which means that (2.37) is also valid for the Bragg case.

The dispersion surface and reciprocal lattice for the reflected waves in vacuum shown in Fig.2.4 is currently widely accepted in RHEED and RHEEM and is useful for identifying the spots positions in RHEED patterns in a simple and visual way. However, it does not reflect the whole physics of the electron reflection; there is no reciprocal rods or reciprocal lattice points in vacuum. The reflected waves in the Bragg case are excited by the Bloch waves in crystal and this "cause-effect" relation depends on continuity of the wave field and its derivative.

As the conservation of energy and interfacial momentum on the boundary and elastic scattering are concerned, we have:

$$(\underline{k}+\underline{q})_\tau = \underline{k}_{q'\tau} \qquad (2.38)$$

$$\chi^2 = \underline{k}_{q'}{}^2 \qquad (2.39)$$

where subscript τ denotes the interfacial component of a wave vector. Referring to Fig.2.1, from (2.38) and (2.39), we immediately obtain:

$$k_{o'x} = \chi_x \qquad (2.40)$$

$$k_{o'y} = \chi_y \qquad (2.41)$$

$$k_{o'x} = -\chi_x \qquad (2.42)$$

$$k_{g'x} = (\chi_x - g_x) \qquad (2.43)$$

$$k_{g'y} = (\chi_y - g_y) \qquad (2.44)$$

$$k_{g'z} = -\sqrt{\chi^2 - (\chi_x - g_x)^2 - (\chi_y - g_y)^2} \qquad (2.45)$$

Equation (2.45) raises two important questions: i) $k_{g'z}$ can be purely imaginary if the value inside the square root is negative when the surface normal $\underline{n}$ does not touch the dispersion sphere S_2. This means that there also exist evanescent wave branches in the outgoing wave, which can also propagate along the surface and concentrate in the region near the surface. These waves coupling with the evanescent waves inside the crystal may correspond to a "surface wave" as discussed by many authors [6-7,13-14]. Numerical evidence on the existence of a "surface wave" will be given later. ii) Equation (2.45) is independent of g_x. For the zero Laue zone, $g_y = 0$. This means that the RHEED pattern consists of a series of semi-circles and each one corresponds to one Laue zone. This is consistent with the kinematic analysis and some RHEED experiments which will be discussed later.

The wave function $\psi(\underline{r})$ in the crystal described by Equation (2.2) and $\Phi(\underline{r})$ in vacuum described by Equation (2.35)

and their derivatives should match each other at boundary
according to the law of continuity. Therefore, we have:

$$\Phi(\underline{r}) = \psi(\underline{r}) \qquad (2.46)$$

$$\partial\Phi(\underline{r})/\partial n_{|\underline{r}=\underline{r}} = \partial\psi(\underline{r})/\partial n_{|\underline{r}=\underline{r}} \qquad (2.47)$$

or

$$\exp[i2\pi\chi_t.\underline{r}] + R_{o'}\exp[i2\pi\underline{k}_{o'}.\underline{r}] + \sum_{g\neq0}R_{g'}\exp[i2\pi(\underline{k}_{o't}+\underline{g}).\underline{r}]$$

$$= \sum_g\sum_j\varepsilon_{(j)}C_g^{(j)}\exp[i2\pi(\underline{k}_{ot}^{(j)}+\underline{g}_t).\underline{r}] \qquad (2.48)$$

$$\chi_n\exp[i2\pi\chi_t.\underline{r}] + \underline{k}_{o'n}R_{o'}\exp[i2\pi\underline{k}_{o't}.\underline{r}] + \sum_{g\neq0}(\underline{k}_{o'n}+\underline{g}_n+\underline{s}_{gn})\exp[i2\pi(\underline{k}_{o't}+\underline{g}_t).\underline{r}]$$

$$= \sum_g\sum_j(\underline{k}_n^{(j)}+\underline{g}_n)\varepsilon^{(j)}C_g^{(j)}\exp[i2\pi(\underline{k}_{ot}^{(j)}+\underline{g}_t).\underline{r}] \quad (2.49)$$

where the subscript n denotes the projection of a vector onto
the surface normal $\underline{n}$ and the subscript t denotes the
projection of a vector onto the surface. Referring to Fig.2.1,
$\underline{n}$ has a negative direction along the z axis. Since $\underline{s}_g$ is
always parallel to $\underline{n}$, we have $\underline{s}_{gt}=0$ and then $\underline{k}_{g't}=\underline{k}_{o't}+\underline{g}_t$.
Equation (2.48) and (2.49) can be true, only if:

$$\underline{k}_{o't}=\underline{k}_{ot}^{(j)}=\chi_t$$

or

$$k_{o'x}=k_{ox}^{(j)}=\chi_x, \quad k_{o'y}=k_{oy}^{(j)}=\chi_y \qquad j=1,2,\ldots.N \qquad (2.50)$$

$$1+R_{o'}=\sum_j\varepsilon^{(j)}C_o^{(j)} \qquad (2.51)$$

$$R_{g'}=\sum_j\varepsilon^{(j)}C_g^{(j)} \qquad (2.52)$$

$$1-R_{o'}=\sum_j(k_n^{(j)}/\chi_n)\varepsilon^{(j)}C_o^{(j)} \qquad (2.53)$$

$$-R_{g'}=\sum_j(k_n^{(j)}+g_n)/(\chi_n-g_n+s_g)\varepsilon^{(j)}C_g^{(j)} \qquad (2.54)$$

There are 2N equation and 2N unknowns; $R_{o'}\ldots R_{g'}\ldots$ and $\varepsilon^{(1)}$,

$\varepsilon^{(2)}$..... $\varepsilon^{(M)}$ and therefore these unknowns can be uniquely solved. Equations (2.51)-(2.54) can also be written in the matrix form:

$$\left| \begin{array}{cc} C & -I \\ A & I \end{array} \right| \begin{array}{c} \{\varepsilon^{(j)}\} \\ \{R_{q'}\} \end{array} = \{E\} \qquad (2.55)$$

where

$$C = \left| \begin{array}{c} C_o^{(1)} \ C_o^{(2)} \dots C_o^{(M)} \\ \dots \dots \dots \dots \\ C_q^{(1)} \ C_q^{(2)} \dots C_q^{(M)} \\ \dots \dots \dots \dots \\ \dots \dots \dots \dots \end{array} \right| \ ; \quad I = \left| \begin{array}{ccccc} 1 & 0 & . & . \\ 0 & 1 & 0 & . \\ . & 0 & 1 & 0 \\ & . & . & 0 & . & 0 \\ & . & . & . & 0 & . \end{array} \right| \ ;$$

$$A = \left| \begin{array}{cccc} (k_{on}^{(1)}/\chi_{on})C_o^{(1)} & (k_{on}^{(2)}/\chi_{on})C_o^{(2)} \dots (k_{on}^{(M)}/\chi_{on})C_o^{(M)} \\ \dots \dots \dots \dots \dots \dots \dots \dots \dots \dots \\ (k_{qn}^{(1)}/\chi_{qn})C_q^{(1)} & (k_{qn}^{(2)}/\chi_{qn})C_q^{(2)} \dots (k_{qn}^{(M)}/\chi_{qn})C_q^{(M)} \\ \dots \dots \dots \dots \dots \dots \dots \dots \dots \dots \\ \dots \dots \dots \dots \dots \dots \dots \dots \dots \dots \end{array} \right|$$

and

$$E = \left| \begin{array}{c} 1 \\ 0 \\ 0 \\ . \end{array} \right|$$

That is:

$$C\{\epsilon^{(j)}\}-I\{R_{g'}\}=E \tag{2.56}$$

$$A\{\epsilon^{(j)}\}+I\{R_{g'}\}=E \tag{2.57}$$

Therefore,

$$\{\epsilon^{(j)}\}=2\,(C+A)^{-1}E \tag{2.58}$$

$$\{R_{g'}\}=1/2\,(C+A)\,\{\epsilon^{(j)}\} \tag{2.59}$$

Thus, both the reflected waves in vacuum and the excited Bloch waves in crystal are solved.

The basic process of the approach can be summarized as the following:

The signs of $S_z^{(j)}$ and $k_z^{\perp(j)}$ are examined numerically, after calculating 2N eigenvalues $k_z^{(j)}$ and eigenvectors $\{C_g^{(j)}\}$, the coefficients of the plane wave components in the Bloch waves, from the dispersion Equation (2.5). Then N eigenvalues $k_z^{(j)}$ and N eigenvectors $\{C_g^{(j)}\}$ of N excited "forward" Bloch waves are taken as the applicable solutions of the problem (Table 2.1). The boundary match between the plane waves in vacuum and the Bloch waves in crystal can solve the coefficients of each Bloch wave and each generated plane wave.

2.5. Numerical development

Fig.2.5 shows an outline of the numerical simulation. The potential in reciprocal space and the reciprocal lattice parameters for the zero Laue zone are calculated by the

relevant part of the multislice simulation program adopted from the HREM simulation facilities at Northwestern University (1). Since the off-diagonal elements in the Hermitian matrix in Equation (2.4) represent interference between beams, the matrix of the reciprocal potential for the zero Laue needs to be converted into the Bloch Hermitian matrix (2). Then a $2N \times 2N$ matrix is constructed to solve Equation (2.4), which converts the problem of solving roots of the polynomial of the 2Nth order into one of searching for eigenvalues of the $2N \times 2N$ matrix. O is a zero submatrix, I the unit submatrix, D the submatrix of Nth order storing the modified Bloch Hermitian submatrix and B diagonal submatrix of Nth order storing $\{g_z\}_N$, the z coordinate of N excited reciprocal lattice points in the zero Laue zone. For the eigenvalue search, a general complex matrix routine in Eispack was used. The interfacial wave vectors of the Bloch waves $\{\underline{k}^{(j)} + \underline{q}\}_t$ are determined by the boundary match and the z components of the wave vector are solved as eigenvalues, while the coefficients of the plane wave components of each Bloch wave $\{C_g^{(j)}\}$ are solved as the eigenvectors (4). After that, the z component of current flow of each Bloch wave is evaluated according to Equation (2.22) (5). $S_z^{(j)}$ and the imaginary part of eigenvalues $k_z^{i(j)}$ are used as the criteria for choosing K excited Bloch waves from all

2N solved ones (6). K is examined to make sure that it is equal to N. If not, the program will stop at this point (7). Numerical error may possibly confuse the judgment of the program only when both $k_z^{i(j)}$ and $S_z^{i(j)}$ are close to zero ($<10^{-3}$). Rare misjudgments of this kind in the program demonstrate the validity of previous physical and analytical analysis. Thereafter, the wave vectors of the reflected waves in vacuum are calculated according to Equations (2.40)-(2.45), where the law of the conservation of energy and interfacial momentum on boundary is obeyed (8). The coefficients of the reflected plane waves in vacuum and the Bloch waves in crystal are obtained by solving Equations (2.51)-(2.54), using a general complex linear equation routine in Linpack (9). Finally, the total wave in the crystal and the total reflected wave in vacuum are constructed from all previously calculated parameters (10). Either elastic diffraction patterns and images are displayed or the various diffraction parameters are analyzed (11).

Fig.2.6 shows the results of this numerical development, which does not include absorption. Intensity maps of both the reflected waves in vacuum and the Bloch wave in crystal are shown in the size of five unit cells by five unit cells, i.e. 28.2 by 28.2 angstrom. The incident electron energy is 100keV

and the incident glancing angle is 42mRad. The beam is along the [010] azimuth. In the diffraction pattern, 7 spots corresponding to 49 excited beams in the crystal form a semicircle and the transmitted beam is excluded. The Bragg spots do not show serious streaking since the crystal surface is assumed to be perfect.

Table 2.1

ALL EXCITED BLOCH WAVES

	WITHOUT ABSORPTION				WITH ABSORPTION	
	EIGENVALUES	ENERGY FLOW			EIGENVALUES	ENERGYFLOW
	(k_{ox})	(S_x)			(k_{oz})	(S_z)
1	(0.73292+ 0.00000i);	0.38051	1		(0.73315+ 0.01586i);	0.38066
2	(-0.73292+ 0.00000i);	-0.38276	2		(-0.73315+-0.01586i);	-0.38294
3	(0.59945+ 0.00000i);	0.26390	3		(0.60116+ 0.03088i);	0.26517
4	(-0.59945+ 0.00000i);	-0.27529	4		(-0.60116+-0.03088i);	-0.27645
5	(0.35425+ 0.14888i);	0.00000	5		(0.37829+ 0.15073i);	0.02119
6	(0.35425+-0.14888i);	0.00000	6		(0.33023+-0.15093i);	-0.28858
7	(-0.35425+ 0.14888i);	0.00000	7		(-0.33023+ 0.15093i);	0.29024
8	(0.24535+ 0.09745i);	0.00000	8		(0.26169+ 0.09211i);	0.34682
9	(0.24535+-0.09745i);	0.00000	9		(0.22763+-0.10719i);	-0.05492
10	(-0.35425+-0.14888i);	0.00000	10		(-0.37829+-0.15073i);	-0.02133
11	(-0.24535+ 0.09745i);	0.00000	11		(-0.22763+ 0.10719i);	0.38846
12	(-0.24535+-0.09745i);	0.00000	12		(-0.26169+-0.09211i);	-0.08743
13	(0.00000+ 0.14944i);	0.00000	13		(0.02384+ 0.15134i);	0.26040
14	(0.11457+ 0.05397i);	0.00000	14		(0.14531+ 0.07004i);	0.90858
15	(0.00000+-0.14944i);	0.00000	15		(-0.02384+-0.15134i);	-0.02356
16	(0.11457+-0.05397i);	0.00000	16		(0.08571+-0.05688i);	-0.10634
17	(-0.11457+ 0.05397i);	0.00000	17		(-0.08571+ 0.05688i);	1.01995
18	(-0.11457+-0.05397i);	0.00000	18		(-0.14531+-0.07004i);	-0.07001

APPLICABLE BLOCH WAVES

1	(0.73292+ 0.00000i);	0.38051	1		(0.73315+ 0.01586i);	0.38066
3	(0.59945+ 0.00000i);	0.26390	3		(0.60116+ 0.03088i);	0.26517

5	(0.35425+ 0.14888i);	0.00000	5	(0.37829+ 0.15073i);	0.02119
7	(-0.35425+ 0.14888i);	0.00000	7	(-0.33023+ 0.15093i);	0.29024
8	(0.24535+ 0.09745i);	0.00000	8	(0.26169+ 0.09211i);	0.34682
11	(-0.24535+ 0.09745i);	0.00000	11	(-0.22763+ 0.10719i);	0.38846
13	(0.00000+ 0.14944i);	0.00000	13	(0.02384+ 0.15134i);	0.26040
14	(0.11457+ 0.05397i);	0.00000	14	(0.14531+ 0.07004i);	0.90858
17	(-0.11457+ 0.05397i);	0.00000	17	(-0.08571+ 0.05688i);	1.01995

Excitation Amplitudes

1	0.187E-02	0.140E-02
3	0.538E+00	0.396E+00
5	0.125E-10	0.383E-11
7	0.611E-10	0.207E-11
8	0.655E+00	0.637E+00
11	0.452E-01	0.347E-01
13	0.381E-13	0.149E-13
14	0.180E-02	0.196E-02
17	0.705E-04	0.598E-04

Table 2.1. List of the Bloch waves for a nine beam calculation of GaAs. The beam direction is along the [01$\bar{0}$] Laue zone axis tilted by 6.5mRad along the [101]) direction. The absorption is 10%. The upper part of the table compares the real and imaginary components of the wave vectors and current flow and the lower is the excitation amplitudes. The incident electron energy is 100keV.

Table 2.2

j=1,2......2N	$S_z^{(j)}$	$k_z^{r(j)}$	$k_z^{i(j)}$	
	$N_s^+=N$	$N_r^+=N$	$N_i^+=$	0 (NA)
				N (WA)
Laue case	$N_s^-=N$	$N_r^-=N$	$N_i^-=$	0 (NA)
				N (WA)
	$N_s^\bullet=0$	$\dot{N_r}^\bullet=0$	$N_i^\bullet=$	2N (NA)
				0 (WA)
	$N_s^+=$? (NA)	$N_r^+=?$	$N_i^+=$	? (NA)
	N (WA)			N (WA)
Bragg case	$N_s^-=$? (NA)	$N_r^-=?$	$N_i^-=$	? (NA)
	N (WA)			N (WA)
	$N_s^\bullet=$? (NA)	$N_r^\bullet=?$	$N_i^\bullet=$	? (NA)
	0 (WA)			0 (WA)

$$N_s^+ + N_s^- + N_s^\bullet = N_r^+ + N_r^- + N_r^\bullet = N_i^+ + N_i^- + N_i^\bullet$$

	(NA)	(WA)
Relation between	$n(N_s^+ \text{ or } N_i^+)=N$	$n(N_s^+ \text{ and } N_i^+)=N$
the populations	$n(N_s^- \text{ or } N_i^-)=N$	$n(N_s^+ \text{ and } N_i^-)=N$
	$N_s^\bullet + N_i^\bullet = 2N$	$N_s^\bullet + N_i^\bullet = 0$
	$N_i^+ + N_i^- \Rightarrow N_s^\bullet$	$N_s^+ \Rightarrow N_i^+ = N$
	$N_s^+ + N_s^- \Rightarrow N_i^\bullet$	$N_i^- \Rightarrow N_s^- = N$

Table 2.2. List of the populations of the positive and negative values of three arrays; $k_z^{r(j)}$, $S_z^{(j)}$ and $k_z^{i(j)}$ (j=1,2.......2N) and their relationship in both the Laue case (transmission) and general case in which the Bragg case (reflection) is included.
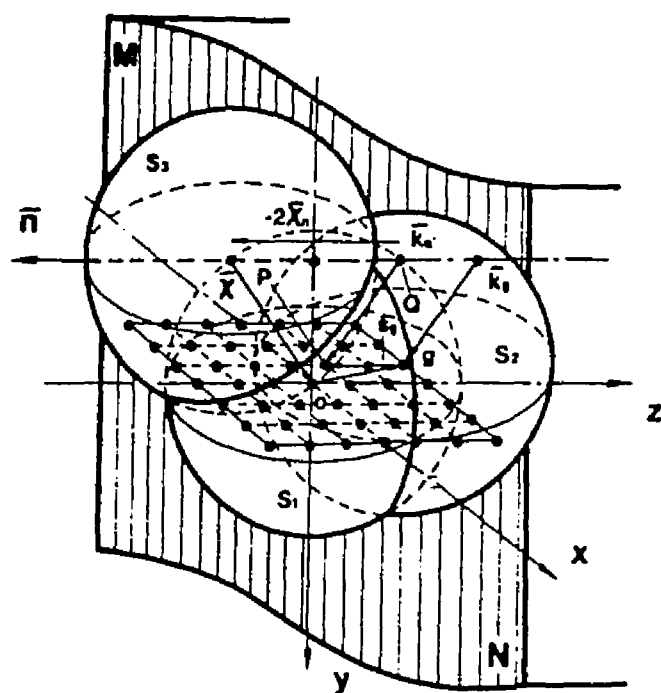
Fig.2.1. Dynamical diagram of dispersion surfaces in vacuum and boundary match in reflection case.
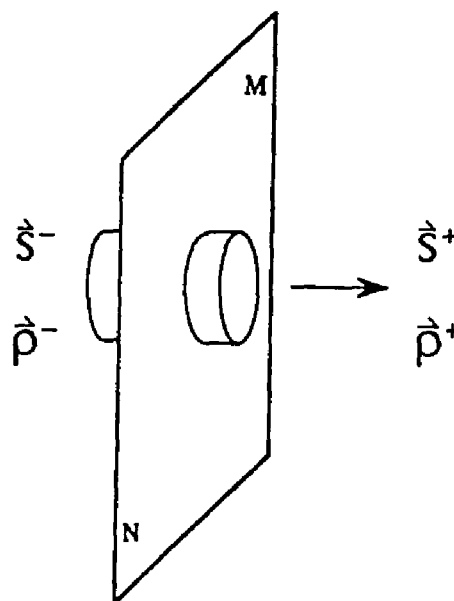
Fig.2.2. Diagram illustrating the continuity of current flow along the boundary.
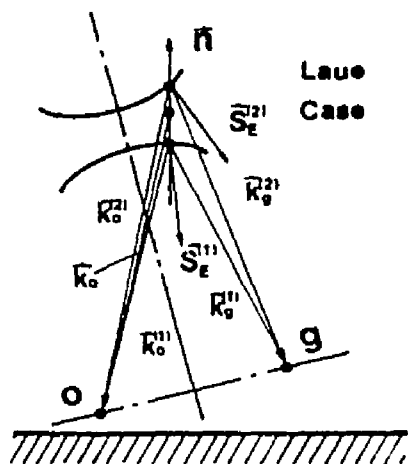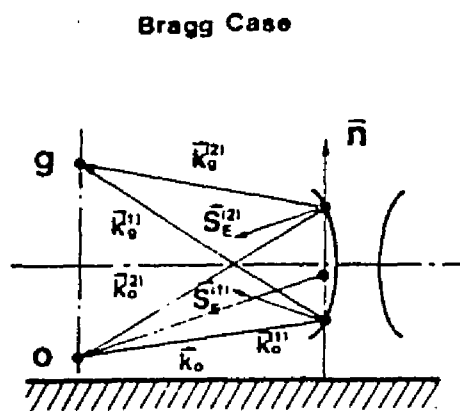
Fig.2.3. Illustration of the relation between the current flow and wave vectors of excited Bloch waves in both transmission and reflection cases. $\underline{S}$: current flow. $\underline{k}^{(j)}$: wave vectors.
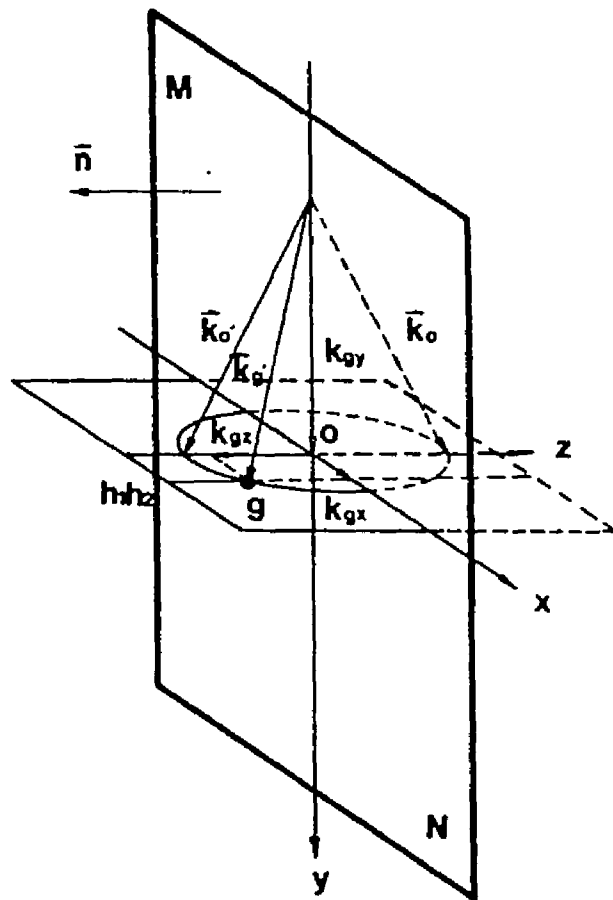
Fig.2.4. Kinematic diagram of Ewald sphere in vacuum and boundary match in reflection case. MN: surface. n: surface normal. k₀:incident wave vector. k_g': reflected waves.
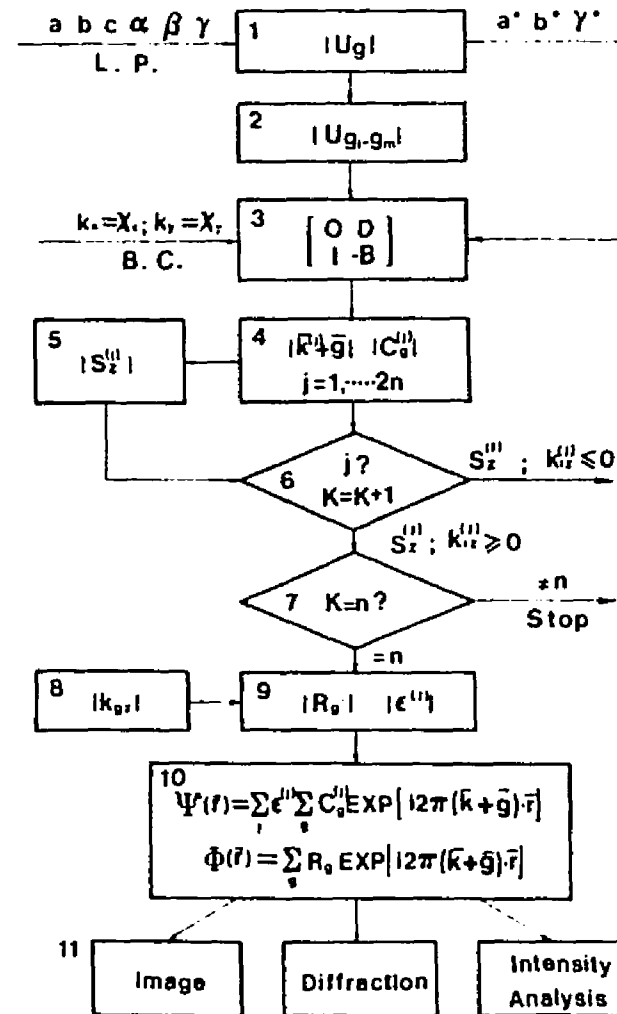
Fig.2.5. An outline of the computer program for calculating the n-beam Bloch wave solution in the reflection case.
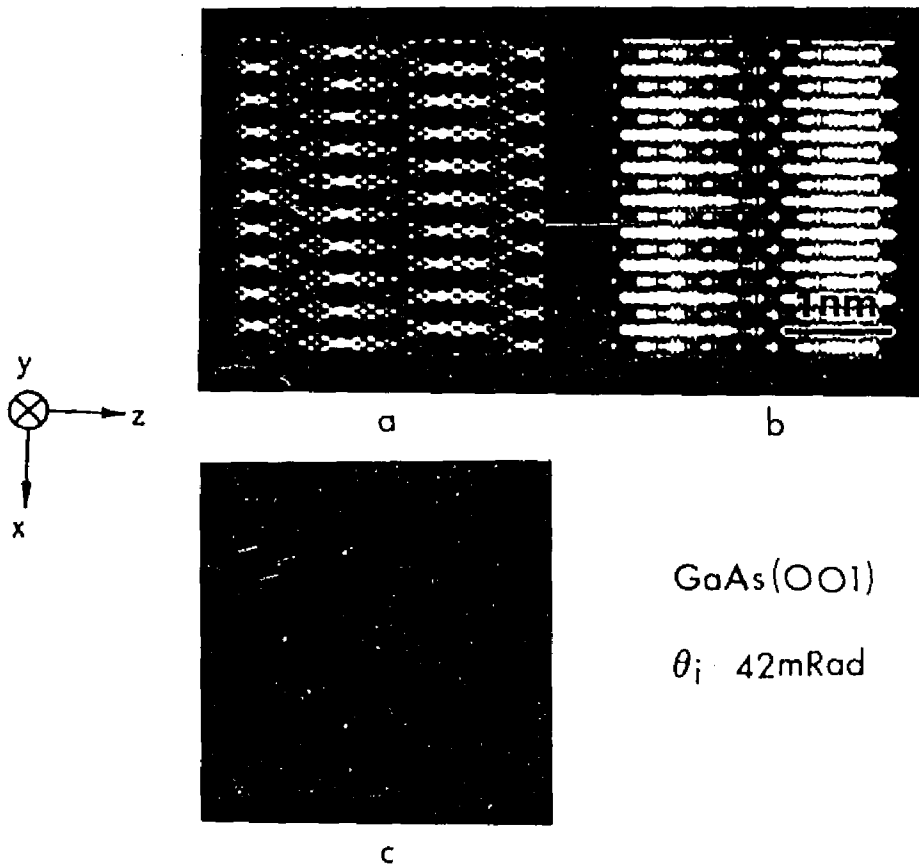
Fig.2.6. Calculated results for GaAs(001) with the incident beam along the [010] azimuth with a tilt of 42mRad for 100keV electrons: (a) intensity map of reflected wave; (b) intensity map of the Bloch wave in the crystal; (c) diffraction pattern.

Chapter III. <u>Consistency between the two approaches:</u>

<u>Bloch wave and multislice in both</u>

<u>transmission and reflection</u>

3.1. <u>Introduction</u>

The physics behind electron diffraction in the Bragg case
has been discussed in Chapter II using the Bloch wave method.
This was accomplished by the introduction of the concept of
current flow, which demonstrated the validity and usefulness
of the method for understanding electron diffraction in the
Bragg case. However, the basic limitations of the Bloch wave
method do not drop out so easily; when a large number of beams
are used, the computation speed is slow, and the method is
also not readily available to simulate surface defects.
Various alternative methods have therefore been proposed as
discussed in Chapter I. These different methods must be
consistent with each other, if they are correct. This suggests
that it is not only necessary but also possible to combine
different methods and let their advantages work together to
provide more powerful approaches. In addition, investigating
the consistency between different methods can provide a clear-
cut mutual proof of the validity of the methods and the
combination between them may reveal more physical information

about electron-crystal interactions and will undoubtedly make electron reflection theory stand on a more solid foundation.

In this chapter, the consistency between the two most mature and well developed computation methods in both the Laue case (transmission) and the Bragg case (reflection) is discussed both analytically and numerically. First, a more rigorous analytical derivation of the multislice formulation is attempted by introducing the Rayleigh-Sommerfeld propagator. Second, the consistency in the Laue case as a necessary precursor to the reflection problem is investigated numerically. Then the result of combining the Bloch wave and multislice method in the Bragg case is analyzed numerically. It is shown that the solution of the Bloch wave approach plays two roles: on one hand, it is the incident wave for further multislice iteration; on the other hand, it is a trial function for a Picard iteration which produces a stationary and convergent solution. Finally, the results are compared to the ones obtained using the approach of Peng and Cowley [1].

3.2. From the Schrodinger equation to multislice

3.2.1. Physics of multislice

One of the ultimate objects of theory development is the unification of different approaches to the understanding of

the universe, which led A. Einstein to desperately try to unify four kinds forces for more than 30 years. This is also true in the field of electron diffraction. The Bloch wave method is a direct application of the Schrodinger equation to electron diffraction, which may provide physical deep insight into electron diffraction. In contrast, the multislice method was first developed in a quite different way using a physical optics approach.

When light propagates in a medium, it experiences two kinds of phase variations if the medium has no absorption and the scattering is considered as elastic: a phase shift caused by medium variation which is described by the optical refractivity of the medium and a phase shift caused by propagation which obeys Huygen's Principle. These two processes are separated in usual optical systems, because the medium is considered as homogeneous and the refractive index only shifts at the boundaries. For an optical system with a series of thin lenses, using the Fresnel approximation, the relation between the incident and outgoing wave is given by:

$$\psi_t = \{ \ldots [\psi_o * \exp(i2\pi\alpha_o\chi^2)] . \exp(i2\pi\beta_o\chi^2) \ldots$$

$$\exp(i2\pi\beta_n\chi^2)\} * \exp(i2\pi\alpha_t\chi^2) . \exp(i2\pi\beta_t\chi^2) \qquad (3.1)$$

where α is the propagation coefficient, β the coefficient of phase shift caused by the medium. Here, the refractive index

shifts only at the boundary between vacuum and the lens, otherwise the wave propagates homogeneously. For wave propagation of a fast electron in a solid, the solid can no longer be considered as homogeneous, because of the short wavelength of fast electrons. Moreover, what we want to know is just the inhomogeneous structure of the solid through the interaction between the electron wave and the solid. Although the separation of the two different processes therefore is impossible in a macroscopic sense, it is still feasible at the microscopic level by applying a differential approximation and then physical optics is still applicable. This is the basic physical background of the initial development of the multislice approach by Cowley and Moodie [2-3].

By analogy to a series of lenses, the bulk material is sliced into a series of thin layers with thickness Δz and then treated as a series of planes onto which the potential of the slice between z and $z+\Delta z$ is projected. These planes are separated by vacuum gaps (Δz) which do not necessarily correspond to any specific spacing of crystallographic planes. The phase shift of the electron wave passing through a slice is given by:

$$q(x,y)=\exp[i\sigma\int_{z_n}^{z_n+\Delta z}\varphi(x,y,z)\,dz]=\exp[i\sigma\varphi_{pn}(x,y)\Delta z] \qquad (3.2)$$

where $\varphi(x,y,z)$ is the potential distribution of the solid, $\varphi_{pn}(x,y)$ the mean value of the potential in the region between z and $z+\Delta z$ and $\sigma=2\pi m\lambda_a/h^2$. If the Fresnel approximation is applied, the phase shift resulting from propagation between slices is given by:

$$p(x,y)=\exp[i2\pi k(x^2+y^2)/2\Delta z] \qquad (3.3)$$

Thus the wave function for the n+1th slice is:

$$\psi_{n+1}(x,y)=[\psi_n(x,y)*p(x,y)].q(x,y) \qquad (3.4)$$

where "*" denotes a convolution and "." a multiplication.

3.2.2. <u>Analytical relation between the Schrodinger equation and multislice</u>

As far as the physical background of the two approaches is concerned, it seems difficult to find both physical and analytical relations between the Schrodinger equation and multislice formulation, because the nature of quantum phenomena is quite different from that of electromagnetic waves. However, the wave nature is common, for which Huygen's Principle is universally applicable as long as the medium is homogeneous, and the results of any wave-medium interaction

are no more than either phase shifts or amplitude variations.

The first rigorous analytic derivation of the multislice formulation from the Schrodinger equation was given by Ishizuka and Uyeda [4] and was based upon five approximations:

i) Separation of the wave function: $\psi(\underline{r}) = \exp[i2\pi \underline{k}.\underline{r}]\phi(\underline{r})$

ii) Fresnel approximation

iii) No back-reflection approximation

iv) Stationary phase approximation

v) High energy approximation

It can be proved that the first two approximations are not only unnecessary, but also inaccurate.

In the Bragg case, the wave field in the plane perpendicular to the beam has two domains: vacuum and crystal. The assumed form of the wave field does not have any clear physical and mathematical background. The Fresnel approximation is not valid in the multislice approach, although so far it is widely used in the literature (but not in numerical programs). The condition for the Fresnel approximation is given by [5]:

$$\Delta z \gg (\pi\rho^4/\lambda)^{(1/3)} \qquad (3.5)$$

where ρ is the maximum radial extent and λ the wavelength of incidence electron. The typical value in multislice is $\rho = 3.0\text{Å}$ and the wavelength of 100keV electron is 0.037Å. Then we

obtain:

$$\Delta z \gg 19\text{Å}$$

This slice spacing value is far beyond the limit ($\approx 1\text{Å}$) required for the validity of stationary phase approximation and the elimination of "upper line effects".

Here, a more rigorous and general derivation of the multislice formulation from the Schrodinger equation is given by introducing the Rayleigh-Sommerfeld propagator [5], which is valid in all space. The time-independent Schrodinger equation in differential form is written as:

$$(\nabla^2 + \underline{k}^2)\psi(\underline{r}) = (2m/h^2)V(\underline{r})\psi(\underline{r}) \qquad (3.6)$$

where $\underline{k}$ is the incident wave vector, $V(\underline{r})$ is the potential energy, and $\underline{r} = (x,y,z)$. (3.6) can be converted into an integral form:

$$\psi(\underline{r}) = \exp[i\underline{k}.\underline{r}] - (2m/4\pi h)\int G(\underline{r}-\underline{r}')V(\underline{r}')\psi(\underline{r}')d\underline{r}' \qquad (3.7)$$

where G is the Green function. Referring to Fig.3.1, the real space vector $\underline{r}$ can be subdivided into two components as far as the wave field in the plane perpendicular to the z axis is concerned. $\underline{r} = (\underline{q}, z)$ and $\underline{r}' = (\underline{q}', z')$ where $\underline{q} = (x,y)$ and $\underline{q}' = (x',y')$. Then the Green's function can be written in the form of the Rayleigh-Sommerfeld propagator:

$$p(\underline{q}-\underline{q}', z-z') = (1/i\lambda)G(\underline{q}-\underline{q}', z-z')$$

$$= \frac{\exp[i2\pi k(z-z')(1+|\underline{q}-\underline{q}'|^2/(z-z')^2)^{(1/2)}]}{i\lambda(z-z')(1+|\underline{q}-\underline{q}'|^2/(z-z')^2)^{(1/2)}} \qquad (3.8)$$

Let $2m/4\pi h=(i/hv)(1/i\lambda)$, where v is the velocity of the incident electrons. Therefore, we have:

$$\psi(\underline{r})=\exp[i2\pi\underline{k}.(\underline{q},z)]+(-i/hv)\iint V(\underline{q}',z')\psi(\underline{q}',z')\times$$

$$p(\underline{q}-\underline{q}',z-z')d\underline{q}'dz \qquad (3.9)$$

The Fourier transform of the R-S propagator is [5]:

$$F_q\{p(\underline{q},z)\}=\exp[i2\pi kz(1-\lambda q^{*2})^{(1/2)}]=P(\underline{q}^*,z) \qquad (3,10)$$

where $\underline{q}^*$ refers to reciprocal vector in the plane at z. $P(\underline{q},z)$ as a propagator satisfies:

$$P(\underline{q}-\underline{q}',z-z')=\int P(\underline{q}-\underline{q}'',z-z'')P(\underline{q}''-\underline{q}',z''-z')d\underline{q}'' \qquad (3.11)$$

Equation (3.11) can be proved as the following: Taking the Fourier transform on the right side of (3.11):

$$F_q\{\int P(\underline{q}-\underline{q}'',z-z'')P(\underline{q}''-\underline{q}',z''-z')d\underline{q}''\}$$

$$=P(\underline{q}^*,z-z'')\exp(i\underline{q}',\underline{q}^*)P(\underline{q}^*,z''-z')$$

$$=F_q\{\int P(\underline{q}-\underline{q}',z-z'\}$$

Similarly, we have:

$$\exp[i2\pi\underline{k}\cdot(\underline{q},z)]=\int \exp[i2\pi\underline{k}\cdot(\underline{q}_o,z_o)]p(\underline{q}-\underline{q}_o,z-z_o)d\underline{q}_o \quad (3.12)$$

Therefore, referring to Fig.3.1, we obtain:

$$\psi(\underline{q},z)=\exp[i2\pi\underline{k}\cdot(\underline{q},z)]+(-i/hv)\int d\underline{q}'\int_{-\infty}^{+\infty}dz' x$$

$$V(\underline{q}',z')\psi(\underline{q}',z')p(\underline{q}-\underline{q}',z-z') \quad (3.13)$$

If the approximation of no back reflection is applied, we have:

$$\psi(\underline{q},z)=\exp[i2\pi\underline{k}\cdot(\underline{q},z)]+(-i/hv)\int d\underline{q}'\int_{-\infty}^{z}dz' x$$

$$V(\underline{q}',z')\psi(\underline{q}',z')p(\underline{q}-\underline{q}',z-z') \quad (3.14)$$

and

$$\psi(\underline{q}_o,z_o)=\exp[i2\pi\underline{k}\cdot(\underline{q}_o,z_o)]+(-i/hv)\int d\underline{q}''\int_{-\infty}^{z_o}dz'' x$$

$$V(\underline{q}'',z'')\psi(\underline{q}'',z'')p(\underline{q}_o-\underline{q}'',z_o-z'') \quad (3.15)$$

Equation (3.14) and (3.15) simply mean that the wave-medium interaction on the region where the z coordinate is larger than z, or z_o will have no effect on the wave fields $\psi(\underline{q},z)$ or $\psi(\underline{q}_o,z_o)$. Then,

$$\psi(\underline{q},z)=\int_{S_o}\exp[i2\pi\underline{k}\cdot(\underline{q}_o,z_o)]p(\underline{q}-\underline{q}_o,z-z_o)d\underline{q}_o$$

$$+(-i/hv)\int_{V_z}d\underline{q}''\int_{-\infty}^{z_o}dz''V(\underline{q}'',z'')\psi(\underline{q}'',z'')p(\underline{q}-\underline{q}'',z-z'')$$

$$+(-i/hv)\int_{V_{II}} d\underline{q}' \int_{z_o}^{z} dz' V(\underline{q}',z')\psi(\underline{q}',z')p(\underline{q}-\underline{q}',z-z')$$

$$=\int_{S_o} \psi(\underline{q}_o,z_o)p(\underline{q}-\underline{q}_o,z-z_o)d\underline{q}_o$$

$$+\int_{V_{II}} d\underline{q}' \int_{z_o}^{z} dz' V(\underline{q}',z')\psi(\underline{q}',z')p(\underline{q}-\underline{q}',z-z') \qquad (3,16)$$

Equation (3.16) is also a standard Volterra equation of the second type, which can be solved as a Picard iteration and always converges over a suitable interval (z_o,z). There are two important features of (3.16): i) the wave function is in general form and ii) no restriction is imposed upon the form of potential $V(\underline{r}')$ in the region between z_o and z, which is important in extending the derivation to the Bragg case in which both the wave function and crystal potential are non periodic districted functions. Equation (3.16) can be expressed as a successive approximation. Let:

$$\psi(\underline{q},z)=\sum_{n=0,\infty}c^n u_n(\underline{q},z) \qquad (3.17)$$

where $c=(-i/hv)$. Substituting (3.17) into (3.16), we have:

$$\sum_{n=0,\infty}c^n u_n(\underline{q},z)=\int_{S_o} \psi(\underline{q}_o,z_o)p(\underline{q}-\underline{q}_o,z-z_o)d\underline{q}_o$$

$$+\sum_{n=0,\infty}c^n\int_{V_{II}} d\underline{q}' \int_{z_o}^{z} dz' V(\underline{q}',z')u_n(\underline{q}',z')p(\underline{q}-\underline{q}',z-z')d\underline{q}'$$

Comparing the coefficients of the same order of c on two sides, we obtain:

$$u_o(\underline{q},z) = \int \psi(\underline{q}_o,z_o) p(\underline{q}-\underline{q}_o,z-z_o) d\underline{q}_o \qquad (3.18)$$

and

$$u_n(\underline{q},z) = \int_{V_{II}} d\underline{q}' \int_{z_o}^{z} d\underline{q}' V(\underline{q}',z') u_{n-1}(\underline{q}',z') p(\underline{q}-\underline{q}',z-z') \qquad (3.19)$$

For n=1,

$$u_1(\underline{q},z) = \int_{V_{II}} d\underline{q}' \int_{z_o}^{z} dz' V(\underline{q}',z') u_o(\underline{q}',z') p(\underline{q}-\underline{q}',z-z') \qquad (3.20)$$

$$= \int_{V_{II}} d\underline{q}' \int_{z_o}^{z} dz' V(\underline{q}',z') [\int_{S_o} \psi(\underline{q}_o,z_o) p(\underline{q}'-\underline{q}_o,z'-z_o) d\underline{q}_o] p(\underline{q}-\underline{q}',z-z')$$

$$= \int_{S_o} d\underline{q}_o \psi(\underline{q}_o,z_o) \int_{z_o}^{z} dz' \int_{V_{II}} d\underline{q}' V(\underline{q}',z') p(\underline{q}-\underline{q}',z-z') p(\underline{q}'-\underline{q}_o,z'-z_o)$$

The integral $\int_{V_{II}}$ in (3.20) can be simplified if the stationary phase approximation is applied [6]. Referring to Fig.3.2, $\int_{V_{II}}$ is given by:

$$\int_{V_{II}} d\underline{q}' V(\underline{q}',z') p(\underline{q}-\underline{q}',z-z') p(\underline{q}'-\underline{q}_o,z'-z_o)$$

$$= V[((z'-z_o)\underline{q}+(z-z')\underline{q}_o)/(z-z_o),z'] \int p(\underline{q}'-\underline{q}_o,z-z_o) p(\underline{q}-\underline{q}',z-z') d\underline{q}'$$

$$= V[((z'-z_o)\underline{q}+(z-z')\underline{q}_o)/(z-z_o),z'] p(\underline{q}-\underline{q}_o,z-z_o) \qquad (3.21)$$

It can be proved geometrically that the propagation function

in $\int_{V_{xx}}$, $p(\underline{q}-\underline{q}',z-z')p(\underline{q}'-\underline{q_o},z-z_o)$ has stationary phase at the point $r_o'=[((z'-z_o)\underline{q}+(z-z')\underline{q_o})/(z-z_o),z']$ (Appendix 3.1,Fig.3.2) and then we obtain:

$$\int_{V_{xx}} V(\underline{q},z')p(\underline{q}-\underline{q}',z-z')p(\underline{q}'-\underline{q_o},z-z_o)d\underline{q}'$$
$$=V[((z'-z_o)\underline{q}+(z-z')\underline{q_o})/(z-z_o)]p(\underline{q}-\underline{q_o},z-z_o) \qquad (3.22)$$

Then,

$$u_1(\underline{q},z)=\int_{S_o} d\underline{q_o}\psi(\underline{q_o},z_o)p(\underline{q}-\underline{q_o},z-z_o)x$$
$$\int_{z_o}^{z} dz'V[((z'-z_o)\underline{q}+(z-z')\underline{q_o})/(z-z_o),z'] \qquad (3.23)$$

For the case of the high-energy electron scattering, the scattering angle α is much smaller than 1. So the region of interaction between the wave at $(\underline{q_o},z_o)$ and medium potential during forward propagation is strictly located in the cone with the cone apex angle α and the cone axis $l_c=(\underline{q_o},z_o)\cap(\underline{q_o},z)$. Therefore, the potential should be projected along the line l_c instead of line $\underline{r_o}\underline{r}$. Then,

$$u_1(\underline{q},z)=\int_{S_o} d\underline{q_o}(\int_{z_o}^{z} dz'V(\underline{q_o},z'))\psi(\underline{q_o},z_o)p(\underline{q}-\underline{q_o},z-z_o)$$
$$=\int_{S_o} v(\underline{q_o},z)\psi(\underline{q_o},z_o)p(\underline{q}-\underline{q_o})d\underline{q_o} \qquad (3.24)$$

The principle of the derivation from (3.23) to (3.24) is the separation between the scattering and propagation of a wave. The wave-medium scattering is coincident with the wave propagation along the line $r_o r$ in (3.23), while only the scattering along the line l_o is considered because of the high energy approximation. The stationary phase approximation is based upon the fact that the value of integral $\int_{V_{II}}$ ("scattering-propagation integral"), largely depends on the localized potential. When n=2 for (3.19), we have:

$$u_2(q,z) = \int_{V_{II}} dq' \int_{z_o}^{z} dz' V(q',z') u_1(q',z') p(q-q',z-z')$$

$$= \int_{V_{II}} dq' \int_{z_o}^{z} dz' V(q',z') [\int_{S_o} dq_o . \int dz'' V(q_o,z'') \psi(q_o,z_o) p(q'-q_o,z'-z_o)]$$
$$\times p(q-q',z-z')$$

$$= \int_{S_o} dq_o . \int_{V_{II}} dq' \int_{z_o}^{z} dz' V(q',z') v(q_o,z') \psi(q_o,z_o) p(q'-q_o,z'-z_o)$$
$$\times p(q-q',z-z')$$

$$= \int_{S_o} dq_o . \int_{z_o}^{z} dz' \ V(q_o,z') v(q_o,z') \psi(q_o,z_o) p(q-q_o,z-z_o)$$

$$= \int_{S_o} dq_o [(1/2) v(q_o,z)^2] \psi(q_o,z_o) p(q-q_o,z-z_o) \qquad (3.25)$$

Then,

$$u_n = \int_{S_o} dq_o [(1/n!) v(q_o, z)^n] \psi(q_o, z_o) p(q-q_o, z-z_o) \qquad (3.26)$$

Substituting (3.18), (3.24-26) into (3.17), we have:

$$\psi(q, z) = \int_{S_o} [\Sigma_{n=0,\infty}(-i/hv)^n v(q_o, z)/n!] \psi(q_o, z_o) p(q-q_o, z-z_o) dq_o$$

$$= \int_{S_o} \exp[(-i/hv) v(q_o, z)] \psi(q_o, z_o) p(q-q_o, z-z_o) dq_o \qquad (3.27)$$

where $v(q_o, z) = \int_{z_o}^{z} V(q_o, z') dz'$ is the projected potential.

Equation (3.27) can be written in the form of convolution:

$$\psi(q, z) = [\psi(q, z_o) . q(q, z-z_o)] * p(q, z-z_o) \qquad (3.28)$$

where $q(q, z-z_o) = \exp[(-i/h) \int_{z_o}^{z} V(q, z') dz']$ and $*$ denotes

convolution. If $z_o = z_n$, $z = z_{n+1}$ we obtain:

$$\psi(q, z_{n+1}) = [\psi_n(q, z_n) . q_n(q, z_{n+1}-z_n)] * p(q, z_{n+1}-z_n)$$

or,

$$\psi_{n+1}(q) = [\psi_n(q) . q_n(q)] * p(q, z_{n+1}-z_n) \qquad (3.29)$$

This is nothing but the multislice formulation due to Cowley

and Moodie [2-3]. From (3.6) to (3.29), the derivation clearly

shows the equivalence between the two approaches. However it

is conditional. When $V(q, z)$ varies slowly along the z axis on

the range (z_o, z), (3.28) can also be approximated as:

$$\psi(q, z) = [\psi(q, z) . q(q, z-z_o)] * p(q, z-z_o) \qquad (3.30)$$

Replacing z_o by z is not only an approximation, but also a

major change of the problem. (3.30) is an equation with an unknown function, which is a simplified and numerically feasible equivalent of Equation (3.16), instead of a successive solution at different thicknesses as given by (3.28) or (3.29). As noticed, the solution of (3.30) is independent of z on (z_o, z) and only depends upon the property of $V(\underline{b}, z)$ on (z_o, z). Obviously, this is meaningful only when the true solution of (3.16) is independent of z and $V(\underline{b}, z)$ is periodic along the z axis. Fortunately, electron diffraction in the Bragg case fulfills these conditions. The independence of z for the wave field in the Bragg case has been proved analytically in Appendix 3.2. This also offers convenience for the consistency investigation in the Bragg case, as will be shown later.

The solution of (3.30) can be solved by the Picard iteration similar to (3.16):

$$\psi(\underline{q}, z) = \lim_{n \to \infty} \psi_{n+1}(\underline{q}, z) \qquad (3.31)$$

where

$$\psi_{n+1}(\underline{q}, z) = [\psi_n(\underline{q}, z) \cdot q(\underline{q}, z-z_o)] * p(\underline{q}, z-z_o) \qquad (3.32)$$

Equation (3.31) shows how to obtain the wave field at $(\underline{q}, z)$, while Equation (3.29) solves the wave field at $(\underline{q}, z_{n+1})$, if the wave field at $(\underline{q}, z_n)$ is known. They are equivalent in the

Bragg case, for which the wave field is independent of z and the crystal potential is periodic along the z axis. In other words, solving the wave field at the thickness deep enough by a multislice iteration is equivalent to solving the Schrodinger equation by a Picard iteration.

3.2.3. Validity conditions for multislice iteration

Referring to Appendix 3.1, the validity condition of (3.29) can be expressed as:

$$6r'^2/\lambda\Delta z \geq 1 \tag{3.33}$$

where r' is the distance over which the potential is considered not to vary appreciably, λ the electron wave length and Δz the slice spacing. This is the condition for the validity of the stationary phase approximation. Equation (3.33) imposed a restriction simultaneously on the property of incident electrons (λ), the property of the medium (r') and the set-up of slices (Δz).

Another validity condition imposed on the parameters Δz was given by Lynch and Goodman & Moodie [7-8], which was called "upper line effects". This argument is mainly based upon the consideration of optical propagation. The propagator in reciprocal space is given by:

$$P(h,k) = \exp[i2\pi\Delta z\lambda|\underline{u}_{hk}|^2/2]$$

$$=\exp[i2\pi\varphi(h,k)\Delta z] \qquad (3.34)$$

where $\underline{u}_{hk}$ is the reciprocal lattice vector for a specific beam (h,k) and $\varphi(h,k)=\lambda|\underline{u}_{hk}|^2/2$ is the excitation error of the hk beam for the Ewald sphere of radius $1/\lambda$. As the magnitude of a particular $\varphi(h,k)$ approaches $1/\Delta z$ in (3.34), the phase shift during the propagation of this beam with respect to the central beam approaches 2π radian. This means that the major value of the phase $(0<\theta<2\pi)$ in the propagator can no longer indicate the phase differences for all orientations. Thus, this particular beam will be artificially reinforced and becomes one due to upper line in the reciprocal lattice corresponding to the planes with c spacing of Δz. In other words, the effect of the beam is confused with that of beam $(0,0,\pm1/\Delta z)$. This occurs because of Δz being taken as a finite value. In a medium, since $\Delta z\rightarrow 0$, the phase differences between different beams caused by propagation must be located in the region of major value. To avoid this undesired effect, the condition is:

$$\varphi(h,k)\Delta z \leq 1$$

or

$$\Delta z \leq 1/\varphi(h,k) \qquad (3.35)$$

In the usual usage of multislice, (3.33) and (3.35) are consistent with each other, although the physical backgrounds

are not related. In most cases, (3.35) is a little more restrictive than (3.33).

As an example, for an incident energy E_o=100keV, (λ=0.037Å), sampling rate 10/Å (d=0.1Å) and $|\underline{u}_{(hk)max}|$=5$\sqrt{2}$Å^{-1}, (3.33) gives:

$$\Delta z \leq 6r'^2/\lambda = 1.62Å$$

and (3.32) gives:

$$\Delta z \leq 2/\lambda |\underline{u}_{hk}|^2 = 1.08Å$$

These two numbers are close to each other and the applicable slice thickness Δz_{max} for 100keV electron is about 1Å. The higher the energy of the incident electron, the larger the slice thickness Δz_{max}.

3.2.4. Normalization

No matter whether $\psi(\underline{r})$ is normalized or not, both (3.6) and (3.29) are valid. If $\psi(\underline{r})$ in (3.6) is normalized over the whole 3-D space, so is $\psi(\underline{q},z_n)$ in (3.29). However, numerically, the normalization consistency between the two equations becomes more complicated. For the Bloch wave method, the wave function is expanded as plane waves in real space. The number of plane waves is finite in a numerical treatment:

$$\psi(\underline{r}) = \sum_{\underline{q}(n)} C_{\underline{q}}^{(j)} \exp[i2\pi(\underline{k}^{(j)}+\underline{q}).\underline{r}] \qquad (3.36)$$

The normalization of $\psi(\underline{r})$ in the whole real space leads to the

normalization in a finite reciprocal space:

$$\sum_{\chi(H)} |C_g^{(i)}|^2 = 1 \qquad (3.37)$$

If the zero Laue zone approximation is applied, the normalization is over a finite area in the reciprocal plane $z=0$. For (3.20) and (3.29), the integral $\int_{S_o}$ and the scattering-propagation integral $\int_{V_\pi}$ are considered as over the whole two dimensional space. $\psi_n(g,z)$ can be normalized in reciprocal space as it is in (3.34). But, the convolution in multislice iteration cannot be applied to the whole of real space. A full real space convolution in 2-D in (3.20) corresponds to a reciprocal space multiplication. If $\psi_n(g,z)$ and $q(g,z-z_n)$ are band limited, the multiplication in the reciprocal space can be reduced down to a finite area. However, $\psi_n(g,z)$ and $q(g,z-z_n)$ are not necessarily band limited functions. A phase grating function is not band limited because a wave is usually scattered by crystal potential in all directions. These intensities scattered into the region outside the calculated area are artificially cut off in each iteration. This is called the "overflow effect" [9]. However, as long as the number of beams calculated is big enough, the multiplication in reciprocal space for a finite area in (3.29) can be close to the convolution over the whole real space in

(3.20). But the successive intensity reductions during the multislice iterations can accumulate, which can affect the consistency between Equations (3.6) and (3.29). A way of solving the problem is to impose normalization of the wave function in reciprocal space after each iteration. That is:

$$\psi_{n+1}(\underline{g}, z_{n+1}) = c_n [\psi_n(\underline{g}, z_n) q(\underline{g}, z_{n+1}-z_n)]^* p(\underline{g}, z_{n+1}-z_n) \qquad (3.38)$$

where c_n is a normalization constant. We then have:

$$\psi_{n+1} = \Pi_{i=1,n} c_i [\psi_o \cdot q_o \ldots \ldots] q_n^* p_n \qquad (3.39)$$

Obviously, $\Pi_{i=1,n} c_i$ only affects the total intensity of wave field ψ_{n+1} but not the intensity distribution.

To summarize, Equation (3.38) is analytically consistent with (3.6) under the conditions (3.33) and (3.35), if the successive normalization in (3.38) is carried out during the numerical iterations. The form of the potential in the phase grating $q(\underline{g}, z_{n+1}-z_n)$ and the wave function $\psi(\underline{g}, z_n)$ are not restricted, which is important for the Bragg case because diffraction in the Bragg case is basically a boundary phenomenon in which the potential is non-periodic and truncated.

3.2.5. <u>Numerical development of the combination of the Bloch wave and multislice</u>

The consistency between the Bloch wave method and

multislice formulation has been proved analytically in the previous sections, which clearly shows the possibility of combining these two approaches to make use of the advantages of each. The scheme of combining the two approaches is shown in Fig.3.3.

The calculation consists of two blocks: one for the Bloch wave calculation and another for the multislice calculation. The Bloch wave calculation for the Bragg case has been discussed in detail in Chapter II. The Bloch wave block is operational in both the Bragg case and the Laue case since the Bloch wave calculation for the reflection requires the solution in the general cases. The only difference is the angle of the incident beam with respect to the entrance surface. The block for the multislice calculation is based on the multislice program by L. D. Marks, which is the computation utility for high resolution THEEM simulation at Northwestern University. This block alone is also operational in both the Bragg case (the method of Peng and Cowley [1]) and the Laue case. The input to the multislice block is the output of the Bloch wave block. The software is operational in six different calculation modes (Table 3.1) and various output data can be obtained from the calculations in different modes.

3.3. <u>Numerical investigation of the consistency between the Bloch wave method and multislice method in transmission</u>

To make the two different approaches work together, it is important to investigate the consistency between them. One should know whether they are consistent and for what conditions they are consistent. Since in the Bragg case, it is difficult to reach a stationary solution by the multislice method, it is tactful to investigate the consistency between them in the Laue case as the first step, which, in addition, can also offer information about the reliability of the programing. This was early done by Self et al.[9], which is reconfirmed here and more details are provided in the following sections.

3.3.1. <u>Effects of the number of beams</u>

One way of evaluating the consistency between the two methods is to plot the amplitude and phase of several low order diffracted beams obtained from the two methods against the thickness. The consistency between the two different approaches can be well presented by the consistency between these curves.

The results for the Bloch wave calculation and multislice calculation are shown in Fig.3.4 (i-vii), which show a series

of comparisons between the two methods for different number of beams. The calculation conditions are as follows: gold is taken as the simulation system, with the incident beam perpendicular to the [010] zone and an incident energy of 100keV. A couple of points should be mentioned:

i) The oscillation periodicities of both the amplitudes (extinction distance) and the phase for different beams are systematically a little smaller than those reported by Self et al. This is mainly due to different ways of calculating the scattering factors; the parameters for X-ray scattering factors were used in current calculations. The error arising from this term was recently discussed by Peng and Cowley [10].

ii) The sign of the phase in current results is opposite to that of Self et al.. This is more likely due to a different choice of zero reference point--here the transmission beam is taken as the reference point.

iii) The number of beams for both methods does not take the forbidden beams for the fcc structure into account, therefore, for the case of 3x3 beams, the actual number of beams calculated is 5x5 in the multislice calculation.

iv) The differences between the Bloch wave method and the multislice method are significant when only a small number of beams are included in the calculation. The reason for these

differences is the "overflow effect" as discussed in Section (3.2.3). The wave distribution will be strongly affected for a small number of beams and the normalization at each slice can not solve the problem since c_n in Equation (3.34) only deals with the total intensity. Nevertheless, the extinction distance of each beam for the two methods is the same no matter how big the divergence between the curves calculated by the two methods.

v) In the current calculation, the largest number of non-extinct beams is 21x21. In other words, the largest total beam number is 41x41. The corresponding sampling array in real space is set up as 64x64. This is in the range that the sampling theorem requires. For the case of a smaller number of beams in reciprocal space, the sampling rate in real space is better than that the sampling theorem requires and the aliasing effect is even smaller.

It is important to examine the convergence of both methods. Fig.3.5 shows the charge density at various depths for both methods as a function of the number of beams used. The figure clearly shows that the consistency between the Bloch wave solutions with 13x13 beams and the multislice solution with 21x21 beams is significantly better than that between the Bloch wave solutions and the multislice solution

both with 13x13 beams. To be more quantitative, Fig.3.6 shows

plots versus thickness of a parameter R(t), where R(t) is

defined as :

$$R_{ij}(t) = \frac{\sum_{x,y}[I_{bi}(x,y) - I_{mj}(x,y)]^2}{\sum_{x,y}I_{bi}(x,y)^2} \qquad (3.40)$$

where I_{bi} and I_{mj} denote the intensities calculated from the

Bloch wave method and the multislice method respectively, t

is the thickness and the subscripts i & j denote the number

of beams. The curves show that when the number of beams is

larger than 11x11, the quantitative agreement is excellent.

The flattening of the curves means that the methodical

differences between these two approaches plays a smaller role

with increasing number of beams, and the numerical errors are

the major reason responsible for the deviation. Fig.3.7 shows

values of a convergence parameter C(t) versus thickness for

different numbers of beams, where C(t) is defined as:

$$C_{mn}(t) = \frac{\sum_{x,y}|I_m(x,y) - I_n(x,y)|}{\sum_{x,y}|I_m(x,y) + I_n(x,y)|} \qquad (3.41)$$

where I_m and I_n denote the amplitude of each point in the

image, subscripts m and n denote the number of beams for the

calculation. The results in Fig.3.7 shows that the magnitude

of $C_{11x11 \atop 13x13}(t)$ for the Bloch wave calculation is close to the

magnitude $C_{13x13 \atop 17x17}(t)$ for the multislice calculation. This indicates that the Bloch wave calculation converges for a smaller number of beams than the multislice. But it is not significant enough to reduce the disadvantage of low computation speed. The curve of $C_{17x17 \atop 21x21}(t)$ demonstrates that the multislice calculation converges well enough when the beam number is larger than 17x17. Compared to $R_{b(13x13) \atop m(21x21)}(t)$, it can be seen that the results of both methods converge to the true solution with increasing number of beams. The monotonic increase of C(t) with the thickness is due to numerical errors accumulating in the direction of wave propagation.

3.3.2. Effects of higher order Laue zones

Since the Bloch wave calculation is currently limited by computation speed, it is difficult to take non-zero Laue zone diffraction into account. The whole unit cell is projected in the direction of the incident beam onto the zero plane. Therefore, to reach consistency between the two methods, the phase grating in multislice was constructed in an equivalent way; the unit cell of gold projected onto the zero plane in the direction [010]. Since "upper line effects" become more serious and the stationary phase approximation is broken for large propagation spacing in multislice calculation, the slice

is subdivided into four subslices in order to reduce propagation space. Each of them contains one fourth of the projected potential of a full cell and corresponds to one fourth of the c spacing of the conventional unit cell (1.0124Å).

In the multislice calculation, there are different ways of subdividing one unit cell and the occupancy of each atom in the unit cell can also be subdivided into different slices. All these operations may lead to the higher order Laue zone effects involved in the calculation. However, these treatments are only a rough approximation to the effects of higher order Laue zones. True representation of them needs three dimensional sampling, which makes the multislice approach infeasible. The effects of the higher order Laue zone were investigated by Lynch [7] qualitatively in 1971. The effects are currently excluded from the calculation, which is justified by the low excitation intensities of higher order Laue zone in the high energy case.

The effects of the slice thickness has been discussed in Section (3.2.3). The inequalities (3.33) and (3.35) provide an estimated value for the slice thickness of about 1Å. For gold, c=4.08Å. If it is subdivided into four slices, then Δz=1.02Å, which is proper for the multislice calculation.

3.4. Numerical investigation of consistency in reflection

For reflection, it is difficult to investigate the consistency between the Bloch wave method and multislice iteration since it is difficult to obtain and verify a stationary solution from the multislice iteration. However, because the wave field both inside and outside the crystal in the plane parallel to the zero Laue zone is stationary in the Bragg case (Appendix 3.2), this provides an alternative way of studying the consistency in the reflection mode: taking a symmetric incidence condition for convenience and investigating the variation of the wave field in the direction of the incident beam. The important point here is that the variation of the wave field during the multislice iteration not only indicates the degree of the consistency between the two methods, but also reveals the extent of the convergence to the true solution in a crystal with a surface potential in the Bragg case. It is more important that the consistency and convergence of the two methods provides a strong mutual proof of the validity of the two methods and the combination of the two.

For the case of reflection there are two basic differences between the Bloch wave block and the multislice block: one is methodical difference and another is the

difference due to the surface truncation i.e. the zero surface potential approximation in the Bloch wave calculation. The former has been investigated both analytically and numerically in Section (3.2) and (3.3), and the latter is new for the Bragg case.

3.4.1. Unit cell

The unit cell set-up for the Bloch wave calculation in the reflection case is not very much different from that in transmission. The only difference is that to reduce the effect of the surface truncation, the surface should be between the atomic planes rather than in the atomic plane. To achieve this, the boundary is fixed at zero and the unit cell is moved into the crystal along the z axis by a quarter of the c spacing as shown in Fig.3.8(i). Note that we are using the conventional notation of the z axis as normal to the surface. The one dimensional potential plotting along the z axis shows the deviation of the surface potential in the Bloch wave mode from that in a real crystal. To be consistent with the unit cell set-up for the surface simulation in a multislice calculation, the wave field is constructed in a large unit cell, which has a size of 16ax1a (a denotes the magnitude of lattice parameter of gold, and the wave fields are displayed

in a size of 8ax2a). For the case with no absorption, the right half of the cell is for the Bloch waves in the crystal and the left half for the reflected wave in vacuum. When an absorption of 10% is included, the crystal wave rapidly damps in the crystal and the surface can be set further towards the right. Here we set the surface position such that the crystal occupies a quarter of the unit cell on the right and the reflected wave three quarters on the left along the z axis. This can further reduce edge effects in the multislice calculation. For the multislice part, the unit cell is similar to that used in profile imaging and has the same size as the unit cell for the Bloch wave: 16ax1a, although the wave is also displayed in the size of 8ax2a (Fig.3.8(ii)). Each atom in the slice was moved a distance of a/4 into the crystal to align with the position of the corresponding atom in the Bloch wave calculation. The full unit cell is projected along [010] and then subdivided into four identical slices, each containing one fourth of the projected potential of the full cell and of thickness 1.0128Å. The size of sampling array for the multislice calculation is 1024x64.

In the following sections, the results as a function of the incident angle, number of beams and absorption are analyzed.

3.4.2. Effects of absorption

To investigate the consistency and convergence of the solution, a deviation parameter was defined as:

$$D(t) = \frac{\sum_{x,y}[I_t(x,y) - I_o(x,y)]^2}{\sum_{x,y}I_o(x,y)^2} \tag{3.42}$$

where I_o denotes the intensity of the wave field calculated by the Bloch wave method and I_t the intensity of the wave field output calculated by multislice iteration. The magnitude of $D(t)$ reflects the consistency of the solution while the derivative of $D(t)$, $dD(t)/dt$ indicates the convergence of the solution. We also apply an intensity analysis by using the convergence parameter defined in (3.41) for the reflection case. In order to avoid undesirable edge effects, the intensity analysis is only applied to the central half of the wave field for the case with no absorption and the right half for the case with absorption. A convention of referring to the output of the Bloch wave program as the thickness $t=0$ is adopted.

Fig.3.9(i) shows the current density output at different thicknesses up to 607.5Å for an incident angle of 25mRad, absorption is not included. The beam geometry is: the [010] zone is taken as the zero Laue zone; the surface normal is coincident with the z axis; the incident beam azimuth with

respect to yz plane is zero. The plane of the figure is parallel to the zero Laue zone. The number of beams calculated in the Bloch wave is 13x13, located in the region $\pm 2x\pm 2 \text{Å}^{-1}$ in reciprocal space. Fig.3.9(ii) shows the plots of the deviation parameter D versus thickness, while Fig. 3.9(iii) shows the plots of convergence parameter C, where (R.W.) denotes the reflected wave, (B.W) the Bloch wave in the crystal and (T.W.) the total wave. The first slice in Fig.3.9(i) is the wave field output from the Bloch wave calculation and its thickness is taken as: t=0Å. The spacing between the two closest slices is 50Å.

For absorption, the commonly used phenomenological treatment was applied for both the Bloch wave calculations and the multislice calculations. The crystal potential in reciprocal space is taken as complex with an imaginary part equal to 10% of the real part.

Fig.3.10 shows the results for the same conditions as those for Fig.3.9, except that an absorption of 10% is included. Comparing Fig.3.10 with Fig.3.9, one can easily find that the wave field in the crystal decays sharply for the case with absorption, while it extends deep into the crystal for the case without absorption. However, the reflected wave is not affected seriously by absorption. The corresponding plots

of D and C against the slice thickness shown in each figure indicate that including absorption can greatly improve the consistency and convergence as mentioned before. This is largely due to reduction of edge effects. The cross points in Fig.3.9(ii) and (iii) at about 500Å indicate that the edge starts moving into the analyzed area. The edge has more serious effects on the reflected waves than the crystal waves. Fig.3.10(ii) shows that the D parameters for the three waves converge to 0.5% after 600 slices, while Fig.3.10(iii) shows that the convergence of the C parameter for the crystal wave is a little better than that for reflected wave, which is mainly due to the different effects of the edge on the two parts. The C parameter can never be zero since the numerical errors can never be eliminated. The reason for the larger scale of C, compared to D, is because C is a first order parameter while D is a second order parameter. The plots of D and C parameters for the crystal wave often start worse and end better, compared to the reflected wave. This is because the methodical errors are more important initially and later on will drop off and the numerical errors become important. The former is usually larger than the latter.

3.4.3. Effects of the number of beams

When the number of beams calculated in the Bloch wave is changed, both the consistency and convergence will be affected. Fig.3.11 and 3.12 show results for the same condition as in Fig.3.10, except for a decrease in the number of beams from 13x13 to 9x9 and 11x11 respectively. The images do not look very different from those for 13x13 beams. Nevertheless, the D and C parameters clearly indicate the effects of the number of beams, although it is not very significant. Fig.3.11(ii) shows that the D parameters of the reflected wave and total wave for 9x9 beams case do not converge well, although those for the crystal wave are not affected significantly, increasing from 0.5% to 0.55%. The behavior of the D and C parameters of all three waves for the 11x11 case are significantly better than for the 9x9 case. The D parameter of reflected waves for the 11x11 case converges to 0.3%, which is 30% smaller than that for the 9x9 case. A reduction also occurs in C. It is interesting that the results for the 11x11 case are even a little better than that for the 13x13 case. This is possibly due to numerical errors in the Bloch wave calculation increasing with the number of beams, since the number of calculations increases with the square of the number of beams. This also shows that the number of beams in the Bloch wave calculation required for the consistency and

convergence for reflection is similar to that for transmission: about 11x11.

3.4.4. Effects of incidence angle

Fig.3.13, 3.14 and 3.15 show the results for the same condition as in Fig.3.10, except the incidence angles changed to 25mRad, 30mRad and 35mRad respectively. A noticeable feature of the wave field for small incidence angle (10mRad) is that it concentrates in the top layer; note also that there is a gap between the top atoms and the vacuum wave with low electron intensity for 10mRad incidence. It should be pointed out that this surface channeling is not the result of the absorption since the calculation with no absorption gives the similar results. The magnitude of both D and C parameters of the reflected wave and total wave for 10mRad incidence decrease considerably and these curves also converge well at 600Å. However, the magnitudes of both D and C parameters of the crystal wave for 10mRad increase significantly compared to those for 25mRad. This possibly is due to the sharp damping of the crystal wave, which reduces the area available for intensity analysis. The magnitudes of both D and C parameters of the reflected wave and total wave for 30mRad and 35mRad incidence shown in Fig.3.14 and 3.15 appear not to be

seriously affected by the change of incidence angle, although the D parameters of the reflected wave and total wave do not converge well at 600Å. Nevertheless, D parameters of the crystal waves in these two cases increase significantly with the incidence angles, and the D parameter of the crystal wave for 35mRad incidence even fails to converge at 600Å and the magnitude is larger than 2% at the same thickness. It appears that the larger the incidence angle is, the worse the consistency and convergence are. There are two basic reasons for this. First, in the multislice calculation, the approximation is generally made that the phase grating does not vary with small changes of the incidence angle and all effects of the changes of incidence angle are included in the propagator. This error mainly affects the consistency and convergence of the crystal wave. Second, when the incidence angle increases, the interaction between the electron wave in the vacuum and the surface potential becomes more important, which affects the consistency and convergence of the reflected wave.

3.4.5. Effects of surface potential

If one studies the wave field in the vacuum in Fig.3.9, 3.10, 3.11 a little more closely, one can observe slight

differences between the reflected wave in the first slice and other slices. The analysis of both D and C parameters of the vacuum waves has already shown the deviation of the solutions in the multislice simulation from the Bloch wave solutions. The major part of the deviation is due to the artificial surface truncation in the Bloch wave calculation. However the effects of the surface truncation in the Bloch wave calculation is much smaller than we except, which is consistent with the results by Howie (1988) [11], but contrary to the conclusion of Britze et al.[12]. This merits further studies.

The arguments given at the beginning of this section proved that the multislice iteration in the reflection case is equivalent to a Picard iteration solution of the Schrodinger equation in integral form. This means that no matter how bad the trial wave function (the Bloch wave output) is, the iteration must converge to the true solution in the potential without surface truncation in the reflection case since the surface potential is automatically included in the phase grating in the multislice calculation. The small effect of the surface truncation in the Bloch wave calculation results in much faster converging speed in the multislice calculation, which leaves more room for the simulation of

surface features.

As mentioned before, the first slice (t=0Å) is the Bloch wave solution which plays two roles here: 1) the incident wave field in the multislice; 2) the initial wave field in the Picard iteration. It is obvious that the deviation should first emerge in the area close to the surface and then become stable and gradually spread out with increasing thickness, since the surface potential decays exponentially with increasing the distance away from the surface. In other words, the convergence regarding the effects of surface potential (since the accumulation of numerical errors during the multislice iteration is unavoidable, the convergence can not be considered as exclusively perfect) should also first emerge in the area close to the surface. To demonstrate this more clearly, the square of the differences between the two nearest slices, $F_{n,n-1}(\underline{g}) = [\psi(\underline{g}, y_n) - \psi(\underline{g}, y_{n-1})]^2$ was studied by projecting $F_{n,n-1}(\underline{g})$ onto the z axis. In the coordination system used here, the incident wave is along the y axis and the z axis points into the crystal surface. The projected intensities of $F_{n,n-1}(\underline{g})$ against z for 25mRad and 30mRad incidence are shown in Fig.3.16 and 3.17 respectively. A peak occurs just at the surface in the first curve of $F_{n,n-1}(\underline{g})$ in each case, as the initial wave is scattered by the surface

potential. The peak gradually moves out and a range with a flat and low intensity gradually increases with the iteration n or slice number m. This becomes clear for m > 5 (n > 250) i.e. after the fifth curve in Fig.3.17. The multiple peaks in curves of $F_{n,n-1}(g)$ with 5 < m < 11 are probably due to either oscillatory convergence of the Picard series, similar to the convergence of the Fourier series, or the accumulation of numerical error. They finally decay to a series of small modulations. One important feature in Fig.3.16 and 3.17 is that the convergence of the Bloch wave in the crystal is well preserved.

The current results show that the effects due to the surface potential on the reflected wave are not significantly incidence angle related. The magnitudes of both D and C parameters of the reflected waves in Fig. 3.10, 3.13, 3.14 do not show a clear trend with the increasing of incidence angle. This appears to be contrary to what one might expect; the surface potential effects should become more serious for larger incidence angle because of the stronger interaction between the larger components normal to the surface of electron wave and surface potential. This is worth further studying both experimentally and theoretically.

3.4.6. Comparison with the solution in multislice-only mode

When the program is shifted to the reflection-multislice-only mode, we obtain the results shown in Fig.3.18(i), (ii) where (i) is the result without absorption and (b) is the result with an absorption of 10%. Here, we are following Peng and Cowley's treatment: a plane wave smoothed by a Gaussian function and towards the crystal surface is introduced into the left part of the unit cell in the vacuum. The tilt angle is 25mRad. Both the wave reflected from the crystal and the wave penetrating into the crystal in slices d,e and f at the areas close to the crystal surface have some correlation with the true stationary solution in Fig.3.9, although the deviation is still obvious. Due to the edge effects it appears, however, that the solution is unstable. If absorption is introduced (Fig.3.18 (ii)), the result is not much better.

3.5. Interim summary

The consistency between the solutions of the Bloch wave method and multislice method in both the Laue case and the Bragg case has been reached with satisfactory accuracy. For the Bragg case, an alternative way of investigating the consistency between the two methods introduces a new view of the problem, which both analytically and numerically shows

that the multislice iteration in reflection is equivalent to a successive Picard iteration that numerically leads to a true solution of the Schrodinger equation in the crystal potential without surface truncation.

The consistency between the Bloch wave calculation and the multislice calculation in both the Laue case and the Bragg case has been studied numerically, such as the effects of slice thickness, beam number and absorption. Studies of the effects of the higher order Laue zone have not been carried out because of high cost of CPU time for both the Bloch wave and multislice calculations when including the higher order Laue zone effects. An approximate high order Laue zone effect in the Laue case for the multislice calculation has been investigated by Lynch [7].

It has been demonstrated that the Bloch wave solution is close to a genuine solution of the dynamical reflection problem, and even though there can be some errors due to the effect of neglecting a surface potential, these can be eliminated by using the multislice as a Picard iteration. This later feature is especially important since it opens up a whole range of different ways of calculating reflection problems. As mentioned before, the Picard solution is unconditionally convergent, and we can expect that the speed

with which it converges will depend upon how good the first wave function is to the true solution. The results of intensity analysis clearly indicate that the Bloch wave solution is quite close to the true solution, and the effects of surface truncation in the Bloch wave calculation are unexpectedly small. Therefore, we can envisage solving problems involving surface relaxations by using a solution generated from a Bloch wave approach and then multislicing it to convergence. Since the multislice is a fast approach, and even faster if one utilizes array processors, this may be an efficient method of solving many otherwise intractable problems.

One obvious problem is edge effects; multislice is not a true numerical solution since it depends upon the periodicity of the system, which leads to edge effects. One can overcome these problems to some extent by using very long unit cells as was done here. A more robust and general approach is possibly to use patching or some other technique to avoid the edge effects. For instance, one possibility would be at each slice to force the edge of the cell, or a region near the edge, to have the same amplitude and phase. This is an area for further numerical research.

One additional point which appears to be quite clear is

that simply using an incident top-hat wave function does not seem to be a reliable approach. Without the additional information from the Bloch wave solution, we cannot see how one can readily identify when the solution is stationary. It is possible that one could stabilize this approach, avoiding the edge effects, and then use the multislice alone to sum the Picard series. If this is possible then this might be a simple method of solving the general reflection diffraction problem in a relatively simple conceptual manner.

With the increase of the number of beams and slices, the computation speed slows down. For the case of 13x13 beams and 600 slices, it needs about 20 hr CPU time on an Apollo 3500. There is still more room for numerical improvement. The Bloch wave calculation now can be separated from the multislice calculation and the Bloch wave solution calculated as the incident wave to the multislice block can be reused for different multislice iterations. This at least reduces 80% of the CPU time.

It is important that the results at this stage have shown the real possibility of combining different computation methods to make them work together, revealing the conditions for the consistency of the various methods, exploiting their relative advantages and providing mutual validity proof. This

will place the theories of electron reflection on a more self-consistent foundation.

Table 3.1

	Transmission	Reflection
Bloch	B-T	B-R
waves		
Multislice	M-T	M-R
Bloch waves + Multislice	B+M-T	B+M-R

Table 3.1. List of all six operational modes of the programing for the BMCR method.
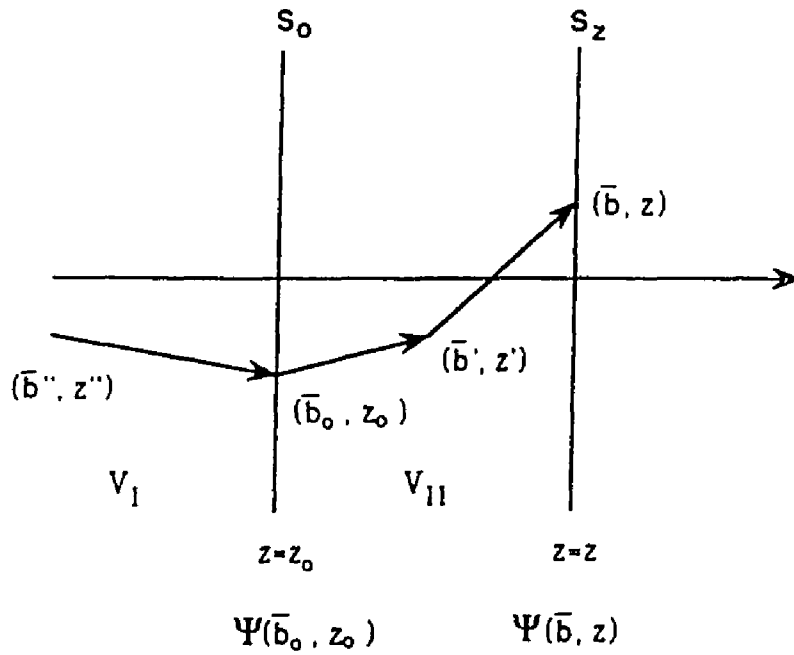
Fig.3.1. Schematic diagram for deriving multislice formula from the Schrodinger equation in integral form. S_o: incidence plane. S_z: exit plane. z: forward propagation orientation.
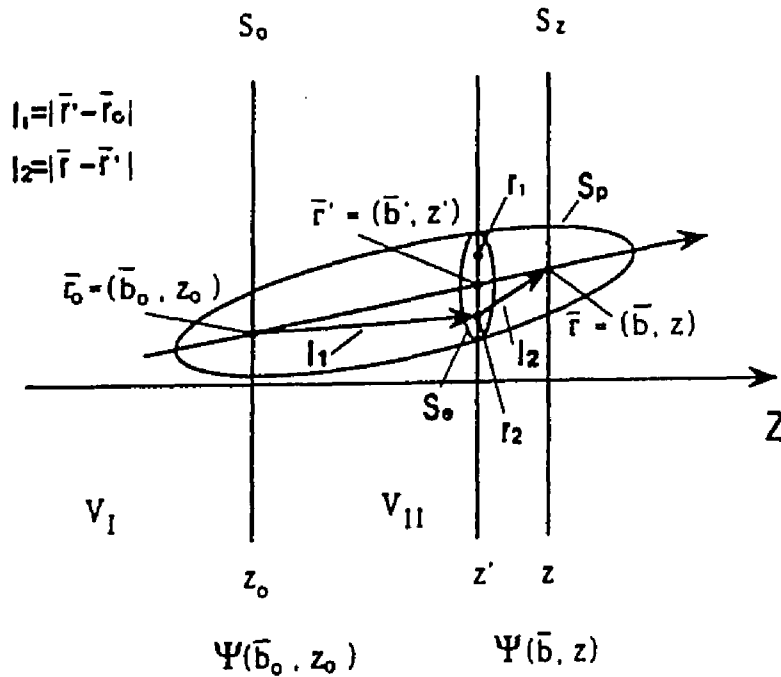
Fig.3.2. Schematic diagram showing the application of stationary phase approximation to the derivation of multislice formula.
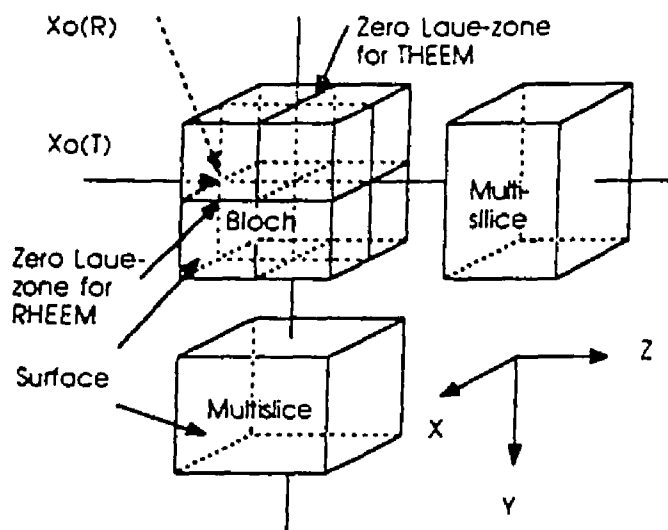
Fig.3.3. Schematic diagram of the program combining the Bloch wave and multislice approaches.
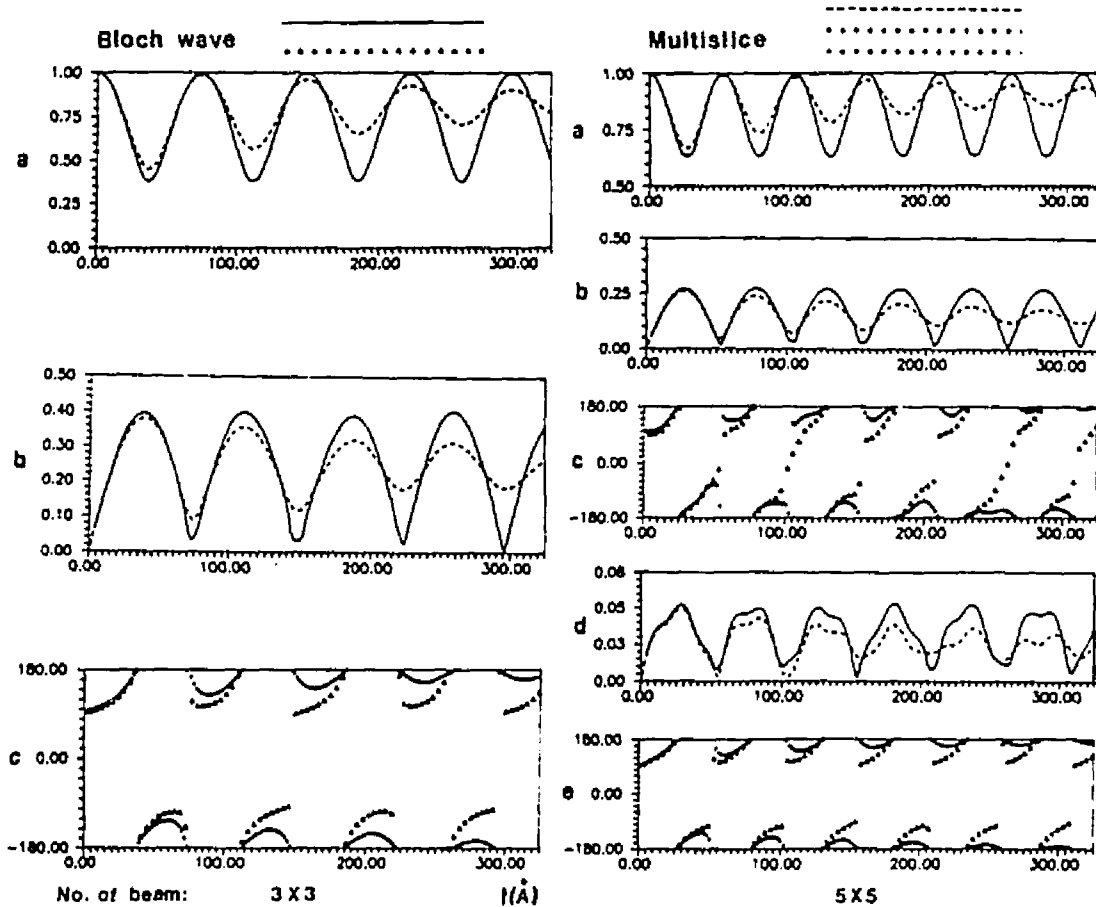
Fig.3.4(i)   **(ii)**

Fig.3.4(iii)

(iv)

Fig.3.4(v)

(vi)
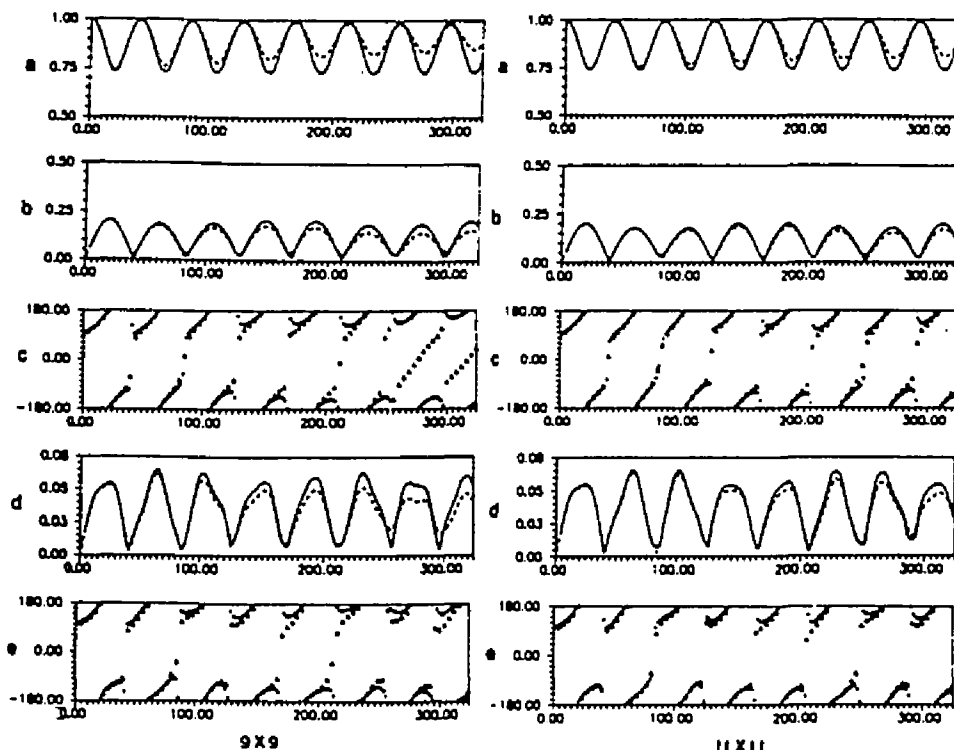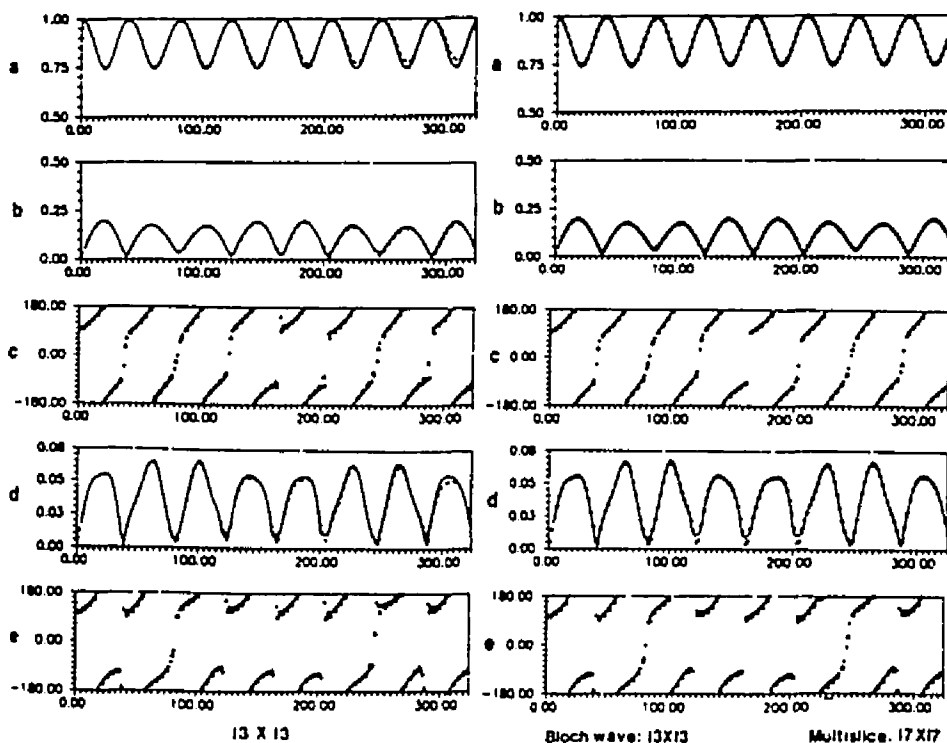
Bloch wave: I3XI3   Multislice: 2IX2I
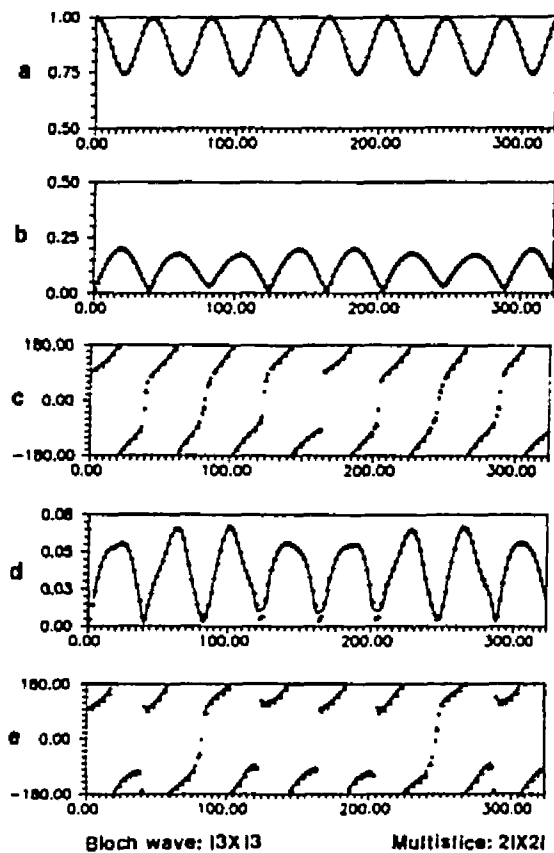
(vii)

Fig.3.4. Plots of the amplitude and phase of the (100), (200) and (440) beams versus thickness for gold along [001] in the transmission case using 100keV electrons: (i)-(vii) show the results for different number of beams and each diagram in (i)-(vii) contains two curves for the same condition calculated by the two methods separately. a), b) and d) are the plots of the amplitude of (100), (000) and (400) beams and c) and e) plots of the phase of (200) and (400).

in the Bloch wave-Only Mode

a b c d
e f g h
Beams: 11x11

a b c d
e f g h
Beams: 13x13
(i)

in the Multislice-Only Mode

a b c d
e f g h
Beams: 11x11

a b c d
e f g h
Beams: 13x13
(ii)

Fig.3.5.(i, ii)

114
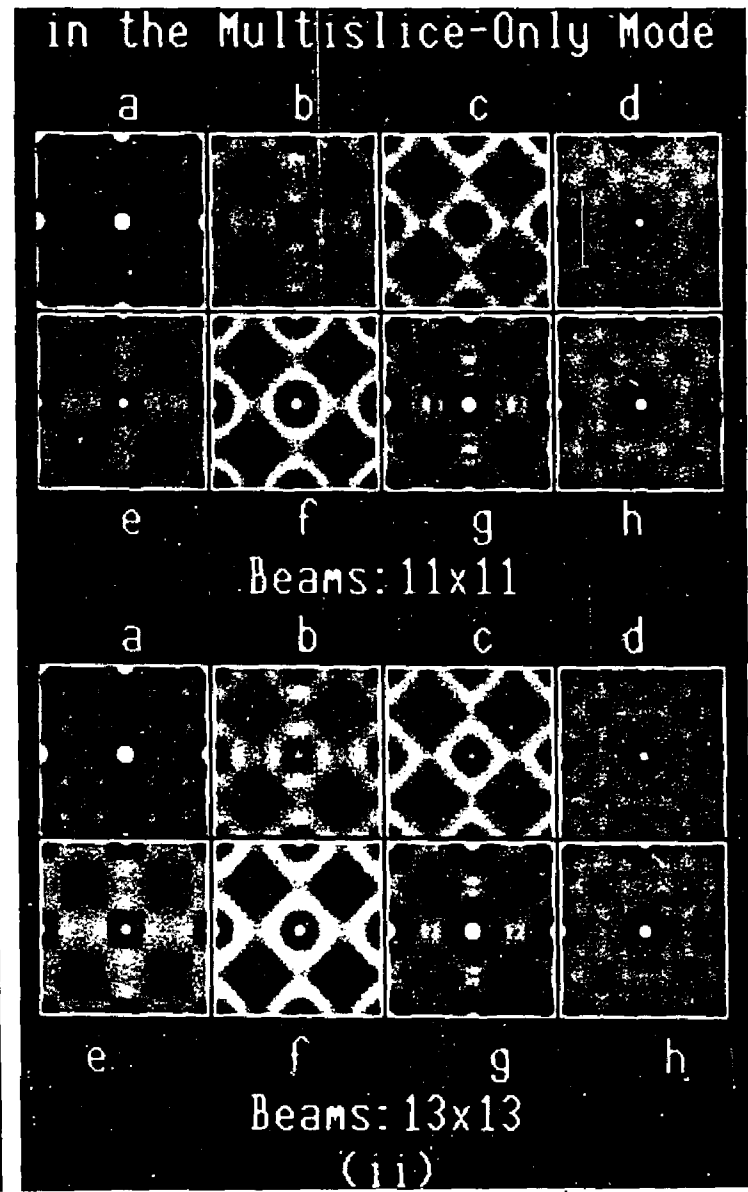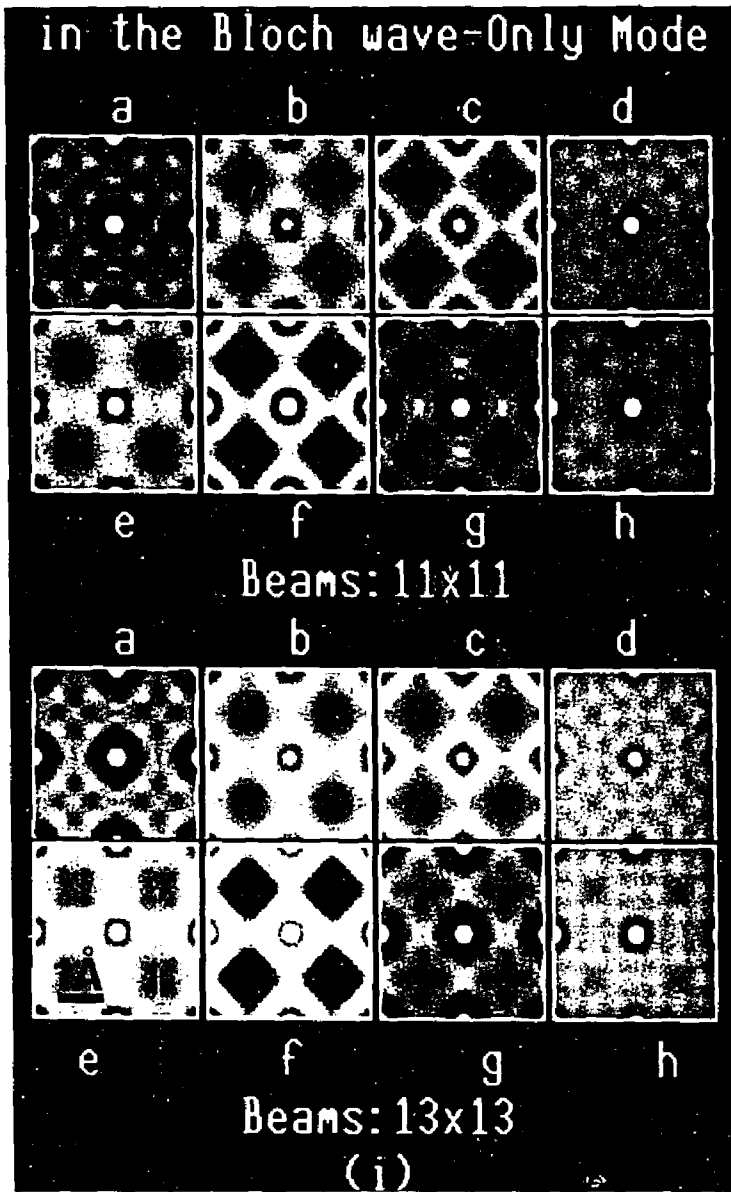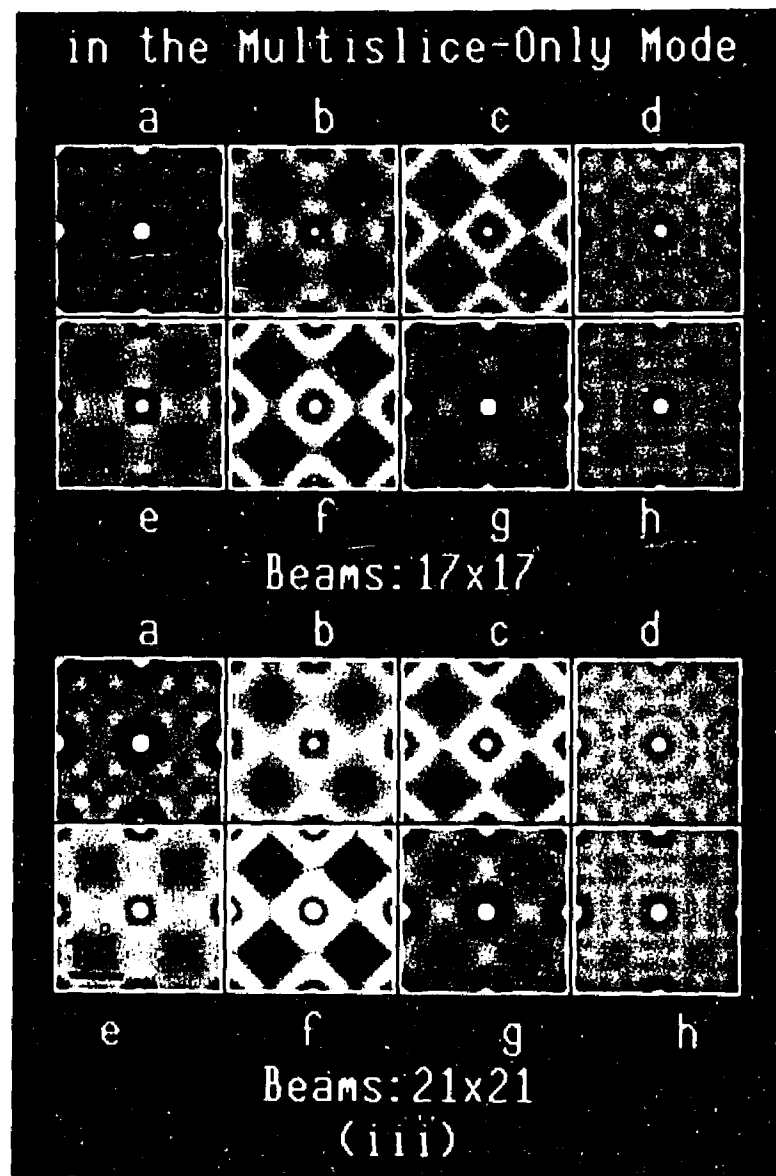
Fig.3.5(iii)

Fig.3.5. Current density outputs at various depths for the Bloch wave method (i) and multislice method (ii, iii) as a function of the number of beams in transmission case. The thicknesses from a) to b) are 20.2, 40.5, 121.5, 162.0, 202.5, 243.0, 303.7, 324.0Å.
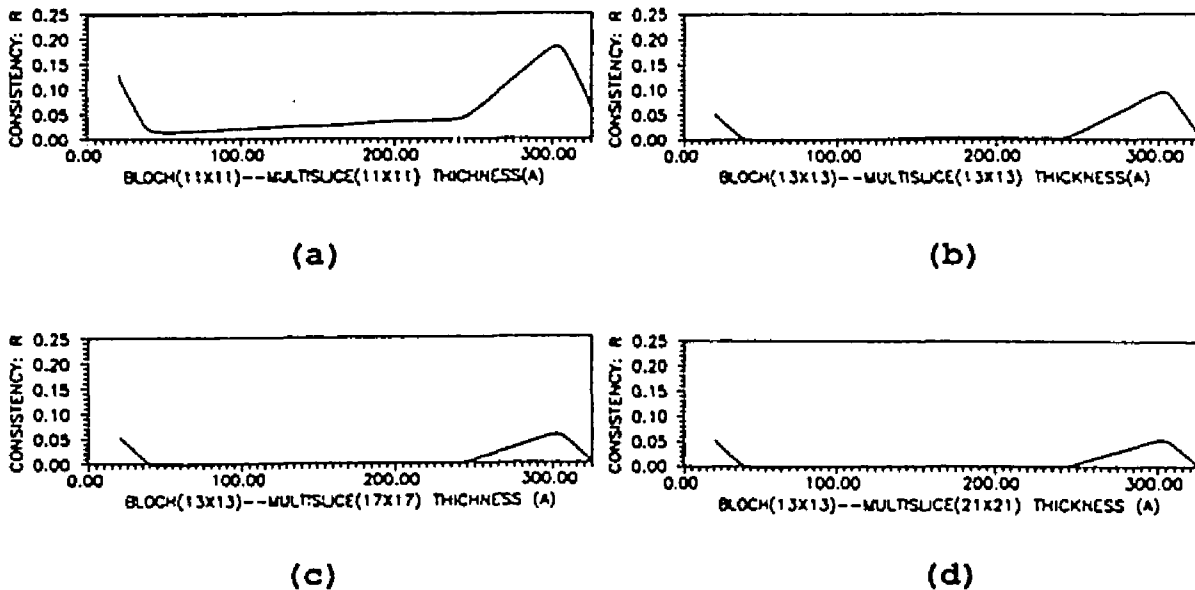
Fig.3.6. Plots of the consistence parameter R versus thickness for different numbers of beams in transmission.
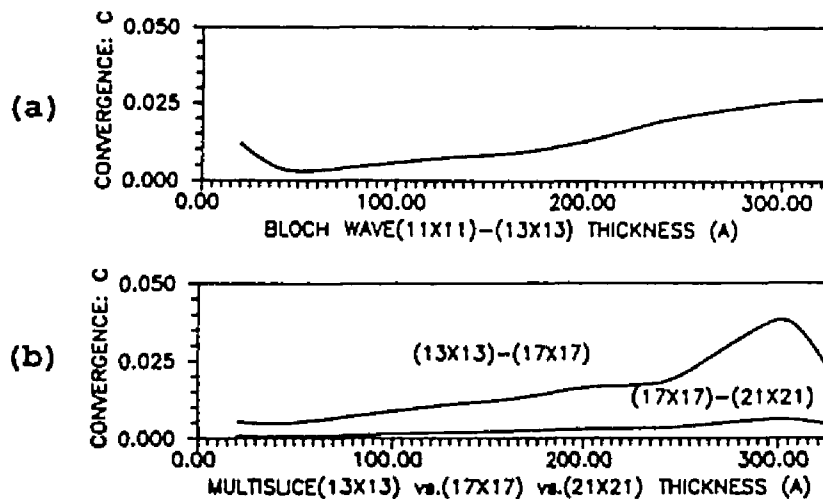
Fig.3.7. Plots of the convergence parameter C versus thickness for different numbers of beams in transmission; a) for the convergence of the Bloch wave method and b) for the convergence of the multislice method.

(a) Bloch wave   (b) Multislice
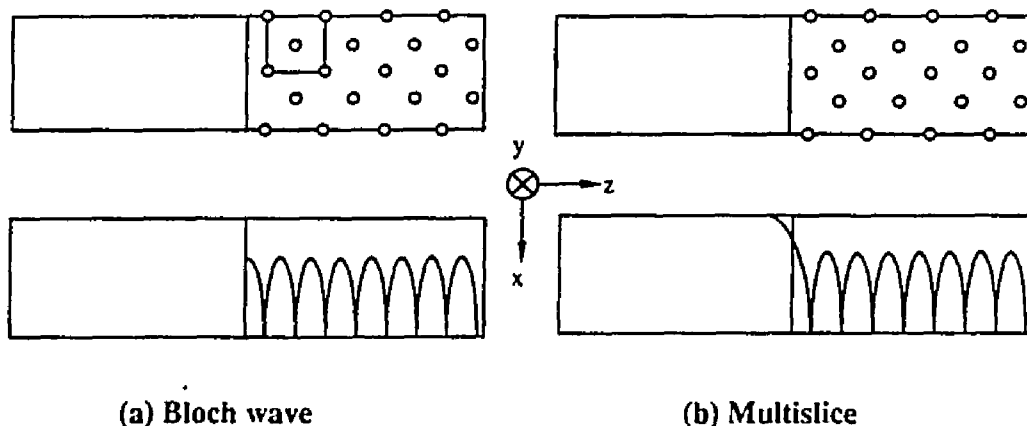
Fig.3.8. The unit cell set up and potential profile for both the Bloch wave block (a) and multislice block (b).

(ii)
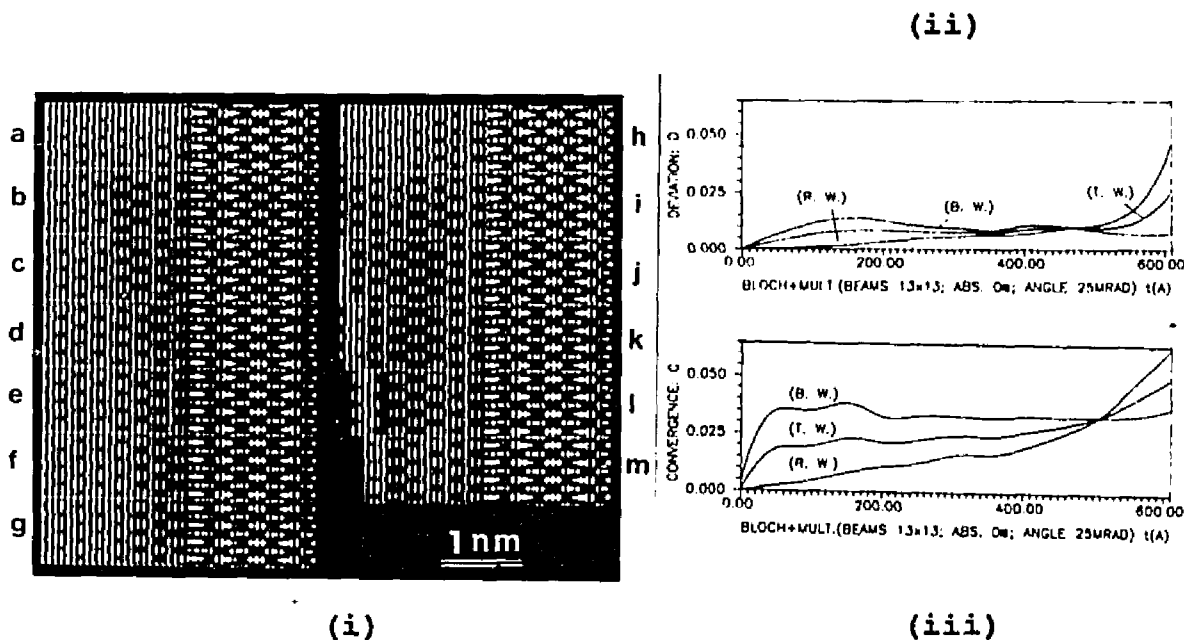
(i)   (iii)

Fig.3.9. (i) Current density outputs at different thicknesses for 25mRad incidence, for 13x13 beams and no absorption. (ii) Plots of the deviation parameters D versus thickness for current density outputs in (i). (iii) Plots of the convergence parameters C versus thickness for current density outputs in (i).
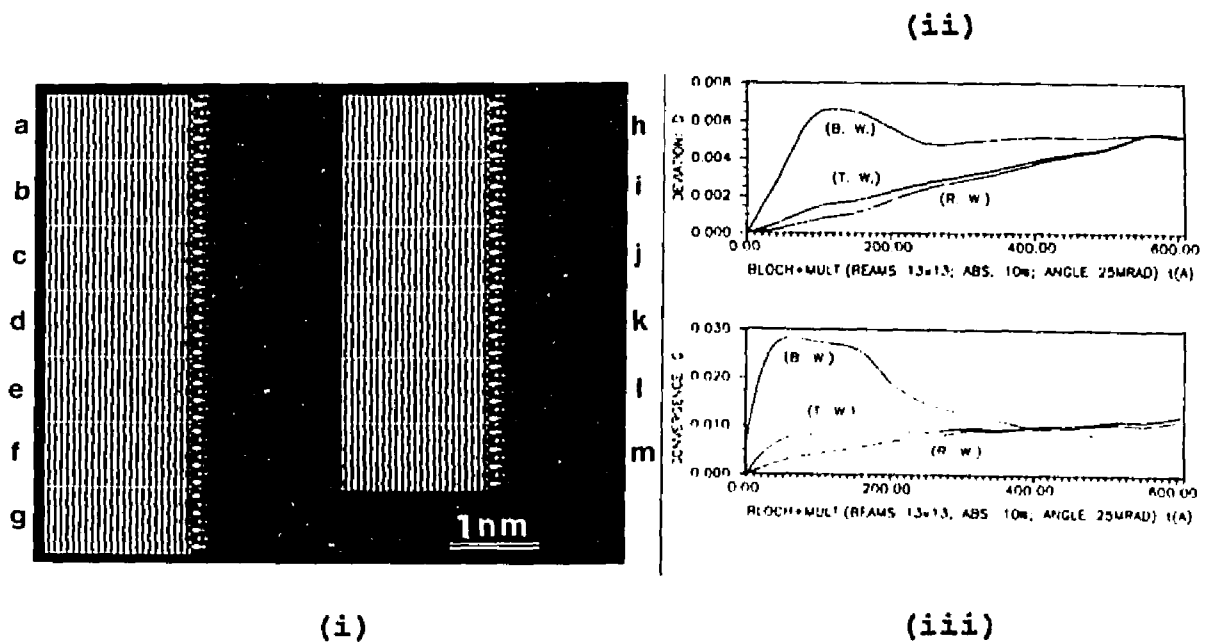
Fig.3.10. (i) Current density outputs at different thicknesses for 25mRad incidence, for 13x13 beams and the absorption of 10%. (ii) Plots of the deviation parameters D versus thickness for (i). (iii) Plots of the convergence parameters C versus thickness for (i).
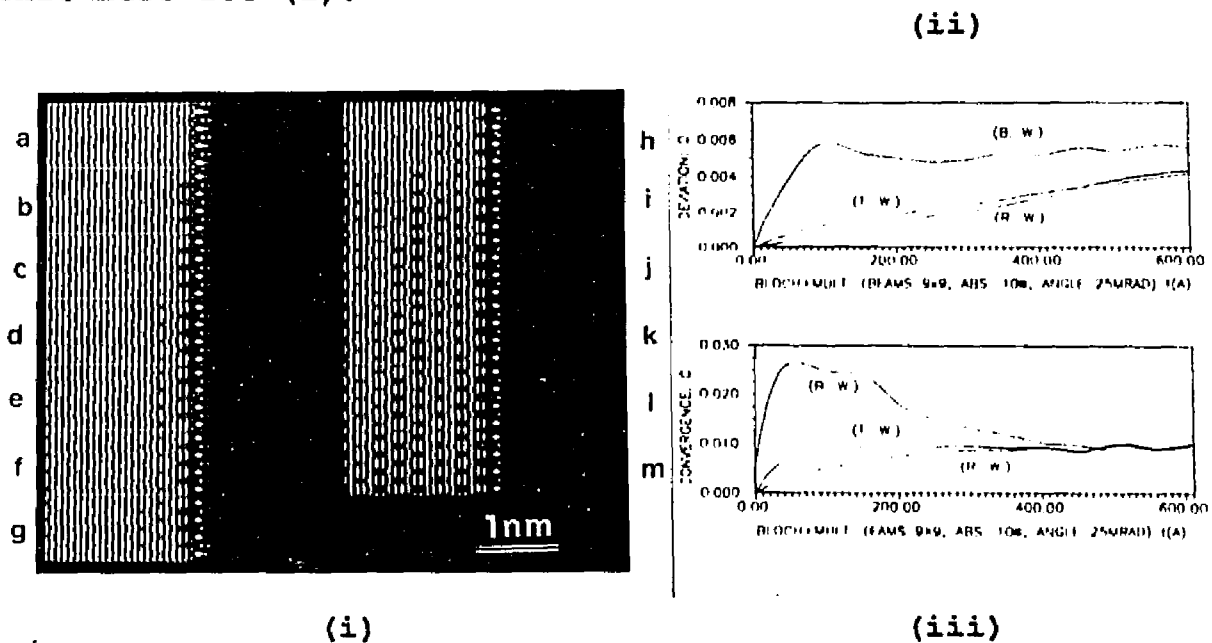
Fig.3.11. Corresponding results under the same conditions as for Fig.3.10, except that the number of beams in the Bloch wave calculation is 9x9.

(ii)

(i)

(iii)
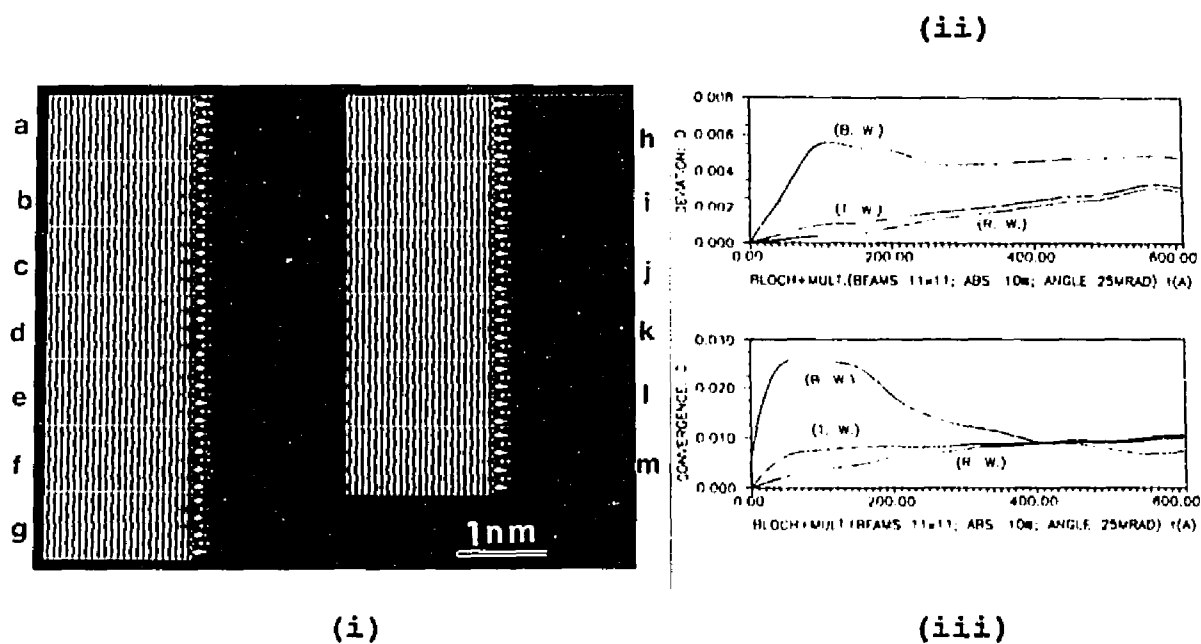
Fig.3.12. Corresponding results under the same conditions as for Fig.3.10, except that the number of beams in the Bloch wave calculation is 11x11.

(ii)

(i)

(iii)
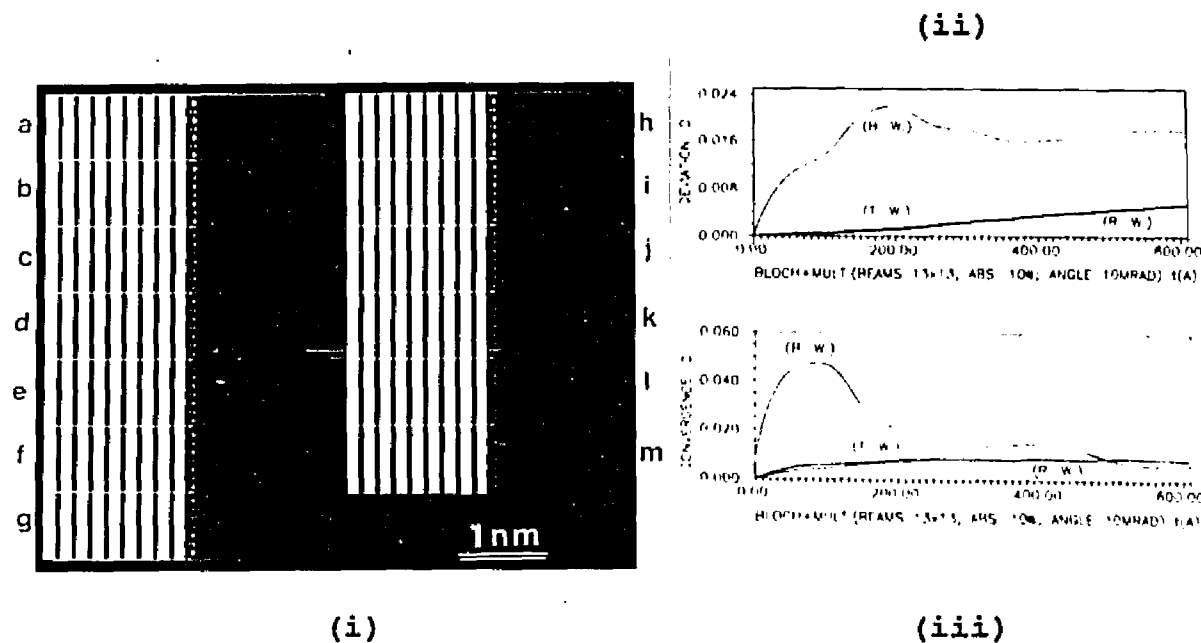
Fig.3.13. Corresponding results under the same conditions as for Fig.3.10, except that the incidence angle is 10mRad.

(ii)

(i)

(iii)
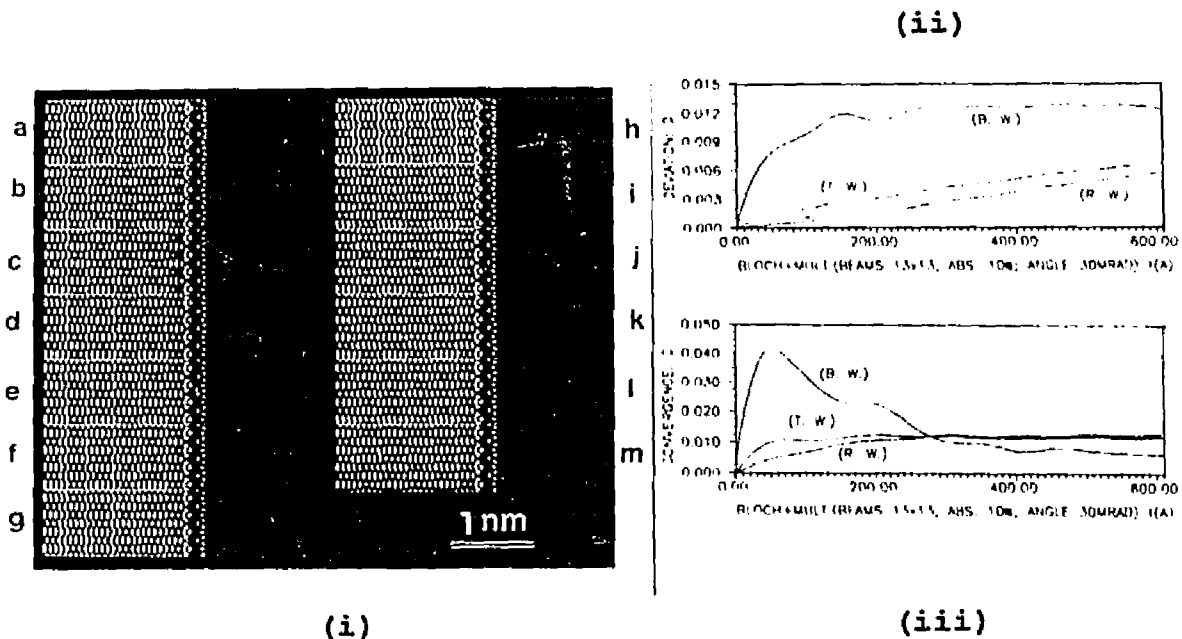
Fig.3.14. Corresponding results under the same conditions as for Fig.3.10, except that the incidence angle is 30mRad.

(ii)

(i)

(iii)
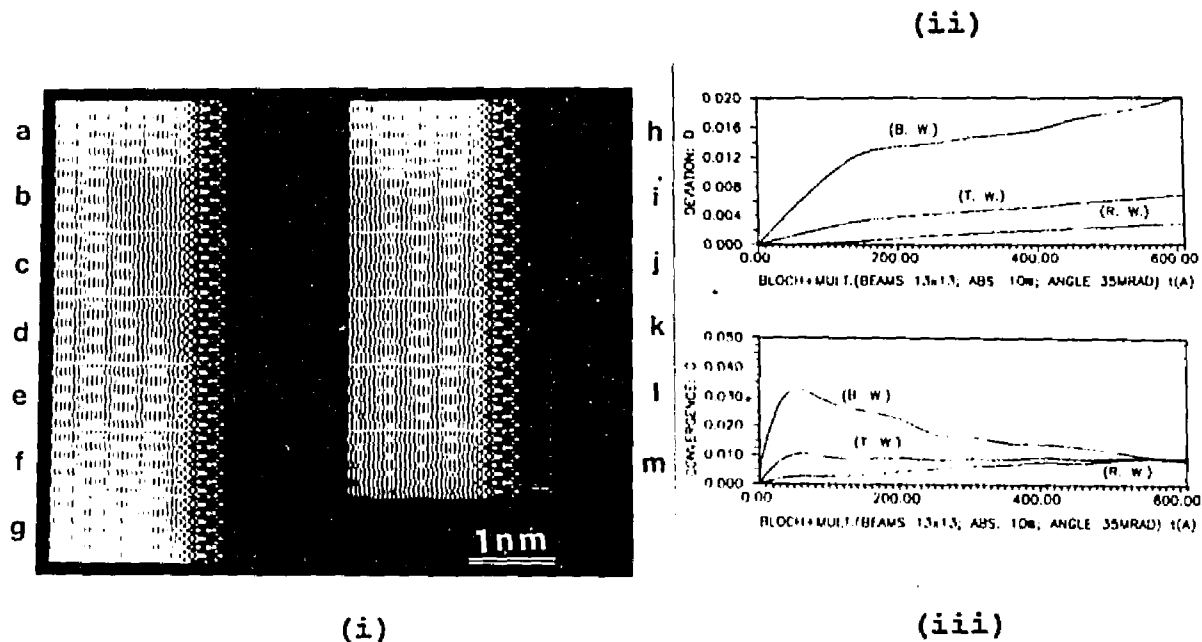
Fig.3.15. Corresponding results under the same conditions as for Fig.3.10, except that the incidence angle is 35mRad.
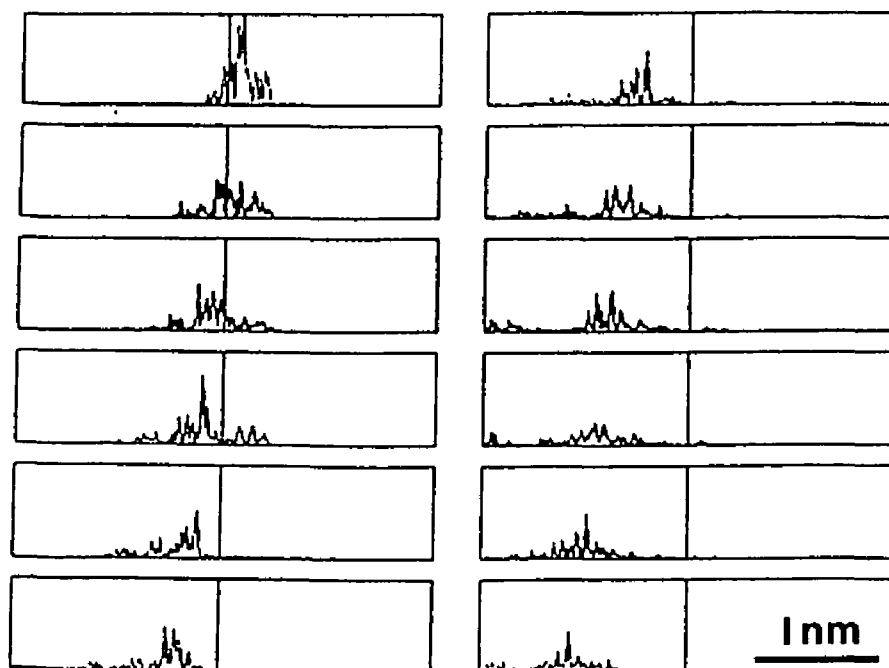
Fig.3.16. Plots of the projected intensity of $F_{n,n-1}(\underline{g})$ against the thickness. Each curve is calculated from the two nearest slices in Fig.3.10, and the incidence angle is 25mRad.
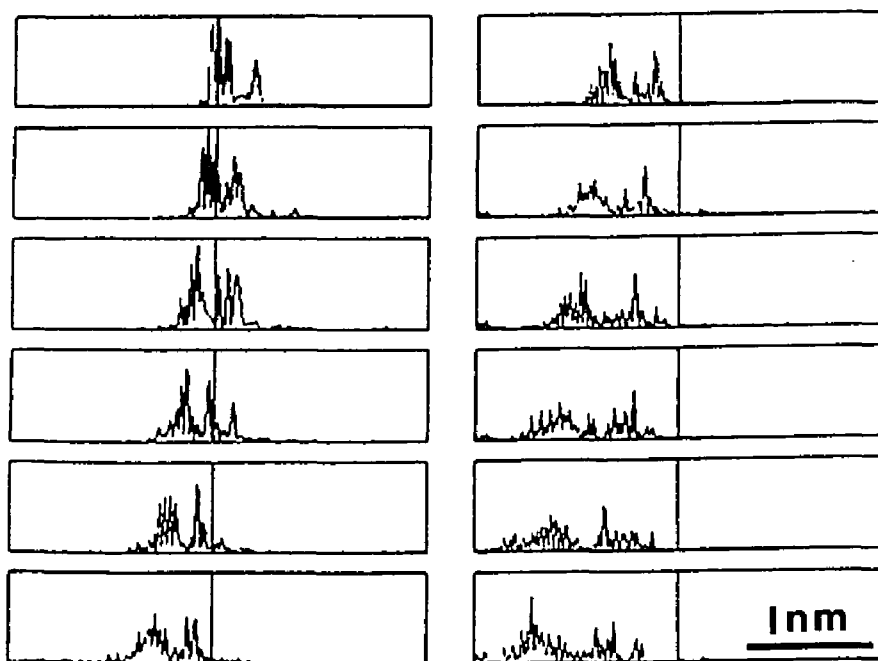
Fig.3.17. Plots of the projected intensity of $F_{n,n-1}(\underline{g})$ against the thickness. Each curve is calculated from the two nearest slices in Fig.3.10, and the incidence angle is 30mRad.
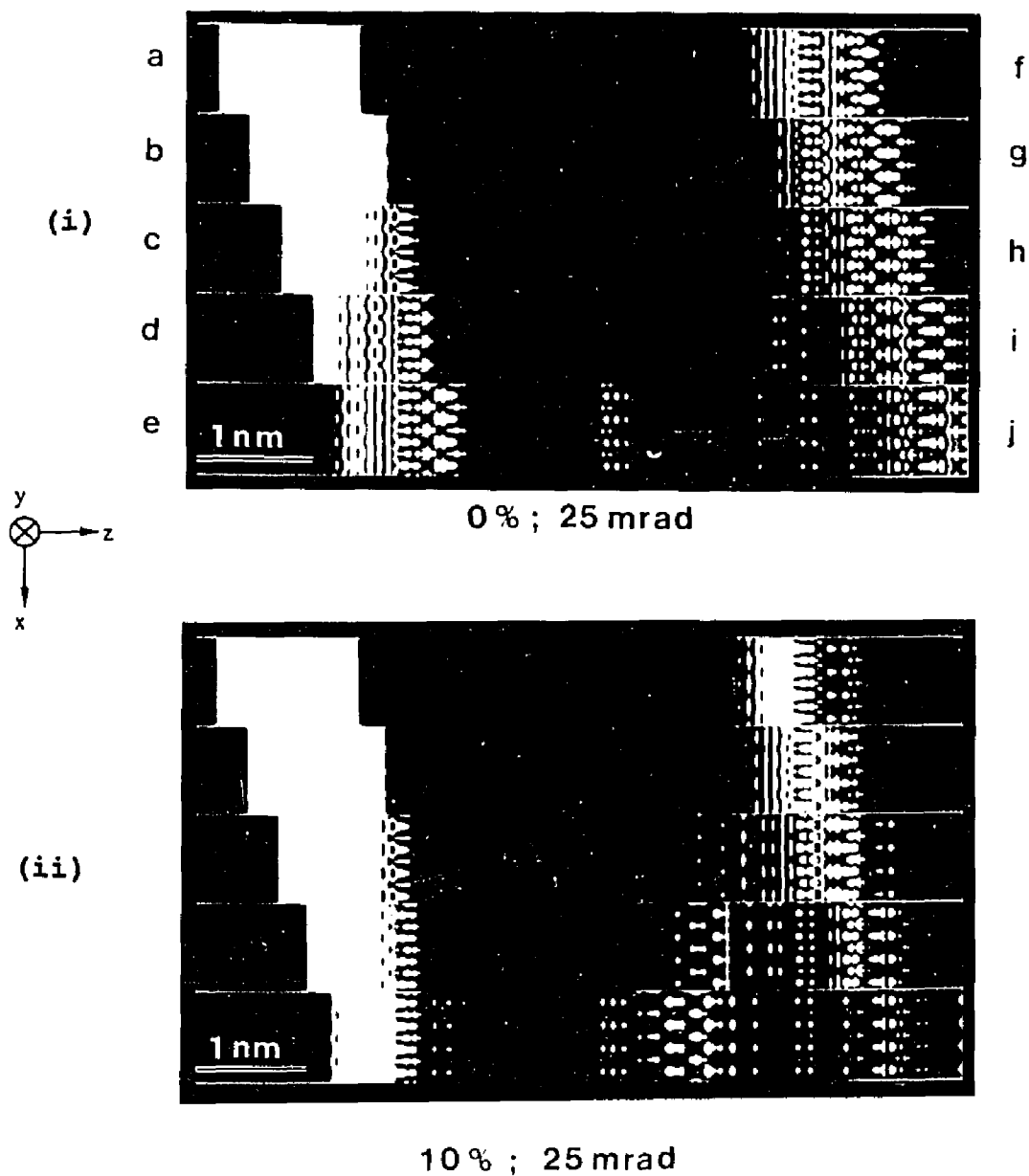
Fig.3.18. Current density outputs at different thicknesses for 25mRad incidence in the multislice-only mode, both with no absorption (i) and 10% absorption (ii). The thicknesses from a) to j) are: 1.0, 20.2, 40.5, 81.0, 162.0, 202.5, 243.0, 283.5, 324.0, 405.0Å.

Chapter IV. <u>Dynamical phenomena in reflection</u>

<u>using the Bloch wave method</u>

4.1. <u>Introduction</u>

The Bloch wave theory has been successfully applied to the interpretation of various dynamical phenomena in THEEM and THEED, such as stacking fault fringes, moire patterns, dislocations, extinction phenomena and the spot splitting of wedged crystals [1]. The only difference between THEEM or THEED and RHEEM or RHEED is the incidence angle. For the former, the incident electron beam is close to the surface normal, while it is nearly parallel to the surface for the later. However, this geometrical shift changes the nature of the boundary value problem significantly as discussed in the previous chapters: wave points occur in the "band gap" and the interaction between the surface potential and incident electrons can no longer be omitted.

However, the obstacles have been largely overcome both analytically and numerically in Chapters II and III. The analysis of the consistency between the Bloch wave method and multislice method for the Bragg case in Chapter III strongly reconfirmed the validity of the Bloch wave argument in the Bragg case in Chapter II. The important advantage of the Bloch

123

wave method is that it can provide physical insight into electron diffraction. In this chapter, several important dynamical phenomena are discussed for the case of electron reflection, namely: spot splitting, extinction distance and anomalous intensity enhancement.

4.2. Dynamical theory of spot splitting in RHEED

4.2.1. Historic review

The earliest reported dynamical phenomena were spot splitting and anomalous intensity enhancement in RHEED [2-3]. The anomalous intensity enhancement was later called surface resonance, for which so far there is no satisfied dynamical explanation. The spot splitting is often related to steps on a vicinal surface.

The important role of surface steps in fields such as chemisorption [4-5] and crystal growth by molecular beam epitaxy (MBE) [6] is well known. One of the earliest and also most common method of exploring surface steps is via their effects upon diffraction patterns in either LEED or RHEED. A particularly simple case is when the steps are regularly distributed and form a periodic structure i.e. a vicinal surface (see for instance Fig.4.1). The presence of an additional surface periodicity due to this step array leads

to extra diffraction spots, most readily observable as a splitting of the single spot from a perfect surface into a number of satellites, as well documented in both LEED [7-9] and RHEED experiments [10-11]. Pukite et al. [12-13] demonstrated that the spacing of these satellite spots could be well described by using simple kinematical theory, while Hsu and Cowley [14] demonstrated in RHEEM that the spot splitting was consistent with the presence of diffraction features. However, kinematical theory is totally unreliable as far as the intensities are concerned.

A more rigorous dynamical diffraction explanation of step spot splitting can be derived from Equation (2.45) by simple geometry and algebra. It will be shown that spot splitting is actually the reflection equivalent of what is after called refractive multiplets in transmission diffraction. In addition, calculated results for the intensities of the satellite spots for a number of simple surfaces are presented.

4.2.2. Physics of spot splitting

In order to understand the source of the spot splitting, it is important to draw analogies between transmission diffraction from a wedged shaped crystal and reflection diffraction from an array of steps. The basic point is that

a stepped surface can be considered as a bulk crystal cut at an angle to a "flat" low index plane, while a wedge crystal is a thin crystal slab with two inclined surfaces (see Fig.4.1).

According to dynamical theory, spot splitting is due to the exit surface projecting the crystal momentum of the electron in the crystal into a series of vacuum wave vectorsdifferent values, because of the inclination of the surface with respect to the zero Laue zone. The fundamental physics behind this kind of splitting is the law of momentum conservation on the boundary.

In the case of THEED, the projection of the crystal momentum $\underline{k}$ on both the entrance and exit surfaces overlap with each other to satisfy the requirement of the conservation of electron momentum, when the two surfaces are parallel to each other (Fig.4.2(a)). If the exit surface is tilted and $\underline{n}_1$ and $\underline{n}_2$ are not parallel with each other, the projection of the crystal momentum on the exit surface is no longer the same and splitting occurs (Fig.4.2(b)). Nevertheless, in the case of RHEED or LEED, the surface is considered both as the entrance and exit surface, for the crystal is physically taken as infinitely thick. Therefore the surface projection of the crystal momentum $\underline{k}$ will not split in RHEED, because the two

surfaces are coincident with each other instead of being angled for a wedged crystal. Nevertheless, there is an overlap of the projection on the exit surface of momentum $\underline{k}_o + \underline{q}$ for the reciprocal lattice vector on the same reciprocal rod perpendicular to the surface crystal, when the surface is normal to the zero Laue zone. This is shown algebraically in Equation (2.45) in which the z component of the reflection wave vectors is independent of g_z. This means that the beams from each zone can only form a semi-circle instead of a two dimensional pattern, regardless of whether one considers kinematical or dynamical diffraction events. Equation (2.45) can be rearranged as:

$$k_{gx'}^2 + k_{gy'}^2 = \chi^2 - (\chi_y - g_y)^2 \tag{4.1}$$

This is the equation for a circle in $k_{gx'}, k_{gy'}$ plane with radius $\sqrt{\chi^2 - (\chi_y - g_y)^2}$. This is consistent with the Ewald sphere construction in kinematic theory (Fig.2.4) and RHEED experiments [15-16]. However, the argument of kinematic theory does not explain the reflection intensity and spots splitting in RHEED and generally the reciprocal lattice in vacuum used by kinematic approach is physically wrong as discussed in Chapter II. The intersection between a reciprocal rod and a sphere can only give one point.

For a dynamical boundary match, the original overlapped projection of the momenta $\underline{k}_o+\underline{g}$ will split into different values (Fig.4.3), when the surface is slightly off the zone axis of the zero Laue zone. These momenta can excite plane waves in the vacuum with different momentum components normal to the surface. In other words, the originally overlapped spots split into a series of spots in the RHEED pattern. The position of these spots can be determined geometrically.

Both dynamical and kinematic theories show that the RHEED patterns should be a series of Laue circles. Each of them corresponds to one Laue zone. Nevertheless, the RHEED patterns obtained in various experiments are divided into two different kinds: one is consistent with what the theories predict and another is not, and has 2-D distributed spots. This fundamental problem so far has not been answered and might be a key to informative RHEED patterns. It merits further study.

In reflection, the reflected waves are taken into account to satisfy the boundary condition at the top surface which is both the entrance and exit surface, as illustrated in Fig.4.3. To match correctly the incoming wave above the crystal and the Bloch waves in the crystal, one has to draw a line normal to the crystal surfaces from the incoming wave to the dispersion surface, and then draw lines normal to the exit surface out

to Ewald spheres for the diffracted beams as illustrated in Fig.4.2. In the transmission cases, two sets of lines are drawn for the top and bottom surface respectively, leading to spot splitting as has been discussed by a number of authors [17-18]. The relationship between the spot splitting and the misorientation of the surface in reflection is more readily seen by reference to Fig.4.3. From such a diagram, the positions of the spots can be indexed by the relationship:

$$\phi_{\pm g}=\sin^{-1}[\cos(\theta_i+\beta^{eff})-(\pm g/k)\sin\beta^{eff}] \tag{4.2}$$

$$\alpha_{o\pm g}=\sin^{-1}[\cos(\theta_i+\beta^{eff})-(\pm g/k)\sin\beta^{eff}]-[\pi/2-\theta_i-\beta^{eff}] \tag{4.3}$$

where

$$\beta^{eff}=\tan^{-1}(\tan\beta\cos\Phi) \tag{4.4}$$

where $\phi_{\pm g}$ is the angle between the outgoing electron beam and the surface normal, $\alpha_{o\pm g}$ the angle between the specularly reflected beam and the satellite beams, β the misorientation angle, Φ the azimuthal angle and g denotes the particular Ewald sphere onto which the matching occurs. Here β^{eff} is the effective surface misorientation angle after taking the beam azimuth with respect to the Laue zone axis into account. This equation gives the same results as that derived by Pukite et al.[12-13] using kinematical theory. Here it is derived using dynamical theory. By using Equation (4.2), the polar plot

shown in Fig.2 of reference [13] can be reproduced for the angular separation between the (200), and (200), spots versus the incidence azimuth angle for a fixed incident angle of θ_i=65mRad. Although it seems obvious that the dynamical and kinematical theories should lead to the same spot position, in fact, this is not true for the transmission diffraction through a wedge crystal. In fact, in transmission the spot positions are actually different since they reflect the dispersion structure rather than simply the wedge angle as predicted by kinematical theory. It should be noted that in the dispersion surface analysis, the additional spots are not a consequence of the additional surface potential due to the steps as might be thought, but instead are due to the boundary conditions.

4.2.3. Numerical results

Numerical results were calculated using the Bloch wave diagonalization method described in detail in Chapter II [19-20]. The presence of a vicinal surface was included in the calculations by using a surface cut at an angle to the zone axis of the crystal. It should be noted that this ignores any effects due to the surface relaxations around steps and only includes single atomic steps.

To show the effect of an inclined surface, Fig.4.4(a) shows a simulated RHEED pattern from a perfect GaAs (001) surface for 100keV electrons with the beam azimuth along (010) and a glancing angle of 2.4° without any absorption. In the calculation, only the zero Laue zone is included, so that only a single semicircular pattern corresponding to the zero Laue zone occurs. Fig.4.4(b) shows a y-modulated presentation of the same data as that in Fig.4.4(a) which shows just single peaks. In this and all the other subsequent y-modulation graphs, the finite width of the diffracted beams is due to the numerical process rather than being a true effect, although a natural width is expected in experiments. Some very fine splitting of the peaks is due to the numerical interpolation. The scale is saturated so that the weaker peaks can be more readily seen. Because there is no misorientation of the top surface, there is no splitting. For comparison, Fig.4.5 shows the results for the same relative orientation but with a vicinal surface with the angle 2.5° off (010). Spot splitting occurs because of the surface misorientation, and the spots are also slightly streaked normal to the surface. The pattern changes from a semicircle to an intensity distribution in two dimensions. It should be noted that the intensities of some of the satellite spots are so low that they are not apparent

in the figures. The pattern also shows that each reciprocal rod has two strong spots i.e. doublets in diffraction patterns which is consistent with experimental results [10,12-13].

Equation (4.2) also indicates that the spacing between the spots increases as the incident angle is reduced. This is demonstrated in Fig.4.6 which shows y-modulated images for the same conditions as Fig.4.4 except that the incident angle in Fig.4.6(a) is 1.5°, and in Fig.4.6(b) 2.9°. The variation in the spot splitting is quite obvious.

The separation of the spots decreases with the surface misorientation angle until the misorientation angle disappears and the surface becomes a flat surface and then the separated spots overlap with each other [17]. The beam azimuth changes the effective misorientation angle i.e. the further off the zone axis, the smaller the effective misorientation angle as observed experimentally [10,12-13]. To demonstrate this point, Fig.4.7(a) and (b) show y-modulated images for the same diffraction conditions as Fig.4.6(a) and (b) respectively, but with an azimuthal angle of 1°. The spacing between the spots in Fig.4.7(a) and 4.7(b) is obviously smaller than that in Fig.4.6(a) and (b).

Calculated results for the Pt (111) surface on the [211] zone show the ratio of the specularly reflected beam to the

(333)s beam as a function of different azimuth for a fixed surface misorientation angle. The results for no absorption and 10% absorption are presented in Fig.4.8. The Pt (111) surface is believed to have very small or even no surface reconstruction and is therefore a good test case. There are two obvious features in Fig.4.8(a) : 1) the intensity ratio for no absorption is generally lower than that with 10% absorption, which means that absorption reduces both the total diffraction intensity and the relative satellite spot intensities; 2) the intensity ratio is lowest at the zero azimuthal angle both with and without absorption. The variation of the intensity ratio about the zero azimuthal angle is possibly related to surface resonance, although this merits further exploration. Fig.4.9 shows a graph of the same ratio as a function of the incident beam angle for the zero azimuthal angle with a fixed misorientation angle and no absorption. The curve shows that the intensity ratio increases sharply when the incidence angle is close to zero, which means that the satellite spots can barely be observed at small angles.

4.2.4. Interim summary

The results obtained are encouraging in terms of

understanding spot splitting effects and there is good agreement between calculated results and experimental observations [10,12-13,15-16]. However, one should acknowledge that some surface phenomena are not included in the above calculations. First, only regularly distributed surface steps were discussed, and there will quite often be irregularly distributed steps on any given surface. The effect of irregularly distributed steps on the diffraction pattern is hard to analyze theoretically, but to first order should be equivalent to an incoherent sum of different stepped surfaces, summed over the probability of finding in any given micro-region a given step separation. This will lead to streaks in the diffraction patterns normal to the surface. Secondly, any effects due to surface relaxations or strain fields around steps have not been included. In principle, there can be a relaxation of the surface stress around a step which can lead to atomic displacements, which we can consider as a strain field. The presence of such a strain field will alter the diffraction to a small but significant extent. In addition, there will also be an effect due to the differences between the potential cut off at the surface which is used here and a potential which is allowed to slowly decay into the vacuum. However, it should be noted that some preliminary calculations

[21] indicate that this has only a minor effect on the diffraction pattern intensities. This is understandable since high energy electron diffraction is only really sensitive to the core potential, not the weak interatomic potential or surface potential. Finally, the images of steps as obtained in RHEEM images have not been considered. In principle, these can be calculated from the current Bloch wave approach, but the long range strain field around a surface step may contribute substantially to the image contrast, which is difficult to take into account in the Bloch wave approach. In general, the theoretical development gives a clear dynamical method of understanding spot splitting and related phenomena in RHEED, although its application to real experimental surfaces remains to be tested.

4.3. Extinction distance in reflection

Although the extinction distance is well understood and explained in transmission, it has not been done yet in reflection. The extinction distance is defined as the periodicity of the intensity oscillation of one particular beam in a crystal in THEEM [21]. These intensity oscillations are due to the interference of two or more Bloch waves with different k_z. In the crystal, each diffracted beam (g) is

composed of a series of the Bloch waves which are characterized by wave vectors $k_{oz}^{(j)}+g_z$ (j=1,2......N) in the direction of wave propagation (z axis). The superposition of these waves will result in the intensity oscillations in the z direction. This can be readily seen in Fig.3.4(i-vii). The amplitude-thickness curves of different diffracted beams in Fig.3.4 shows that the extinction distance for gold at 100keV is about 50Å. This is because the difference between the central beam and the diffracted beams is only a constant phase; $2\pi g_z z$. In the Bloch wave calculations for both transmission and reflection cases, the difference between eigenvalues $k_{oz}^{(j)}$ is usually not larger than several reciprocal angstrom. They are small for transmission compared to reflection. Therefore, it is expected that the periodicities of the beam intensity oscillations in reflection are much smaller than that in transmission.

Since the intensity of the central beam usually is much stronger than that of diffracted beams, the total charge density oscillation in the direction of electron wave should be consistent with the oscillation of central beam. This makes the observations of extinction phenomena in real space possible.

For the case of multiple waves, it is difficult to derive

an analytical formulation for the periodicity. It is possible to make a two-beam approximation to estimate the periodicity, when the amplitude of one or two waves greatly surpasses that of other waves, for both transmission and reflection cases.

Equation (2.13) can be rearranged as:

$$\psi(\underline{r}) = \sum_q \phi_q = \sum_q \exp[i2\pi(\underline{k}_{ry} + \underline{g}_{ry}) \cdot \underline{r}_{ry}] \times$$

$$\sum_j \varepsilon^{(j)} C_q^{(j)} \exp[-2\pi k_{iz}^{(j)} z] \exp[i2\pi(k_{rz}^{(j)} + g_z) z] \qquad (4.4)$$

Then,

$$|\phi_q|^2 = |\sum_j \gamma_q^{(j)} \exp[i2\pi k_{rz}^{(j)} z]|^2 \qquad (4.5)$$

where

$$\gamma_q^{(j)} = \varepsilon^{(j)} C_q^{(j)} \exp[-2\pi k_{iz}^{(j)} \cdot z] \qquad (4.6)$$

(4.5) can be expressed more explicitly as the following [22]:

$$|\phi_o|^2 = \exp(-t/\xi_o')(1 - \sin^2\beta \sin^2\chi) \qquad (4.7)$$

$$|\phi_q|^2 = \exp(-t/\xi_q') \sin^2\beta \sin^2\chi \qquad (4.8)$$

where $\chi = [t\cosec(\beta/2\xi_q)] + i[t\sin(\beta/\xi_q')]$, $\cotan\beta = w = \xi_q s_q$,

$\xi_q = U_q/K\cos\theta_q$, $\xi_o' = U_o'/K\cos\theta_o$ and $\xi_q' = U_q'/K\cos\theta_q$.

It should be pointed out that all arguments and derivations for the two-beam approximation in transmission case [21-22] are valid for reflection and the only difference is due to the geometrical interpretation of various parameters. From Equation (4.8), it can be seen that the intensities of both the transmitted and diffracted beams

oscillate with a periodicity given by $t=2\pi\xi_g$, if the exact

Bragg condition is satisfied ($\beta=\pi/2$, w=0). If the high energy

approximation or small angle approximation is employed (i.e.

$\theta_o=\theta_g=\theta_n$) with an incidence angle of $\theta_i=10\text{mRad}$, the estimated

oscillation periodicity for GaAs (010) zone is:

$$2\pi\xi_g=K\cos\theta_g/U_g$$

$$=15\text{Å} \tag{4.9}$$

This has been demonstrated in numerical results

calculated for the multiple-beam case, which are shown in

Fig.4.9. Fig.4.9 shows nine pictures of simulated Bloch wave

current density images in the crystal with different incident

angles from GaAs (001) surface. The incident energy as before

is 100keV, and θ_i is the incident angle. The picture is in the

plane perpendicular to the y axis i.e. the [010] zone axis.

The size of each picture is nine unit cells by nine unit cell

i.e. 50.57 by 50.57 in angstroms. Pictures (a)-(c) are the

results without absorption. For absorption, the potential with

the usual phenomenological treatment of absorption is adopted.

Pictures (d)-(f) show the results with the imaginary part

equal 1% of the real part of the potential and pictures (g)-

(i) show the results with the imaginary part equal to 10% of

the real part of the potential. Pictures (d)-(i) clearly show

the intensity decaying in the bulk along the z direction resulting from absorption, while the same intensity oscillation periodicity occurs in the case of 1%. In the case of 10%, the intensity decay is so quick that the oscillation has no room to emerge. This indicates that the Bloch waves in GaAs for low incident angle have significant intensity in the rang of 10-15Å for 10% case. The intensity oscillation periodicities for the three incidence angles shown in Fig.4.9 are about 8~25Å. For θ_i=10mRad, it is about 13Å. This is quite close to the analytical analysis of the two-beam approximation. Fig.4.10 shows the y-modulated density images for θ_i=8mRad for different absorption.

4.4. Surface resonance in electron reflection

4.4.1. Historic review

Surface resonance is a big topic in electron reflection and a vast amount of literature can be found on it. Initially, surface resonance referred to a pure experimental observation of intensity enhancement of reflected beams in RHEED. Later on, it was also observed in LEED and various theoretical explanations were proposed. However, up to now there is no conclusive and convincing theory available to explain the nature of the phenomenon. The corresponding phenomenon in X-

ray reflection has never been reported. Is it only limited to electron reflection? If this is true, why? What is the real physical background behind this commonly observed phenomenon? All these questions merit further exploration. What are done here is to review the history of studies on this phenomenon and contribute a little more to the literature based upon a Bloch wave analysis.

An intensity enhancement in RHEED was first observed and reported as "second kind of intensity anomaly" by Kikuchi et al. in 1933 [10]. The "first kind of intensity anomaly" was the spot splitting which was discussed in Section 4.2. The "second kind of intensity anomaly" was confirmed in RHEED experiments by Miyake et al. in 1954 [23]. The nature of the phenomenon was that the intensity of the specular reflection is enhanced when the spot crosses a Kikuchi line having an oblique angle to the crystal surface. It was Miyake et al. who first tried to give a comprehensive dynamical explanation on the phenomenon based on the Bloch wave method. Miyake et al. made several important points on this issue, although the theoretical background of them were not clear (even now I still don't think they have been clarified).

i) The condition that the incident spot lies on one of the Kikuchi lines is the same as the condition for the Bragg

reflection of the incident beam by the corresponding lattice plane. Therefore enhancement of the specular reflection can occur if the incident electrons suffer a Bragg reflection on a certain lattice plane when the boundary surface is a mirror plane of the crystal lattice.

ii) The enhancement is especially noticeable when the wave of the Bragg reflection in a side direction is expected to travel nearly parallel to the crystal surface. (This is the first mention of the possibility of a surface wave.)

iii) Though the enhancement of the specular reflection first came to attention by its coincidence with the Kikuchi lines, the role of the Kikuchi lines seems to indicate a geometrical relation between the incident electron beam and the crystal, and no more. (If the inelastic scattering is included, which may also be responsible for the phenomenon, this comment may not be true).

iv) The total reflection of the interior wave at the surface plays an important role in producing enhancement.

v) The proper choice of the wave points in reciprocal space is essential for solving the Bloch wave problem in the Bragg case.

All these points later were extended conceptually by various authors, although the real physical and analytical

foundation of most of them has not been established.

The corresponding phenomenon in LEED was studied in a more systematic and rigorous way by McRae et al. in the 1960's and 1970's [24-30]. The concept of "surface resonance" or "surface-state resonance" was first introduced to denote the intensity anomaly in low energy electron reflection diffraction. The LEED experiment was first done on the NaF and LiF (001) surface in a UHV chamber [25]. The authors measured the intensity curves vs. incidence energy at a fixed incidence angle, instead of the rocking curve, by changing the incidence glancing angle. The curves show the resonance peaks moving towards the lower energy side when the incidence angle increases. This indicates that resonance in LEED is correlated to the momentum normal to the surface, which is similar to the intensity anomaly observed in RHEED and explained by Miyake et al.. In RHEED, the Kikuchi lines indicate the geometrical condition for the resonance phenomena. At the same time, the authors observed a phenomena called resonance minima, one which has not been reported in RHEED, in which the intensity of the (00) beam always has a minimum associated with the emergence of a new beam [24]. It is interesting to point out that these phenomena were first predicted by the theory of LEED developed by the same authors [24]. Miyake and Hayakawa

[11] in 1970 first attempted to relate the intensity anomaly in RHEED with the resonance effect in LEED, which was mainly based on experimental observation in both low and high energy ranges. The authors concluded that these two effects are of essentially the same nature. Since then, the term "surface resonance" is widely accepted in the field of RHEED.

More recently, studies of the resonance effects in RHEED were carried out on Pt (111) surface by Marten et al.[31]. Combining the dynamical theory of RHEED developed by Maksym and Beeby [32] with the concept of surface bound state developed by McRae [30], the author raised a new term called monolayer resonance. He attributed the electron reflection enhancement anomaly to the scattering from and simultaneously channelling "inside" the topmost atom layer parallel to crystal surface before they are diffracted back into the specular beam.

Though these years, various terms referring to the reflections intensity enhancement have become popular in the fields of LEED and RHEED [33-34], such as "surface state resonance", "surface bound state resonance", "monolayer resonance", "surface resonance". It seems that different people use them with different characters and understanding and these terms appear more often to denote an experimental

fact rather than an unified, well established and convincing explanation of a physical process.

4.4.2. The origin of the concept of "surface resonance"

The concept of surface resonance in reflection originated from resonance scattering [35]. Scattering theory in quantum mechanics indicates that when the phase shift of a partial wave in the scattered wave field is close to zero, the partial wave usually dominates the scattering and is said to be in "resonance" with the scattering potential. This happens when the energy of a particle with an angular momentum quantum number l approaches an energy level with the same angular momentum quantum number in the potential well. The physical significance of this is that an incident particle which has nearly the right energy to be bound by the potential tends to concentrate there and produce a large distortion in the wave function and hence a large amount of scattering. The above concept is easily extended to the field of electron-solid interaction, although an analytical solution of the extension has not yet been completed.

Another conceptional source for surface resonance is the resonance theory of nuclear reactions [36]. A simple introduction to the theory is given as the following. The wave

function of a system of N+1 particles consisting of one incidence particle plus N target particles can be described as:

$$\psi(\underline{r}_o, \underline{r}_1, \ldots \ldots \underline{r}_N) = \sum_i \psi_i(\underline{r}_1, \underline{r}_2 \ldots \ldots \underline{r}_N) u_i(\underline{r}_o) \qquad (4.10)$$

where ψ_i is the wave function describing the state i of the target particles and $\underline{r}_o$ denotes the coordinate of the incident particle. If E is the energy of the whole system, we have the static Schrodinger equation for the system as:

$$H\psi = E\psi \qquad (4.11)$$

where

$$H = H_N(\underline{r}_1, \underline{r}_2 \ldots \ldots \underline{r}_N) + T_o + V(\underline{r}_o, \underline{r}_1, \ldots \ldots \underline{r}_N) \qquad (4.12)$$

H_N is the Hamiltonian for the N particles of the target, T_o is the kinetic energy operator for variable $\underline{r}_o$, and V is the potential energy of the incidence particle in the field of the target. The wave function ψ_i satisfies:

$$H_N\psi_i = \varepsilon_i\psi_i \qquad (4.13)$$

i.e. the eigenstates of the target. Substituting (4.10) into (4.11) and employing the orthogonal properties of the set ψ_i, we obtain:

$$(T_o + V_{ii} + \varepsilon_i - E) u_i = -\sum_{i \neq j} V_{ij} u_j \qquad (4.14)$$

and

$$V_{ij}(\underline{r}_o) = (\psi_i, V\psi_j) \qquad (4.15)$$

If only coupling between the scattering channel of ground state and the scattering channel of excitation channel is considered, (4.14) can be simplified to the matrix form:

$$(T_o + V_{oo} - E) u_o = -V_o \Phi \tag{4.16a}$$

$$(H-E) \Phi = -V_o^+ u_o \tag{4.16b}$$

where

$$\Phi = \begin{vmatrix} u_1 \\ u_2 \\ \cdot \\ \cdot \\ u_N \end{vmatrix} \tag{4.17}$$

and the matrix operator H is defined by:

$$H_{ij} = T_o \delta_{ij} + V_{ij} + \varepsilon_i \delta_{ij} \quad (i, j \neq 0) \tag{4.18}$$

and

$$V_o = (V_{o1}, V_{o2} \ldots \ldots V_{oN}) \tag{4.19}$$

where

$$V_o^+ = \begin{vmatrix} V_{o1}^* \\ V_{o2}^* \\ \cdot \\ \cdot \\ V_{oN}^* \end{vmatrix} \tag{4.20}$$

To obtain an equation for u_o, we need to eliminate Φ. Solving (4.16b), we obtain Φ in terms of u_o:

$$\Phi = V_o^+ u_o (E^+ - H)^{-1} \qquad (4.21)$$

Here, E^+ is defined as:

$$E^+ = E + i\eta \quad (\eta \rightarrow 0^+). \qquad (4.22)$$

Then,

$$[T_o + V_{oo} + V_o (E^+ - H)^{-1} V_o^+ - E] u_o = 0 \qquad (4.23)$$

Now we have the effective potential:

$$\underline{V} = V_{oo} + V_o (E^+ - H)^{-1} V_o^+ \qquad (4.24)$$

and u_o becomes one of eigenstates of Hamiltonian $\underline{H} = T_o + \underline{V}$:

$$\underline{H} u_o = E u_o \qquad (4.25)$$

In general, the spectrum of H will consist of a discrete part and a continuum. Let the eigenfunctions for the states in the discrete part be Φ_n with eigenvalue ξ_n:

$$H\Phi_n = \xi_n \Phi_n \qquad (4.26)$$

The eigenfunctions for the continuum states are $\Phi(\xi', \alpha)$ where the eigenvalue is ξ' and α labels the various states having a common variable ξ':

$$H\Phi(\xi', \alpha) = \xi' \Phi(\xi', \alpha) \qquad (4.27)$$

It is the discrete state which is responsible for the resonance. For the weak coupling limit, we have:

$$V_{ij} = 0$$

Then H becomes diagonal so that ξ_n are of the form:

$$\xi_n = \begin{vmatrix} 0 \\ \cdot \\ u_i^n \\ 0 \\ \cdot \end{vmatrix}$$

where u_i^n satisfies a simple Schrodinger equation:

$$(T_o + V_{ii}) u_i^n = -(\varepsilon_i - \xi_n) u_i^n \tag{4.28}$$

It should be pointed out that u_i^n is different from u_i completely. It is a bound state of the incidence particle when it moves into the field of a target at excited state if $i \neq 0$. Then $\underline{V}$ can be expressed in terms of Φ_n and $\Phi(\xi', \alpha)$ as the following:

$$\underline{V} = \sum_n \frac{V_o |\Phi_n\rangle\langle\Phi_n| V_o^+}{E - \xi_n} + \int d\alpha \int_0^\infty d\xi' \frac{V_o |\Phi(\xi', \alpha)\rangle\langle\Phi(\xi', \alpha)| V_o^+}{E^+ - \xi'} \tag{4.29}$$

The resonance for the particle-target interaction occurs when E is close to one of ξ_n. In other words, the resonance will occur at the energies for which a particle in the absence of coupling with the incident channel could be in a stationary bound state in the field of target particles in an excited state. For the experiment, E is usually adjustable by changing the kinetic energy of incidence particle T_o. Under this condition, the effective potential is dominated by the nth

term in it:

$$\underline{V} = \underline{U}_n + \frac{V_o | \Phi_n \rangle \langle \Phi_n | V_o^+}{E - \xi_n} \qquad (4.30)$$

Physically, the bigger the effective potential $\underline{V}$ in $\underline{H}$, the stronger the scattering in the entrance channel. u_o $(u(\underline{r}_o))$ represents the amplitude of scattering in entrance channel.

The resonance theory for nuclear reaction presented here seems ready to explain similar phenomena in other particle system such as electron-solid interaction. However, the analogy can not be made so easily. In the case of high energy reflection, the kinetic energy of the incident electron is much higher than crystal potential. In other words, the scattered incident electron in the crystal can not stay in the electronic bound states of the crystal. This is quite different from the nuclear reaction in which nuclear potential field is very strong. This means that bound electronic states are not involved in elastic diffraction processes. In addition, the experimental results show that the condition of electron surface resonance is only related to the normal component of the momentum of incident electrons instead of their whole kinetic energy. These two facts apparently can not be directly included in the above theory.

4.4.3. The first McRae theory of surface resonance in LEED

The key points of the McRae's theory [24-25] are:

i) Introduction of the concept of effective wave field to solve the Schrodinger equation in integral form. The author defined the total wave field $\psi(\underline{R})$ as the sum of the primary field and the field emitted by all of the atoms, while the effective field $\psi^*(\underline{R})$ incident on a given atom is the sum of the primary field and the field emitted by all of the atoms other than the given atom. This is an analogy to the Onsager model of dipole-dielectric medium interaction in dielectric theory [37].

$$\psi(\underline{R})=\exp[i2\pi\underline{K}.\underline{R}]-\sum_{\bullet}.\int \exp[i2\pi K|\underline{R}-\underline{R}'|](4|\underline{R}-\underline{R}'|)^{-1}x$$

$$T(\underline{R}',\underline{R}_{\bullet})\psi^*(\underline{R}')d\underline{R}' \qquad (4.31)$$

ii) Expanding the effective wave field into the form:

$$\psi^*(\underline{r},z)=\phi^*(\underline{r},z)\exp[i2\pi\underline{k}.\underline{r}] \qquad (4.32)$$

where, $\underline{r}$ is parallel to the surface and $\underline{k}$ is the surface projection of the wave vector of the primary wave $\underline{K}$.

iii) After introducing the effective atomic-scattering factor $\langle f\rangle$, an important expression for total wave is:

$$\psi(\underline{R})=\exp[i2\pi\underline{K}.\underline{R}]+(i2\pi/A)\sum_{\bullet}Re[F(\underline{K}_{\bullet}^-\underline{K})/K_{\bullet}]\exp[i2\pi\underline{K}_{\bullet}.\underline{R}] \qquad (4.33)$$

where F is effective atomic scattering factor.

$$K_v = (K^2 - |\underline{k}+\underline{v}|^2)^{1/2} \qquad (4.34)$$

K_v^- is a propagation vector whose surface and surface-normal projections are respectively $\underline{k}+\underline{v}$ and $-K_v$. An important character of K_v^- is that it satisfies the following relations:

$$|\underline{K}_v|^2 = \underline{K}^2 \qquad (4.35)$$

$$\underline{K}_{v,s}^- = \underline{k}+\underline{v} \qquad (4.36)$$

They are valid for the wave far away from the crystal and under this condition they are nothing but the law of energy conservation and the law of momentum conservation on the boundary. For the wave in the crystal, (4.34) is no longer valid, because the crystal potential must be taken into account. The amplitude of the reflection coefficient for the beam designated by the reciprocal vector parallel to the surface is:

$$C_v = (i/K_v) F(\underline{K}_v^-, \underline{K}) \qquad (4.37)$$

iv) For a fixed incidence angle, $|C_v|^2$ can be plotted as a function incidence energy i.e. a function of K_v. The reflectivity peaks on the plot corresponds to the resonance phenomena. For a simple ideal model of a 2-D crystal consisting of isotropic atomic scatters with one atom in each unit cell, the amplitude reflection coefficients are:

$$C_o \propto 1/AK_o|K_v|$$

$$C_v = (i/AK_v)\phi f \qquad\qquad (4.38)$$

and the reduced effective field is:

$$\phi = \begin{cases} A|K_v|/2\pi f & K<|k+v| \\ \\ -A|K_v|/2\pi f & K>|k+v| \end{cases} \qquad (4.39)$$

When $|K| \rightarrow |k+v|$ i.e. $K_v \rightarrow 0$, $\phi \rightarrow 0$, and C_o, $C_v \rightarrow \infty$. As K pass through any threshold value $|k+v|$, which is equivalent to the condition for the spot in RHEED crossing a Kikuchi Line, the reduced effective field goes to zero and suffers a phase change of $(1/2)\pi$, and reflectivity of both specular beam and Bragg diffracted beam (C_o and C_v) are enhanced greatly. According to the above analytical analysis, the physical meaning of surface resonance in LEED can be interpreted as that, at the resonance condition, a electron wave can propagate in the layer in phase with the atoms, which means that the contribution to reduced effective field of an atom due to all the other atoms in layer, is in phase. Then the balance between the field emitted by each atom and the effective field incident on it can only be maintained if the effective field is zero, otherwise it will result in infinite wave field. This in-phase mechanism simultaneously enhances the reflected wave greatly.

There is one point on which the above theory contradicts the conventional Bloch wave approach. According to the Bloch wave analysis, the surface normal component of wave vectors in the crystal do not obey the relation $K_z = (K^2 - |\underline{k} + \underline{v}|^2)^{1/2}$, because the kinetic energy of electron in a crystal is not conserved. This is due to the fact that the theory considers the crystal as one consisting of a series of 2-D atomic planes without thickness. This may work for LEED. But it is apparently questionable for high energy case, because the diffraction is basically three dimensional in RHEED and the normal component of incidence wave vector is modulated by the crystal potential, which varies along the inward normal direction. The interpretation of zero effective wave field at the resonance condition is not very clear from a physical point of view. Another disadvantage of the theory is that the math conceals physics—the mathematics appears too complicated to explore the physics behind them.

4.4.4. The second McRae theory of surface resonance in LEED

In 1970's, McRae started a new approach to interpreting electron surface resonance in LEED, which is directly analogous to the resonance theory of nuclear reaction discussed in Section 4.4.2. The main point of the theory is

the following: electrons incident on a crystal surface can be temporarily trapped in surface states at an energy level above the vacuum level. These states are temporary stationary surface states which are observed as narrow fluctuations of elastic scattering intensity with respect to variation of electron energy and incidence direction.

With a 2-D free electron approximation, the behavior of incident electron in the plane parallel to the surface is considered as nearly free electron and that in the direction normal to the surface is governed by the laterally averaged potential:

$$U_o(z) = A^{-1} \cdot \int U(\underline{r}, z) \, d\underline{r} \qquad (4.40)$$

where A denotes unit area on the surface. Then the bound surface states for $U_o(z)$ are given:

$$|n_{\underline{q}}\rangle = \psi_n(z) \exp[i2\pi(\underline{k}_s + \underline{q}) \cdot \underline{r}] \quad n = 1, 2 \ldots \qquad (4.41)$$

where $\psi_n(z)$ is the nth surface-state solution of the Schrodinger equation for the potential in (4.40). The forbidden gaps derived from $U_o(z)$ have the effect of confining electrons in the surface region of the crystal. The plane factor of (4.41) represents free-electron motion parallel to the surface, where $\underline{q}$ denotes a vector of the reciprocal net

of the surface and $\underline{k}$ denotes the momentum in the plane parallel to the crystal surface. The electron energies corresponding to the bound surface states in (4.41) are:

$$E_{n\underline{q}}(\underline{k}_n) = e_n + E_{-\underline{q}}(\underline{k}_s) \tag{4.42}$$

where e_n denotes the energy eigenvalue corresponding to ψ_n in (4.41) and:

$$E_{-\underline{q}}(\underline{k}_s) = (1/2)|\underline{k}_s + \underline{q}|^2 \tag{4.43}$$

The beam threshold function $E_{-\underline{q}}(\underline{k})$ for different $\underline{q}$ values defines a surface band structure for a 2-D crystal, for $U_o(z) \to \text{const.}$. For $U_o(z) \neq \text{const.}$, the surface band structure for a given level n is displaced to lower energy level by a fixed amount equal to the binding energy e_n. The typical values of the binding energy e_n of an level with n=1 is 0.5-3eV. This number indicates that the 2-D free electron approximation may not be valid in RHEED, because the energy component normal to the surface for the Bragg beams in RHEED is usually ~eV. The trapping of incident electrons caused by the surface states with energy level e_n doesn't seem to happen to most Bragg beams in high energy case since a large part of the reflected electrons can not stay on those states. However, this argument is still valid for the wave nearly parallel to the surface, the "surface wave" or "the Bragg reflection in a side

direction" by Miyake et al. [2].

In general, resonance scattering denotes the capture of an incident particle by a temporary and virtual energy state of the target or a compound state formed by target and the incident particle. A given compound state can generally decay by several channels which are characterized individually by the final quantum states of the target and the scattered particles. Resonance scattering is considered to occur with appreciable probability only in a narrow range of incidence energy and momentum characteristic of the compound state which is expressed by (4.41). The coherent superposition of the resonance and direct contribution to the scattering amplitude results in a fluctuation of scattering, whose probability varies relatively slowly with respect to the incidence condition, and whose intensity is centered at values of incidence energy and momentum for which the magnitude of the resonance contribution is at a maximum. But the theory dose not explain how the coherency can be attained.

By analogy to (4.30), when ξ_n in (4.30) is taken as the surface state energy expressed by (4.42), we have:

$$\underline{V} = U_n + \frac{V_o |\Phi_n\rangle\langle\Phi_n| V_o^+}{E - E_{-q} - e_n} \qquad (4.44)$$

When the incident energy E is close to $E_{-g}+e_n$, the effective potential $\underline{V}$ and $\underline{H}$ increases. The larger the effective potential of $\underline{H}$, the stronger the scattering in the entrance channel.

These are the basic ideas of the second theory of the electron surface resonance by McRae. Although the theory apparently has made quite successful analogy between the resonance phenomena in nuclear reaction and electron surface resonance by introducing 2-D free electron description and to some extent indicated its correlation with the Bloch wave approach [11,23,31], it is still a qualitative theoretical speculation rather than a systematic and quantitative theory of electron surface resonance.

With the 2-D free electron approximation, the bound surface states described by (4.41) are characterized by the 1-D potential described by (4.40) and only associate with the transverse energy of incidence electrons. The bound states are generally the states with zero current flow or zero group velocity and pure imaginary $\underline{k}$ vector for the dispersion relation (E-$\underline{k}$ relation) [36]. This means that these states are not different from the evanescent Bloch states in the Bloch wave method. They are just different ways of interpreting on the same phenomenon. However, in Section 4.4.5, it will be

shown that the analyses of both evanescent and non-evanescent Bloch states together with the internal and external electron reflectivity still does not complete the story of surface resonance.

4.4.5. Surface resonance in RHEED by a Bloch wave analysis

Using the Bloch wave method to analyze surface resonance was first attempted by Miyake et al. [23] and Kohra et al. [38]. However, the numerical calculation was carried out only for four-beam case and the analytical formalism for the determination of wave points was not given. Later on, Britze et al. [39] used the Bloch wave method for the general n-beam case developed by Colella [40] and Moon [41] to calculate the rocking curve of the specular beam for a Si(001) surface for 10keV electron. The authors applied the WKB method to the surface potential treatment and both measured and calculated the resonance peaks. The agreement between the experiment and theory was claimed to be reached to certain extent. Nevertheless, the limitation of the method as discussed in Chapter II was not overcome.

The Bloch wave method in the Bragg case developed in Chapter II and verified through the investigation of the consistency between the Bloch wave approach and multislice

iterations in Chapter III is applied here for the analysis of the surface resonance.

Equation (2.45) shows that when the surface normal $\underline{n}$ is tangential to the dispersion sphere S_1 (Fig.2.1) and k_{qz}' becomes zero, the corresponding wave branch will propagate along the surface without decaying, which was called "the Bragg wave in a side direction" and later "surface wave " by Miyake et al.[11,23]. When $k_{qz}'=0$, we have:

$$\underline{k}_q = \chi_s + \underline{g}_q \tag{4.45}$$

and corresponding energy of the Bragg beam:

$$E_q = h^2 \underline{k}_q^2 / 2m_e \tag{4.46}$$

$\underline{k}_q$ and E_q are nothing but emergence threshold momentum and energy for the particular Bragg beam $\underline{q}$.

It was claimed by Miyake et al. that the occurrence of the surface wave in RHEED is always accompanied with the anomalous enhancement, which later on was concluded to be the same as the surface resonance phenomena in LEED by Miyake et al.. Nevertheless, so far, these conclusions are still not very much beyond theoretical speculations, rather than the results of a systematic theory and convincing and quantitative experimental observation.

First, the correlation between the existence of "surface wave" i.e. the Bragg beam with threshold momentum and energy

and coincidence between the Kikuchi line and specular beam can be proved analytically using the boundary conditions expressed in (4.45) and (4.46). When the component normal to the surface of the wave vector of an outgoing Bragg reflection beam $\underline{k}_2'$ equals zero ($k_{2x}'=0$), which means either the Bragg reflection beam propagates along the surface or the beam has the emergence threshold momentum and energy, we obtain:

$$\chi_z^2 = g_z^2 - 2g_x\chi_x \tag{4.47}$$

where only the zero Laue zone is considered i.e. $g_y=0$ in the coordination set-up shown in Fig.2.1.

The Bragg incidence condition simply means that the projection of the incident wave vector on the Laue zone plane is a reciprocal lattice vector. Then, we have:

$$\chi_z = g_z^{P}; \quad \chi_x = g_x^{P} \tag{4.48}$$

substituting (4.48) into (4.47):

$$g_z^{P2} = g_z^2 - 2g_x g_x^{P} \tag{4.49}$$

where superscript p denotes an arbitrary reciprocal lattice vector. Equation (4.49) is the condition which the incident beam must satisfy for $k_{2x}'=0$, where $\underline{g}$ denotes one of excited reciprocal lattice rod in the zero Laue zone. The RHEED pattern shown in Fig.7 (Miyake and Hayakawa) [11] gives a good experimental example. If the pattern is transformed to the coordination used in Fig.2.1, the x axis is along the [01$\underline{1}$]

direction and the surface normal [011] is along the z axis. Then we obtain:

$$g_x{}^P=0; \quad g_x{}^P=g_{0\underline{6}6} \tag{4.50}$$

Therefore, when $g_x=g_{0\underline{6}6}$ or $g_x=g_{06\underline{6}}$, $k_{gx}'=0$. In other words, the two spots $g_{0\underline{6}6}$ and $g_{06\underline{6}}$ are excited as surface waves, although they do not occur on the diffraction pattern because of defects and absorption of the surface. The picture shows that the intensity enhancement of the specular spot occurs when it overlaps with the lattice point $(g_x, g_x) = (0, g_{0\underline{6}6})$.

Secondly, it can be shown that the condition $k_{gx}'=0$ is also consistent with the condition for the resonance effects in LEED given by McRae [24-25]. The vectors in (4.34) can be converted into the form currently used as the following:

$$\underline{K}=\chi \tag{4.51}$$

$$\underline{k}=\chi_x\underline{x}_o-\chi_y\underline{y}_o \tag{4.52}$$

$$\underline{v}=g_x\underline{x}_o+g_y\underline{y}_o \tag{4.53}$$

Substituting (4.51-4.53) into Equation (4.34), we obtain:

$$\chi_z{}^2=g_x{}^2-2g_x\chi_x-g_y{}^2+2g_y\chi_y \tag{4.54}$$

If only the zero Laue zone is considered ($g_y=0$), (4.54) is reduced to (4.47).

Mathematically, when the condition $k_{gx}'=0$ is satisfied for the particular Bragg incident angle, the rows in matrix A in Equation (2.55) corresponding to particular lattice parameters

$\underline{q}$ will become infinite. This means that the mathematical treatment shown in Equations (2.51)-(2.54) does not work. However, the equations still have solution if the two sides of Equation (2.53), (2.54) are not divided by $\chi_n - g_n + s_g$ (k_{gz}'). Nevertheless, this special mathematical condition may give an interpretation of the intensity enhancement, at least partially.

From a Bloch-wave viewpoint, there are in fact two different effects which occur near the resonance condition $k_{gz}'=0$ and lead to changes in the net reflectivity. It should be mentioned that reflectivity is a powerful concept since there is conservation of the net current flow. These two effects correspond to total internal reflection of Bloch waves or total external reflection of diffracted waves. It should be noted that for electrons, a solid is polyrefringent since the current flow $\underline{S}$ for each Bloch wave leads to a different refractive index, and we have n diffracted waves, so we can expect a large number of internal/external reflection conditions. Analysis based solely upon total internal reflection due to the mean inner potential is not adequate since reflection is determined by the behavior of $\underline{S}$, not the wave vector. The two effects will be discussed with reference to Fig.4.11-4.15 which show respectively the rocking curve for

the reflected wave, the total reflectivity, the wave vector
of some of the reflected waves, the real and imaginary and the
current flows of the two major Bloch waves, all for GaAs near
the [010] zone.

The rocking curves from GaAs (001) surface at 100keV
incident energy with and without absorption are shown in
Fig.4.11. The absorption treatment is the same as that given
previously. The shape of the two curves with absorption is
slightly lower than that without absorption. Totally 49 beams
are included. θ_i is the incident angle between the electron
beam and surface and I the intensity of specular spot. The
azimuth of incident beam is along the direction of [010]. The
intensity is presented in a relative scale, in which the
intensity is taken as unity for GaAs near to a [110] zone.

The first effect is the total reflection of a particular
diffracted wave which changes from an escaping plane wave to
a trapped evanescent wave on the outside of the surface. This
occurs when the condition $k_{gz}'=0$ is satisfied for the
particular Bragg incident angle, which can be seen by
comparing Fig.4.11, 4.12, 4.13. There are peaks in both the
intensity of specularly reflected beam and the total
reflectivity at the condition where a reflected beam is
transiting from evanescent to escaping, i.e. has a zero

imaginary component, although there are not the strongest features in Fig. 4.11 and 4.12.

The second effect is that when some of the Bloch waves within the crystal change from propagating into the crystal to being evanescent in character, total internal reflection of Bloch waves occurs. This occurs in the region where the normal to the Ewald sphere is in the "band gap" between the Bloch-wave dispersion surfaces. Since an evanescent wave has $S_z=0$ (for the case without absorption, conservation of current indicates that this should lead to a maximum in the reflectivity). This can be seen by comparing Fig.4.14 and 4.15 with the total reflectivity in Fig.4.12, for instance, the zero in the current flow in Fig.4.14(a) at about 18.5mRad and the corresponding peak in Fig.4.12.

Although the above arguments provide some rationalization for the various peaks in the net reflectivity, they do not give a complete explanation. This indicates that the idea that total internal and external reflection is responsible for the intensity maxima--surface resonance is not sufficient. It is apparent from the curves showing the excitations of the different Bloch waves as a function of angle that there are very large variations in these which are due to the boundary conditions rather than simply to changes in $\underline{S}$ arising from

variations in the real and imaginary components of the wave vectors. For instance, the maximum in the total reflectivity at about 23.5mRad correlates well with the zero excitation of the Bloch wave shown in Fig.14(b). From this, it can be concluded that although resonance effects based upon total internal and external reflection are important, they do not explain all the intensity variation and many of these must be due to some combination of the boundary conditions and the changing character of the Bloch waves.

4.4.6. Interim summary

One can see that tremendous and enduring efforts have already been made to understand the phenomena of surface resonance "intensity enhancement anomaly" in electron reflection--in both high and low energy cases. The major steps can be listed as the following according to a time series:

i) Kikuchi, S. and Nakagawa, S. (1933) [10]

The first observation of "intensity enhancement anomaly" in RHEED

ii) Miyake, S. and Kohra, K. and Takagi, K. (1954) [23]

The first Bloch wave analysis of the phenomena of "intensity enhancement anomaly" and "surface wave" in RHEED.

iii) Kohra, K., Moliere, K., Nakano, S. and Ariyama, M. (1962)

[38]

The first numerical Bloch wave analysis of the phenomena for a four-beam case.

iv) McRae, E. G. (1966, 1967) [24-25]

The first McRae's theory on the surface resonance phenomena in LEED.

v) Miyake, S. and Hayakawa, K. (1970) [11]

Unified the understanding of "intensity enhancement anomaly" in RHEED with the explanation on "surface resonance" in LEED. Since then, "electron surface resonance" has become a widely accepted term referring intensity variation anomaly in both low and high energy electron reflections.

vi) McRae, E. G. (1976, 1978) [27-28]

The second McRae's theory on surface resonance phenomena in LEED.

vii) Britze, K. and Meyer-Ehmsen, G. (1978) [39]

Calculating the rocking curves in RHEED by using the Bloch wave method for the general n-beam case developed by Colella and Moon [41-42] and introducing the WKB method for the surface potential.

viii) Marten, H. and Meyer-Ehmsen, G. (1985) [31]

Raised the concept of "monolayer surface resonance" by using a multislice approach (slices set to be parallel to the

surface) developed by Maksym, P. A. and Beeby, J. L. [32].

ix) Peng, L. M. and Cowley, J. M. (1988) [42]

Studied the "electron surface resonance" by using a multislice approach (slices set to be perpendicular to the surface) developed by Cowley, L. M. and Moodie, A. F. [43]. x) Ma, Y. and Marks, L. D. (1989) [20]

Using the newly developed Bloch wave method and the concepts of current flow and internal and external reflection to explain the physics of "electron surface resonance".

However, all these efforts have not finished the story of "surface resonance". On the contrary, they seem to make more stories from the story. It is apparent that a systematic, convincing and self-consistent theory on "electron surface resonance" valid for both low and high energy electron reflection has not yet come. It should be noted that all above-mentioned approaches, except the second McRae's theory (vi), use elastic scattering theory. The fact is that the inelastic scattering process may also play an important role in 'electron surface resonance'. However, the difficulty and stagnation in the development of inelastic diffraction theory is well known and the theoretical development of a combination of electron diffraction and electron energy loss spectroscopy (EEL) is very slow. But the true understanding of "electron

surface resonance" may well rely on the understanding in both

lelastic and inelastic diffraction processes, electron

spectroscopy (EEL, RHEEL) and the combination of them.
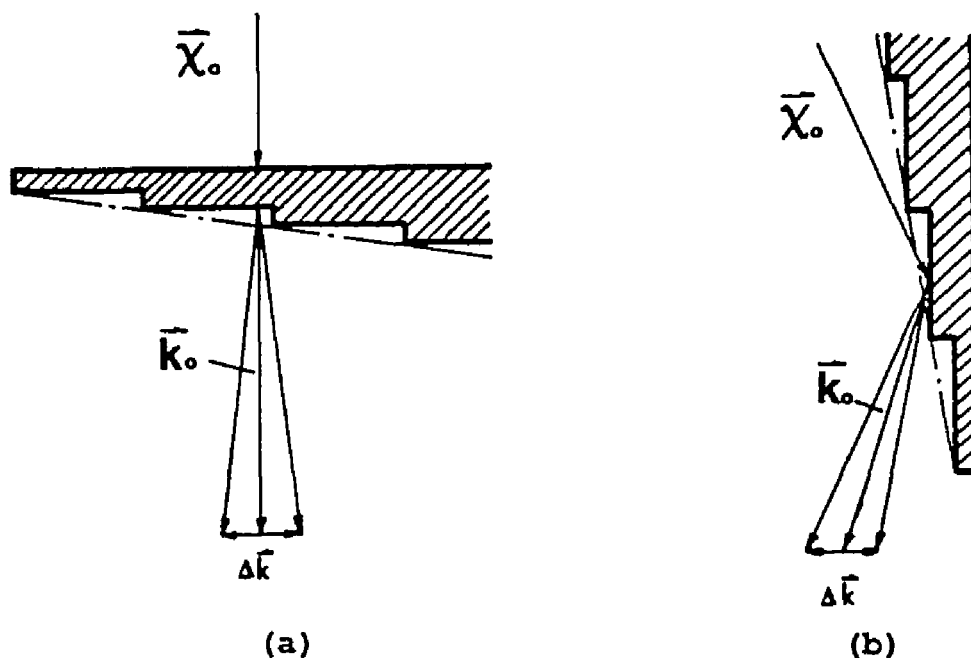
Fig.4.1. Comparison of the experimental configurations that lead to spot splitting in (a) transmission high-energy electron diffraction (THEED) and (b) reflection high-energy electron diffraction (RHEED).
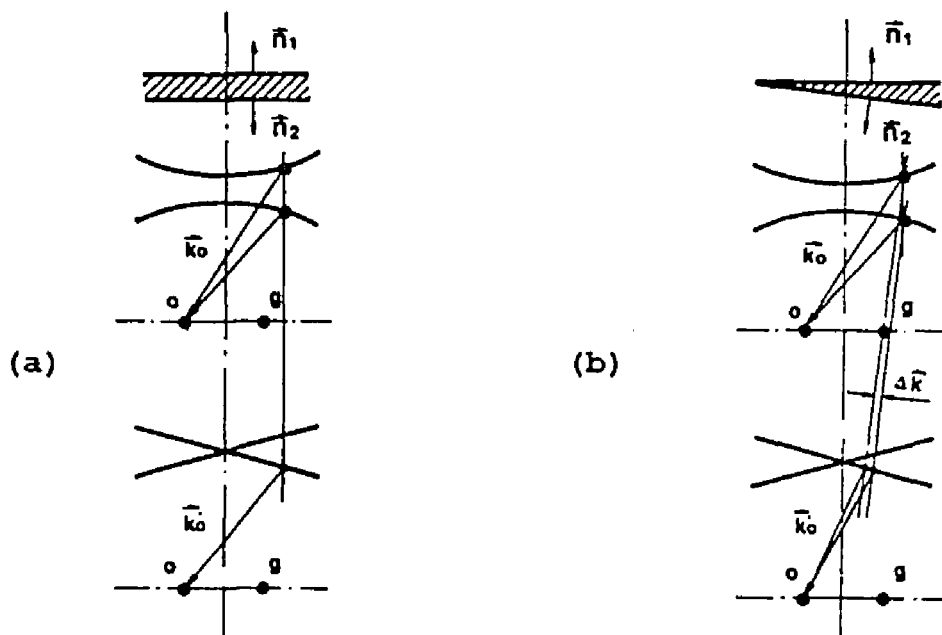
Fig.4.2. Illustration of Bloch wave matching using the dispersion surface for a crystal slab (a) and a wedged-shaped crystal (b) in THEED.

(a)

(b)

(c)

(d)
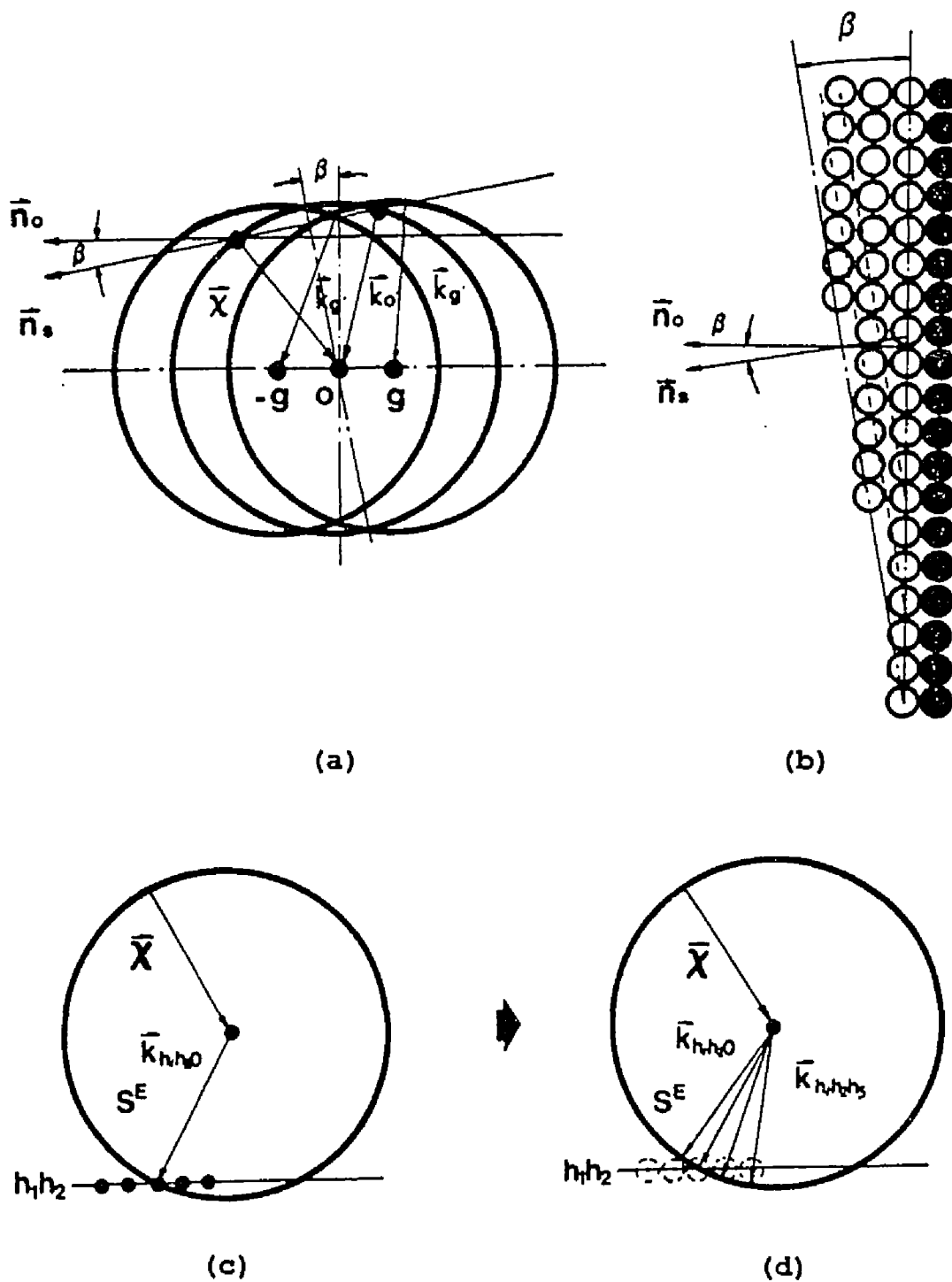
Fig.4.3. Illustration of Bloch wave matching for RHEED in (a), with the relative geometry of the beams with respect to the surface shown in (b). The specular beam is the overlap of a series of outgoing waves from flat surface (c), while it is split into a series of satellites for vicinal surface (d).
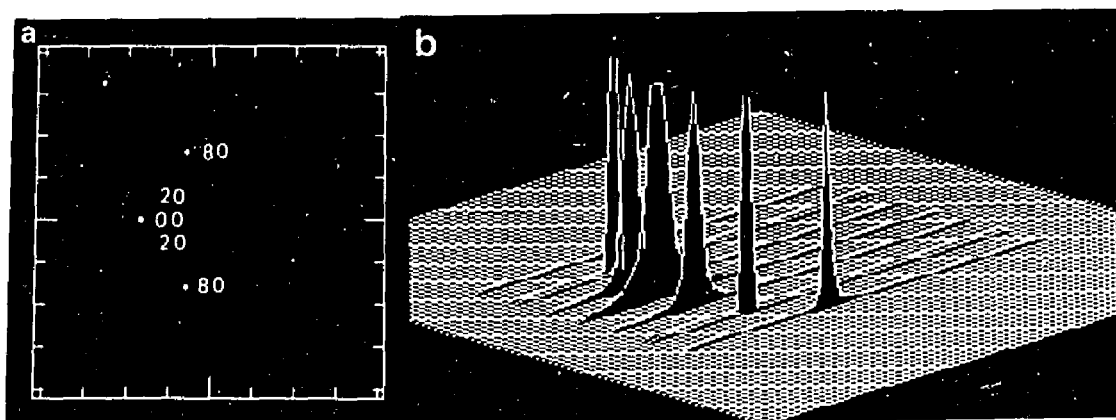
Fig.4.4. Simulated RHEED patterns for a GaAs(001) surface with the incidence beam near to [010] and a glancing angle of 2.4° without any absorption: (a) diffraction pattern and (b) y-modulated representation of the same.
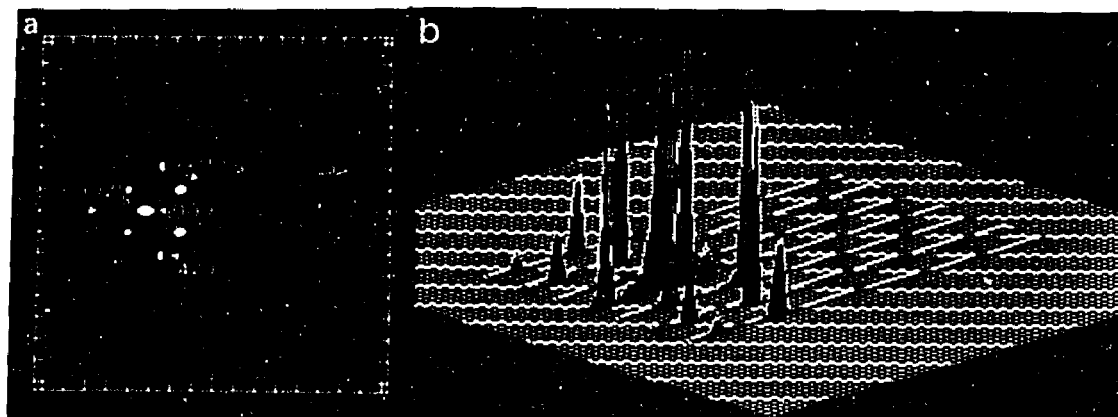
Fig.4.5. Simulated RHEED patterns for a GaAs(001) surface for the same conditions as in Fig.4.4 but with a vicinal surface 2.5° off (010) zone axis: (a) diffraction pattern and (b) y-modulated representation of the same.
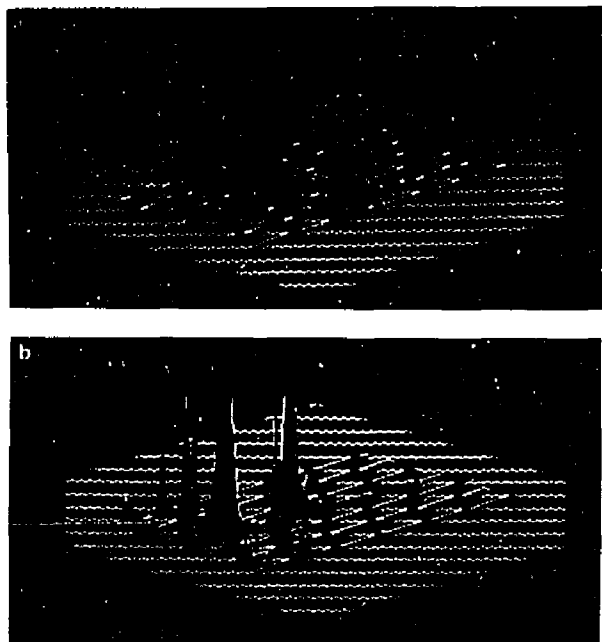
Fig.4.6. Y-modulated RHEED patterns for the same conditions as for Fig.4.4, except for incident angles of 1.55° and 2.86° in (a) and (b), respectively.
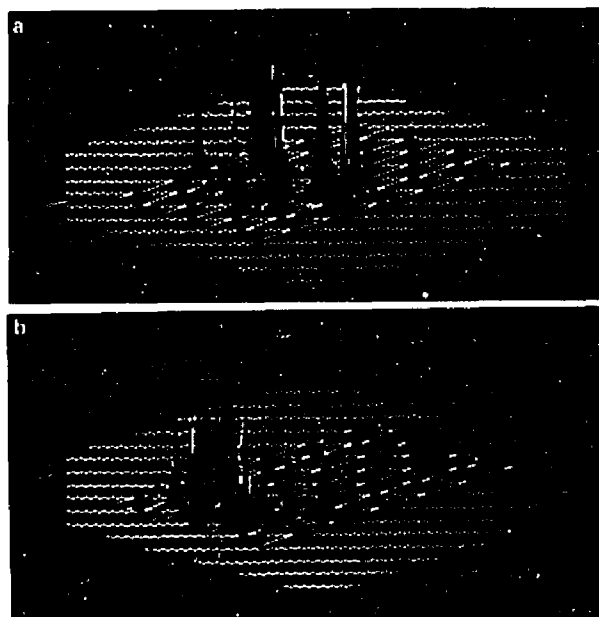
Fig.4.7. Y-modulated RHEED patterns for the same conditions as in Fig.4.6(a) and (b), respectively, with a change of the azimuthal angle to 1°.

(a)   (b)
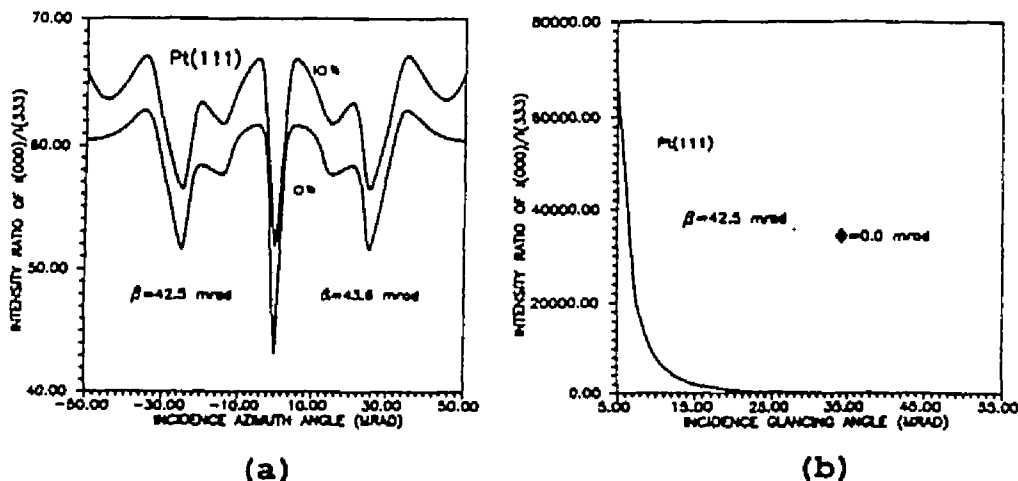
Fig.4.8. Plots of the ratio of the intensity of the specular
beam to the (333), beam as a function of azimuthal angle for
a fixed incidence angle (a) and as a function of the incident
glancing angle for a fixed azimuthal angle.

θ(mrad)   0   1%   10%
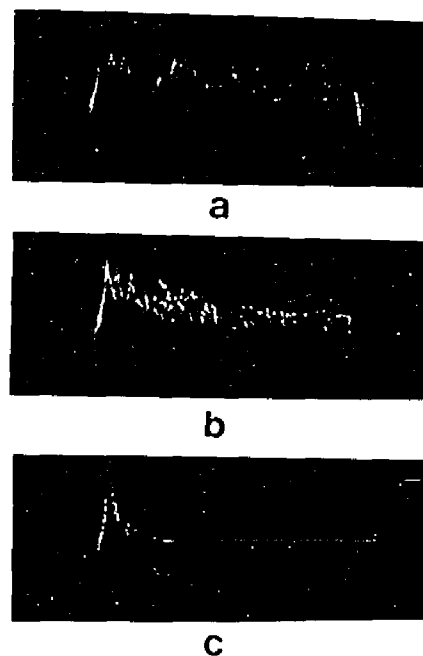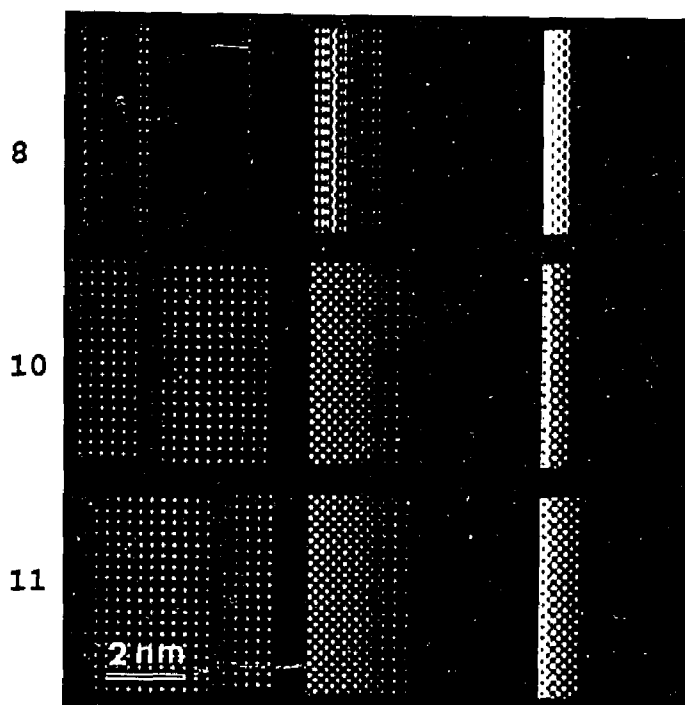
GaAs(001)

Fig.4.9. Intensity maps for GaAs
crystal at different glancing angles,
with different absorption, 100keV and
the [010] azimuth.

Fig.4.10. Y-modulated
maps of the first row
in Fig.4.9, θ_i=8mRad.
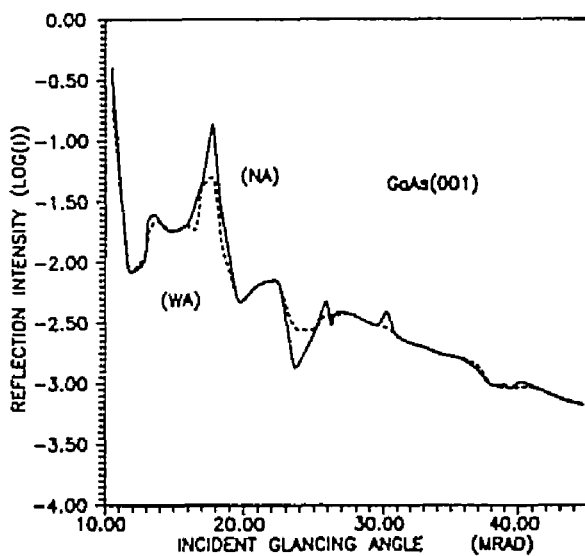
Fig.4.11. Specular rocking curves calculated for GaAs (001) surface with and without absorption for 100keV and the [010] azimuth.
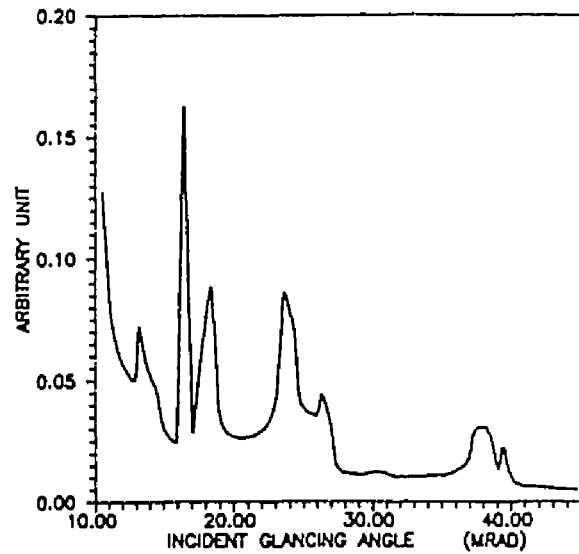
Fig.4.12. Total reflectivity as a function of incidence angle for the same conditions as in the Fig.4.11
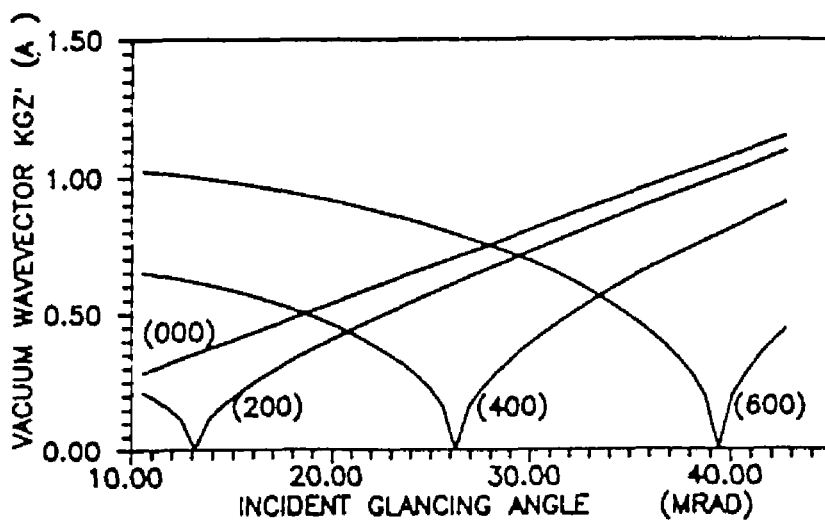
Fig.4.13. Plots of the vacuum wave vectors as a function of incidence angle. When the curves are decreasing the wave vector is purely imaginary, and when the wave vector is increasing the value is fully real.
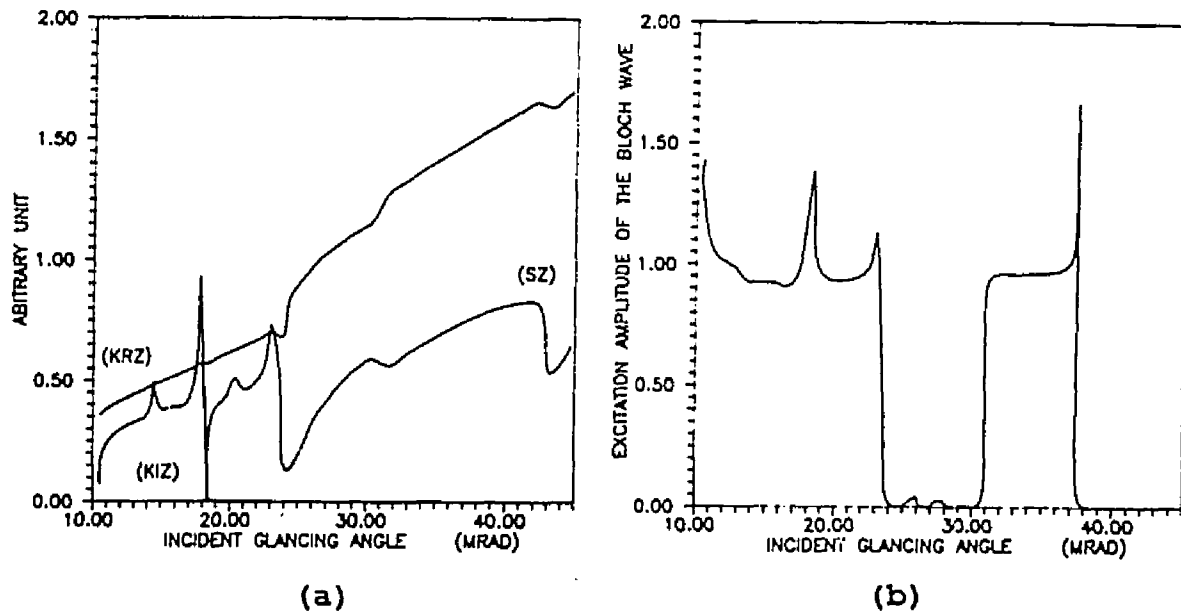
Fig.4.14. Plots for the strongest Bloch wave. (a) The real and imaginary components of the wave vector $\underline{k}^r$ and $\underline{k}^i$ respectively and the current flow $\underline{S}_x$. (b) The excitation amplitude.
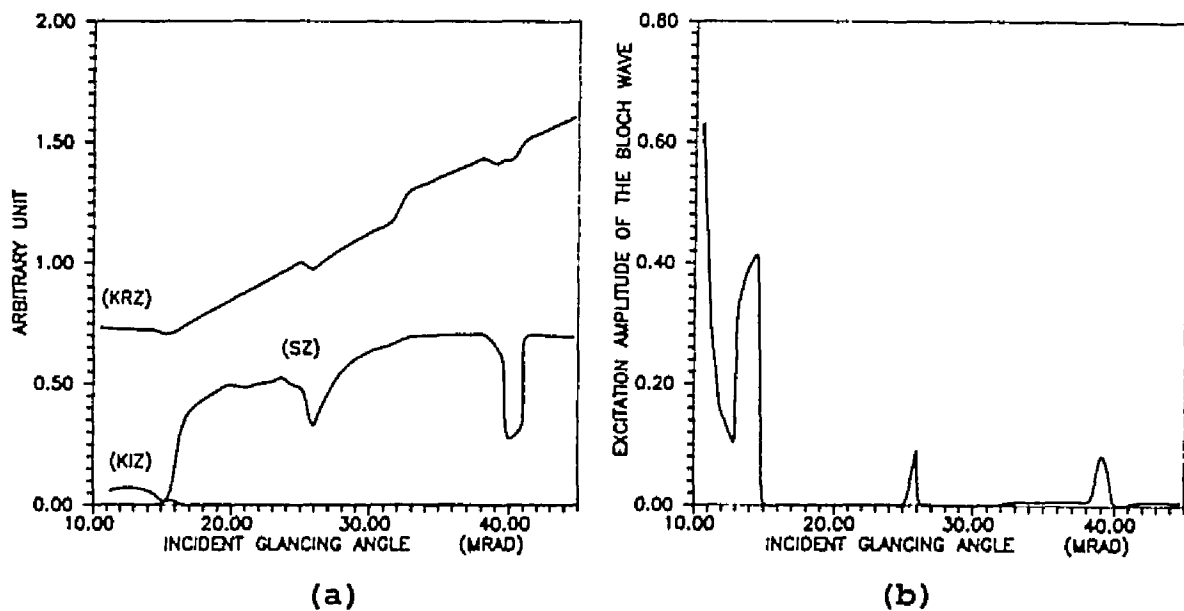
Fig.4.15. As for Fig.4.14, but for the next strongest Bloch wave.

Chapter V. <u>Surface phenomena in RHEED and RHEEM</u>

<u>by the BMCR method</u>

5.1. <u>Introduction</u>

In the previous chapters, the Bloch wave solution in the Bragg case and the consistency between this solution and its propagation in multislice have been studied [1-2]. These have laid down a solid foundation for combining the different methods to work together and the method of "Bloch Wave + Multislice Combined for Reflection" (BMCR) has emerged as a new approach to electron reflection.

In this chapter, the primary results of simulating various surface phenomena i.e. the stationary solutions defective surface are presented using the BMCR method. I will describe simulations of the effects of surface reconstructions and adsorption on RHEED patterns. Simulations of surface steps and their effects on the wave field are analyzed numerically. The existence of the surface wave which is related to electron surface resonance phenomena is demonstrated. Finally, an infinitely convergent (convergence not limited by iteration thickness) true stationary solution for an arbitrary surface for HEER has been obtained by using a method which I called "the edge patching method" or "the EPMO method" (Edge Patching

in the Multislice Only mode). A simple comparison between a simulated RHEED pattern and an experimental result is given.

5.2. Surface reconstruction and adsorption in RHEED

The observation of surface reconstructions and chemisorption by RHEED dates back to the 1960's. Sewell and Cohen [3] first reported observation of an oxygen-nickel structure on the nickel (001) and (111) surfaces by RHEED in 1965. In the same year, Mitchell et al. [4] showed the existence of a 2x1 reconstruction on the copper (001) surface in RHEED patterns. Later on, studies in this field intensified. Simmon et al. [5] carried out both LEED and RHEED studies of the absorption of oxygen on (100), (110) and (111) single crystal surfaces of copper, while Siegel et al. [6] developed a UHV RHEED camera for the study of surface absorption. Investigations on copper surfaces were also made by Trepte et al. [7]. In the late 1970's, Ino's group [8-9] successfully used RHEED to study the reconstruction of the Si(111) surface. The patterns obtained were more detailed than any others. However, the analyses of these results were only kinematical, i.e. geometrical analyses of the spot positions.

In this section, results of dynamical simulations of surface reconstructions and adsorption in RHEED using the

newly developed BMCR method are presented. Fig.5.1 shows the unit cell construction for the Bloch wave calculation (a) and the multislice (b). The system used is fcc gold and absorption is included by taking the imaginary potential as 10% of the real potential in both the Bloch wave and multislice calculations. The size of the unit cell is 8ax2a (a denotes the magnitude of primitive vector of conventional unit cell of gold). For the 2x1 reconstruction or adsorption, the y dimension of the unit cell needs to be two times larger. To satisfy the sampling theorem, the maximum x dimension of the unit cell is 8a when the maximum array size allowed in the program is used. This may result in more edge effects during the multislice because the x dimension of the unit cell is half that used in Chapter III. To reduce the edge effects, the surface is moved further towards the right in the unit cells indicated in both (a) and (b), which leaves more room for the reflected waves. This is feasible, because when the absorption is included, the rapid intensity decay in the crystal damps edge effects on the right. In the calculation, the surface is set at (3/4,0). The sampling array is 512x128. The coordination in the calculation is as follows: the z-axis [001] is from the left to the right towards the crystal; the x-axis [100] down and the y-axis [010] inward normal to the

page. The y-axis is along the direction of the incident wave.

All calculations were performed for 100keV incident electrons.

For the 2x1 gold surface reconstruction, one gold atom is placed on the site indicated in (b) for each of the four slices. For a 2x1 oxygen chemisorbed surface, the gold atom was replaced by an oxygen atom. The first 50-100 slices are for the simulation of flat surface to make the incident or trial wave function closer to the true solution for a free surface with a surface potential.

Fig.5.2 shows the outputs of wave fields for the 2x1 gold reconstruction in (i) and 2x1 oxygen adsorption (ii). The total thickness from a to 1 is 607.5Å. The thickness difference between any two nearest slices is 50Å and the incidence angle is 30mRad. The first slice is the solution of the Bloch wave calculation. As expected, the figure shows that the wave disturbance for the 2x1 gold reconstruction is much stronger than that for the case of 2x1 oxygen adsorption, because gold is a stronger scatter. The incident wave starts to be scattered by the surface at the third slice. In the subsequent slices, the incident wave appears to be scattered into the lower atom position, even though there is no atom on that site. This is clearer when the incident wave is excluded and only the Bragg reflected waves are presented, as shown in

Fig.5.3. The slices in Fig.5.3 correspond one-to-one to the outputs in Fig.5.2. The size of each slice in Fig.5.3 is 4ax2a. Each slice in Fig.5.3 extends from the surface into the vacuum (from right to left) a distance of 16.2Å as indicated in the figure.

The edge effects in Fig.5.2 appear quite serious because the size of unit cell is limited by the sampling array and the incidence edge has already moved into the surface. The reflected wave fields in slices i to l of Fig.5.3 show the same effects. This still will erode the accuracy of the numerical investigation in the Bragg reflected wave fields and the calculation would lose reliability when the incident edge completely moves into the crystal, because it is no longer a stationary solution.

Fig.5.4(i) shows the Bragg reflected waves in reciprocal space i.e. the RHEED patterns excluding the incidence beam, in which each pattern corresponds to a slice in Fig.5.3(i) labeled with the same letter. Fig.5.4(ii) is a convergence analysis of 5.4(i), and Fig.5.5 corresponds to Fig.5.3.(ii). The convergence analyses for both 5.4(i) and 5.5(i) show stability after 300Å. One can also directly observe consistency between the patterns k and l.

To display the patterns more clearly, Fig.5.6 shows the

y-modulated images of (a) and (1) for both Fig.5.4(i) and 5.5(i). There are a couple of points in Fig.5.6 to note:

i) the (01) and (0$\bar{1}$) forbidden spots emerge at 556.8Å, because of the existence of 2x1 surface adatoms.

ii) 2x1 reconstruction spots occur between each two nearest Bragg spots.

iii) The intensities of the reconstruction spots for the 2x1 gold reconstruction are noticeably stronger than that for 2x1 oxygen adsorption.

iv) The intensities of (03) and (0$\bar{3}$) are noticeably stronger than (01) and (0$\bar{1}$) and the reconstruction spots.

v) The intensity of the specular spot for the 2x1 gold reconstruction (t=556.8Å) declines significantly, compared to that for perfect flat surface (t=0), while the intensity of the specular spot for 2x1 oxygen adsorption (t=556.8Å) does not change noticeably. This information can be directly subjected to experimental analysis.

5.3. Surface steps

Investigation of surface step distributions in real space can provide useful information with respect to crystal growth, evaporation, surface phase transformations and mechanical properties [10]. Single atomic steps have been observed in

electron microscopes on various specimens prepared by different techniques [11-15]. Various surface phenomena correlating with surface steps have been intensively studied by both RHEEM and RHEED: e.g. surface phase transformations [11], step related surface dislocations [12], reverse contrast of steps with defocus [14].

Many different explanations have been proposed for the mechanism of step contrast. Cowley and Peng [16] considered steps as phase objects with phase contrast arising from the defocus, deviation from the Bragg condition and displacement of the objective aperture, while Turner and Cowley [17] suggested that a surface step can split the electron beam into Bragg-Bragg (BB) and Bragg-Laue (BL) beams and the interference between the two produce fringes along the step.

A dynamical interpretation of step contrast was first attempted by Peng et al. [18] using the multislice approach. However, the calculations were performed without a clear indication of reaching a stationary solution. We now have more favorable conditions to perform simulations of surface steps.

Fig.5.7 shows the unit cell constructions of a step-up (a) and a step-down (b). The system in the calculation is fcc gold, and absorption is included by taking the imaginary potential as 10% of the real potential in both the Bloch wave

and multislice. The size of the unit cell is 16ax1a while the results are displayed as 8ax2a and the sampling array is 1024x64. The coordination set-up is the same as that used in Section 2. The surface is also set at (3/4,0). For an atomic step-up, one row of gold atoms is added to the surface in each multislice iteration, while for an atomic step-down, one row of gold atoms is taken from the surface in each multislice iterations. The first 100 slices are used for the steady wave field in the crystal with surface potential. The remaining 500 slices are inserted with steps.

Fig.5.8 and 5.9 show the results of the calculation with the surface steps included. The total thickness in each case is 607.5Å and the thickness difference between output slices is 50Å. Fig.5.8 shows the results for 25mRad incidence, while Fig.5.9 shows the results for 30mRad incidence for both step-up (a) and step-down (b). One of the most important features of these results is that the wave fields converge to the original stationary state after about 250Å (from d to h), during which the wave fields are disturbed by the steps. The transition range of 200-250Å both begins and ends with the stationary states. The results clearly indicate that the simulation of wave disturbance resulted from the steps has not been seriously affected by the incoming edge after 607.5Å,

which is a necessary condition for the validity of the analysis. However, they still should not be considered as true stationary solutions. The edge patching method discussed later will solve this problem. Comparing (a) with (b) in both Fig.5.8 and 5.9, one can see that the wave disturbance of a step-up is better confined than that of a step-down and the transition range of a step-up (about 250Å) is a little shorter than that of a step-down (>250Å). This phenomenon so far has no experimental confirmation.

For comparison, Fig.5.10 shows the wave fields in vacuum for a surface with one step-down (a), the flat surface (b) and the surface with one step-up (c). The incidence angle is 30mRad and the size of each slice 4ax1a, which extends into the vacuum a distance of 4a. The stability of the vacuum waves in (b) tests the reliability of the simulation. The Bragg reflected wave fields excluding the incidence wave are shown in Fig.5.11, which correspond to Fig.5.10, except that the size of the displayed slices is 8ax1a i.e. twice as large as that in Fig.5.10 along the [001] axis (see Fig.5.1). The wave disturbance due to the step appears clearly in Fig.5.11 and the electron intensity distribution for a step-down appears to be reflected further away from the surface than that for a step-up.

To simulate RHEEM in an electron microscope, the specular beam is exclusively picked for imaging and the optical axis tilted to be coincident with the specular beam. One dimensional images for the last slice in Fig.5.10 (a), (b) and (c) (t=556.8Å) are shown in Fig.5.12(i). They are the plots of wave intensities versus the distance from the surface into vacuum (0-6x4.0497Å, from right to left). Each column is a focal series from -3000Å to 3000Å in Fig.5.10 (a), (b), (c). The defocus step Δf=1000Å. The contrast reversal with defocus is quite clearly demonstrated. However, it should be pointed out that there is a considerable amount of numerical errors in the calculation due to a limited cell size and the one dimensional images simulated here should be handled cautiously. For example, the width of each Bragg peak shown in the y-modulated patterns in Fig.5.6 indicates the existence of numerical errors. Theoretically, all Bragg peaks should be narrow and converged to one point in an ideal crystal potential and there should be no contrast from the flat surface, when a single beam is used. We consider that the numerical errors are mainly responsible for the contrast in the images we obtained from a free surface. The errors are also involved in the imaging calculation. To partially correct the errors, Fig.5.12(ii) shows the results of subtracting the

middle column, 1-D pictures of the flat surface from each of other two columns, 1-D pictures of the surfaces with steps. It is obvious that the step contrast is enhanced after the subtraction. To quantitatively estimate the errors, the contrast level of each picture is calculated as CL=SD/MEAN, where SD is the standard deviation and MEAN is the mean level of the picture and then CL are averaged over each focal series. For a step-up, a flat surface and a step-down, we obtained average contrast level from Fig.5.12(i) of 0.58, 0.13, 0.31. After the correction, as shown in Fig.5.12(ii), we obtained 1.41, 0, 0.87. Obviously, the errors are large: from 22% to 40%. Note that the results seem to suggest that the contrast level of a step-up is generally higher than that of a step-down.

5.4. Surface wave

Surface wave is a topic which has a long history in high energy electron reflection. The concept of a surface wave dates back to the time when Kikuchi et al. [19] first observed the intensity enhancement of the specular spot in RHEED, the "second kind of anomaly" (later on called "surface resonance"). The surface wave was later considered to be associated with surface resonance.

From the discussion in the previous chapters, however, it is apparent that a consistent, and convincing theory of electron surface resonance phenomena, valid for both low and high energy cases, has not appeared.

In this section, some results concerning "surface wave", using the newly developed BMCR method are presented, which clearly indicated the possible existence of a "surface wave". However, I will only present the numerical results and not attempt further theoretical speculation.

Fig.5.13 shows the y-modulated diffraction patterns at three different thicknesses for 100keV electrons and a gold (001) surface: 506.2, 556.8, 607.5Å, for three different surfaces--a surface with a step-up, a flat surface and a surface with a step-down. The incident angle is 35mRad and an absorption of 10% is included. The step is introduced at 101.2Å. It should be noted that the threshold incidence for the emergence of (04) spots is 36.6mRad, which is close to 35mRad. The patterns calculated for a surface with steps appear quite different from those for a flat surface, although the positions of the three basic reflection spots remained unchanged. It should be pointed out that there is no intensity comparison between the two different surfaces because of different normalization and display conditions.

For a surface with a step-up, spot broadening is apparent. The beam broadening in reflection caused by surface features is similar to the beam broadening in transmission caused by defects in the bulk crystal. Secondly, all of the three Bragg reflected beams have a small satellite. We have discussed the correlation between spot splitting and regular surface steps elsewhere [20] by using a Bloch wave argument. Here, the results from the BMCR method also implicate splitting from a single step. In each pattern of the surface with a step-down, two additional spots occur near the intersections between the Laue circle and the x axis in reciprocal space. These two beams are apparently parallel or nearly parallel to the surface. It is obvious that these two spots are the results of a step-down, compared to the patterns from a flat surface and the surface with a step-up. This also shows that a step-down may make the surface wave more visible. However, the true physical mechanism of the emergence of these spots merits further study and a clear experimental conformation. Nevertheless, theoretical ·speculation of the existence of surface wave which is either a "Bragg reflection in a side direction" in the sense of Miyake et al. [21] or a "wave trapped in surface state" in the sense of McRae [22], is not necessarily related to steps or other surface features.

There should also be additional spots along the x axis in the patterns of the flat surface and the surface with a step-up. It is possible that the intensities of these spots might be extremely low because of the special geometry and absorption at the surface. These regions are displayed separately and the results are shown in Fig.5.14. The spots are there, but they have extremely lower intensities: only $10^{-4}-10^{-5}$ of the intensities of the spots shown in Fig.5.13. Apparently, these waves have no way to emerge in the experiments and will be concealed in the background of inelastic scattering. Fig.5.14 shows the spots of the "surface wave" in the patterns of the last two output slices: t=506.2, 556.8Å for the flat surface and the surface with a step-up. The intensity for a flat surface is weaker than for a surface with a step-up, which implies that steps or other surface features tend to "release" the surface wave.

At this stage, we can at least conclude that a "surface wave" may be a truly detectable entity in high energy electron reflection and the best system for the observation would be an atomic smooth surface with some down steps.

5.5. Edge patching method

In the Bragg case, it has been noted that the intensity

of the wave field $I(\underline{r})=\psi(\underline{r})\psi(\underline{r})^*$ is independent of the distance along the beam direction when only the zero Laue-zone is taken into account. In other words, in the Bragg case, the electron wave has the following form:

$$\psi(\underline{r})=\psi(\underline{q},y)=\psi'(\underline{q})\exp[i\phi(y)] \qquad (5.1)$$

Here, the z axis is inward normal to crystal surface and the incident beam direction is along the y axis. $\underline{q}$ is a real space vector in the plane perpendicular to the y axis.

Equation (5.1) has been verified numerically by both the Bloch wave method and the BMCR method. A simple analytical proof is also given by Appendix 3.2.

Substituting Equation (5.1) into Equation (3.29), we obtain:

$$\psi'(\underline{q})\exp[i\phi(y_{n+1})]=\{\psi'(\underline{q})\exp[i\phi(y_n)]\cdot P_q(\underline{q},y_{n+1}-y_n)\}*P_r(\underline{q},y_{n+1}-y_n)$$

$$(5.2)$$

As indicated before, the phase term $\phi(y)$ has a linear relation with y: $\phi(y)=cy$. If the reference phase is taken as $\phi(0)=0$ and the thickness of each iteration is the same, then (5.2) can be rewritten as:

$$\psi'(\underline{q})\exp[i(n+1)c\Delta y]=\{\psi'(\underline{q})\exp[inc\Delta y]\cdot P_q(\underline{q},\Delta y)\}\cdot P_r(\underline{q},\Delta y) \quad (5.3)$$

Equation (5.3) shows two aspects of the multislice iteration in the Bragg case: on one hand, for $\psi'(\underline{q})$, each iteration is

equivalent to a Picard iteration cycle; on the other hand, each iteration makes a constant increment in phase to the wave field $\exp[ic\Delta y]$. This means that the difference between the wave fields of any two slices is only a constant phase term: $\exp(imc\Delta y)$. We note that the multislice iteration in the Bragg case is similar to the Picard iteration, but not exactly the same. This Picard iteration-like character of the multislice calculation as well as the 2-D dependence of the wave intensity in the Bragg case forms the basis for the development of "the edge patching method".

As mentioned in Chapter III, the BMCR method uses the BWO trial wave function for a more favorable condition for HEER simulation. However, this does not eliminated edge effects. Therefore, it is still not an infinitely convergent method.

It is obvious that to obtain a convergent stationary solution not limited by iteration thickness for an arbitrary crystal surface, one must solve the problem of the inward moving edge. As discussed before, there is only a constant phase difference $\exp[imc\Delta y]$ between any two slices for the multislice iterations in the Bragg case. The deteriorated edge can be replaced by the edge of the input wave field as long as it is multiplied by a proper phase term $\exp[mc\Delta y]$. and c can be calculated either analytically or numerically. We call

this "patching" approach. It should be pointed out that it is not necessary to repair the deteriorated edge for each iteration because the moving edge seriously deteriorates the solution only after a certain number of iterations. The rate of deterioration of the edge depends primarily upon three parameters: incidence energy (E_o), incidence angle (θ_o) and slice thickness (Δz) and the frequency of repairing has been set as self-adjustable in the program.

Fig.5.15(i) and (ii) show the comparison between the wave field calculated with and without the edge patching method. Both of them are calculated for the Au(001) surface and 100keV incident electron. The incident angle is 30mRad and absorption is included by taking the imaginary potential as 10% of the real potential in both the Bloch wave and multislice calculations. The conditions and coordination system used for the calculations are the same as those for Fig.3.14. The thickness between any two adjacent slices in (i) is 50.6Å, while it is 101.2Å in (ii) i.e. the total thickness calculated in (ii) is twice as large as that in (ii): 1113.2Å. (i) was calculated using the BMCR method without edge patching, while (ii) was calculated using the BMCR method with the edge patching. The replaced edge in (ii) is 1/3 of the area of the vacuum wave along the z axis. The continuity between the

patched area and non-patched in (ii) is clearly demonstrated and the deteriorated edge has disappeared. In other words, a stationary solution not limited by iteration thickness has been obtained. However, this is still not a real proof of the infinity of convergence, because here, the Bloch wave solution as an input wave of multislice iteration is already quite close to the true stationary solution and so is the replaced edge area cut from the original input Bloch wave. If the Bloch wave is far from the true stationary solution, there will be discontinuity between the patched edge area and the non-patched area, because the patched edge area is now very different from the true stationary solution generated in the non-patched area by the multislice iterations. However, the results show that this discontinuity does not matter for the area in which the true stationary solution has been reached. This is shown in Fig.5.16(i) and (ii), which correspond to Fig.5.2 (i) and (ii). All of the calculation conditions in the two figures are the same, except that here the edge patching method is used and 2050 iterations are calculated. The series of output slice numbers are: 1,100, 200, 300, 400, 500, 600, 700, 800, 900, 1100, 1300, 1500, 1700, 2050. Thus we have calculated wave fields for thickness up to 2075.5Å which is much thicker than what was previously possible. For the last

four slices in either Fig.5.16(i) or (ii), the stationary wave field from a surface with either reconstruction or adsorption has already moved into the patching edge area. The wave field in the patched area is quite different from the stationary wave field in the non-patched area on the right because it is cut from the solution for a free surface. Nevertheless, when we continue the iterations, this inconsistency does not affect the stationary solution of an imperfect surface in the non-patched area. This can be further demonstrated in reciprocal space. Fig.5.17(i) and (ii) show the RHEED patterns corresponding to Fig.5.16(i) and (ii). Fig.5.18(i) and (ii) show the y-modulated patterns corresponding to the last four RHEED patterns in Fig.5.17(i) and (ii). The stationary character of these solutions is apparent. The vacuum wave in each slice is the superposition of two parts, the incident wave and the Bragg reflected waves. The Bragg reflected wave front always moves away from the crystal surface while the incident wave front moves towards the crystal surface. This is the major source of the edge effects.

Along the y axis, both the Bragg reflected wave and the incident plane wave have the same phase difference between any two slices. When edge patching is carried out, both of them are multiplied by a phase term. In the case of poor trial

function, the Bragg reflected wave components may be far from the true solution, but the incident plane wave is always the same. Because the wave front of the reflected waves always move away from the crystal, it does not matter if the Bragg reflected waves in the patched area are far from the true solution. What is important is to preserve the continuity of the incident plane wave field. This argument provides a method to reach an infinitely convergent true stationary solution not limited by the slice thickness for any kinds of crystal surfaces.

This argument also implies that a plane wave should also be usable as a trial wave, since only the incident plane wave component in the replaced patched edge area is significant. In other words, we now have another independent computation method which we call "the edge patching method in multislice-only mode" (the EPMO method).

When the computation program (Chapter III) is shifted to the Multislice-only & Reflection mode, we obtain the results shown in Fig.5.19, which correspond to Fig.5.16. All of the calculation conditions are as the same as those for Fig.5.16, except for the input trial wave function which is now a tilted plane wave (30mRad) instead of the BWO solution of a perfect surface. There is now only one plane wave component left in

the patched area which acts like an "infinite plane wave source". This simulates the real condition of an electron microscope which usually has a beam size of several tens of nanometers. The results show that an incident beam with this size can be modeled as an infinite plane wave not only in the Laue case but also in the Bragg case.

Fig.5.20(i) and (ii) show the wave fields calculated for a perfect Au(001) surface with different incident angles: (i) for 25mRad and (ii) for 30mRad. The results correspond to Fig 3.10(i) and Fig.3.14(i) and the calculation conditions are the same for the two cases with the exception that here the EPMO method is used instead of the BWO or BMCR method and that the series of output slice numbers are: 1, 100, 300, 600, 900, 1000, 1100, 1200, 1300, 1500, 1700, 2050. The last four slices in Fig.8 (i) and (ii) show the consistency between the three methods. A more precise numerical analysis of the consistency between these methods can be easily carried out using the intensity analysis methods used in Chapter III. The consistency parameters have been calculated from the last ones of the slices of Fig.5.20(i) and (ii) (the EPMO solutions), the first ones of the slices in Fig.3.10(i) and Fig.3.14(i) (the BWO solutions) and the last ones of the slices in Fig.3.10(i) and Fig.3.14(i) (the BMCR solutions).

For 25mRad: $R_{EPMO-BWO}=0.056$; $R_{EPMO-BMCR}=0.068$

For 30mRad: $R_{EPMO-BWO}=0.071$; $R_{EPMO-BMCR}=0.055$

R is defined by Equation (3.40). As far as numerical accuracy is concerned, these values of the consistency parameter show that the solutions of the three methods are consistent with each other. However, they are not so good as the consistence data between the BWO and BMCR method (<1%)(Fig.3.10, 3.14). There are two basic sources of errors: 1) a large number of iterations and 2) the edge patching continuously introduces a small phase error (about 1mRad). The results show that the errors have not jeopardized the final solution. Nevertheless, we should be careful in using the EPMO method for a quantitative analysis of the experimental data.

5.6. Comparison between the results by the EPMO method and experiments

Although the validity of the EPMO method has been theoretically verified by its consistency with the Bloch wave method (the BWO method) and the BMCR method for different surfaces with sufficient rigor, it is still necessary to demonstrate its consistency with experiments. Here is a simple example.

Fig.5.21(a) shows an experimental RHEED pattern taken

from the GaAs(001) surface by Cho [23]. A schematic diagram of the GaAs(001) surface viewed at normal incidence is shown in Fig.5.21(b). The incident glancing angle is less than 1°, and the azimuth is along [1̲1̲0]. The incident electron energy is 40keV. The pattern corresponds to the 2x8 reconstruction on the GaAs(001) surface: one missing row along the incident beam and seven missing rows in the direction perpendicular to the incident beam. The specular spot is centered and the two outside spots corresponding to the 1x1 surface are indexed as (01) and (01̲) respectively. For the GaAs(001) surface, the size of the 1x1 surface unit cell is 3.9894x3.9894Å. Therefore, for 1° incident angle, the values of the threshold energy for (01) and (02) spots are 30.1keV and 111.7keV respectively. Thus, for 40keV incidence energy, (02) spots cannot emerge in the pattern. The two inside spots are due to the missing row reconstruction along the incident beam direction [1̲1̲0].

To simulate this pattern, multislice calculations were performed under the same conditions as those for the RHEED pattern in Fig.5.21(a). Fig.5.22(a) is a diagram of the primitive unit cell of GaAs along the [1̲1̲0] zone axis. Fig.5.22(b) and (c) show the slice construction for multislice for a perfect surface and a surface with the missing row

reconstruction respectively. Both of them are Ga termination surfaces. For a missing row reconstruction along [1$\underline{1}$0] direction (perpendicular to incident beam), the top-most Ga atoms are taken off with a certain periodicity through continuous multislice iterations. For the 2x8 reconstruction, one Ga atom is left for every 8 unit cells along the beam direction, while for the 2x16 reconstruction one Ga atom is left for every 16 unit cells along the beam direction.

Fig.5.23 shows calculation RHEED patterns for three different surfaces: (a) perfect GaAs(001) surface, (b) GaAs(001) surface with a 2x8 reconstruction and (c) GaAs(001) surface with a 2x16 reconstruction. The incident glancing angle is 1°. These calculated patterns show that this incident angle is a little larger than that for the experimental pattern in Fig.5.21(a). As expected, for a perfect GaAs(001) surface, there are only three spots in the calculated RHEED pattern in (a): one specular spot (0,0) and the two (0,1) spots. As shown in (b) and (c), for the 2xn reconstruction, two reconstruction spots occur between the (00) specular spot and the two (01) spots. They are indexed as (0,1/2) and (0,$\underline{1/2}$) respectively. The intensities of the two reconstruction spots in (b) are significantly stronger than the corresponding ones in (c). This is because each reconstructed

atomic row along the beam direction for the 2x8 reconstruction possesses two times as many atoms as the corresponding ones for the 2x16 reconstruction, and the scattering effects is stronger. In other words, the intensity ratio between the reconstruction spots and the specular spot can give at least qualitative information about the reconstruction in the direction perpendicular to the incident beam. As expected, the calculated pattern in (c) matches with better the experimental RHEED pattern in Fig.5.21(a). Compared with (b) and (c), the specular spot in (a) is much weaker than that in (b) and (c). This means that the reconstruction can enhance the specular beam significantly in this case. Conversely, in the case of the 2x1 reconstruction on Au(001) surface, the specular beam is weaken by reconstruction dramatically (Fig.5.7, 5.18). The physics behind this phenomenal difference is not clear.

Here, we have only a qualitative comparison between the RHEED simulated using the EPMO method and experimental RHEED pattern. However, this clearly indicates that the application of the EPMO method to quantitative analyses of HEER experiments has promise.

5.7. Interim summary

The primary results obtained by means of the BMCR method

in this chapter can be considered as the last step of the three-step development of the method.

i) Solving the n-beam Bloch wave problem in the Bragg case.

ii) Investigating the consistency and the conditions for the consistency between the Bloch wave method and multislice iterations in the Bragg case.

iii) Applying the BMCR method to some real problem and testing the potential of the method.

The results appear to be encouraging. The importance of the ideas of "verification" and "combination" associated with the BMCR method has been demonstrated.

It has been proved that the edge patching method finally solves the problem of the edge effects, which can be considered as either an improvement of the BMCR method or an independent computation method for HEER (the EPMO method) due to the argument of the "infinite plane source". An infinitely convergent true stationary solution for an arbitrary surface for HEER has been obtained using the EPMO method. A simple demonstration of its consistency with experimental results in Section 5.5 clearly shows the promising prospect of the application of the EPMO method to HEER experimental analyses.

The computation speed for the BMCR method has been brought down to the speed of the EPMO method when the Bloch

wave solution is used as a reusable trial function. For the simulations of 600 slices of sampling size 1024x64 on Apollo 3500, the CPU time will not exceed 6 hours. This is manageable on many computation facilities.

However, both the BMCR and EPMO methods only provide a new apparatus for solving the problem instead of a solution of problems. Further applications of these two methods will definitely explore more physical insights of HEER.
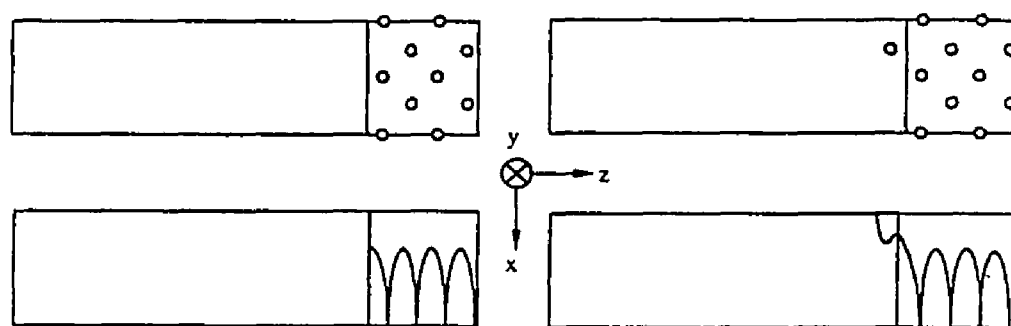
(a) Bloch wave   (b) Multislice

Fig.5.1. Unit cell set-up for the simulation of surface reconstruction adsorption. (a) Unit cell for the Bloch wave calculation. (b) Unit cell for multislice calculation.

2x1 Au Re.

2x1 O Ads.
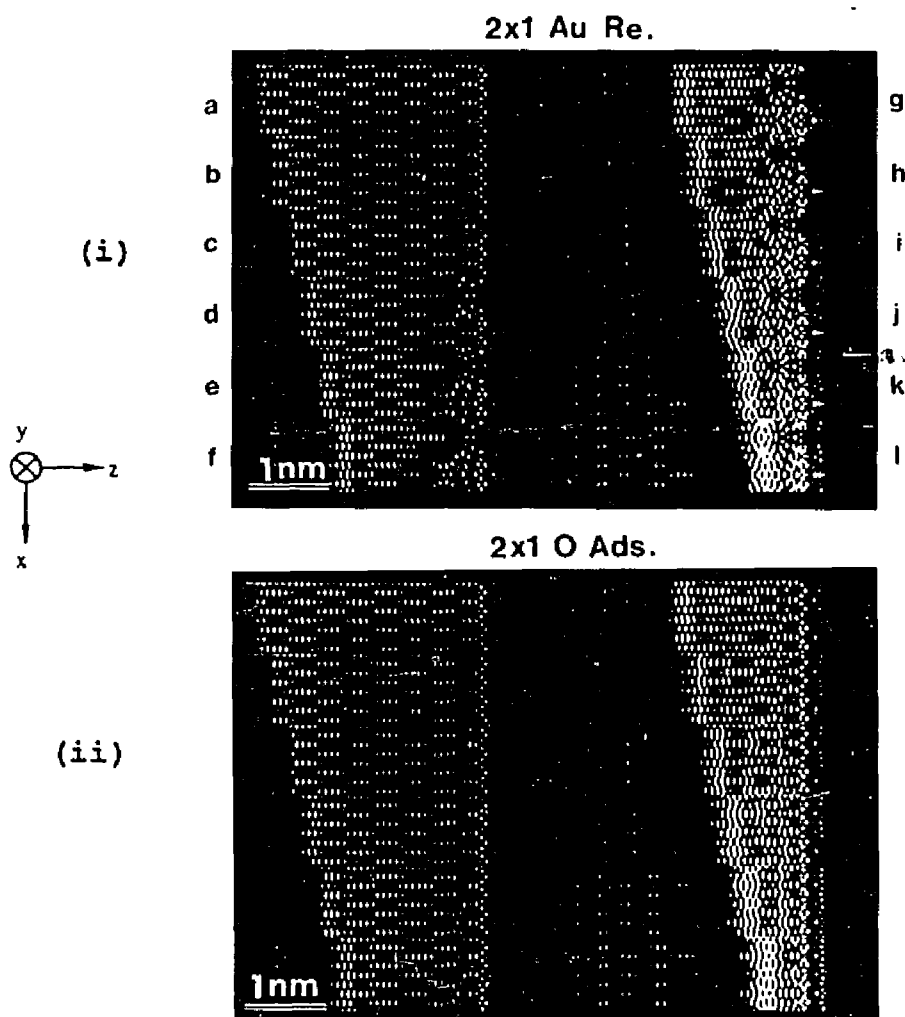
Fig.5.2. Wave field outputs from multislice iterations for 2x1 gold reconstruction (i) and 2x1 oxygen adsorption (ii).

(i)

(ii)
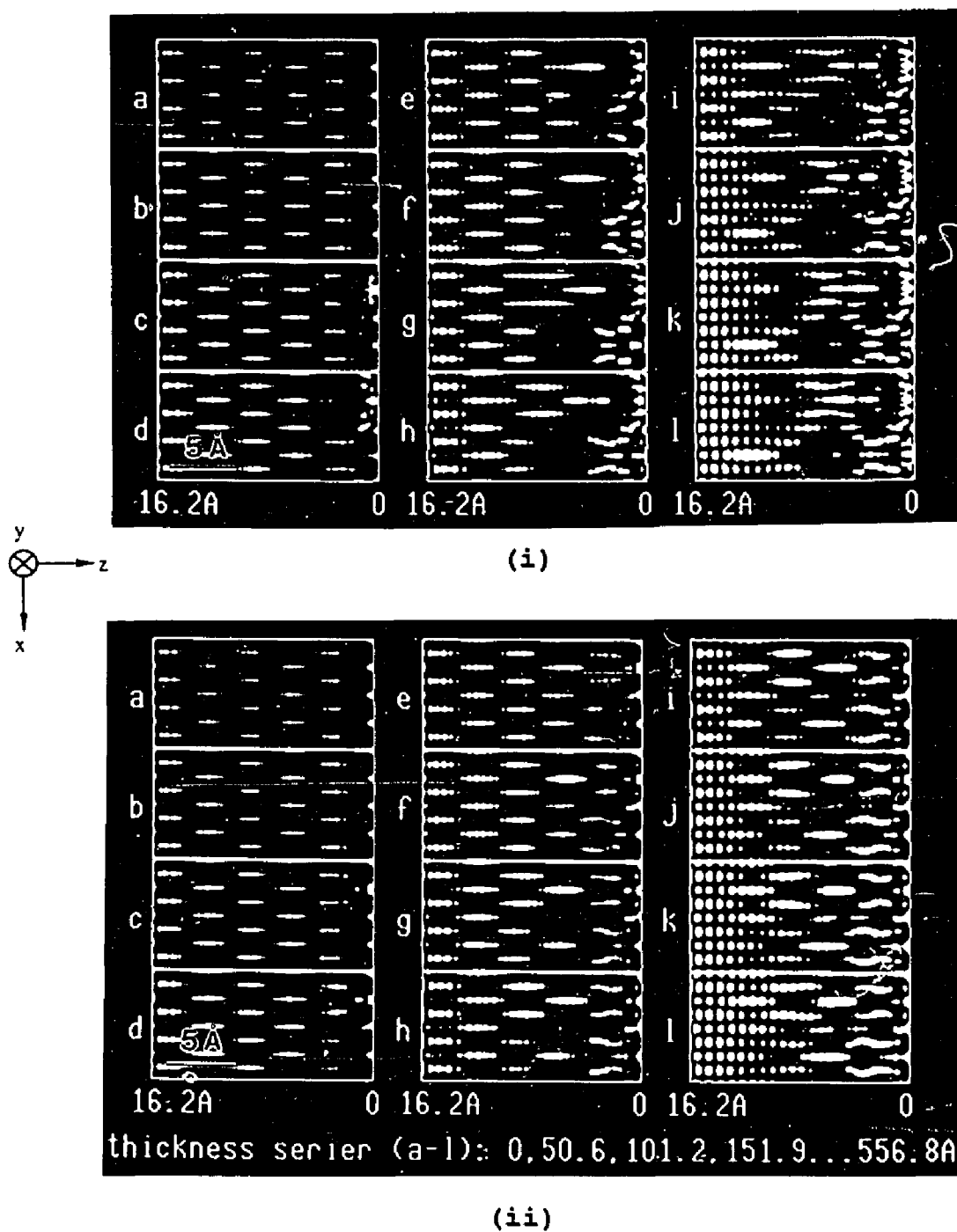
Fig.5.3. Outputs of the Bragg reflected wave fields, excluding
incident wave, from the multislice iterations, for 2x1 gold
reconstruction (i) and 2x1 oxygen adsorption (ii). The rest
of the conditions are the same as those in Fig.5.2.
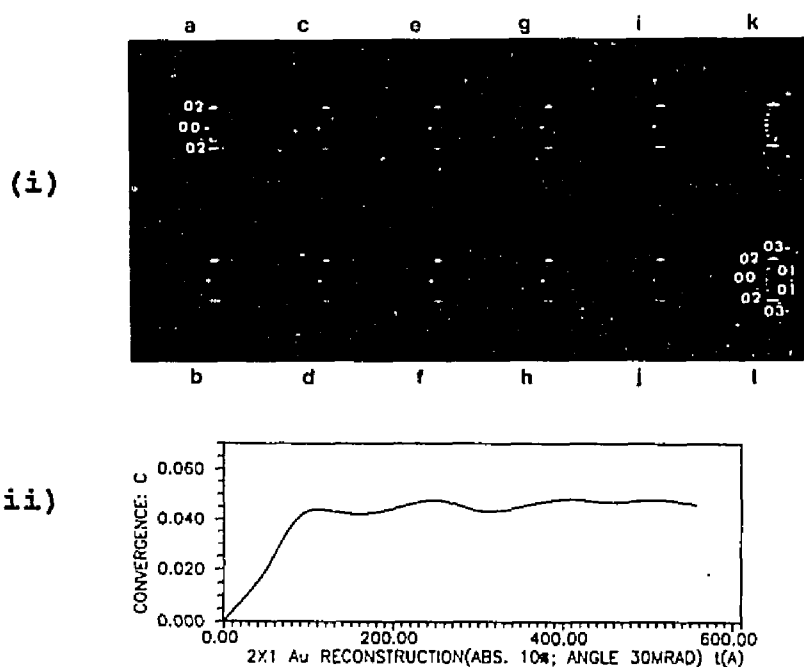
Fig.5.4. (i) RHEED patterns excluding the incident beam, one-to-one corresponding to the output slices in Fig.5.2(i). (ii) The convergence curve of (i).
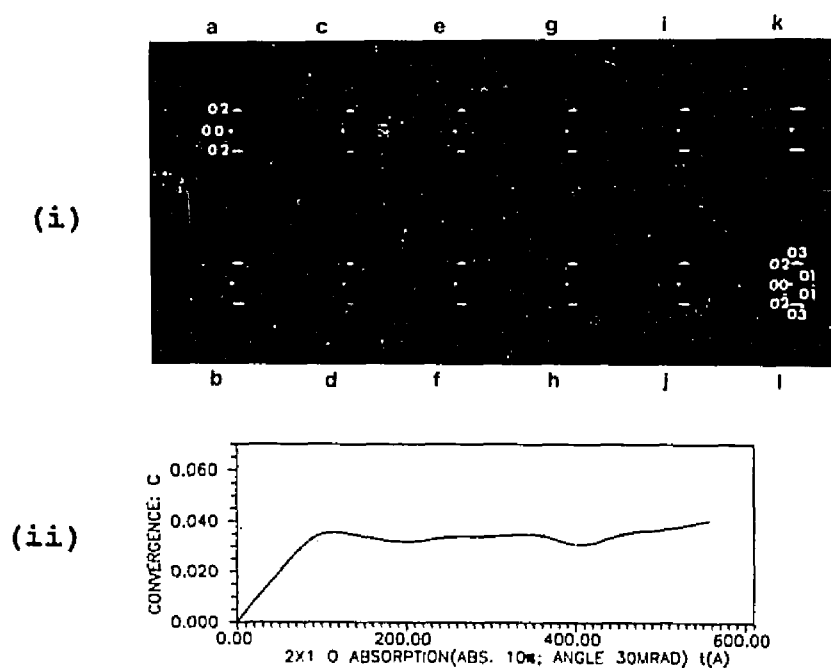
Fig.5.5. (i) RHEED patterns excluding the incident beam, one-to-one corresponding to the output slices in Fig.5.2(ii). (ii) The convergence curve of (i).

2×1 Au Surface Reconstruction
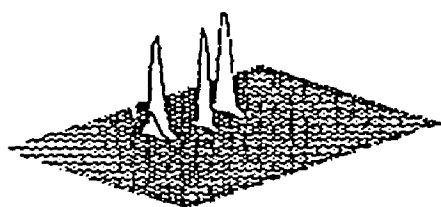
Thickness: 0   556.8 A
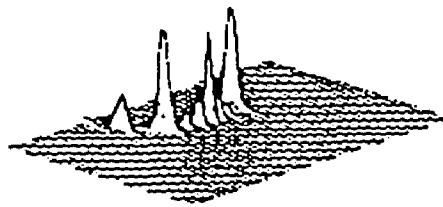
2x1 0 Surface Absorption
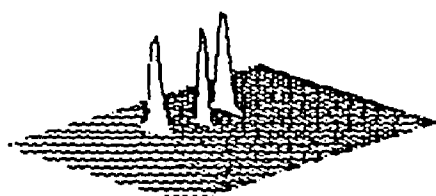
Thickness: 0   556.8 A
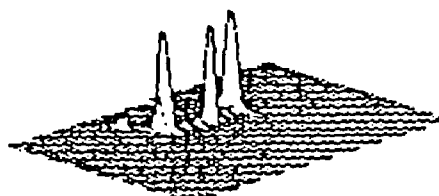
Fig.5.6. Y-modulated patterns corresponding to a and 1 in Fig.5.4(i) and Fig.5.5(i).

Bloch wave   Bloch wave

Multislice   Multislice
(a) Step-up   y   (b) Step-down
                     ⊗——z
                     x
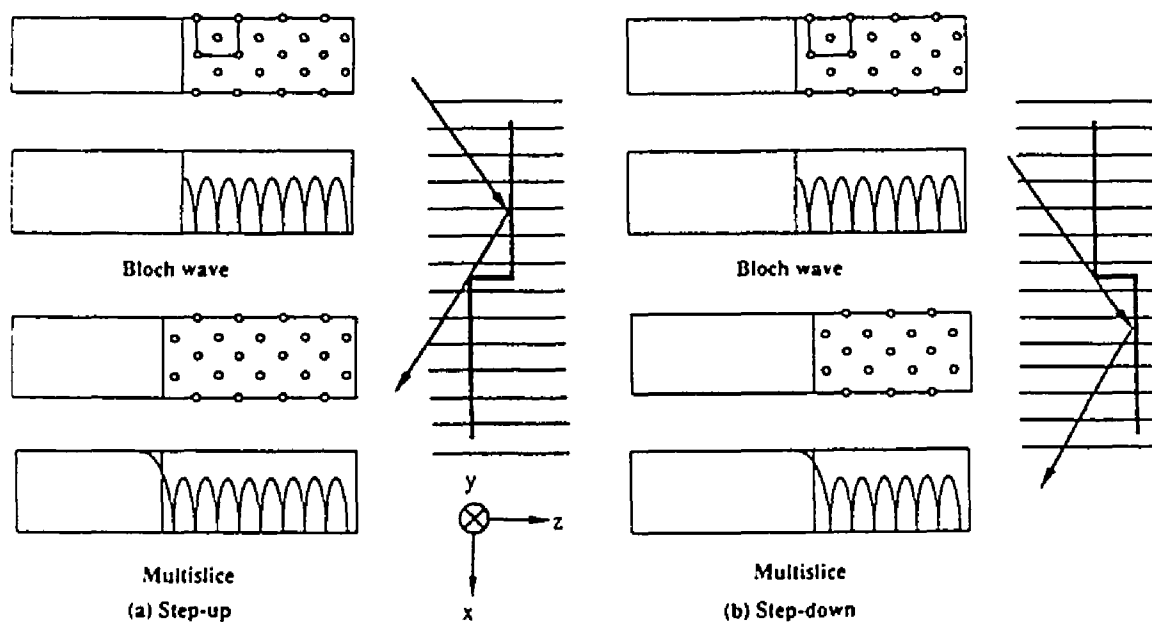
Fig.5.7. Unit cell set-up for simulations of step-up (a) and step-down (b). Upper two are the unit cells for the Bloch wave calculation and lower two are the unit cells for multislice iterations.

Up 25mrad

Down 25 mrad
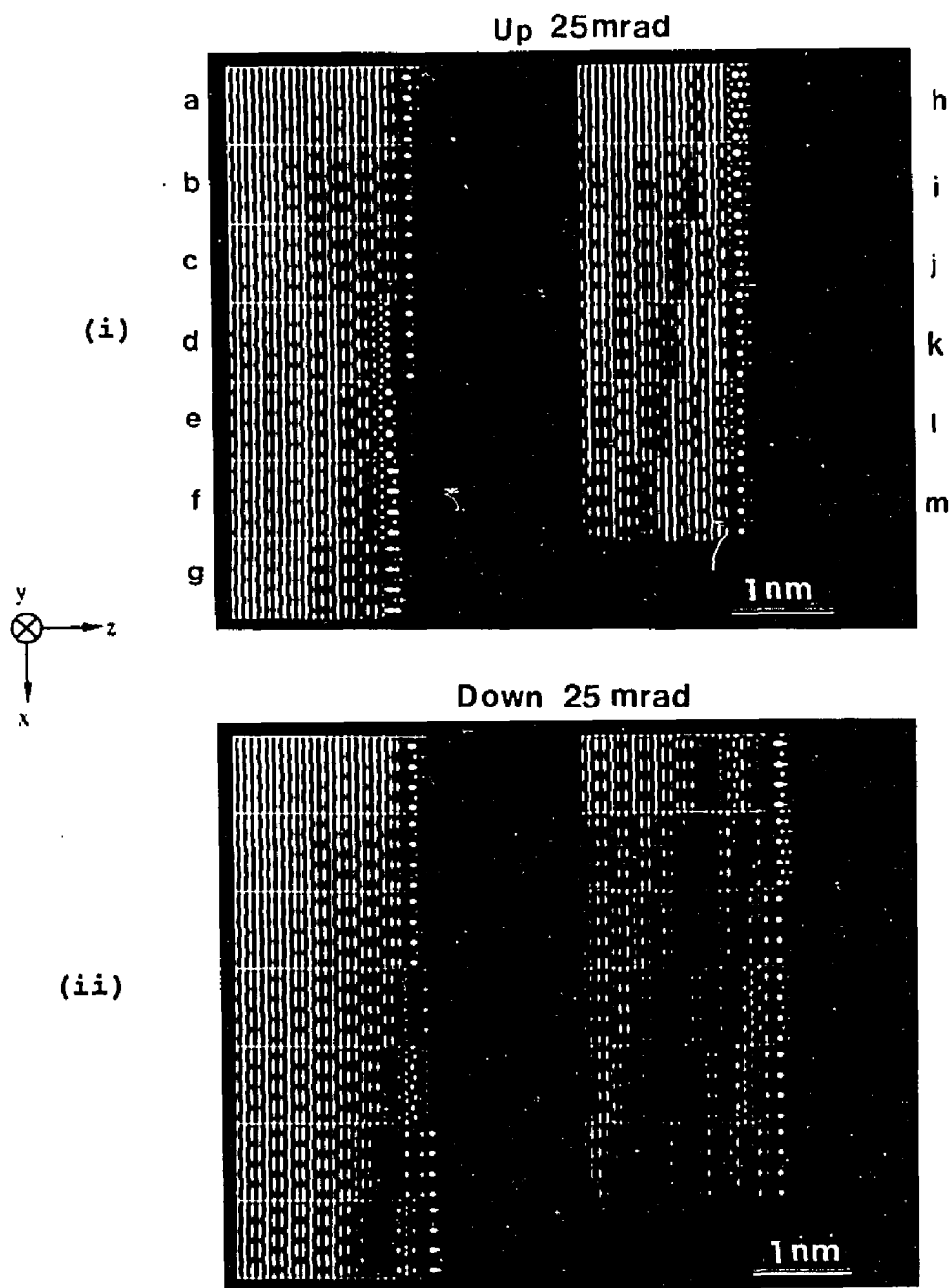
Fig.5.8. Wave field outputs from multislice iterations for the simulations of step-up (i) and step-down (ii). They are introduced at slice c. The thicknesses of the first and last slices are 0 and 607.5Å respectively. The thickness difference between two nearest slices is 50Å and the beam incidence 25mRad.

Up 30 mrad

(i)

a
b
c
d
e
f
g

h
i
j
k
l
m

1 nm

Down 30 mrad

(ii)

1 nm
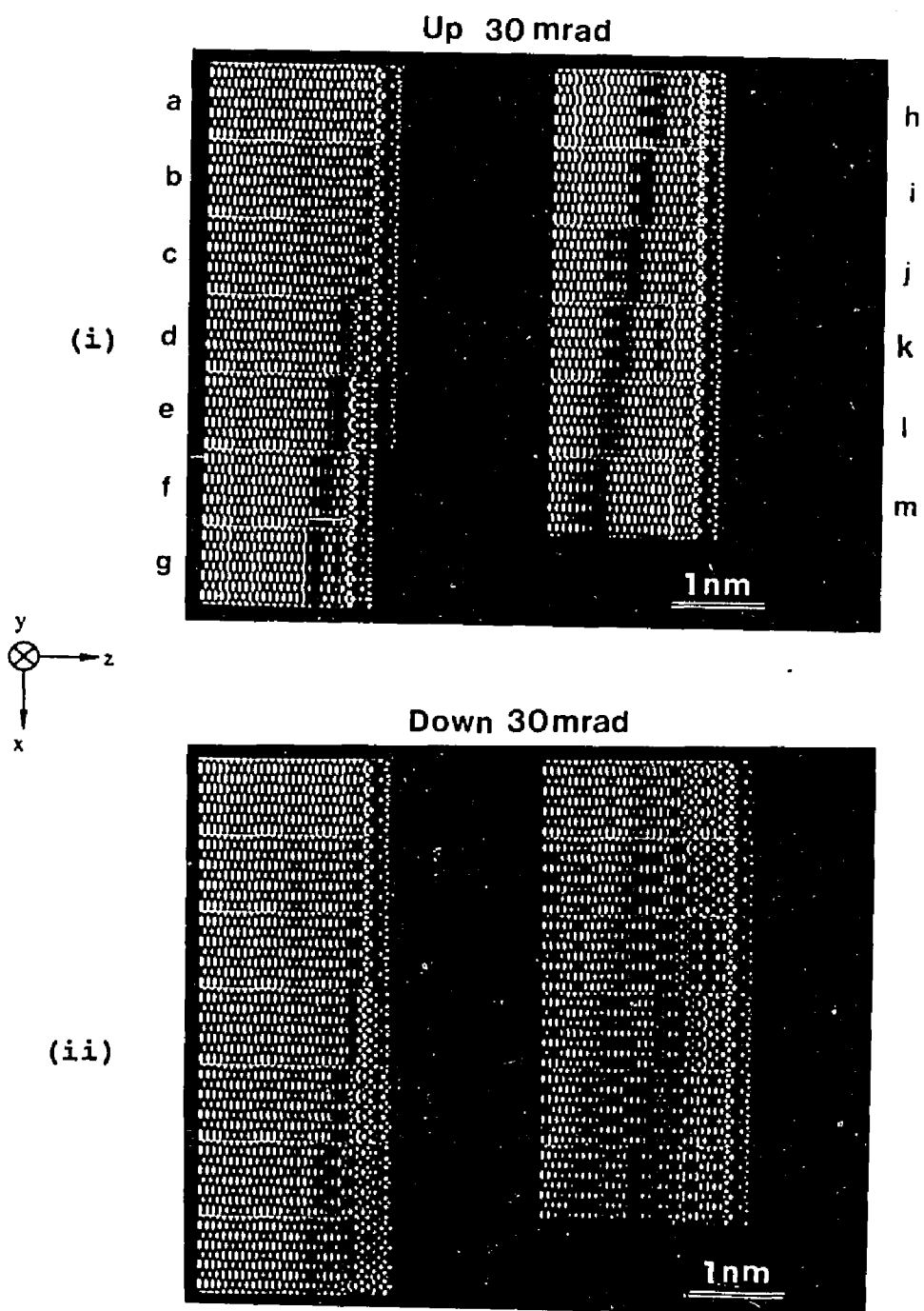
Fig.5.9. Wave field outputs from multislice iteration under the same conditions as those for Fig.5.8, except the beam incidence is 30mRad.
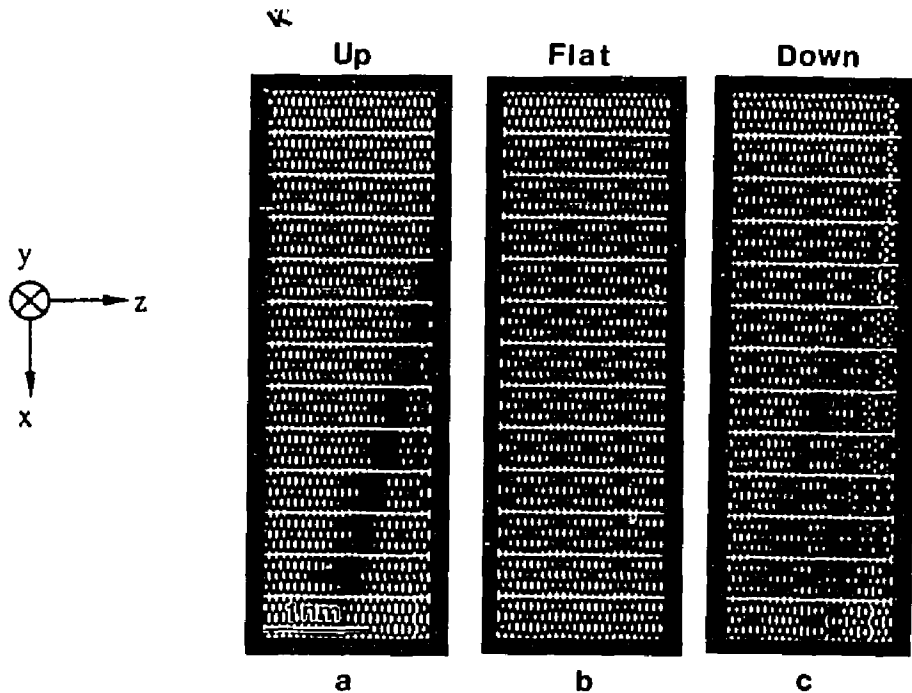
Fig.5.10. Wave field outputs in vacuum which include the Bragg reflected waves and the incident wave from multislice iterations for the simulations of the surface with step-up (a), flat surface (b) and the surface with step-down (c).
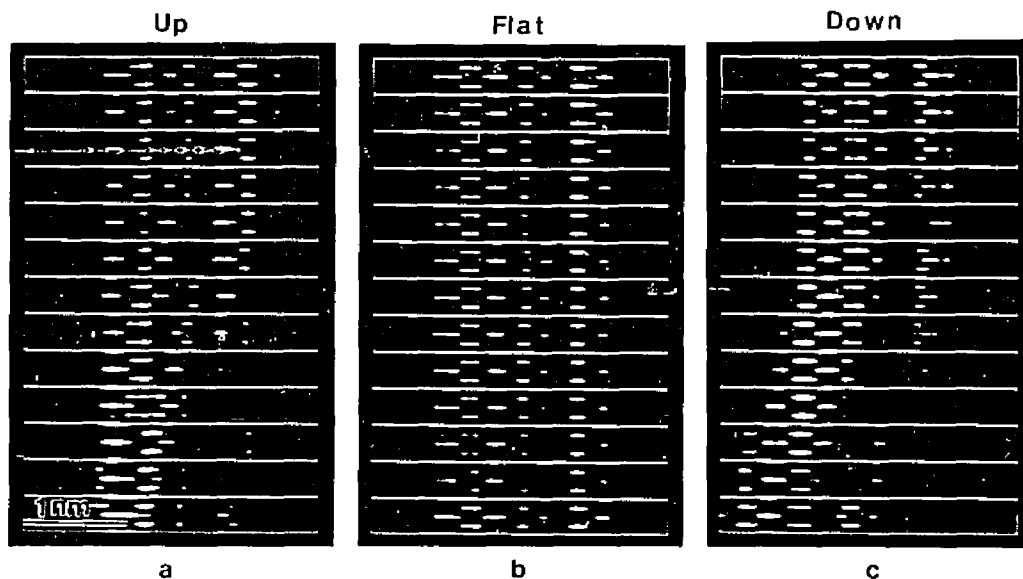
Fig.5.11. Wave field outputs excluding the incident beam in vacuum, which one-to-one correspond to those in Fig.5.10, except that the size of unit cells displayed is 8ax1a.
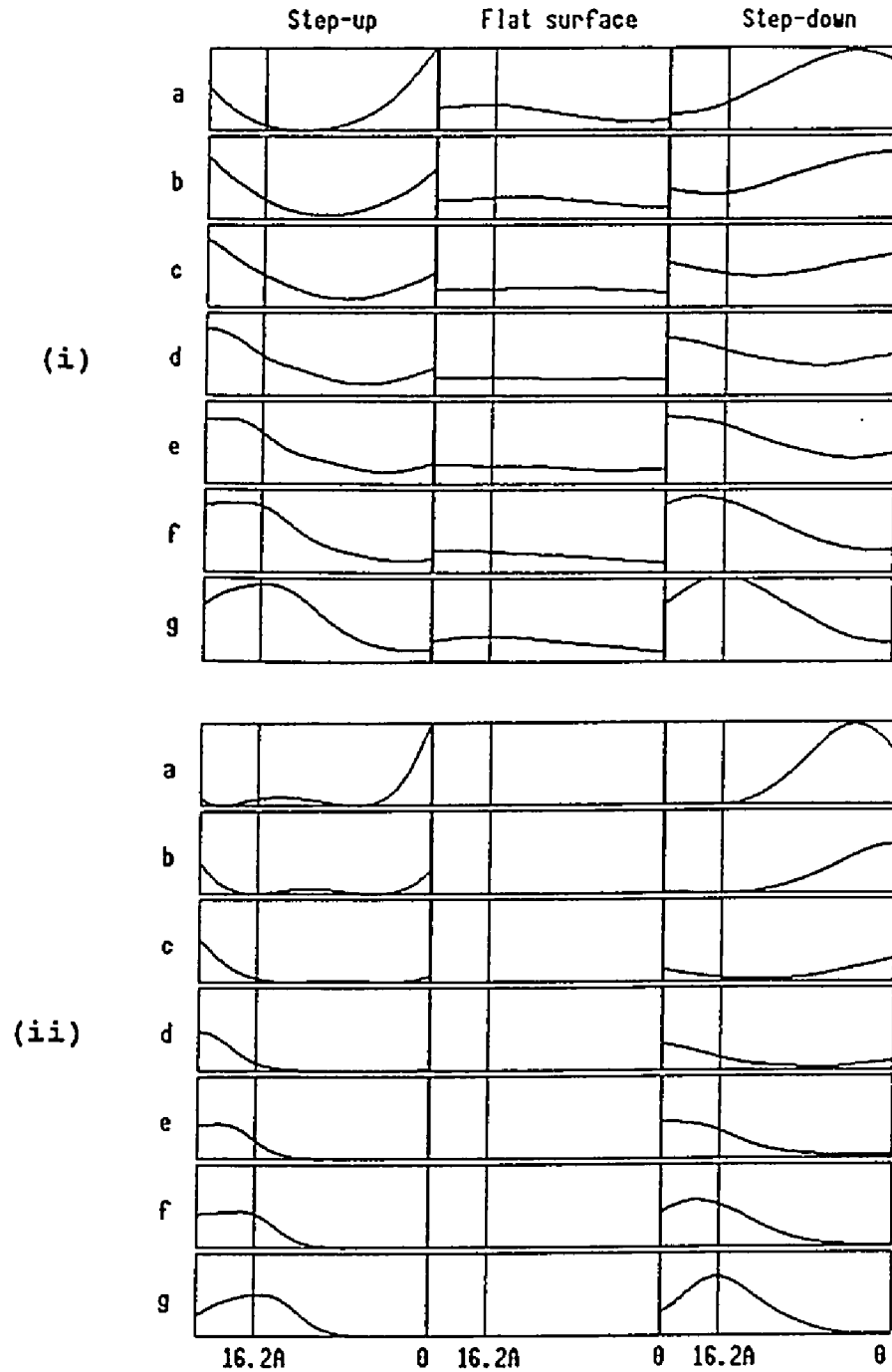
Fig.5.12. (i) Focal series of one dimensional imaging contrasts by using specular beam alone, crossing the wave disturbance caused by steps in the last slice in Fig.5.10(a), (b) and (c) (t=556.8Å). The defocus range is from -3000Å to 3000Å and defocus step is 1000Å. (ii) Results of subtracting the middle column from each of three columns in (i).
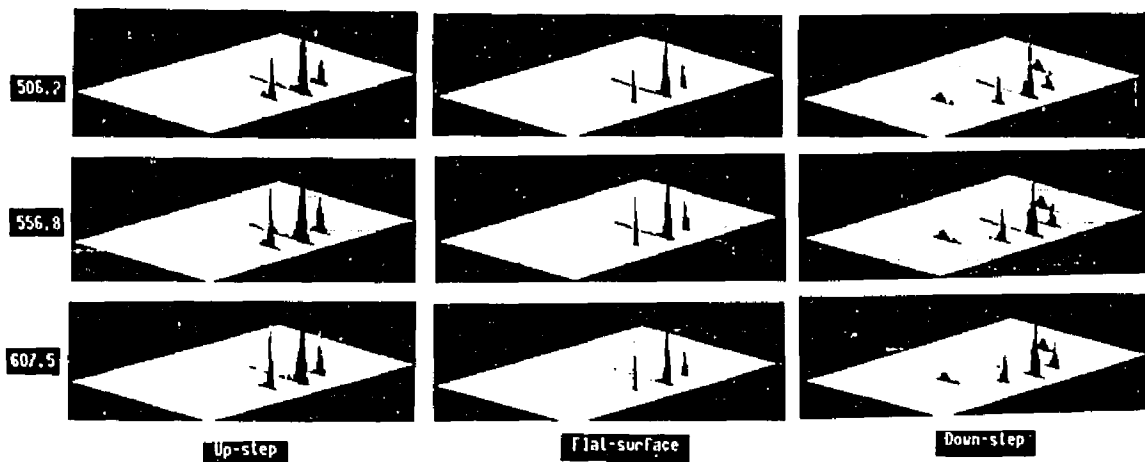
Fig.5.13. Y-modulated images of diffraction patterns at three different thicknesses; 506.2, 556.8, 607.5Å, for three different surfaces; the surface with step-up, flat surface and the surface with step-down. The beam incidence is 35mRad and absorption 10%. The step is introduced at t=101.2Å
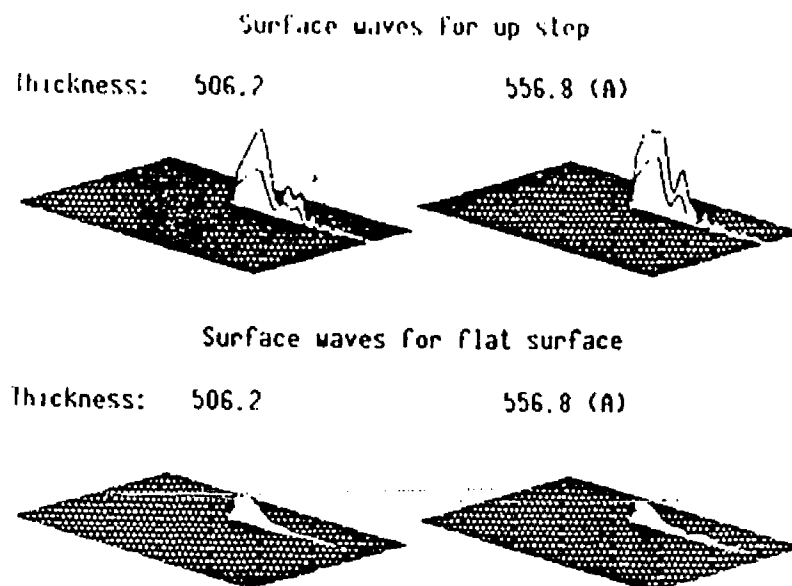
Fig.5.14. Spots of surface waves in the patterns of last two output slices; t=506.2, 556.8Å, for the flat surface and the surface with a step-up.
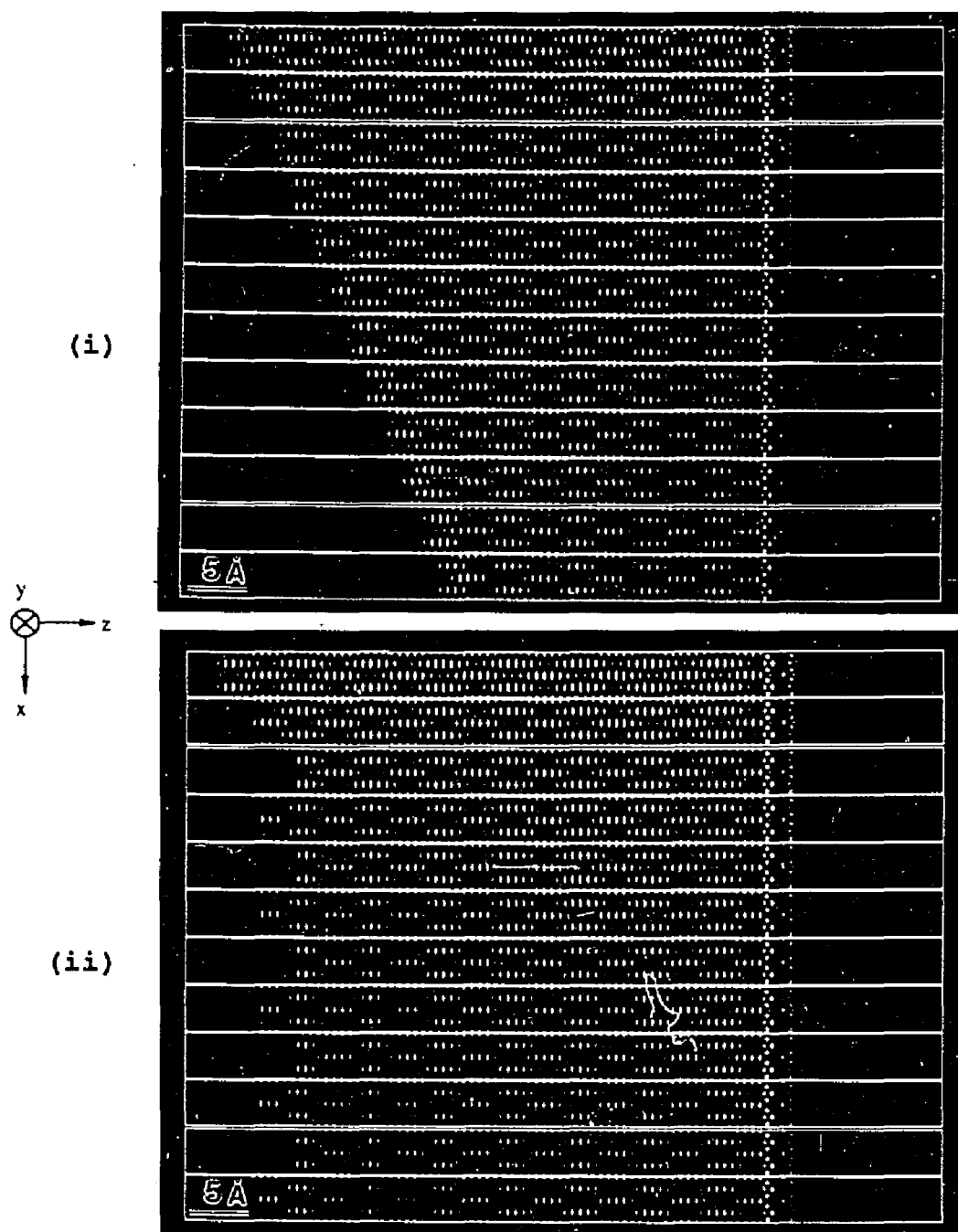
Fig.5.15. (i) Wave fields calculated without the edge patching
method. The thickness difference between two nearest slices
is 50.6Å. (ii) Wave fields calculated with the edge patching
method. The thickness difference between two nearest slices
is 101.2Å. Both (i) and (ii) were calculated for Au(001)
surface, 100keV electron, 30mRad incidence and 10% absorption.
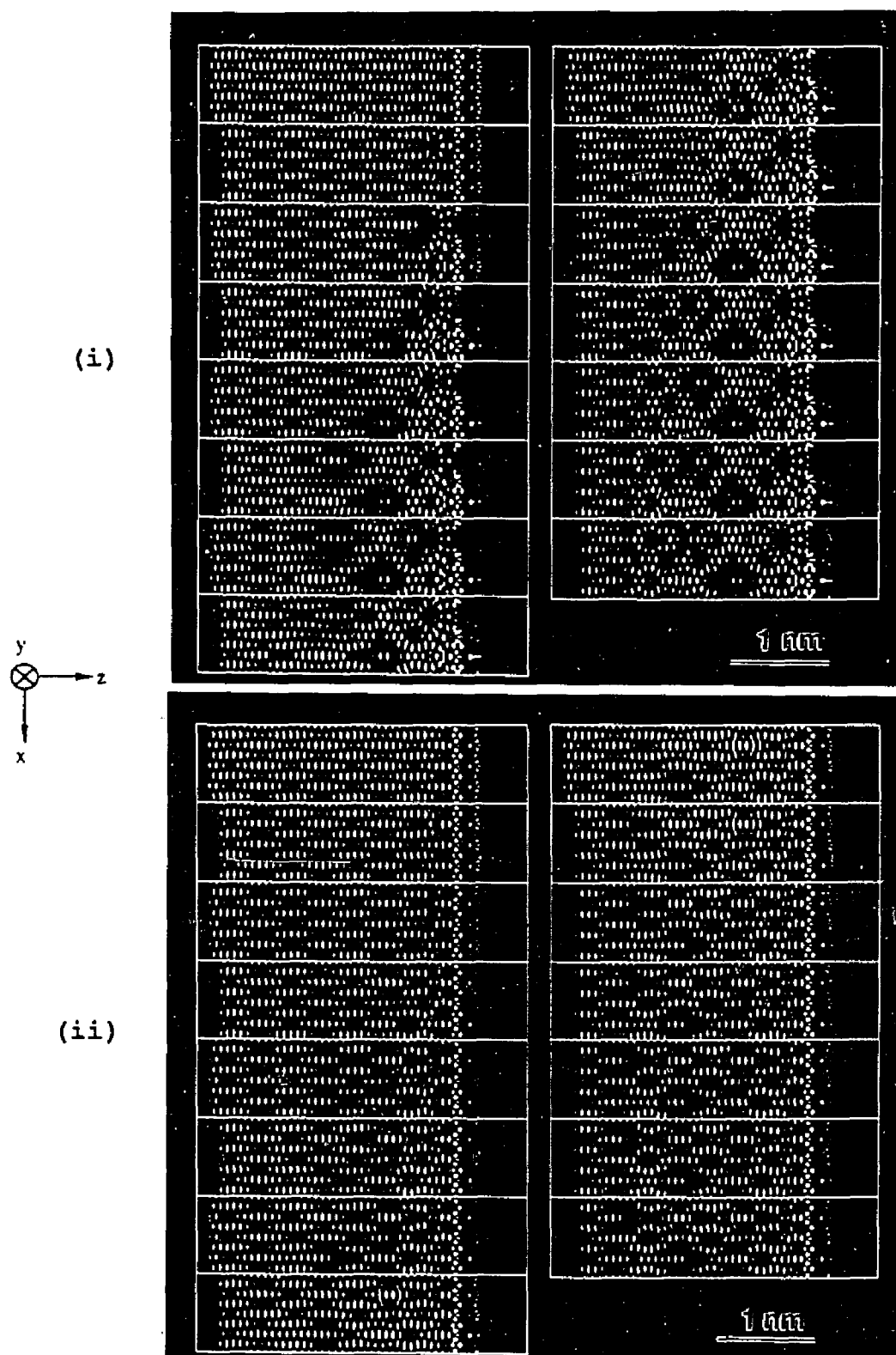
Fig.5.16. Wave fields calculated for the 2x1 Au(001) surface
(i) and the 2x1 oxygen adsorption on Au(001) surface (ii).
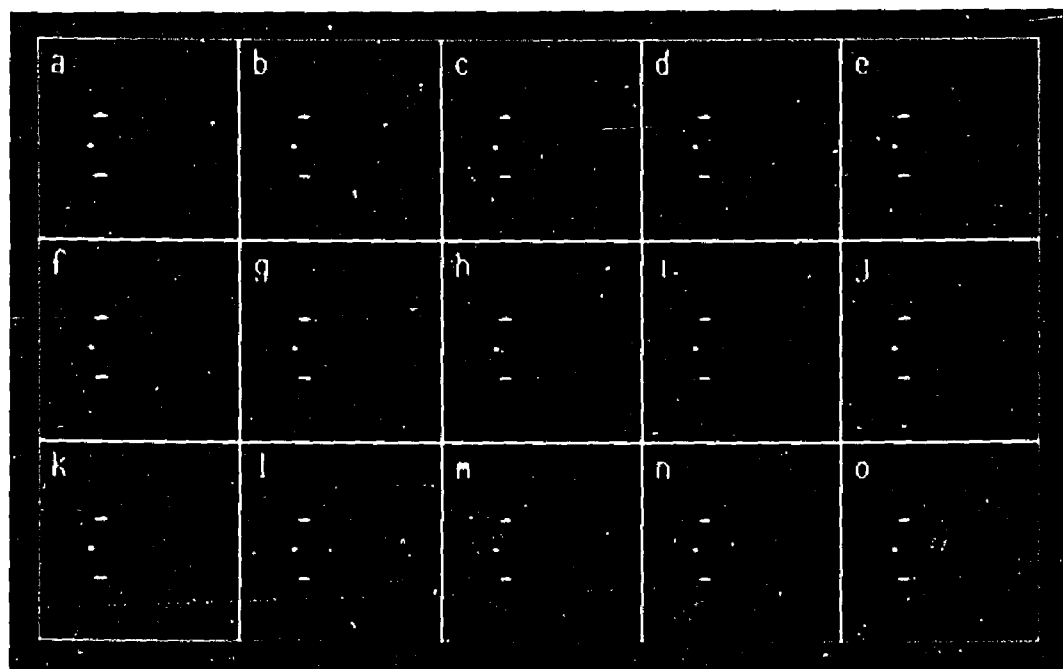
(i)
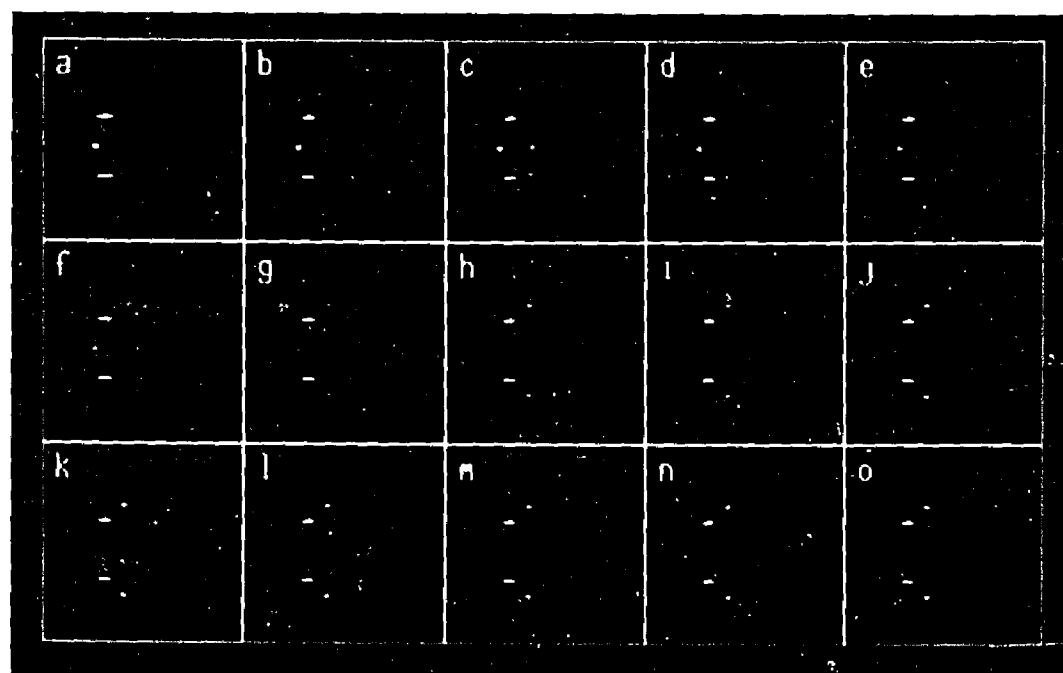
(ii)

Fig.5.17. (i) RHEED patterns corresponding to Fig.5.16(i).
(ii) RHEED patterns corresponding to Fig.5.16(ii).

2x1 Au(001) Surface Reconstruction

Slice No.: 1300   1500
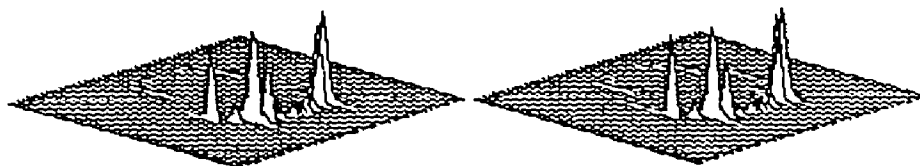
Slice No.: 1700   2050

(i)
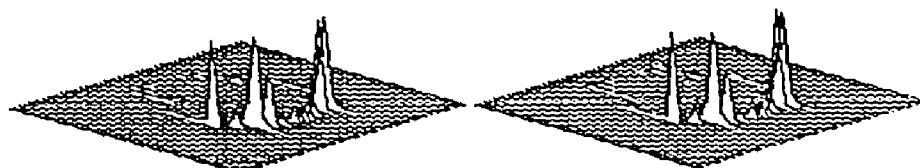
2x1 O Absorption on Au(001) Surface

Slice No.: 1300   1500
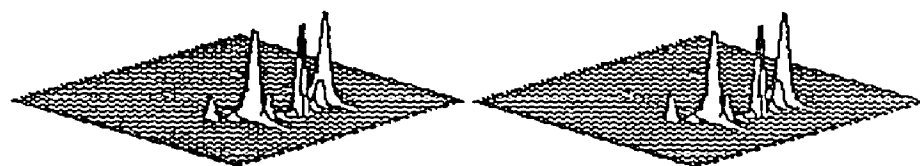
Slice No.: 1700   2050
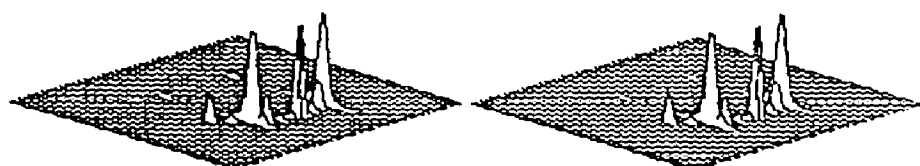
(ii)

Fig.5.18. (i) Y-modulated patterns corresponding to the last four RHEED patterns in Fig.5.17(i). (ii) Y-modulated patterns corresponding to the last four patterns in Fig.5.17(ii).

(i)

(ii)

y ⊗→z
x
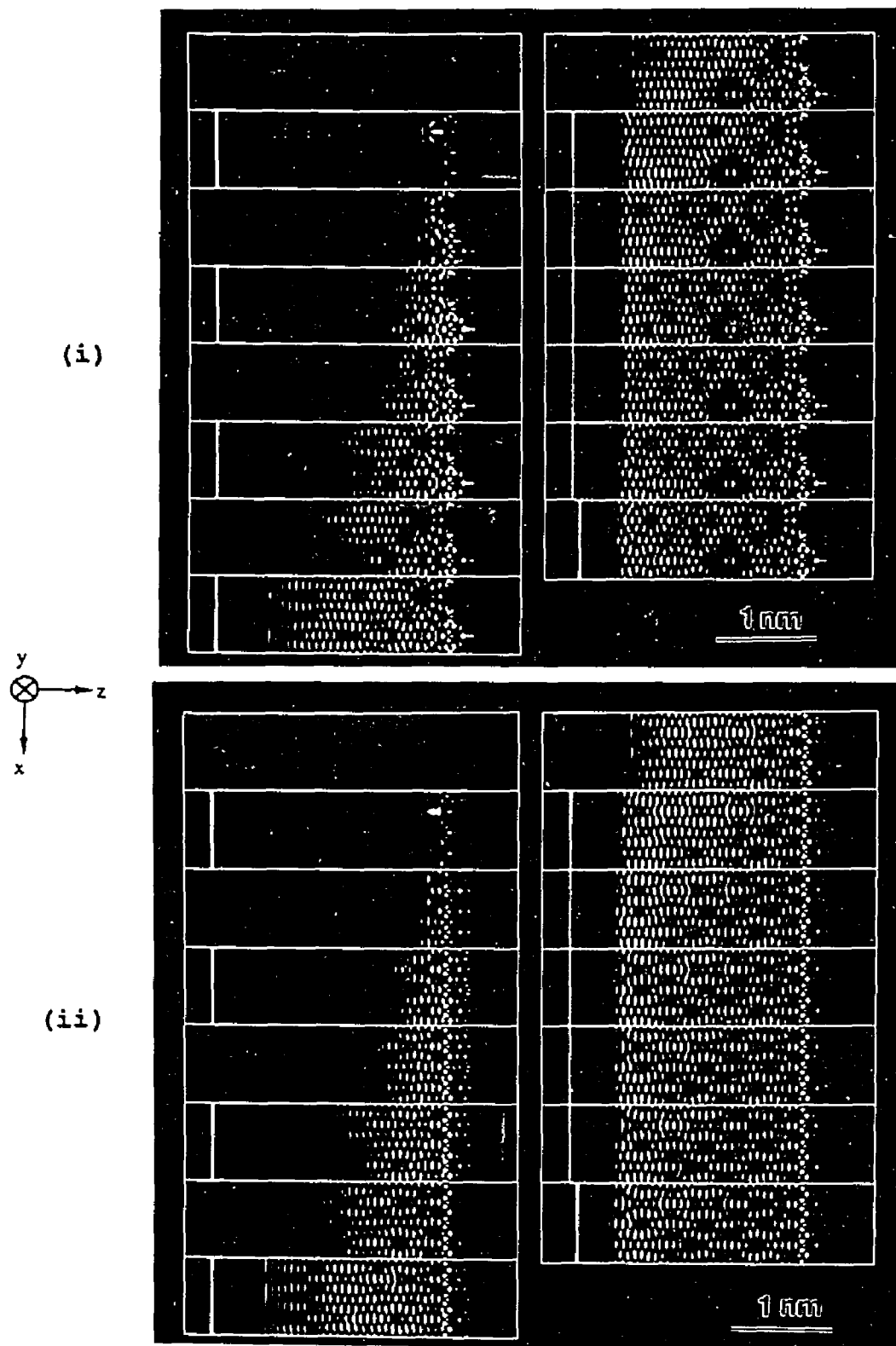
Fig.5.19. (i), (ii) Wave fields for the same conditions as those for Fig.5.16, except that the EPMO method is used here.
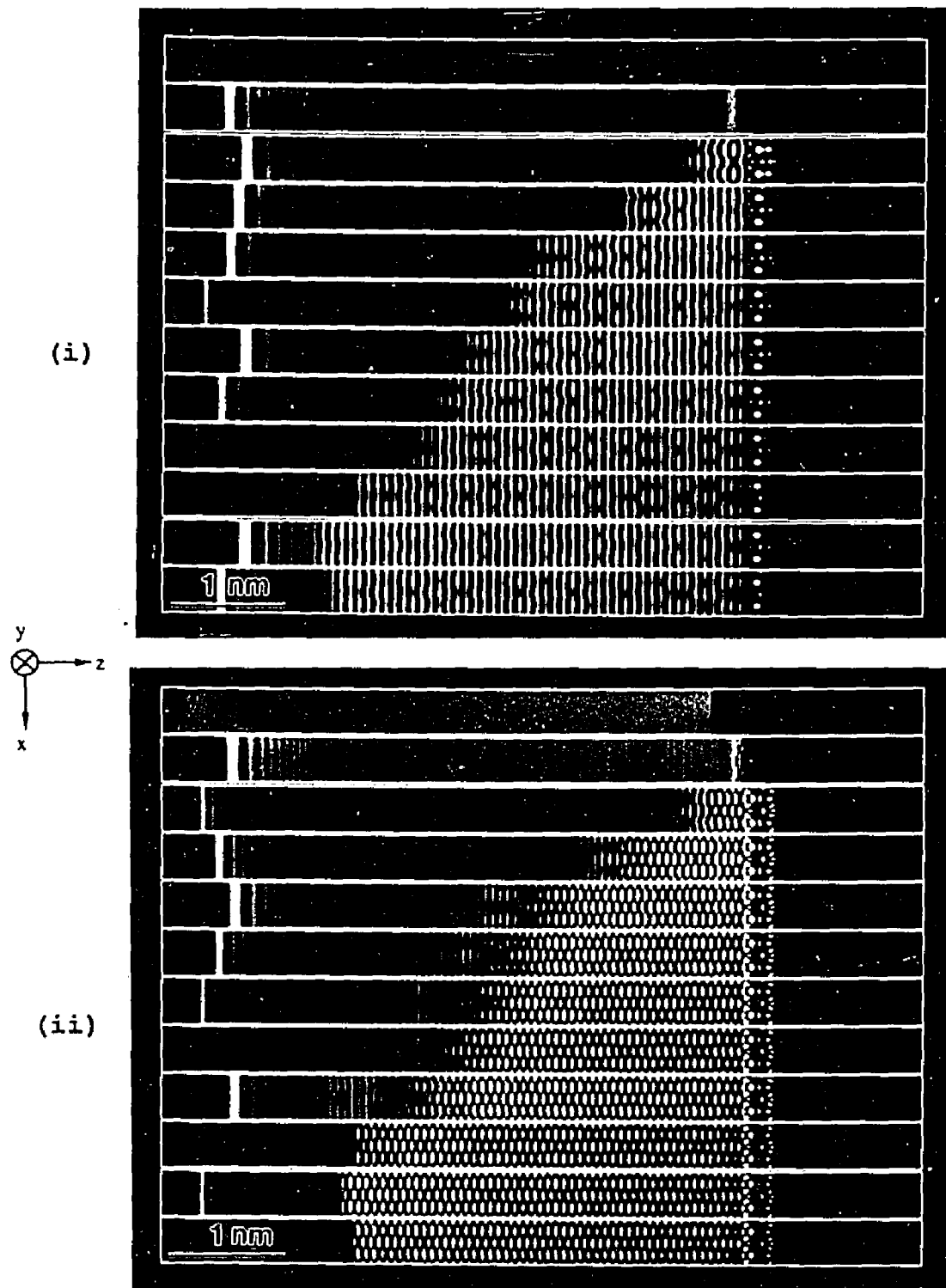
Fig.5.20. Wave fields calculated for perfect Au(001) surface, 100keV incident electrons, 10% absorption and 25mRad incidence for (i) and 30mRad incidence for (ii).

(a)   (b)
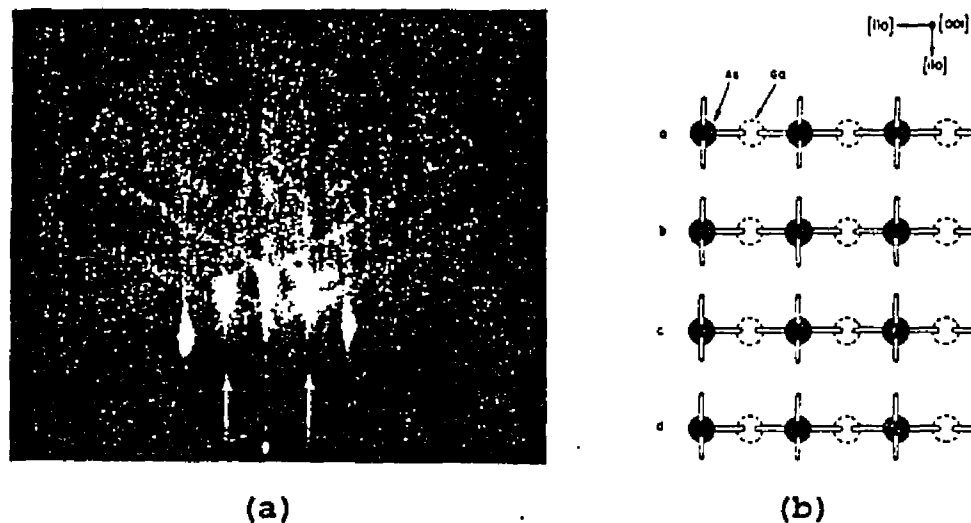
Fig.5.21. (a) Experimental RHEED pattern taken from GaAs(001) surface by Cho (1971). The incident angle is less than 1° and azimuth is along the [110] orientation. Electron energy is 40keV. (b) Schematic diagram of GaAs(001) surface view at normal incidence.
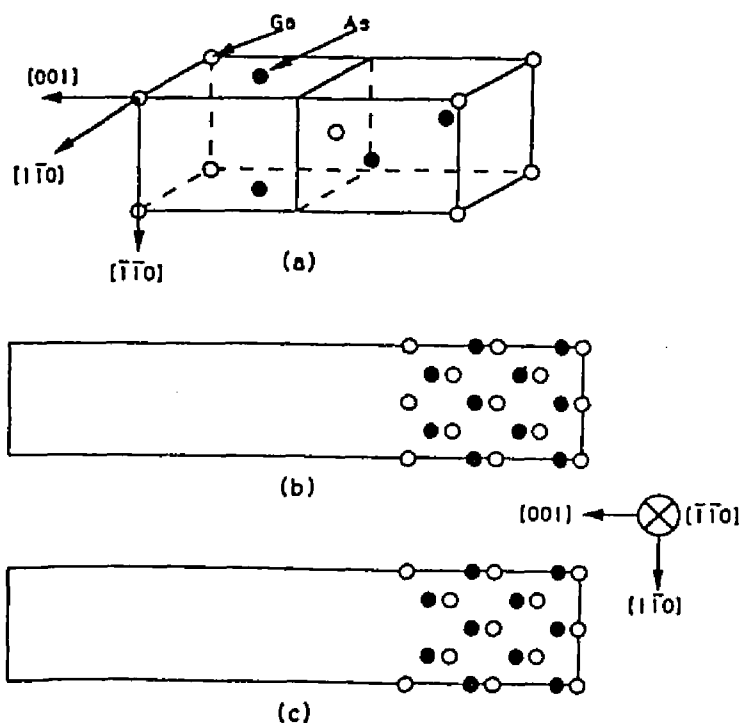
Fig.5.22. (a) Diagram of the primitive unit cell of GaAs along the [110] zone axis. Slice constructions for multislice calculations for a perfect GaAs(001) surface (b) and GaAs(001) surface with one missing row reconstruction along the incident beam.
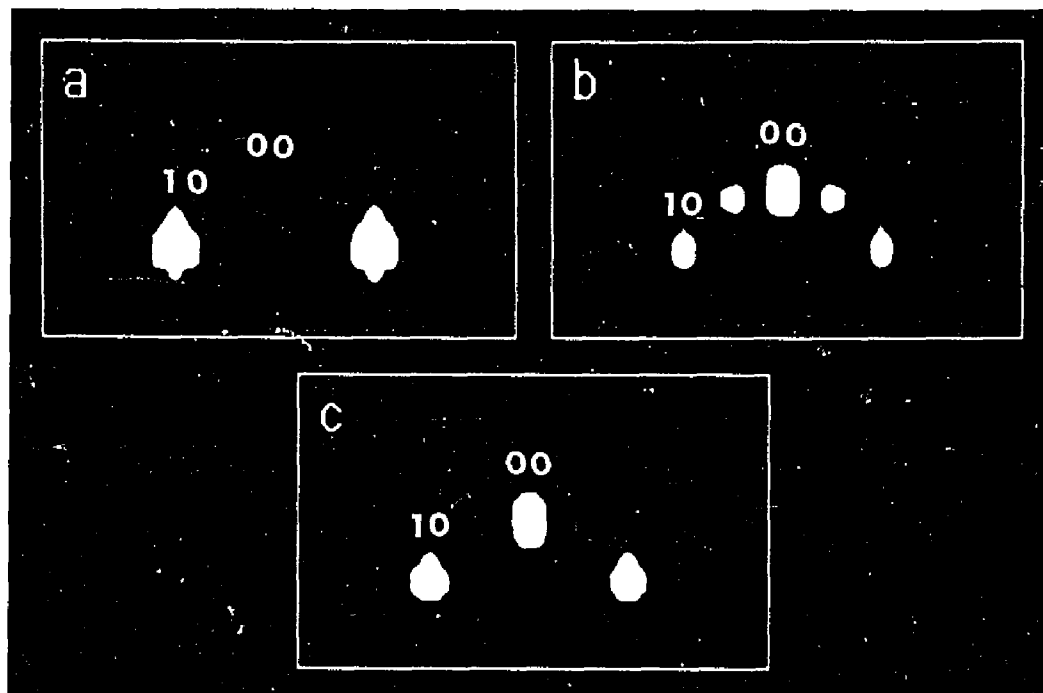
Fig.5.23. Calculated RHEED patterns for three different surface: (a) perfect GaAs(001) surface, (b) GaAs(001) surface with the 2x2 reconstruction and (c) GaAs(001) surface with the 2x8 reconstruction. Electron energy is 40keV. The incident glancing angle is 1° and the azimuth is along [110] orientation.

Chapter VI. Supplement: Ballistic surface diffusion

6.1. Introduction

To study surfaces, RHEED and RHEEM have proved to be important techniques parallel to various other approaches, such as scanning electron microscopy (SEM), high resolution electron microscopy (HREM) etc. Unfortunately, in all these beam-probe techniques, the electron beam both probes and changes the structure of a surface. In particular, two unwanted processes can occur, enhanced thermal surface diffusion due to electron beam heating and athermal surface diffusion by either an electronic mechanism [1] or by direct knock-on of a surface atom. Except for highly insulating materials, experiments (in transmission) have shown that the temperature rise due to beam heating is small, of the order of 10 degrees [2-3], and can therefore be neglected. For athermal processes, the incoming electrons can cause electronic transitions which are converted into atomic motion leading to either preferential desorption of one species [4-6], or surface diffusion [1]; electron-stimulated desorption and diffusion for which various models have been proposed [7-10]. However, a knock-on mechanism for surface diffusion has not been investigated in detail. In the following sections,

a numerical study of this process, athermal ballistic surface diffusion due to the Rutherford scattering is described. Note that this process is analogous to stimulated migration of point defects in a solid.

6.2. Model and numerical development

Ballistic surface diffusion can be divided into two steps; the initial scattering of the electrons which provides an impulse to the target atom and the actual diffusion of the atom (after the electron has left). The former is a collision process and finishes in a very short time, about 10^{-19} seconds. The latter is the dynamical motion of the scattering atoms in the surface potential, and takes place with the more leisurely time scale of thermal vibrations, i.e. 10^{-12} seconds. Our approach here is to consider first the diffusion problem for a range of different vectors for the initial atom momentum, and then later to tie in the results from these calculations of the probability that the atom will diffuse or be sputtered, with calculations of the actual initial momentum of the target (which is a function of the beam energy and direction relative to the surface).

To model the dynamical motion of surface atoms, we used a Lennard-Jones potential, with 6 rows and 20 atoms in each

row (Fig.6.1(a), (b)), taking those of gold [11] for our parameters. (A Lennard-Jones potential was used solely as a pragmatic choice to make the problem tractable). The blackened atoms in both figures are the atoms whose classical trajectories were numerically integrated. The case shown in Fig.6.1(a) models an adatom, while Fig.6.1(b) models a flat surface, and in both cases the initial velocity from the Rutherford scattering was given to the black atoms only. The approximation of reducing a 3-D problem to 2-D is based on the assumption that the surface potential well has central symmetry. A fourth order Runge-Kutta method was employed for the numerical calculations and the dynamical calculations of the trajectories of adatom or in-surface atom were performed as a function of the energy and initial displacement direction of the surface atom.

6.3. Analysis

Of interest is the critical energy when the adatom or in-surface atom just surmounts the potential barrier built up by the neighboring atoms. First, all the other atoms were assumed fixed. Fig.6.2 shows two typical trajectories of an adatom, in a) when the surface atom just surmounts the surface barrier and b) when the adatom is just reflected. Similar trajectories

were obtained for the in-surface case. Fig.6.3(a) and (b) show the critical curves of the energies for these situations; only atoms with kinetic energy above the curve will diffuse. These two curves clearly show a smooth behavior with functionality no matter how complicated the trajectories of the surface atoms are. For the adatom, the critical curve has a simple parabolic character, while the critical curve of an in-surface atom appears more complicated. This is because for the in-surface case, the movable atom is strongly interacting with its four neighboring atoms.

Similar calculations for the case in which one neighboring atom is movable were also performed for both adatom and in-surface atom. Fig.6.4(a) shows the case when the adatom is just reflected by the potential barrier, while Fig.6.4(b) shows when it just surmounts the barrier. The neighboring atom vibrates around its equilibrium position in both cases. The calculations indicated that the time required for the ballistic diffusion process of one adatom or in-surface atom is around 10^{-13}s and the time required for the kinetic energy of an adatom or in-surface atom to be transferred to its neighbors atoms is about 10^{-12}-10^{-13}s. The results showed no big change in the critical curve, and the assumption that the neighboring atoms are fixed appears to be

a reasonable approximation.

For the scattering process we applied Ruthford scattering theory using the scattering geometry shown in Fig.6.5. The energy transferred to a single surface atom by a single scattered electron is given by the equation;

$$E = E_{max} \cos^2(\theta) \tag{6.1}$$

where E_{max} is the maximum energy that the electron can transfer to the atom:

$$E_{max} = 2E_a (E_a + 2mc^2) / Mc^2 \tag{6.2}$$

where E_a is the incident energy. Substituting (6.1) into the equation for the critical curve,

$$f(\theta) = E/E_a \tag{6.3}$$

we then obtain the following relationship:

$$E_{max}/E_a = f(\theta) / \cos(180 - \theta'' - \theta) \tag{6.4}$$

Different values of θ'' represent different geometries of the surface with respect to the direction of the incident electron. The physical significance of Equation (6.4) is that the energy required for the diffusion of a surface atom is a function of the ejection angle θ and the angle between the surface and beam direction θ''. Plotting E_{max}/E_a vs θ for different θ'', we obtain a series of critical curves for E_{max} as shown in Fig.6.6(a) and (b) for the adatom and in-surface atom

cases respectively.

These curves were then used to determine the scattering angle range within which the scattered atoms can be diffused as shown in Fig.6.7. η is the value of E_{max}/E_a for the given accelerating voltage. The scattering probability of the adatom or in-surface atom is then given by:

$$M_a = \int_\Omega \sigma(\theta)\, n_a\, d\Omega(\theta) \qquad (6.5)$$

where the physical significance of M_a is the probability of one surface atom being scattered into a solid angle Ω per incident electron per second, $\sigma(\theta)$ the differential Rutherford scattering cross-section, and n the electron flux. If we substitute for the quantities in (6.5), we obtain:

$$M_a = 4\pi n_a (ZZ'e/2\mu v^2)^2 \cdot \int_{\theta_1}^{\theta_2} |\sin(\theta''+\theta)| \times$$

$$\{1+\{1+\sin^2 2(\theta''+\theta)/[m/M-\cos 2(\theta''+\theta)]^2\}^{-1/2}\}^{-2} d\theta \qquad (6.6)$$

where Z is the atomic number of surface atom after the modification for the Coulomb screening, $Z'=1$ for an electron, m the reduced mass and v the relativistic velocity of the electron. The inverse of M_a, $T_a=1/M_a$ has units of (atom.s/ST), where ST denotes the times for each atom to be scattered. Its physical significance is the time required for every atoms in

a monolayer to be displaced. The upper and lower limits, θ_1 and θ_2 are determined by the value of E_{max} which were calculated from the kinetic energy of the incident electrons.

6.4. Results

To provide some hard data, an accelerating voltage of 200keV and a current density of 1.8Å.cm^{-2} have been taken. The calculated results for different surface geometries for both adatom case and in-surface case are shown in Table 6.1. They indicate that the time required for scattering of one monolayer is about several hundred seconds for this specific voltage and metal. (Note that this value should be compared with the intrinsic thermal diffusion of the surface which is expected to be in general far faster.) The time for profile imaging position $\theta''=0$ is longer than that for other positions, indicating that the profile imaging technique is less influenced by knock-on damage.

In general, T_s is inversely proportional to the square of atomic number Z, i.e. the heavier the atom, the shorter the "sitting time" T_s. T_s is also related to the cohesive energy E_s, and larger cohesive energies make the critical curve steeper and reduce the diffusible angular range, and therefore increase T_s. The effect of the energy of incident electrons on

T_a is shown in two ways. At higher energies the relativistic electron velocity v increases, reducing the cross section for scattering and therefore increasing T_a but it also makes the diffusible angle range $\theta_1-\theta_2$ wider which reduces T_a. To some extent these two effects offset each other. At low energy (V_a <300kV), the velocity dominates, and the time required for the diffusion of one monolayer increases with accelerating voltage. At higher energies the velocity does not increase so fast (due to relativistic effects) and the diffusible range effect will dominate.

6.5. Interim discussion

The results indicate that ballistic surface diffusion is strongly dependent upon the properties of materials. There exists a threshold voltage for ballistic surface diffusion which for Au is about 135kV. One problem was encountered when the attempt was made to reconcile these results with some experimental data on the surface sputtering threshold for gold obtained by Cherns et al. [12]. The authors obtained a value of 459kV. At this voltage the maximum energy transferred to an atom is 7.22eV which is approximately twice as large as the cohesive energy. There are three possible reasons for this discrepancy. First, there may have been a contamination layer

in the experiments, so that the "sputtering threshold" might in fact represent the threshold to sputter gold through a 20Å carbon contamination layer. Alternatively, 459kV may represent the threshold due to a more complicated multi-atom sputtering process, rather than the threshold of simple sputtering. It seems quite likely that there may be more complicated damaging processes at higher voltages, both for sputtering and for athermal diffusion. A final possibility hinges on the fact that for most metals a better approximation for the pairwise potential is an oscillating pseudopotential; in this case the (classical) threshold energy will be the energy difference between the minimum and the first maximum of the pseudopotential, which could exceed the binding energy. It would clearly be of interest to see the results of careful electron microscope imaging work at different temperatures.

One feature of the results to note is that the surface geometry has a strong effect on ballistic surface diffusion and the ballistic diffusion for a profile surface appears to be the weakest, whereas the prospect is clearly not so good for plan view imaging, particularly of the exit surface of specimens where we can expect fairly severe damage.

Table 6.1

$\theta"$	$\theta_1-\theta_2$		M_a (ST/atom.s$\times 10^{-3}$)		T_a (atom.s/ST)	
	adatom	in-surf.	adatom	in-surf.	adatom	in-surf.
90	0.75-2.35	1.20-1.90	13.88	1.48	72	675
75	1.71-2.58	1.60-2.10	5.55	0.71	180	1401
45	1.82-2.96	2.07-2.95	4.88	3.04	205	329
0	2.45-3.10	2.7-3.14	4.23	1.26	236	793

Table 6.1. Ballistic surface diffusion data calculated for different surface geometries for both adatom case and in-surface case.
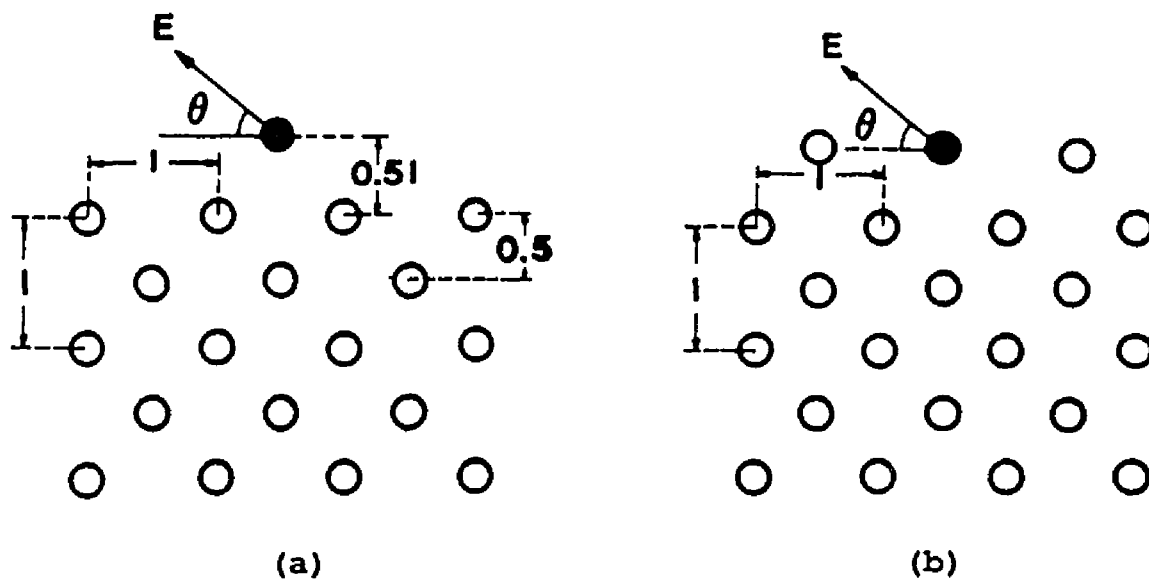
Fig.6.1. The arrangement of the gold atoms in 2-D lattice for the dynamical calculation a) in the case of the surface adatom and b) in the case of the in-surface atom.
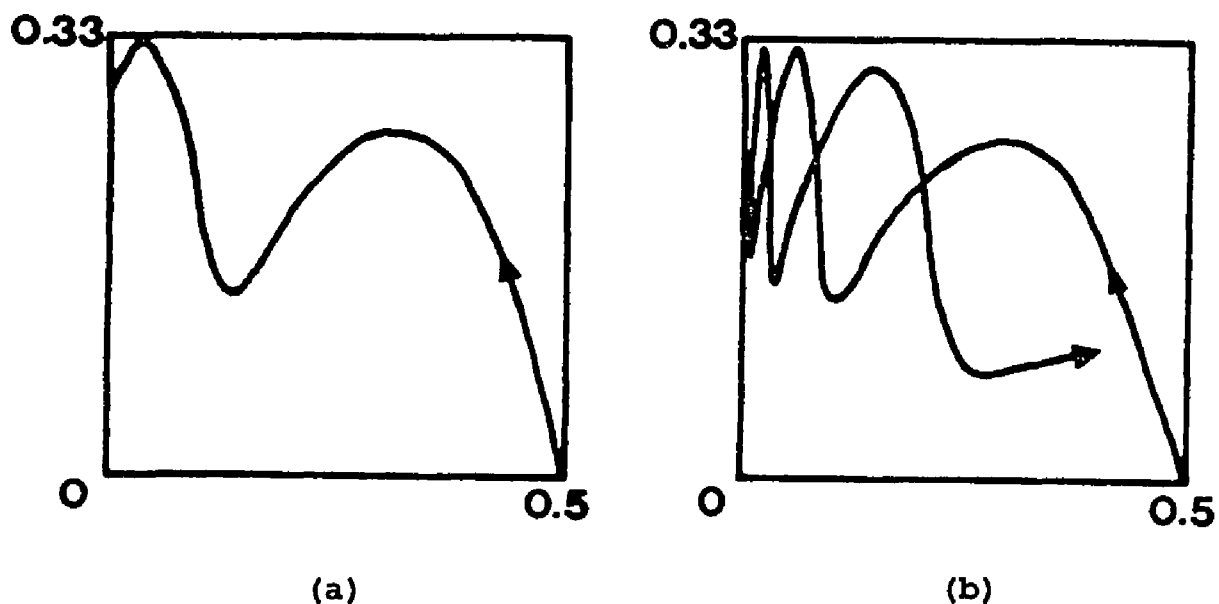
Fig.6.2. The trajectories of an adatom a) when the atom just surmounts the surface barrier and b) when the adatom is just reflected by the barrier in the case of fixing other atoms.
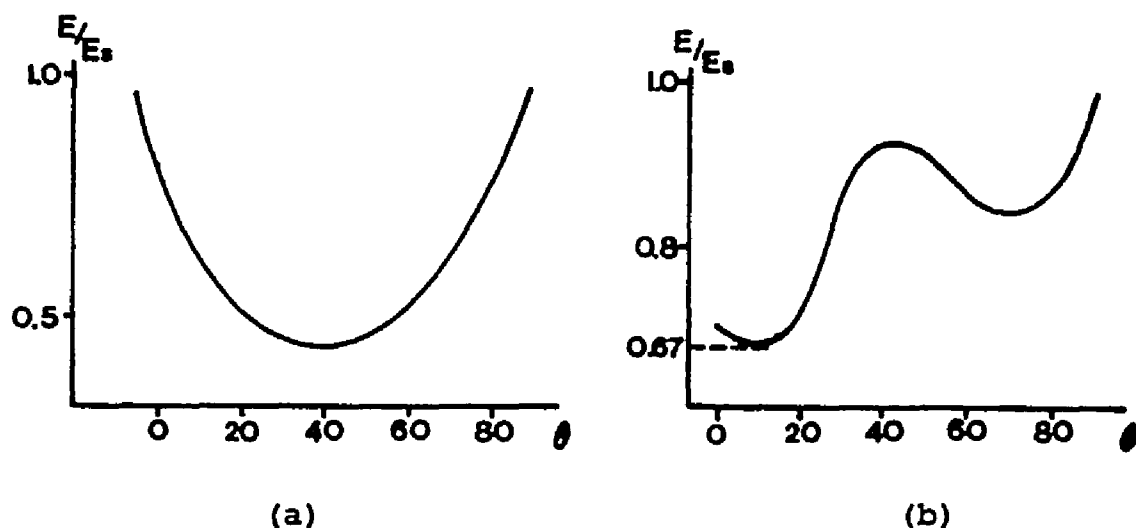
Fig.6.3. The curves of the critical energy for the surface atom surmounting the surface potential barrier as the function of ejection angle of the excited atom a) in the case of adatom on the surface and b) in the case of the in-surface atom.
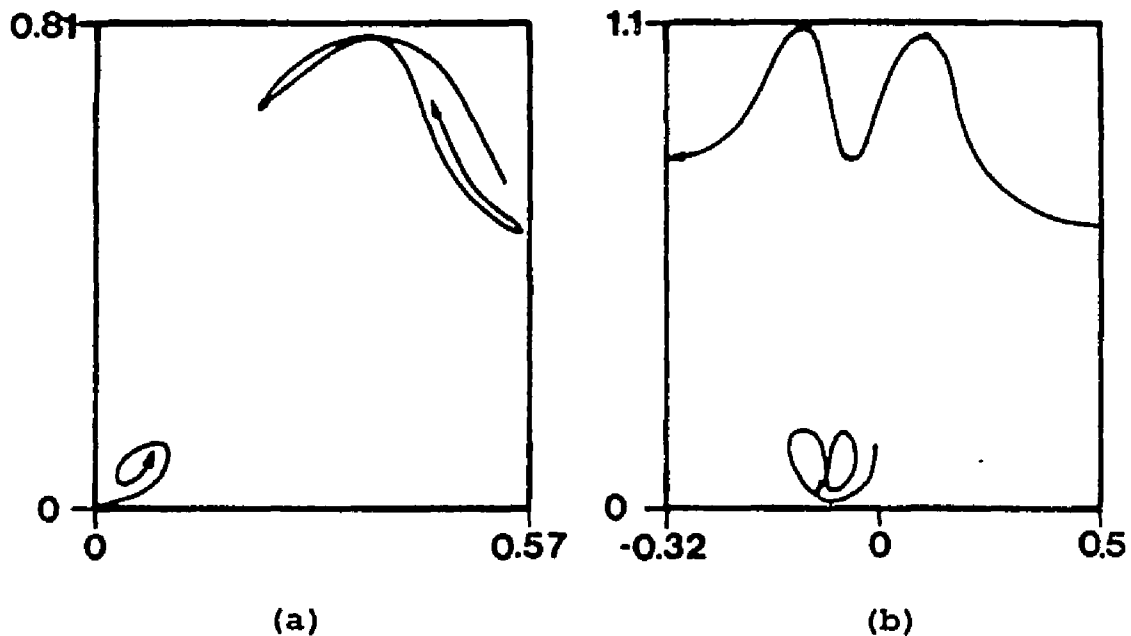
Fig.6.4. The trajectories of an adatom in the case that one neighboring atom is movable, a) when the adatom is just reflected by the surface barrier and b) when the adatom just surmounts the surface barrier.
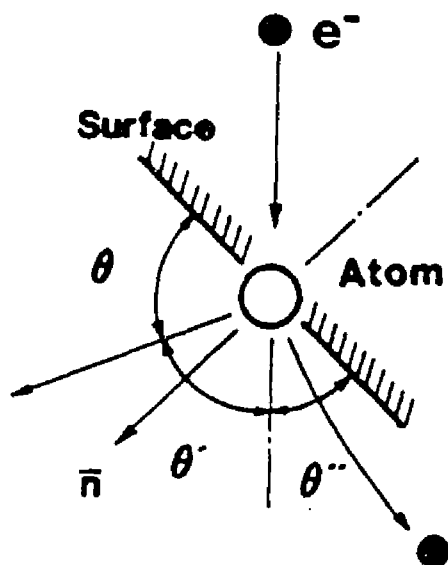
Fig.6.5. The scattering geometry between the incident high energy electron and the surface atom.

Fig.6.6   (a)

(b)
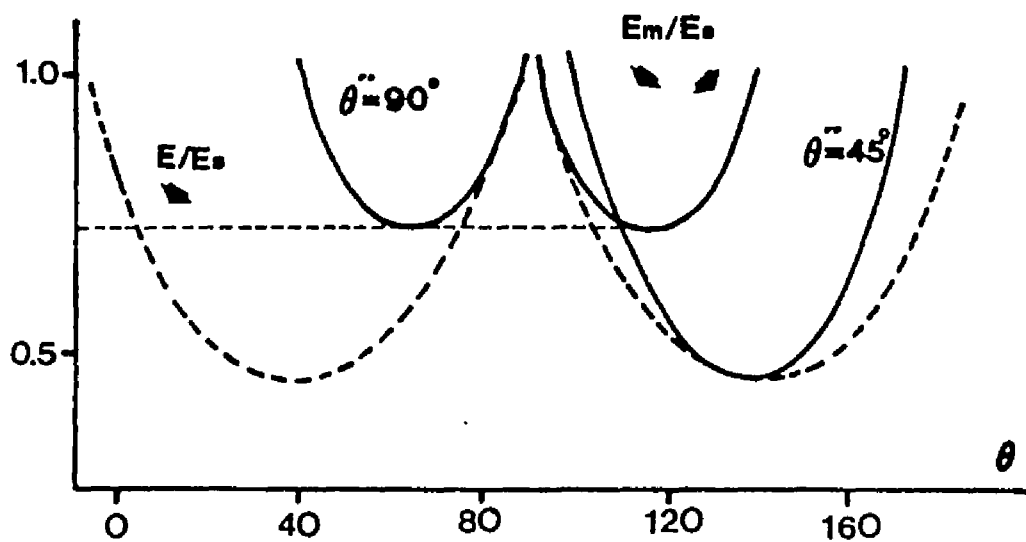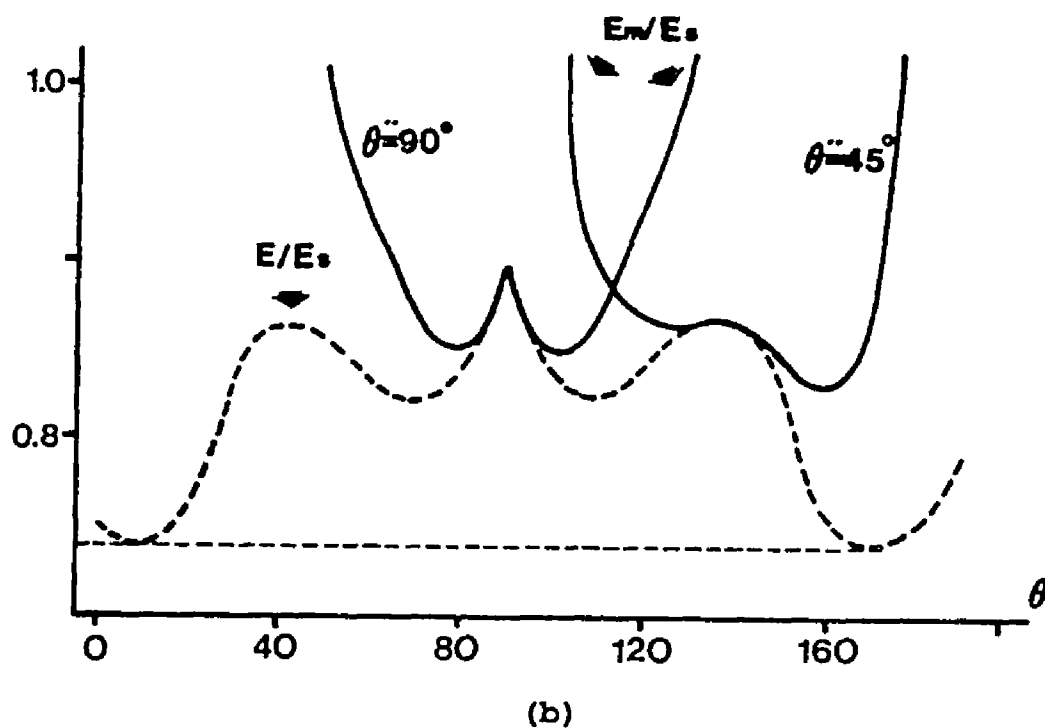
Fig.6.6. The curves of the minimum incident energy required for diffusing a) an adatom and b) an in-surface atom as the function of the ejection angle of the atom for the different angles between the surface and the incident momentum.
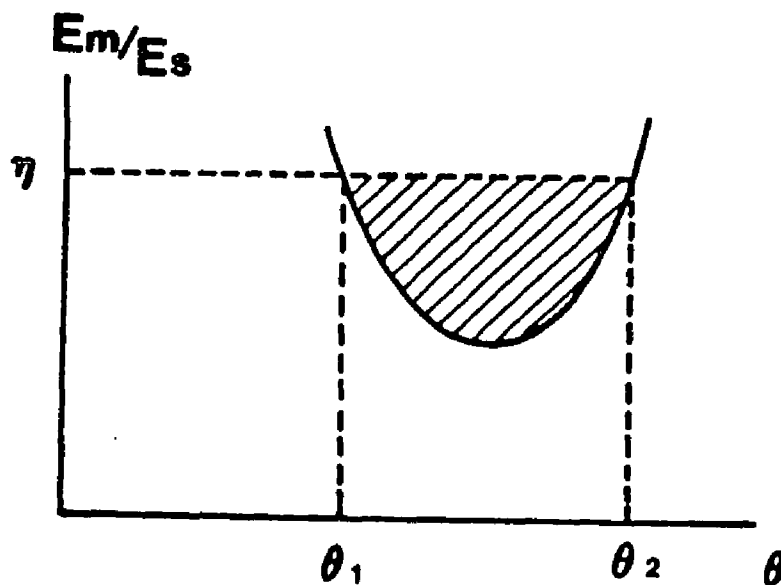
Fig.6.7. The illustration of determining the diffusible angle range $\theta_1-\theta_2$.

Chapter VII. <u>Conclusion</u>

High energy electron reflection (HEER) is an important field in surface science and consists of three major branches; RHEED, RHEEM and RHEEL (or EEL). All of them, specially RHEED and RHEEL have experienced development over many decades both experimentally and theoretically. Regardless of stagnation in the theoretical development in this field, the value of these techniques has been confirmed in surface science. However, further exploitation relies on further developments in theory.

A major obstacle to the theoretical development of high energy electron reflection--the confusion around the wave points in the "band gap" and the nature of evanescent waves in the Bragg case has been removed by introducing the concept of current flow and a new boundary condition. This, I believe, will make the Bloch wave method again play an important role for the understanding of the physics of electron reflection as it does for electron transmission. However, the limits of the method--low computation speed and lack of flexibility for the simulations of various surface phenomena will not vanish because of its solid physical foundation and various alternative approaches still need to be developed.

The bridge between the Bloch wave method and multislice

creates a new computation method called "the BMCR method" (Bloch wave + Multislice Combined for Reflection), but also implicitly indicated the possibility of establishing bridges between various alternative computation methods in electron reflection and making the advantages of different methods work together. From a theoretical viewpoint, it is important that consistency and the conditions for consistency between different methods can provide a mutual proof of each one and a combination of them. Apparently, the Bloch wave method can play the role of a "calibration standard" for various alternatives, although it may not very conveniently employed for reconstructed or related surfaces.

A major obstacle to the multislice calculation in the Bragg case, "edge effects", has been removed and an infinitely convergent solution for an arbitrary surface for HEER has been obtained by the edge patching method (the EPMO method).

However, the newly developed Bloch wave approach in the Bragg case, the BMCR method and the edge patching method (the EPMO method) should only be considered as the means to get closer to the true solution rather than the solution itself. From my point of view, two very fundamental and basic problems in high energy electron reflection remained unanswered, or incompletely answered, and merit further study:

i) the source of two dimensional diffraction patterns observed in RHEED.

ii) the true source of "electron surface resonance". At present, the term "electron surface resonance" still means more as an experimental fact rather than as a physical concept. These two problems may be the keys to the door of informative HEER.

More generally, further studies in this field can be carried out along the following suggested directions;

i) Pursuing deeper understanding of the physics of high energy electron reflection; the nature of the Bloch waves in the Bragg case, the mechanism of current flow and the effects of surface potential etc. using the newly developed Bloch wave method in the Bragg case and exploring the application of the method to experimental analyses.

ii) Pursuing more applications of the BMCR method to experiments.

iii) Examining the consistency between various alternative computation methods in this field to verify their valid conditions and find possibility of combining them together.

iv) Studying the effects of inelastic scattering on electron diffraction in the Bragg case and the theory of inelastic electron diffraction in the Bragg case.

v) Studying the way of incorporating the theory of electron diffraction in the Bragg case with the theory of electron spectroscopy.

Without doubt, any progress made in these directions can significantly improve the understanding of HEER.

REFERENCES

References for Chapter I

[1] Ruska, E. (1933). "Images of surfaces which reflect electrons in the electron microscope", Z. Phys. 83, 492-497

[2] Nishikawa, S. and Kikuchi, S. (1928). "Diffraction of cathode rays by mica", Nature, 121, 1019-1020

[3] Nishikawa, S. and Kikuchi, S. (1928). "Diffraction of cathode rays by calcite", Nature, 122, 726

[4] Marsh, J. B. and Fransworth, H. E. (1964). "Low-energy electron diffraction studies of (100) and (111) surfaces of semiconducting diamond", Surface Sci. 1, 3-21

[5] McRae, A. U. (1964). "Adsorption of oxygen on the (111), (100) and (110) surfaces of clean nickel", Surface Sci. 1, 319-348

[6] Telieps, W. and Bauer, E. (1985). " An analytical reflection and emission UHV surface electron microscope", Ultramicroscopy, 17, 57-66

[7] Harris, J. J., Joyce, B. A. and Dobson, P. J. (1981). "Oscillations in the surface structure of Sn-doped GaAs during growth by MBE", Surface Sci. 103, L90-96

[8] Wood, C. E. C. (1981). "RED intensity oscillations during MBE of GaAs", Surface Sci. 108, L441-443

[9] Harris, J. J., Joyce, B. A. and Dobson, P. J. (1981). "Comments on RED intensity oscillations during MBE of GaAs", Surface Sci. 108, L444-446

[10] Cowley, J. M. and Hojlund Nielsen, P. E. (1975). "Magnification variations in reflection microscopy using diffracted beams", Ultramicroscopy, 1, 145-150

[11] Hojlund Nielsen, P. E. and Cowley, J. M. (1976). "Surface imaging using diffracted electrons", Surface Sci. 54, 340-354

[12] Neave, J. H. and Joyce, B. A. (1983). "Dynamics of film growth of GaAs by MBE from RHEED observation", Appl. Phys. A31, 1-8

[13] Van Hove, J. M., Lent, C. S., Pukite, P. R. and Cohen, P. I. (1983). "Damped oscillations in reflection high energy electron diffraction during GaAs MBE", J. Vac., Sci. Technol. B1(3), 741-746

[14] Ino, S. (1977). "Some new techniques in reflection high energy electron diffraction (RHEED) application to surface structure studies", Jpn. J. Appl. Phys. 16, 891-908

[15] Miyake, S and Hayakawa, K. (1970). "Resonance effects in low and high energy electron diffraction by crystals", Acta Cryst. A26, 60-70

[16] Shimizu, N., Tanishiro, T., Takayangi, K. and Yagi, K. (1987). "On the vacancy formation and diffusion on the Si(111)7x7 surfaces under exposures of low oxygen pressure studies by in situ reflection electron microscopy", Surface Sci. 191, 28-44

[17] Cowley, J. M. (1982). "Energy loss of fast electrons at crystal surfaces", Phys. Rev. B25, 1401-1404

[18] Wang, Z. L. and Cowley, J. M. (1988). "REELS and RHEED characterization of electron resonance channeling in crystal surfaces", Ultramicroscopy, 26, 233-238

[19] Borries, B. v. (1940). "Sublichtmikroskopische Auflosungenbei der Abbildung von Obserflachen im Ubermikroskop", Z. Phys. 116, 370-379

[20] Cossleft, V. E. (1952). "Electron microscopy of solid surfaces", Nature, 170, 861-863

[21] Fert, C. and Saport, R. (1952). "Electron microscopy by reflection", Acad. Sci. Paris, 235, 1490-1492

[22] Menter, J. W. (1953). "Direct observation of solid surfaces at high resolution by reflection electron microscopy", J. of Photo. Sci. 1, 12-20

[23] Haine M. E. and Hirst, W. (1953). "The adaptation of an

electron microscope for reflection and some observations on image formation", Brit. J. Appl. Phys. 4, 239-244

[24] Page, D. H. (1960). "The chromatic field aberrations and their correction in a three lens reflexion electron microscope", Brit. J. Appl. Phys. 9, 268-270

[25] Osakabe, N., Tanishiro Y., Yagi, K. and Honjo, G. (1980). "Reflection electron microscopy by clean and gold deposited (111) silicon surfaces", Surface Sci. 97, 393-408

[26] Osakabe, N., Tanishiro, Y., Yagi, K. and Honjo, G. (1981). "Direct observation of the phase transition between the (7x7) and (1x1) structures of clean (111) silicon surfaces", Surface Sci. 109, 353-366

[27] Osakabe, N., Tanishiro, Y., Yagi, K. and Honjo, G. (1981). "Image contrast of dislocations and atomic steps on (111) silicon surface in reflection electron microscopy", Surface Sci. 102, 424-442

[28] Hsu, T. (1983). "Reflection electron microscopy (REM) of vicinal surfaces of fcc metals", Ultramicroscopy, 11, 167-172

[29] Hsu, T. and Cowley, J. M. (1983). "Reflection electron microscopy (REM) of fcc metals", Ultramicroscopy, 11, 239-250

[30] Hsu, T., Iijima, S. and Cowley, J. M. (1984). "Atomic and other structures of cleaved GaAs(110) surfaces", Surface Sci. 137, 849-856

[31] De Cooman, B. C., Kuesters, K. H., Carter, C. B., Hsu, T. and Wicks, G. (1984). "Reflection electron microscopy of epilayers grown by molecular beam epitaxy", Phil. Mag. 50, 849-856

[32] Uchida, Y., Jager, J. and Lehmpfuhl, G. (1984). "Direct imaging of atomic steps in reflection electron microscopy", Ultramicroscopy, 13, 325-328

[33] Uchida, Y., Lehmpfuhl, G. and Jager, J. (1984). "Observation of surface treatments on single crystals by reflection electron microscopy", Ultramicroscopy, 15,

119-130

[34] Shimizu, N., Tanishiro, Y., Kobayshi, K., Takaynagi, K. and Yagi, K. (1985). "Reflection electron microscope study of the initial stages of oxidation of Si(111)7x7 surfaces", Ultramicroscopy, 18, 453-462

[35] Yao, N. and Cowley, J. M. (1988). "Characterization of double contours and twin images in REM", Proceeding of the 46th annual meeting of EMSA, 686-687

[36] Uchida, Y. and Lehmpfuhl, G. (1987). "Observation of double contours of monatomic steps on single crystal surfaces in reflection electron microscopy", Ultramicroscopy, 23, 53-60

[37] Lehmpfuhl, G. and Uchida, Y. (1988). "Electron diffraction conditions for surface imaging", Ultramicroscopy, 26, 177-188

[38] Uchida, Y. and Lehmpfuhl, G. (1987). "Reflection electron microscopic observation of crystal surfaces on a Si cylindrical specimen", Surface Sci. 188, 364-377

[39] Yamamoto, Y. and Spence, J. C. H. (1983). "Surface imaging of III-V semiconductors by reflection electron microscopy and inner potential measurements", Thin Solid Film, 104, 43-55

[40] Marks, L. D., (1983). "Direct imaging of carbon-covered and clean gold(110) surfaces", Phys. Rev. Lett. 51, 1000-1002

[41] Marks, L. D. et al. (1985). "Direct atomic imaging of solid surfaces. IV. Dislocation on Au(100)", Surface Sci. 157, L367-372

[42] Kang, Z. C. (1982). "The surface of diamond studies by TEM and STEM reflection diffraction imaging", J. Microsc. Spectrosc. Electron, 7(1), 33-39

[43] Yagi, K. (1987). "Reflection electron microscopy", J. Appl. Cryst. 20, 147-160

[44] Hsu, T. and Iijima, S. (1985). "Reflection electron microscopy studies of techniques crystal lattice

termination at surfaces", Springer Ser. in Surface Sci. 2, 55-59

[45] Hsu, T. and Iijima, S. (1982). "Reflection electron microscopy (REM) of surface steps and dislocations on GaAs (110)", Electron microscopy 1982, 1, 301-303

[46] Iijima, S. and Hsu, T. (1982). "Application of electron microscopy to material science", Electron microscopy 1982, 1, 293-294

[47] Petroff, P. M. (1984). "Electron microscopy of semiconductors reconstructed surfaces", Mater. Res. Soc. Symp. Proc. 31,117-125

[48] Griffith, J. E. (1986). Proceeding of 44th annual meeting of EMSA, 640-641

[49] Yamamoto, N. and Muto, S. (1984). "Direct observation of $Al_xGa_{1-x}As$/GaAs superlattice by REM", Jpn. J. Appl. Phys. 23, L806-L808

[50] Cowley, J. M. and Kang Z. C. (1983). "STEM imaging and analysis of surfaces", Ultramicroscopy, 11, 131-140

[51] Takayanaki, K. (1982). "High resolution surface study by in-situ UHV transmission electron microscopy", Ultramicroscopy, 8, 145-161

[52] Tanishiro Y., Takayanagi, K., Kobayashi, K., Yagi, K. (1981). "In-situ reflection electron microscope study of metal deposition on clean Si(111) surface", Acta Cryst. A37(Sup), C-300

[53] Finch, G. I. and Wilman, H. (1937). "Study of surface structure by electron diffraction", Ergeb. Exakt. Naturw. 16, 353-436

[54] Miyake, S. (1937). "Study of oxide films on metal surface with cathode-ray diffraction. II. Iron, chromium, nickel and their alloy", Sci. Pap. Inst. Phys. Chem. Res. (Tokyo), 31, 161-173; ibid. "Electron diffraction by oxides of antimony formed on stibnate", 34, 565-583

[55] Uyeda, R. (1940). "Cathode-ray investigation of thin layers formed on some single crystals. III. Silver film

on sulfide crystals", Proc. Phys-Math. Soc. Japan, 22, 1023-1033

[56] Kainuma, Y. and Uyeda, R. (1950). "On the structure of adsorbed organic long-chain molecules on the cleavage surface of molybdenite", J. Phys. Soc. Japan, 5, 199-200

[57] Trepte, L., Manzel-Kopp, C. and Manzel, E. (1967). Surface Sci. 8, 223-232

[58] Sewell, P. B., Cohen, M. (1965). "observation of gas adsorption phenomena by reflection high-energy electron diffraction", Appl. Phys. Lett., 7, 32-34

[59] Cho, A. Y. (1971). "GaAs epitaxy by a molecular beam method: observation of surface structure", J. Appl. Phys. 42, 2074-2081

[60] Menadue, J. F. (1972). "Si(111) surface structures by glancing incidence high-energy electron diffraction", Acta Cryst. A28, 1-11

[61] Henderson, R. C. and Polito, W. J. (1969). "Reflection high energy electron diffraction of silicon fractional order structures", Surface Sci. 14, 473-477

[62] Henderson, R. C. and Polito, W. J. and Simpson, J. (1970). "Observation of SiC with Si(111) surface investigated by RHEED", Appl. Phys. Lett., 16, 15-18

[63] Radi, G. (1970). "Complex lattice potential in electron diffraction calculated for a number of crystals", Acta Cryst. A26, 41-56

[64] Gotoh, Y. and Ino, S. (1978). "Surface structure of Ag on Si(111) surface investigated by RHEED", Jpn. J. Appl. Phys. 17, 2097-2109

[65] Ino, S. (1980). "An investigation of the Si(111)7x7 surface structure by RHEED", Jpn. J. Appl. Phys. 19, 1277-1290

[66] Houzay, F., Moison, J. M. and Bensoussan, M. (1984). "Aluminum growth on (100) indium phosphide", J. Vac. Sci. Technol. B3, 756-759

[67] Houzay, F., Heoc, P., Bensoussan M. and Barthe, F.

(1985). "The interface between(100) InP and epitaxially grown Al", J. Vac. Sci. Technol. B3, 1212-1216

[68] Bertrand, O., Floquet, N. and Jacquot, D. (1985). "The crystallographic shear planes of the non-stoichiometric molybdenum oxides as revealed by RHEED investigation from the $Mo_{18}O_{52}$(100) surface", Surface Sci., 164, 305-319

[69] Pukite, P. R. and Cohen, P. I. (1987). "Multilayer steps formation after As adsorption on Si(100): nucleation of GaAs on vicinal Si", Appl. Phys. Lett. 50, 1739-1741

[70] Van Hove, J. M. and Cohen, J. M. (1981). "Development of steps on GaAs during molecular beam epitaxy", J. Vac. Sci. Technol., 20(3), 726-729

[71] Cohen, P. I., Pukite, P. R., Van Hove, J. M. and Lent, C. S. (1986). "Reflection high energy electron diffraction studies of epitaxial growth on semiconductor surface", J. Vac. Sci. Technol. A4(3), 1251-1258

[72] Aurts, J., Gerits, W. M. and Larsen, P. K. (1986). "Observation on intensity oscillations in reflection high-energy electron diffraction during epitaxial growth of Si(001) and Ge(001)", Appl. Phys. Lett. 48, 931-933

[73] Pukite, P. R., Van Hove, J. M. and Cohen, P. I. (1983). "Sensitive reflection high-energy electron diffraction measurement of the local misorientation of vicinal GaAs surfaces", Appl. Phys. Lett. 44, 456-458

[74] Bethe, H. (1928). "Theorie der Beugung von Elektronen an Kristallen", Ann. Phys. 87, 55-129

[75] Ashcroft N. W. and Mermin, N. D. (1975). Solid State Physics, p138

[76] Miyake, S., Kohra, K. and Takagi, M. (1954). "The nature of the specular reflection of electrons from a crystal surface", Acta Cryst. 7, 393-401

[77] Kohra, K., Moliere, K., Nakano, S. and Ariyama, M. (1962). "Anomalous intensity of mirror reflection from the surface of a single crystal", Jpn. J. Phys Soc. 17(Sup.) B-II, 82-85

[78] Kawamura, T., Ohkawa, Y. and Miyake, S. (1976). "The temperature effect and surface state resonance in medium energy electron diffraction by crystal", Jpn. J. Phys. Soc. 40, 226-232

[79] Colella, R. (1972). "N-beam dynamical diffraction of high-energy electrons at glancing incidence, general theory and computation methods", Acta Cryst. A28, 11-15

[80] Colella, R. and Menadue, J. F. (1972). "Comparison of experimental and n-beam calculated intensities for glancing incidence high-energy electron diffraction", Acta Cryst. A28, 16-22

[81] Moon, A. R. (1972). "Calculation of reflected intensities for medium and high energy electron diffraction", Z. Naturforsch, 27a, 390-395

[82] Britze, K. and Meyer-Ehmsen, G. (1978). "High energy electron diffraction at Si(001) surfaces", Surface Sci., 77, 131-141

[83] Darwin, C. G. (1914). "Theorie dur dispersion, reflection und brechung", Phil. Mag. 27, 315-333, 675-690

[84] Maksym, P. A. and Beeby, J. L. (1981). "A theory of RHEED", Surface Sci. 110, 423-436

[85] Sturkey, L. (1962). "The calculation of electron diffraction intensities" Proc. Phys. Soci. 80, 321-254

[86] Ichimiya, A. (1983). "Many-beam calculation of reflection high energy electron diffraction (RHEED) intensities by the multi-slice method", Jpn, J. Appl. Phys. 22, 176-180

[87] Maksym, P. A. and Beeby, J. L. (1982). "Reflection high energy diffraction by the Ag(001), Ag(110) and Ag(111) surfaces", Appl. Surface Sci., 11/12, 663-676

[88] Maksym, P. A. and Beeby, J. L. (1984). "Calculation of MEED intensities in the 5-10keV electron energy range", Surface Sci. 140, 77-84

[89] Maksym, P. A. (1985). "Analysis of intensity data for RHEED by the MgO(001) surface", Surface Sci. 149, 157-174

[90] Peng, L. M. and Cowley, J. M. (1986). "Dynamical diffraction calculations for RHEED and REM", Acta Cryst. A42, 545-552

[91] Peng, L. M. and Cowley, J. M. (1988). "A multislice approach to the RHEED and REM calculation", Surface Sci. 199, 609-622

[92] Cowley, J. M. and Moodie, A. F. (1957). "The scattering of electron by atoms and crystals. I. A new theoretical approach", Acta Cryst. 10, 609-619

[93] Cowley, J. M. and Moodie, A. F. (1959). "The scattering of electron by atoms and crystals. II. The effects of finite source size", Acta Cryst. 12, 353-359

[94] Cowley, J. M. and Moodie, A. F. (1959). "The scattering of electrons by atoms and crystals. III. Single-crystal diffraction patterns", Acta Cryst. 12, 360-375

[95] Shuman, H. (1977). "Bragg diffraction imaging of defects at crystal surfaces", Ultramicroscopy, 2, 361-369

[96] Hirsch, S. P., Howie, A., Nicholson, P. B., Pashley, D. W. and Whelan, M. J. (1977). Electron microscopy of thin film 2nd Edit. p248-249

[97] Van Dyck, D. (1980). "The real space method for dynamical electron diffraction calculations in high resolution electron microscopy. I. Principles of the method", Ultramicroscopy, 15, 29-40

References for Chapter II

[1] Metherell, A. J. (1975). Electron microscopy in materials science Eds. Valdre, U. and Ruedl, E. Vol.2, p401-550

[2] Bethe, H. (1928). "Theorie der Beugung von Elektronen an Kristallen", Ann. Phys. 5, 55-129

[3] Stern, R. M., Perry, J. J. and Bondreaux, D. S. (1969). "Low-energy electron-diffraction surfaces and band structure in three dimensional mixed Laue and Bragg reflection", Rev. Mod. Phys. 41, 275-295

[4] Faddeeva, V. N. (1959). Computational method of linear algebral, New York: Dove, 231-260

[5] Moon, A. R. (1972). "Calculation of reflection intensities for medium and high energy electron diffraction", Z. Naturforsch, A27, 390-395

[6] Kohra, K., Moliere, K., Nakano, S. and Ariyama, M. (1962). "Anomalous intensity of mirror reflection from the surface of single crystal", Jpn. J. Phys. Soc. 17, B-II, 82-85

[7] Miyake, S. Hayakawa, K. and Mida, R. (1986). "Variation of emission yield of X-ray from crystals with diffraction condition of exciting electrons", Acta Cryst. A24, 182-191

[8] Azaroff, K. (1970). X-Ray Diffraction, p230

[9] Kouach, L. D. (1985). Advanced Engineering Mathematics, p598

[10] Pari, A. Z. (1985). Nonrelativistic Quantum Mechanics, p73

[11] Marks, L. D. and Ma, Y. (1988). "Current flow in reflection electron microscopy and RHEED", Acta Cryst. A44, 392-393

[12] Colella, R. and Menandue, J. F. (1972). "Comparison of experimental and n-beam calculated intensities for glancing incidence high-energy electron diffraction",

Acta Cryst. A28, 16-22

[13] Miyake, S. and Hayakawa, K. (1970). "Resonance effects in low and high energy electron diffraction by crystals", Acta Cryst. A26, 60-70

[14] Miyake, S., Kohra, K. and Takagi, M. (1954). "The nature of the specular reflection of electrons from a crystal surface", Acta Cryst. 7, 393-401

References for Chapter III

[1] Peng, L. M. and Cowley, J. M. (1986). "Dynamical diffraction calculations for RHEED and REM", Acta Cryst. A42, 545-552

[2] Cowley, J. M. and Moodie, A. F. (1957). "The scattering of electrons by atoms and crystals. I. Anew theoretical approach", Acta Cryst. 10, 609-619

[3] Cowley, J. M. and Moodie, A. F. (1959). "The scattering of electrons by atoms and crystals. II. The effects of finite source size", Acta Cryst. 12, 353-359

[4] Ishizuka, K. and Uyeda, N. (1977). "A new theoretical and practical approach to the multislice method", Acta Cryst. A33, 740-749

[5] Gaskill, J. D. (1978). Linear system, Fourier transforms, p364, p366

[6] Eckart, C. (1948). "The approximate solution of one-dimensional wave equations", Rev. Mod. Phys. 20, 399-417

[7] Lynch, D. F. (1971). "Out-of-zone in dynamic electron diffraction intensities from gold", Acta Cryst. A27, 399-407

[8] Goodman, P. and Moodie, A. F. (1974). "Numerical evaluation of n-beam wave function in electron scattering by the multi-slice method", Acta Cryst. A30, 280-290

[9] Self, P. G., O'Keefe, M. A., Buseck, P. R. and Spargo, A. E. C. (1983), Ultramicroscopy, 11, 35-52

[10] Peng, L. M. and Cowley, J. M. (1988). "Errors arising from numerical use of the Mott formula in electron image simulation", Acta Cryst. A44, 1-5

[11] Howie, A. (1988). personal communication.

[12] Britze, K. and Meyer-Ehmsen, G. (1978). "High energy electron diffraction at Si(001) surfaces", Surface Sci. 77, 131-141

References for Chapter IV

[1] Hirsch, P., Howie, A., Nicholson, R. B., Pashley, D. W. and Whelan, M. J. (1977). Electron microscopy of thin crystal 2nd Edit. p195-271

[2] Nishikawa, S. and Kikuchi, S. (1928). "Diffraction of cathode rays by calcite", Nature, 122, 726

[3] Nishikawa, S. and Kikuchi, S. (1928). "Diffraction of cathode rays by calcite", Nature, 121, 1019-1020

[4] Somorjai, G. A. (1981). Chemistry in two dimensions: Surface, p126

[5] Somorjai, G. A. (1978). "Surface science", Science, 201, 489-497

[6] Ploog, K. (1986). "Molecular beam epitaxy of semiconductor quantum wells and superlattices", J. Cryst. Growth, 79, 887-889

[7] Ellis, W. P. and Schwoebel, R. L. (1968). "LEED from surface steps on UO_2 single crystals", Surface Sci. 11, 82-98

[8] Henzer, M. (1970). "LEED-investigation of step arrays on cleaved germanium (111) surfaces", Surface Sci. 19, 159-171

[9] Hottier, F., Theeten, J. B., Masson, A. and Domange, J. L. (1977). "Comparison LEED and RHEED examine of stepped surfaces; application to Cu(111) and GaAs(001) vicinal surfaces", Surface Sci. 65, 563-577

[10] Kikuchi, S. and Nakagawa, S. (1933). "Die anomale Reflection der schnellen Elecktronen an die Einkristalloberflache", Sci. Rap. Inst. Phys. Chem. Res. (Tokyo), 21, 256-265

[11] Miyake, S. and Hayakawa, K. (1970). "Resonance effects of low oxygen pressure studied by insitu reflection electron microscopy", Acta Cryst. A26, 60-70

[12] Pukite, P. R., Van Hove, J. M. and Cohen, P. I. (1983).

"Sensitive reflection high-energy electron diffraction measurement of the local misorientation of vicinal GaAs surfaces", Appl. Phys. Lett. 44, 456-458

[13] Pukite, P. R. and Cohen, P. I. (1987). "Multilayer steps formation after As adsorption on Si(100): nucleation of GaAs on vicinal Si", Appl. Phys. Lett. 50, 1739-1741

[14] Hsu, T. and Cowley, J. M. (1983). "Reflection electron microscopy(REM) of vicinal surfaces of fcc metals", Ultramicroscopy, 11, 239-250

[15] Ino, S. (1977). "Some new techniques in reflection high energy electron diffraction (RHEED) application to surface studies", Jpn. J. Appl. Phys. 16, 891-908

[16] Ino, S. (1980). "An investigation of the Si(111)7x7 surface structure by RHEED", Jpn. J. Appl. Phys. 19, 1277-1290

[17] Cowley, J. M. and Rees, A. L. G. (1946). "Reflection effects in electron diffraction", Nature, 158, 550-551

[18] Honjo, G. (1947). "Anomalies in electron-diffraction Degye-Scherrer ring", J. Phys. Soc. Japan, 2, 133-140

[19] Marks, L. D. and Ma, Y. (1989). "Current flow in reflection electron microscopy and RHEED", Acta Cryst. A45, 392-393

[20] Ma, Y. and Marks, L. D. (1989). "Bloch-wave solution in the Bragg case", Acta Cryst. A45, 174-182

[21] Hirsch, P., Howie, A., Nicholson, P. B., Pashley, D. W. and Whelan, M. J. (1977). Electron microscopy of thin crystals, 2nd Edit. (1977) p202

[22] Metherell, A. J. F. (1976). "Diffraction of electron by perfect crystal" in Electron microscopy in materials science, 1976, Vol. 2, 469-500

[23] Miyake, S., Kohra, K. and Takagi, M. (1954). "The nature of the specular reflection of electrons from a crystal surface", Acta Cryst. 7, 393-401

[24] McRae, E. G. (1966). "Multiple-scattering treatment of

low-energy electron-diffraction intensities", J. Chem, Phys. 45, 3258-3276

[25] McRae, E. G. and Caldwell, C. W. (1967). "Observation of multiple scattering resonance effects in low energy electron diffraction studies of LiF, NaF and graphite", Surface Sci. 7, 41-67

[26] McRae, E. G. (1971). "Surface-state resonances in low-energy electron diffraction", Surface Sci. 25, 491-512

[27] McRae, E. G. and Caldwell, C. W. (1976). "Elastic-scattering resonances observed in very low energy electron reflection at oxygenated Ni(001) surfaces", Surface Sci. 57, 63-76

[28] McRae, E. G. and Caldwell, C. W. (1978). "Electronic surface resonances and crystal surface structure", Surface Sci. 74, 285-306

[29] Gersten, J. I. and McRae, E. G. (1972). "Low-energy electron diffraction amplitudes", Surface Sci. 29, 483-500

[30] McRae, E. G. (1979). "Electronic surface resonances of crystals", Rev. Mod. Phys. 51, 541-568

[31] Marten, H and Meyer-Ehmsen, G. (1985). "Resonance effects in RHEED from Pt(111)", Surface Sci. 151, 570-584

[32] Maksym, P. A. and Beeby, J. L. (1981). "A theory for RHEED", Surface Sci. 110, 423-438

[33] Peng, L. M. and Cowley, J. M. (1986). "Dynamical diffraction calculations for RHEED and REM", Acta Cryst. A42, 545-552

[34] Wang, Z. L., Liu, J., Lu P. and Cowley, J. M. (1989). "Electron resonance reflections from perfect crystal surfaces and surfaces with steps", Ultramicroscopy, 27, 101-112

[35] Schiff, L. I. (1971). Quantum mechanics, 3rd Edit. p127-129

[36] Feshbach, H. (1958). "Unified theory of nuclear

reactions". Ann. Phys. 5, 357-390

[37] Smyth, C. P. (1955). Dielectric behavior and structure, 1955, p23

[38] Kohra, K., Moliere, K., Nakano, S. and Ariyama, M. (1962). "Anomalous intensity of mirror reflection from the surface of a single crystal", Jpn. J. Phys. Soc. 17(Sup.) B-II, 82-85

[39] Britze, K. and Meyer-Ehmsen, G. (1978). "High energy electron diffraction at Si(001) surfaces", Surface Sci. 77, 131-141

[40] Colella, R. (1972). "N-beam dynamical diffraction of high-energy electrons at glancing incidence general theory and computational methods", Acta Cryst. A28, 11-15

[41] Moon, A. R. (1972). "Calculation of reflected intensities for medium and high energy electron diffraction", Z. Naturforsch, 27A, 390-395

[42] Peng, L. M. and Cowley, J. M. (1988). "Surface resonance effects and beam convergence in REM", Ultramicroscopy, 26, 161-168

[43] Cowley, J. M. and Moodie, A. F. (1957). "The scattering of electron by atoms and crystals", Acta Cryst. 10, 609-619

References for Chapter V

[1] Ma, Y. and Marks, L. D. (1989). "Bloch-wave solution in the Bragg case", Acta. Cryst. A45, 174-182

[2] Ma, Y. and Marks, L. D. (1989). "Bloch waves and multislice in transmission and reflection diffraction", Submitted to Acta Cryst. in press.

[3] Sewell, P. B. and Cohen, M. (1965). "The observation of gas adsorption phenomena by reflection high-energy electron", Appl. Phys. Let. 7, 32-34

[4] Mitchell, D. F., Simmons, G. W. and Kenneth, R. L. (1965). "Comparison of low-energy electron diffraction and low-angle, high-energy electron diffraction techniques for the observation of chemisorption", Appl. Phys. Let. 7, 172-175

[5] Simmons, G. F., Mitchell, D. F. and Kenneth, R. L. (1967). "LEED and HEED studies of the interaction of oxygen with single crystal surfaces of copper", Surface Sci. 8, 130-164

[6] Siegel, B. M. and Menadue, J. F. (1967). "Quantitative reflection electron diffraction in a ultra high vacuum camera", Surface Sci. 8, 206-216

[7] Trepte, L., Menzel-Kopp, C. and Menzel, E. (1967). "Surface structures on spherical copper crystals after adsorption of oxygen", Surface Sci. 8, 223-232

[8] Ino, S. (1977). "Some new techniques in reflection high energy electron diffraction (RHEED) application to surface structure studies", Jpn. J. Appl. Phys. 16, 891-908

[9] Ino, S. (1980). "An investigation of the Si(111)7x7 surface structure by RHEED", Jpn, J. Appl. Phys. 19, 1277-1290

[10] Somorijai, G. A. (1981). Chemistry in two dimension: surface, 1st Edit. p126

[11] Osakabe, N., Tanishiro, Y., Yagi, K. and Honjo, G.

(1980). "Reflection electron microscopy of the phase transition between the (7x7) and (1x1) structures of clean (111) silicon surfaces", Surface Sci. 97, 393-408

[12] Osakabe, N., Tanishiro, Y., Yagi, K. and Honjo, G. (1981). "Image contrast of dislocations and atomic steps on (111) silicon surface in reflection electron microscopy", Surface Sci. 102, 424-442

[13] Hsu, T. and Cowley, J. M. (1983). "Reflection electron microscopy (REM) of fcc metals", Ultramicroscopy, 11, 239-250

[14] Hsu, T., Iijima, S. and Cowley, J. M. (1984). "Atomic and other structures of cleared GaAs(110) surfaces", Surface Sci. 137, 551-569

[15] Shimizu, N., Tanishiro, Y., Kobayshi, K., Takayanagi, K. and Yagi, K. (1985). "Reflection electron microscope study of the initial stages of oxidation of Si(111)7x7 surfaces", Ultramicroscopy, 18, 453-462

[16] Cowley, J. M. and Peng, L. M. (1985). "The image contrast of surface steps in reflection electron microscopy", Ultramicroscopy, 16, 59-68

[17] Turner, P. S. and Cowley, J. M. (1981). "STEM and CTEM observations of interference between Laue- and Bragg-diffracted electrons in images of polyhedral crystals", Ultramicroscopy, 6, 125-138

[18] Peng, L. M. and Cowley, J. M. (1986). "Dynamical diffraction calculation for RHEED and REM", Acta Cryst. A42, 545-552

[19] Kikuchi, S. and Nakagawa, S. (1933). "The anomalous reflection of fast electrons from the surfaces of single crystals. II.", Sci. Pap. Inst. Phys. Chem. Res. (Tokyo), 2, 256-265

[20] Marks, L. D. and Ma, Y. (1989). "Dynamical theory of spot splitting in RHEED", Ultramicroscopy, 29, 183-191

[21] Miyake, S., Kohra, K. and Takagi, M. (1954). "The nature of the specular reflection of electrons from a crystal surface", Acta Cryst. 7, 393-401

[22] McRae, E. G. (1979). "Electronic surface resonances of crystals", Re. Mod. Phys. 5, 357-390

[23] Cho, A. Y. (1971). "GaAs epitaxy by a molecular beam method: observation of surface structure", J. Appl. Phys. 42, 2074-2081

References for Chapter VI

[1]   Bourgoin, J. C. and Corbett, J. W. (1972). "A new mechanism for interstitial migration", Phys, Lettes. 38A, 135-137

[2]   Luzzi, D. (1986). "The electron irradiation induced crystalline to amorphous transition in Cu-Ti intermetallic compounds", PhD thesis at Northwestern University, USA, p269

[3]   Fisher, S. B. (1970). "On the temperature rise in electron irradiated foils", Rad. Eff. 5 (1970) 239-243

[4]   Marks, L. D., Petford, A. K. and O'Keeffe, M. (1985). "Electron beam induced desorption: W on WO_3", Proc. 43rd Ann EMSA, 266-267

[5]   Petford, A. K., Marks, L. D. and O'Keeffe, M. (1986). "Atomic imaging of oxygen desorption from tungsten trioxide", Surface Sci. 172, 496-508

[6]   Feibelman, P. J. and Knotek, M. L. (1978). "Reinterpretation of electron-stimulated desorption data from chemisorption systems", Phys. Rev. B18, 6531-6537

[7]   Menzel, D. and Gomez, R. (1964). "Desorption from surfaces by slow-electron impact", J. Chem. Phys. 40, 1164-1165

[8]   Knotek, M. L. and Feibelman, P. J. (1978). "Ion desorption by core-hole Auger decay", Phys. Rev. Lett. 40, 964-967

[9]   Knotek, M. L. (1983). "Surface chemical information from electron- and photon-stimulated desorption", Phys. Scripta, T6, 94-103

[10]   Knotek, M. L. (1984). "Stimulated desorption from surfaces", Phys. Today, September 1984, 24-32

[11]   Doll, J. D. and McDowell, H. K. (1982). "Theoretical studies of surface diffusion: self-diffusion in the fcc system", J. Chem. Phy. 77, 479-483

[12] Chern, D., Finnis, M. W. and Mathews, M. D. (1977). "Sputtering of gold foils in a high voltage electron microscope a comparison of theory and experiment", Phil. Mag. 35, 693-714

Appendix 2.1

If the current flow $\underline{S}$ is conserved along MN (Fig.2.2), we have:

$$\lim_{t\to 0}\int \underline{S}d\underline{S}=-A^+S_\perp(\underline{r}^+,E)+A^-S_\perp(\underline{r}^-,E)$$

$$=A^+[S_\perp(\underline{r}^+,E)-S_\perp(\underline{r}^-,E)]$$

$$=0 \qquad\qquad (A2.1.1)$$

Then,

$$S_\perp(\underline{r}^-,E)=S_\perp(\underline{r}^+,E) \qquad\qquad (A2.1.2)$$

Therefore, for $\rho_\perp$, we have:

$$\lim_{t\to\infty}\int \rho_\perp d\underline{S}=A^+[\rho_\perp(\underline{r}^-)-\rho_\perp(\underline{r}^+)]$$

$$=A^+[\int_0^\infty ES_\perp(\underline{r}^-,E)\,dE-\int_0^\infty ES_\perp(\underline{r}^+,E)\,dE]$$

$$=A^+\int_0^\infty E[S_\perp(\underline{r}^-,E)-S_\perp(\underline{r}^+,E)]\,dE$$

$$=A^+\int_0^\infty E.0dE=0 \qquad\qquad (A2.1.3)$$

Then,

$$\rho_\perp(\underline{r}^-)=\rho_\perp(\underline{r}^+) \qquad\qquad (A2.1.4)$$

Conversely, if $\underline{\rho}$ is conserved along MN, i.e. $\rho_\perp(\underline{r}^-)=\rho_\perp(\underline{r}^+)$, we have:

$$\int_0^\infty E[S_\perp(\underline{r}^-, E) - S_\perp(\underline{r}^+, E)]dE = 0 \qquad (A2.1.5)$$

The continuity of $S_\perp$ with respect to E leads to (A2.1.2).

Appendix 2.2

In the real world, all the waves are in the form of wave packets since the momentum of a real system always has a continuous distribution. In particular, a wave packet in one dimension can be formed by superposition of plane waves:

$$\psi(x,t) = \int_{-\infty}^{\infty} f(k) \exp[i2\pi(kx - E(k)t/h)]dk \qquad (A2.2.1)$$

where $k = k^r + ik^i$ and we assure that the momentum of a plane wave is only distributed along the real axis and the plane wave has the same rate of decay for the simplicity. Therefore, we have:

$$\psi(x,t) = \exp[i2\pi k^i x] \int_{-\infty}^{\infty} f(k^r) \exp[i2\pi(k^r x - E(k)t/h]dk^r \qquad (A2.2.2)$$

$f(k^r)$ is considered as a smooth and well behaved function concentrated in the region Δk^r around $k^r = k_o^r$. Expanding $E(k)$ around $k^r = k_o^r$ on the real axis of k, we have:

$$E(k) = E(k_o^r + ik^i) + (k^r - k_o^r)dE(k^r + ik^i)/dk^r_{|kro} + \ldots \ldots \qquad (A2.2.3)$$

Substituting (A2.2.3) into (A2.2.2), we get:

$$\psi(x,t) = \exp[i2\pi(k_o^r x - E(k_o^r + ik^i)t/h)]\exp[-2\pi k^i x] x$$

$$\int_{k_o^r - \Delta k^r}^{k_o^r + \Delta k^r} dk^r f(k^r) \exp[i2\pi(k^r - k_o^r)(x - dE(k_o^r)/dk^r.t)]$$

$$=\exp[i2\pi k_o^r x - E(k_o^r)t/h]\exp[-2\pi k^i x]F(x-dE(k_o^r)/dk^r.t) \quad (A2.2.4)$$

F is an envelope function, the Fourier transform of f. The phase velocity of the monochromatic wave is:

$$v^p = E(k_o^r)/hk_o^r \quad\quad\quad (A2.2.5)$$

The group velocity is:

$$v_g = dE(k_o^r)/d(hk^r) \quad\quad\quad (A2.2.6)$$

Appendix 2.3

The current flow of a matter wave is:

$$\underline{S}^{(j)}=(h/im)\,[\psi^{(j)*}(\underline{r})\,\nabla\psi^{(j)}(\underline{r})-\psi^{(j)}(\underline{r})\,\nabla\psi^{(j)*}(\underline{r})] \qquad (A2.3.1)$$

The wave in the form of the Bloch wave can be expressed by

$$\psi^{(j)}(\underline{r})=\sum_{\underline{q}}C_{\underline{q}}^{(j)}\exp[i2\pi(\underline{k}^{(j)}+\underline{q})\cdot\underline{r}] \qquad (A2.3.2)$$

and

$$\psi^{(j)*}(\underline{r})=\sum_{\underline{q}}C_{\underline{q}}^{(j)*}\exp[-i2\pi(\underline{k}^{(j)*}+\underline{q})\cdot\underline{r}] \qquad (A2.3.3)$$

Then,

$$\nabla\psi^{(j)}(\underline{r})=\sum_{\underline{q}}i2\pi(\underline{k}^{(j)}+\underline{q})\,C_{\underline{q}}^{(j)}\exp[i2\pi(\underline{k}^{(j)}+\underline{q})\cdot\underline{r}] \qquad (A2.3.4)$$

$$\nabla\psi^{(j)*}(\underline{r})=\sum_{\underline{q}}(-i2\pi)(\underline{k}^{(j)*}+\underline{q})\,C_{\underline{q}}^{(j)*}\exp[-i2\pi(\underline{k}^{(j)*}+\underline{q})\cdot\underline{r}] \qquad (A2.3.5)$$

From (A2.3.3) and (A2.3.4), we obtain:

$$\psi^{(j)*}(\underline{r})\,\nabla\psi^{(j)}(\underline{r})=\sum_{\underline{q}'}\sum_{\underline{q}}i2\pi(\underline{k}^{(j)}+\underline{q})\,C_{\underline{q}}C_{\underline{q}'}^{(j)*}\exp[i2\pi(\underline{k}^{(j)}-\underline{k}^{(j)*}+\underline{q}-\underline{q}')\cdot\underline{r}]$$

$$(A2.3.6)$$

From (A2.3.1) and (A2.3.5), we get:

$$\psi^{(j)}(\underline{r})\,\nabla\psi^{(j)*}(\underline{r})=\sum_{\underline{q}'}\sum_{\underline{q}}-i2\pi(\underline{k}^{(j)*}+\underline{q})\,C_{\underline{q}}^{(j)*}C_{\underline{q}'}^{(j)}\exp[i2\pi(\underline{k}^{(j)}-\underline{k}^{(j)*}+\underline{q}'-\underline{q})\cdot\underline{r}]$$

$$(A2.3.7)$$

Therefore,

$$\underline{S}(\underline{r})=(h/2im)\,(\sum_{\underline{q}'=\underline{q}}+\sum_{\underline{q}'}\sum_{\underline{q}}') \qquad (A2.3.8)$$

where

$$\sum_{\underline{q}'=\underline{q}}=\exp[-i2\pi\underline{k}^{i(j)}\cdot\underline{r}]\sum_{\underline{q}}i2\pi[(\underline{k}^{(j)}+\underline{q})+(\underline{k}^{(j)*}+\underline{q})]\,|C_{\underline{q}}^{(j)}|^{2}$$

and $\sum_{\underline{q}'}\sum_{\underline{q}}'$ is the crossing term. We have:

$$\int_{\Omega} \Sigma_{\underline{q}'} \Sigma_{\underline{q}} \cdot d\underline{S} = 0 \qquad (A2.3.9)$$

The superscripts r and i denote the real and imaginary parts of $\underline{k}$ vector respectively. Ω is the area of a unit cell. Finally, we have:

$$\underline{S} = (2\pi h/m) \exp[-2\pi \underline{k}^{i(j)} \cdot \underline{r}] \Sigma_{\underline{q}} |C_{\underline{q}}^{(j)}|^2 (\underline{k}^{r(j)} + \underline{q}) \qquad (A2.3.10)$$

Appendix 2.4

The continuity equation of probability is given by the following:

$$dP(\underline{r},t)/dt + \nabla.\underline{S} = -2V_i(\underline{r})P(\underline{r},t) \qquad (A2.4.1)$$

Since ψ is a stationary solution, we have:

$$dP/dt = d(\psi\psi^*)/dt = 0 \qquad (A2.4.2)$$

Then,

$$\nabla.\underline{S} = -2V_i/h(\psi\psi^*) \qquad (A2.4.3)$$

Substituting (A2.3.2), (A2.3.3) and (A2.3.9) into (A2.4.3), we obtain:

$$\nabla.\underline{S} = (-4\pi^2 h/m)\exp[-2\pi\underline{k}^{i(j)}.\underline{r}][\Sigma_q|C_q^{(j)}|^2(\underline{k}^{r(j)}+\underline{q}).(\underline{k}^{i(j)})]$$

$$= -2\pi\underline{S}\underline{k}^{i(j)} \qquad (A2.4.4)$$

and

$$\psi\psi^* = \Sigma_q|C_q^{(j)}|^2\exp[-4\pi\underline{k}^{i(j)}.\underline{r}] +$$

$$\exp[-4\pi\underline{k}^{i(j)}.\underline{r}]\Sigma_{q'}\Sigma_q C_q^{(j)}C_{q'}^{(j)*}\exp[i2\pi(\underline{q}-\underline{q}').\underline{r}] \qquad (A2.4.5)$$

$$-2\pi\underline{S}.\underline{k}^{i(j)} = -(2V_i(\underline{r})/h)[\Sigma_q|C_q^{(j)}|^2\exp[-4\pi\underline{k}^{i(j)}.\underline{r}] + \Sigma_q\Sigma_{q'}] \qquad (A2.4.6)$$

After integrating over a unit cell, we obtain:

$$-2\pi\underline{\hat{S}}\underline{k}^{i(j)} = (2/h)\int_V \exp[-4\pi\underline{k}^{i(j)}\underline{r}]V_i(\underline{r})d\underline{r} \qquad (A2.4.7)$$

where $\underline{\hat{S}}$ is the average value of $\underline{S}$ over one unit cell and it has the same orientation as $\underline{S}$ does. Since the right hand side of (A2.4.7) is necessarily positive, we have:

$$\underline{S}.\underline{k}^{i(j)} \geq 0 \qquad (A2.4.8)$$

Appendix 3.1

The phase term of the propagation function $p(\underline{b}'-\underline{b}_o, z'-z_o)p(\underline{b}-\underline{b}', z-z')$ can be expressed as:

$$\Theta(\underline{r}, \underline{r}', \underline{r}_o) = kf(\underline{r}, \underline{r}', \underline{r}_o) = k(|\underline{r}'-\underline{r}_o| + |\underline{r}-\underline{r}'|) \qquad (A3.1.1)$$

The constant phase hypersurface $f(\underline{r}, \underline{r}', \underline{r}_o) = d$ is a prolate spheroid S_p with its major axis $\underline{r}_o\underline{r}$ (Fig.3.2). The foci of S_p are $\underline{r}_o$ and $\underline{r}$. The intersection of S_p with plane $z=z'$ is a ellipse S_e. In other words the constant phase curves on plane $z=z'$, $\Theta(\underline{b}')=$const. are a series of ellipses with center $\underline{r}_a$ and foci on $\underline{r}_1$ and $\underline{r}_2$. According to the principle that the shortest distance between two points is the straight line connecting the two points, $d(x', y')$ has one and the only one extreme at $\underline{r}_c$ which is the global minimum. That is:

$$\nabla_{\underline{b}'}d(\underline{b}')_{|\underline{r}'_o\to0} = 0 \qquad (A3.1.2)$$

The range for the validity of stationary phase approximation can be estimated as follows. For simplicity, let's suppose $\underline{b}_o=\underline{b}$. Then $\underline{r}-\underline{r}_o$ is coincident with the z axis. Then the origin is translated to $\underline{r}_o$ and the equation of S_p is given by:

$$\frac{\underline{r}'^2}{a'^2} + \frac{z'^2}{(d^2/4)} = 1 \qquad (A3.1.3)$$

where $a'^2=d^2/4-c^2$ and $c=(z-z_o)/2$. $\underline{r}'$ is the vector in the plane

at z=z'. Then,

$$d^2(\underline{r}')=2[(\underline{r}'^2+z'^2+c^2)+\sqrt{((\underline{r}'^2+z'^2+c^2)^2-4c^2'z^2)}] \qquad (A3.1.3)$$

Let

$$\frac{d(d^2(\underline{r}'))}{dr'} = 2[2r'+\frac{2(r'^2+z'^2+c^2)r'}{\sqrt{(r'^2+z'^2+c^2)^2-4c^2z'^2}}]$$

$$= 4[1 + \frac{2(r'^2+z'^2+c^2)}{\sqrt{(r'^2+z'^2+c^2)^2-4c^2z'^2}}]r'=0$$

Then r'=0. Therefore,

$$d^2(0)=2[z'^2+c^2+c^2-z'^2]=4c^2 \quad (|z'|<c)$$

or

$$d(0)=2c$$

Thus we have:

$$\frac{d(d(r'))}{dr'} = \frac{2}{d(r')}[1 + \frac{2(r'^2+z'^2+c^2)}{\sqrt{(r'^2+z'^2+c^2)^2-4c^2z'^2}}]r' \qquad (A3.1.5)$$

Then the derivative of d versus r' at the area close to r'=0 is

approximately given by:

$$\frac{d(d(r'))}{dr'}\bigg|_{r'\approx0} \approx \frac{1}{c}(1 + \frac{2(c^2+z'^2)}{|c^2-z'^2|})r' \qquad (A3.1.6)$$

Since 0<|z'|<c, we have:

$$\frac{d(d(r'))}{dr'}\bigg|_{r'\approx0} \geq \frac{3}{c}r' = 6\frac{r'}{(z-z_o)}$$

or

$$\frac{d\Theta(r')}{dr'}\bigg|_{r'=0} \geq 6\ k\ \frac{r'}{(z-z_o)} \qquad (A3.1.7)$$

There should be $d\Theta(r')/dr' \geq 2\pi/r'\text{Å}^{-1}$. Substituting these conditions into (A3.1.7), we have:

$$\frac{6r'}{\lambda(z-z_o)} \geq 1$$

or $\qquad\qquad (z-z_o) \geq 6r'^2/\lambda \qquad\qquad (A3.1.8)$

(A3.1.8) is quite close to the one given by Ishizuka et al.[4]:

$$\frac{2\pi r'}{\lambda(z-z_o)} \geq 1 \qquad\qquad (A3.1.9)$$

If the sampling rate is 10/Å, it means that the crystal potential is considered slow variation on the scale of 0.1Å, i.e. $r'=0.1$Å. For 100keV electron, $\lambda=0.037$Å. Then,

$$z-z_o \geq 1.64\text{Å}$$

Appendix 3.2

The 3-D dependence of the Bloch wave in the Laue case is well known as far as only the zero-Laue zone is concerned, however the 2-D dependence of the Bloch wave in the Bragg case still appears confusion. Here is a simple analytical proof of it.

Let us refer to Equation (2.3), (2.36)-(2.54) which actually can be found in text books about electron diffraction. The key element in (2.3) is:

$$K^2 - (\underline{k}^{(j)} + \underline{g})^2 \qquad (A3.2.1)$$

(A3.2.1) can be expanded as the following, if the z axis is chosen as inward normal to the crystal surface:

$$K^2 - (k_x + g_x)^2 - (k_y + g_y)^2 - (k_z^{(j)} + g_z)^2 \qquad (A3.2.2)$$

For the Bragg case, in the coordination used in the thesis, the zero-Laue-zone-only means $g_y=0$. If we consider the boundary condition (2.50), then both k_y and g_y can be cancelled in (A3.2.2). Consequently, the eigenvectors $\{C_g^{(j)}\}$ as the solutions of dispersion Equation (2.5) are independent of both k_y and g_y. Therefore, the coefficients of the Bragg reflected waves in vacuum $\{R_g\}$ and the coefficients of the Bloch waves in crystal $\{\varepsilon^{(j)}\}$ as the solutions of Equation (2.51-52) and (2.53-54) are also independent of both k_y and g_y. So the plane

wave phase factor $\exp[i2\pi(k_y + g_y).y]$ undoubtedly can be factored out of the summation symbol Σ in both Equation (2.2) and (2.3). In other words, it will not affect the intensity of the wave field and the intensity of the wave field is independent of y, i.e. the thickness along the direction of incident beam. All these arguments are also valid for reflected waves in vacuum.

However, this is not true for the Laue case. For the Laue case, the zero-Laue-zone-only means $g_z=0$. Then none of the three coordinates in (A3.2.2) can be eliminated by the boundary conditions in Equation (2.51-52). Therefore, the Bloch wave in the Laue case is 3-D dependent, while the Bloch wave in the Bragg case is 2-D dependent, as far as only the zero Laue zone is concerned.

<u>VITA</u>

<u>Name</u>: Ma, Yiqun. **<u>Date of Birth</u>:** June 30, 1956 at Shanghai, P. R. China. **<u>Education</u>:** July, 1982 – B.S. (E.E.) Xi'an Jiaotong University, Xi'an, P. R. China. Dec., 1989 – Ph.D. (M.S.) Northwestern University, Eavnston, IL 60208, U. S. A. **<u>Experience</u>:** Research Assistantship, 1985-1989, Northwestern University, U.S.A. **<u>Address</u>:** Department of Materials Science and Engineering, Northwestern University, 2145 Sheridan Road, Evanston, IL 60208, U.S.A.

Dissertation:
   "Dynamical theory for high energy electron reflection"

Publication:
   1) "Knockon Surface Diffusion" by Y. Ma and L. D. Marks. G. W. Bailey, Ed., Proceedings of the 44th Annual Meeting of the Electron Microscopy Society of America. 394-395
   2) "Current Flow in Reflection Electron Microscopy and RHEED" by L. D. Marks and Y. Ma. Acta Cryst. (1988). A44, 392-393
   3) "Bloch Wave Solution in the Bragg Case" by Y. Ma and L. D. Marks. Acta Cryst. (1989). A45, 174-182
   4) "Bloch Waves and Multislice in Transmission and Reflection Diffraction" by Y. Ma and L. D. Marks. Acta Cryst., in press
   5) "Dynamical Theory of Spot Splitting in REM and RHEED" by L. D. Marks and Y. Ma. Ultramicroscopy (1989). 29, 183-191
   6) "Ballistic Surface Diffusion" by Y. Ma and L. D. Marks Submitted to Ultramicroscopy, in press.
   7) "Self-Consistent Solution of the Reflection Diffraction Problem" by L. D. Marks and Y. Ma. Submitted to Ultramicroscopy, in press.
   8) "Surface Phenomena in RHEED and RHEEM" by Y. Ma and L. D. Marks. Submitted to Acta Cryst.